TU Delft

Delft University of Technology

Autonomous crack healing in Cr_2AlC and Ti_2AlC MAX phase

Shen, Lu

DOI
10.4233/uuid:bece20f8-1d72-425e-b4b1-5d817e54f762

Publication date
2016

Document Version
Final published version

Citation (APA)
Shen, L. (2016). *Autonomous crack healing in Cr_2AlC and Ti_2AlC MAX phase*. [Dissertation (TU Delft), Delft University of Technology]. https://doi.org/10.4233/uuid:bece20f8-1d72-425e-b4b1-5d817e54f762

Important note
To cite this publication, please use the final published version (if applicable).
Please check the document version above.

Copyright
Other than for strictly personal use, it is not permitted to download, forward or distribute the text or part of it, without the consent of the author(s) and/or copyright holder(s), unless the work is under an open content license such as Creative Commons.

Takedown policy
Please contact us and provide details if you believe this document breaches copyrights.
We will remove access to the work immediately and investigate your claim.

This work is downloaded from Delft University of Technology.
For technical reasons the number of authors shown on this cover page is limited to a maximum of 10.

Autonomous crack healing in Cr_2AlC and Ti_2AlC MAX phase

Lu Shen

Autonomous crack healing in Cr_2AlC and Ti_2AlC MAX phase

Proefschrift

ter verkrijging van de graad van doctor
aan de Technische Universiteit Delft,
op gezag van de RectorMagnificus prof. ir. K.C.A.M. Luyben,
voorzitter van het College voor Promoties,
in het openbaar te verdedigen op
dinsdag 22 november 2016 om 10:00 uur

door

Lu Shen

Master in Materials Science and Engineering
Delft University of Technology
geboren te Jinhua, Zhejiang, China.

This dissertation has been approved by

Promotor: Prof. dr. ir. S. van der Zwaag and
Copromotor: Dr. ir. W. G. Sloof

Composition of the doctoral committee:

Rector Magnificus	Delft University of Technology
Prof. dr. ir. S. van der Zwaag	Delft University of Technology, promotor
Dr. ir. W. G. Sloof	Delft University of Technology, copromotor

Independent members:

Prof. dr. J. M. Schneider	RWTH Aachen
Prof. dr. ir. K. van Breugel	Delft University of Technology
Prof. dr. I. M. Richardson	Delft University of Technology
Prof. dr. R. F. Mudde	Delft University of Technology
Dr. ir. M. B. de Rooij	University of Twente

This work is funded by the German Research Foundation
(Deutsche Forschungsgemeinschaft, DFG, SPP 1568, SL184/1-2).

Keywords: Cr_2AlC , Ti_2AlC , Self-healing, Erosion , High temperature

Copyright © 2016 by Lu Shen

ISBN 978-94-6186-723-0

All rights reserved. No part of the materials protected by this copyright notice may be reproduced or utilized in any form or by any means, electronic or mechanical, including photocopy, recording or by any information storage and retrieval system, without written permission from the author.

Author email: shenluemma@gmail.com

Printed by Proefschriftmaken.nl

Contents

1 Introduction 1

1.1 Background 1

1.2 Scope and outline of the thesis 6

References 8

2 Synthesis of high-purity isotropic or textured Cr_2AlC bulk ceramics by SPS of pressure-less sintered powder 9

2.1 Introduction 10

2.2 Materials and Methods 11

2.2.1 Synthesis 11

2.2.2 Characterization 12

2.3 Results and Discussion 13

2.3.1 Pressure-less sintering 13

2.3.2 Spark Plasma Sintering 14

2.3.3 Mechanical properties 19

2.4 Conclusions 22

References 23

3 The high temperature oxidation behaviour of Cr_2AlC and silicon doped Cr_2AlC 27

3.1 Introduction 28

3.2 Experimental procedures 29

3.2.1 Sample synthesis and preparation 29

3.2.2 Experimental techniques. 30

3.2.2.1 Thermal gravimetric analysis 30

3.2.2.2 Microstructure and composition analysis 30

3.3 Results and discussion 32

3.3.1 Composition and microstructure 32

3.3.2 The Oxidation behaviour of Cr_2AlC 34

3.3.3 The oxidation behaviour of $Cr_2Al_{(0.93)}Si_{(0.07)}C$ 38
3.4 Conclusions 42
References 43
4 Repeated crack healing in MAX Phase ceramics revealed by 4D in situ synchrotron X-ray tomographic microscopy 45
4.1 Introduction 46
4.2 Methods 48
4.2.1 Material preparation 48
4.2.2 Mechanical testing rig and laser-based heating system 48
4.2.3 X-ray tomographic microscopy 49
4.3 Results 50
4.3.1 4D X-ray tomographic microscopy and thermomechanical testing 50
4.3.2 Crack initiation and healing 51
4.3.3 Crack healing kinetics 55
4.4 Discussion 57
References 58
5 Crack healing behaviour of Cr_2AlC MAX phase studied by X-ray tomography 61
5.1 Introduction 62
5.2 Experiment 63
5.3 Results 65
5.3.1 2D X-ray tomographic cross sections of crack at different healing stages 65
5.3.2 3D crack face gap maps at different stages of healing 67
5.3.3 Microstructure of healed area 69
5.4 Discussion 71
5.4.1 Dependence of crack healing kinetics on crack location 71
5.4.2 Healing mechanism of Cr_2AlC 75
5.4.3 The effect of chromium particles 77

5.5 Conclusions 80

References 80

6 Reducing the erosive wear rate of Cr_2AlC MAX phase ceramic by oxidative healing of local impact damage 83

6.1 Introduction 84

6.2 Materials and Methods 86

6.2.1 Synthesis of Cr_2AlC 86

6.2.2 Sample preparation 87

6.2.3 Erosion and healing experiments 87

6.2.4 Microstructure and compositional analysis 88

6.3 Results and discussion 89

6.3.1 Material characterization 89

6.3.2 Erosion of Cr_2AlC 89

6.3.3 Oxidation induced healing 92

6.4 Conclusions 94

References 95

7 The effect of microstructure, erodent and thermal healing on the erosion rate of Cr_2AlC MAX phase material under high velocity particulate impact conditions 99

7.1 Introduction 100

7.2 Experimental details 101

7.2.1 Sample preparation 101

7.2.2 Characterisation technique 102

7.2.3 Erosion test set up 103

7.3 Results and discussion 105

7.3.1 Composition, microstructure, hardness and toughness of Cr_2AlC 105

7.3.2 Erosion rates of as-produced Cr_2AlC as a function of the erodent type and target material properties 107

7.3.2.1 Effect of erodent type 107

7.3.2.2 Effect of target materials properties. 109
7.3.3 Effect of high temperature oxidation on erosion rate. 111
7.4 Conclusions 114
References 114
8 Demonstrating the self-healing behaviour of some selected ceramics under combustion chamber conditions 117
8.1 Introduction 118
8.2 Materials and Methods 121
8.2.1 Synthesis 121
8.2.2 Characterisation 122
8.2.3 Initiation of local crack damage 123
8.2.4 Crack healing in combustion chamber 126
8.3 Results 127
8.3.1 Materials Characterisation 127
8.3.2 Oxidation of TiC, Ti_2AlC and Cr_2AlC in air and combustion environments 128
8.4 Conclusions 132
References 133
Summary 137
Samenvatting 141
总结 145
Resumen 149
Acknowledgements 153
List of publications 157
Curriculum vitae 159

1 Introduction

1.1 Background

Jet turbine engines are very complex and expensive installations which have to operate very reliably under very demanding thermal and mechanical conditions. Operating reliably means that the construction is very resistant to damage formation, or more precisely to damage propagation. In the case of jet turbine blades it is not only the macroscopic stresses due to gravitational forces on the moving blades and high pressure differences on the stationary vanes, but also the impact of solid particles, such as airborne sands, exhausts and ash particles, contributes to local damage formation. Such erosion damage generally does not lead to component failure but can lead to massive material removal leading to significant dimensional changes and loss of efficiency of the engine [1-4]. Figure 1.1 shows the dimensional changes of a new turbine blade after a period of service under severe solid particle erosion conditions [5].

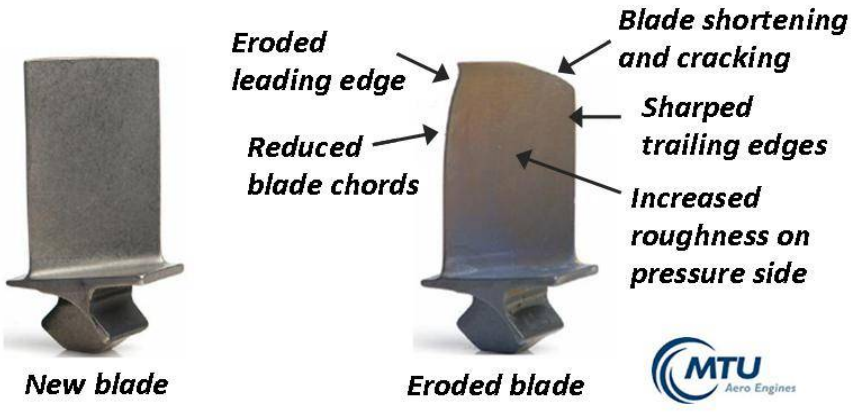

Figure 1.1 Turbine blade before (left) and after (right) operation with named damages. After [5]

To prevent such erosion damage the turbine blades can be coated with a hard coating which would reduce the local plastic deformation preceding the material removal and switch the erosion mechanism to chipping [6]. It has been proven that the erosion rate of

IN718 was dramatically reduced by applying a hard Cr_7C_3 coating but an even stronger reduction in wear rate was obtained for a Cr_2AlC coating which has a lower hardness than Cr_7C_3, see Figure 1.2.

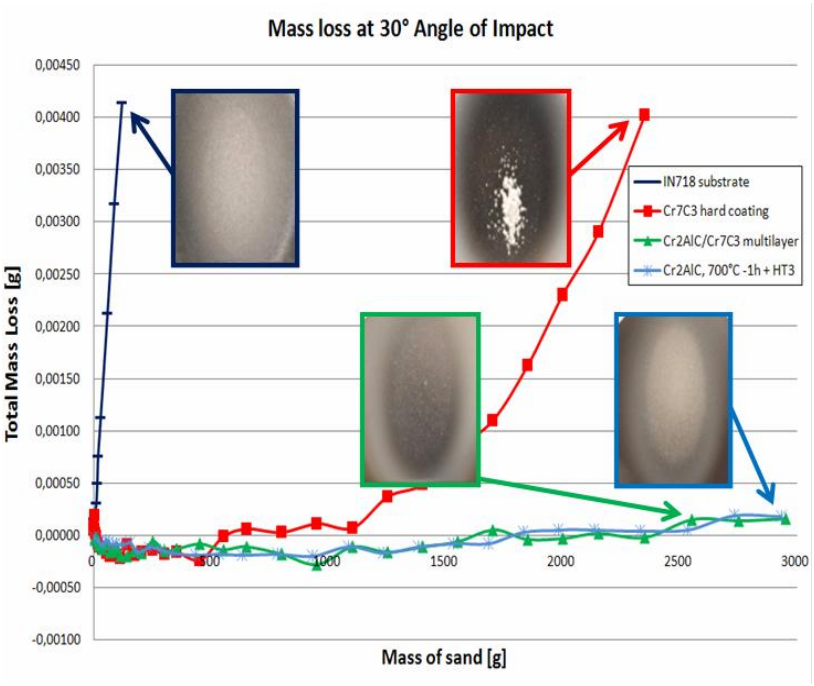

Figure 1.2 Mass loss of IN718 uncoated (dark blue) and coated with Cr_7C_3 (red), Cr_2AlC/Cr_7C_3 multilayers (green) and Cr_2AlC (blue).

An alternative approach to applying a strong and hard coating which either shows no damage or fails completely by chipping (the 'damage prevention' approach) [7], would be to use a coating which would not chip but instead would form a network of microcracks which 'heal' repeatedly and autonomously and in this manner 'manages' the occurrence of damage [7].

Self-healing of micro- or meso-cracks has now been demonstrated for almost all sorts of materials, but autonomous healing of micro-cracks at high temperatures such as occur in the hot sections of a jet engine has only been demonstrated for self healing ceramics. For self healing ceramics (and other self healing materials) two concepts have been established: extrinsic self healing and intrinsic self healing. In the case of extrinsic healing the healing reaction is made possible by the inclusion of healing particles in an inert ceramic matrix prior to sintering. In case of cracking of such materials, the cracks intersect the healing particles and trigger a chemical (i.e. oxidative) reaction which leads to a reaction product filling the crack and establishing a strong, well-adhering deposit in

the crack. Such a healing system concept works but it has the drawback that the healing reaction can locally take place only once, which is not desirable in case of repetitive damage formation such as during solid particle erosion.

The alternative approach is that of 'intrinsic healing' in which case the material itself is the source of the healing reaction and multiple healing can occur as long as the material is present. Earlier research in Delft showed that Ti_2AlC is one of such rare materials which can show autonomous healing at high temperatures in oxygen containing atmospheres. Ti_2AlC is one of the relatively recently discovered MAX (M is the transitional metal, A is element from IIIA to IV A and X is carbon or nitrogen) phase materials. Because of its lamellar structure and the combined metallic and ceramic bonds it has both metallic and ceramic properties, such as thermal and electrical conductivity, easy machinability, thermal damage tolerance, oxidation resistance and excellent high-temperature hardness [8-12]. Its crack healing ability has been demonstrated for microcracks induced by 3-point bending tests and the system showed even the ability to heal a crack multiple times [13]. The healing action is based on the spontaneous formation of Al_2O_3 and some TiO_2 which deposit in the crack and bond strongly to the matrix (see Figure 1.3).

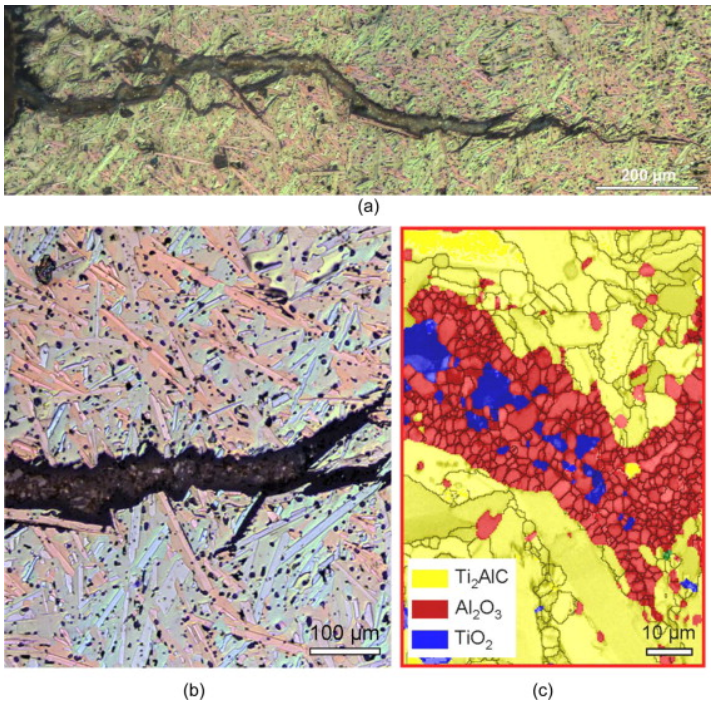

Figure 1.3 (a) Low magnification optical image of 3 point bending test induced cracks healed in air at 1200 °C for 100h; (b) Enlarged optical image taken from (a); (c) EBSD phase map of a detail of the healed damage zone. After [13]

The formation of the new oxides in the (indentation induced) microcracks did not only fill the cracks but also restored the flexural strength at room temperature (see Figure 1.4 (a)). As Figure 1.4 (b) shows, the degree of healing was such that after healing the final crack did not form at the location of the healed cracks but elsewhere.

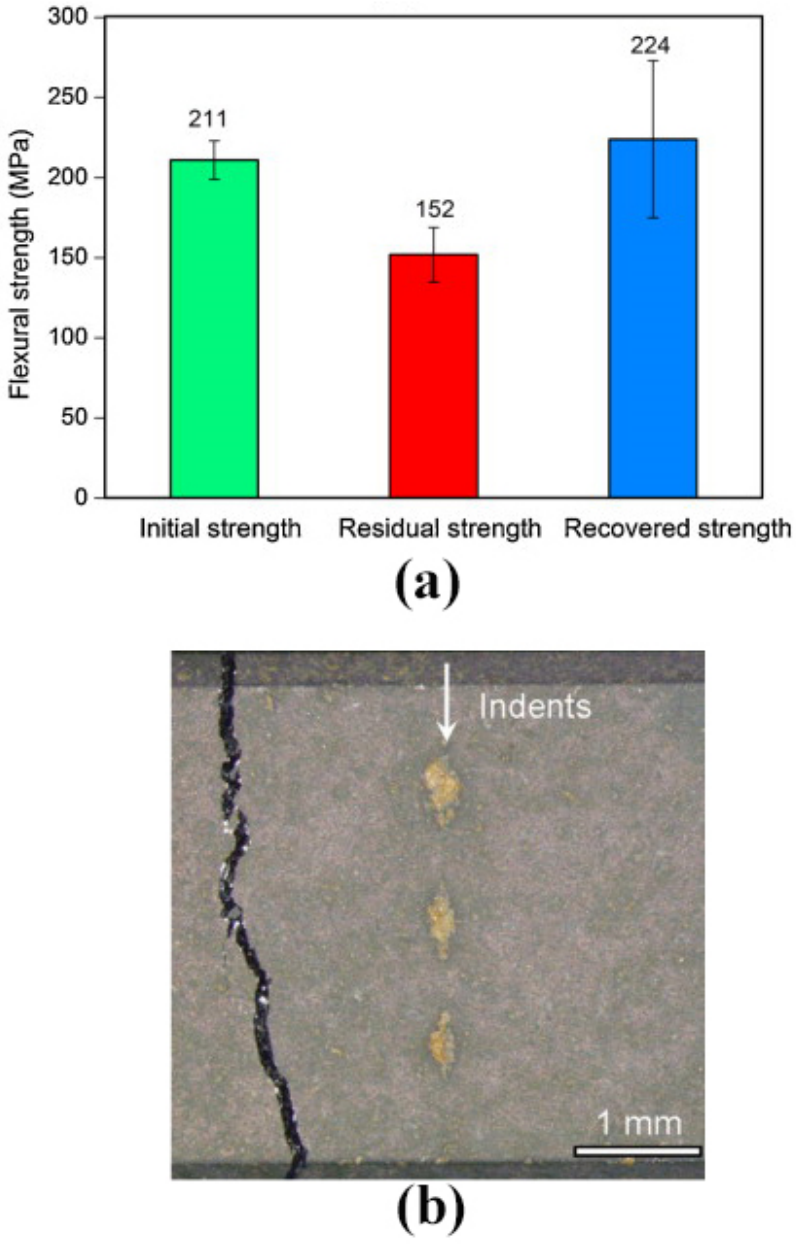

Figure 1.4 (a)Flexural strength of the virginal Ti_2AlC, after creating crack damage and after crack healing, respectively; (b) optical image of fractured Ti_2AlC bar after healing of crack damage inducd by a Knoop indenter. After [13]

The self healing capability was also demonstrated in Cr_2AlC, another member of the MAX Phase family. The indentation induced cracks were filled with pure Al_2O_3 as shown

in Figure 1.5, which is more favourable than the mixture of two oxidation products Al_2O_3 and TiO_2 observed for Ti_2AlC as the adhesion of TiO_2 to the matrix seems to be weak.

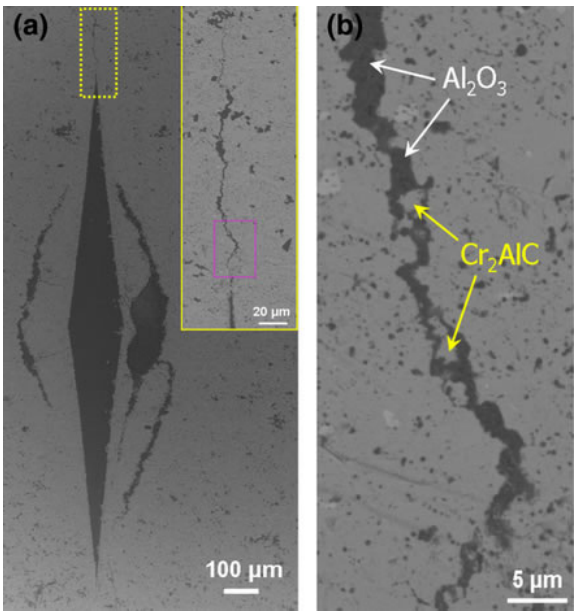

Figure 1.5 Backscattered electron images of polished Cr_2AlC after healing at 1100°C for (a–b) 4 h. (a) low magnification image of the healed zones around indentation on the polished surface. The insert is an enlarged image taken from the marked area in (a). (b) an enlarged image taken from the marked area in the inset in (a). [14]

Other recent research in Delft predicted which of the 79 known MAX phase compositions would show high temperature healing based on (i) a preferential oxidation and dominant diffusion of A element, (ii) a volume expansion upon oxidation, (iii) a good adhesion [12]. This analysis indicated Cr_2AlC to be a very interesting self-healing MAX phase grade.

Another issue regarding the self healing performance is the oxidation kinetics which determines the rate of crack filling. This oxidation kinetics within the faceted crack may be rather different from the oxidation kinetics as conventionally measured using smooth free surfaces. The local oxidation kinetics within a crack has not been determined yet, but is most certainly an interesting (but experimentally very hard to determine) parameter to monitor. Earlier work [15] has shown that the bulk oxidation kinetics of Cr_2AlC is much slower than Ti_2AlC. The option of improving the kinetics by doping supplemental elements such as Si [16] in the Cr_2AlC is appealing, but has not been studied either.

As mentioned earlier in this chapter Cr_2AlC has been used experimentally as a protective layer on turbine blades and this coating was shown to be very effective, but there is no

evidence to link the superior performance to a potential healing reaction of particle impact induced local contact damage. It would be of great interest to the field of self healing ceramics to learn more about the self healing behaviour of this material by combining deep fundamental studies of the filling behaviour of indentation induced cracks as a function of the structure and composition of the Cr_2AlC MAX phase material for quasi-static laboratory conditions as well as erosive conditions close to those encountered in a real turbine.

1.2 Scope and outline of the thesis

The aim of this research is to identify, understand and quantify the self healing ability of MAX phase to realize the knowledge-based design of crack and erosion damage healing materials. The work is formulated in such way that it tries to answer the following questions:

1) How to synthesize pure bulk MAX phase Cr_2AlC in a more efficient way?
2) What is the role of Si in accelerating the oxidation kinetics of Cr_2AlC?
3) How do the cracks get filled along the total length of the crack ?
4) How to better quantify the crack healing kinetics?
5) What is the erosion and healing behaviour of Cr_2AlC?
6) How good is the crack healing ability in Cr_2AlC under real combustion chamber condition?

In Chapter 2, we describe the work done to synthesize pure Cr_2AlC bulk samples potentially suitable for further erosion and healing testing. Given its versatility Spark Plasma Sintering (SPS) was selected as the most appropriate manufacturing technique as this technique can be used for mixtures of elemental powders as well as powders having more or less the intended composition. The synthesis procedure is described in detail and the results of the microstructural characterisation of the SPS produced samples in terms of phase purity diversity in grain size. The effects they have on mechanical properties are discussed.

In Chapter 3, the oxidation kinetics of SPS Cr_2AlC under different temperatures is studied and the influence of Si on the oxidation kinetics is evaluated by analysing the

microstructure of the Al_2O_3 layer formed in terms of grain size and composition. A simple model is presented to explain the unusual time dependence of the growth kinetics.

In Chapter 4, for the first time ever multiple crack healing in Ti_2AlC is monitored and quantified by high resolution 4D in-situ synchrotron X-ray tomography. The crack propagation path and evolution of the crack closure are evaluated real time as a function of the position in the crack and number of the healing treatments. Such detailed measurements, with a volumetric resolution better than 1 μm^3, present a unique insight into the healing processes as well as the strength of the healed crack.

In Chapter 5, the crack healing kinetics of Cr_2AlC is quantified by lower resolution X-ray tomography and external cracking and healing. While at a lower resolution the measurements give detailed insight into the local healing kinetics and the effects of local impurities due to incomplete reactions during the SPS production of the material could be visualised.

In Chapter 6, the erosion mechanism of a fully dense Cr_2AlC is studied by the room temperature normal impact with micro glass beads for a range of impact velocities. The erosion rates before and after high temperature healing treatment are compared to detect the occurrence of an effective healing reaction as well as the depth to which both damage formation and healing reaction extend .

In Chapter 7, the erosion resistance of lower quality (i.e. not fully dense) Cr_2AlC material is studied as a function not only of the particle velocity but also of the particle type. Again the erosions rates before and after healing are used as a measure to monitor the degree and depth of healing.

In Chapter 8, the crack healing ability of pre-damaged intrinsic self healing Cr_2AlC and Ti_2AlC MAX phases as well as extrinsic healing composites of Al_2O_3 containing TiC healing particles is studied under simulated jet-engine combustion chamber conditions and compared to the results of self healing experiments under quasi-static gas flow conditions.

References

1. Chen, X. and J.W. Hutchinson, *Particle impact on metal substrates with application to foreign object damage to aircraft engines.* Journal of the Mechanics and Physics of Solids, 2002. **50**(12): p. 2669-2690.
2. Chen, X., R. Wang, N. Yao, A.G. Evans, J.W. Hutchinson, and R.W. Bruce, *Foreign object damage in a thermal barrier system: mechanisms and simulations.* Materials Science and Engineering: A, 2003. **352**(1-2): p. 221-231.
3. Drexler, J.M., A.D. Gledhill, K. Shinoda, A.L. Vasiliev, K.M. Reddy, S. Sampath, and N.P. Padture, *Jet engine coatings for resisting volcanic ash damage.* Adv Mater, 2011. **23**(21): p. 2419-2424.
4. Wang, M., N.A. Fleck, and A.G. Evans, *Elastodynamic Erosion of Thermal Barrier Coatings.* Journal of the American Ceramic Society, 2011. **94**: p. 160-167.
5. Schrade, M., S. Staudacher, and M. Voigt. *Experimental and Numerical Investigation of Erosive Change of Shape for High-Pressure Compressors*. in *ASME Turbo Expo 2015: Turbine Technical Conference and Exposition*. 2015. American Society of Mechanical Engineers.
6. S. van der Zwaag and J.E. Field, *The effect of thin hard coatings on the Hertzian stress field.* Philosophical Magazine A, 1982. **46**(1): p. 133-150.
7. S. van der Zwaag, *An Introduction to Material Design Principles: Damage Prevention versus Damage Management*, in *Self Healing Materials: An Alternative Approach to 20 Centuries of Materials Science*, S. van der Zwaag, Editor. 2007, Springer Netherlands: Dordrecht. p. 1-18.
8. Barsoum, M.W., *$M_{N+1}AX_N$ phases: a new class of solids; thermodynamically stable nanolaminates.* Progress in Solid State Chemistry, 2000. **28**(1-4): p. 201-281.
9. Barsoum, M.W., Yoo, H. -I., Polushina, I. K., Rud, V. Yu., Rud, Yu. V., El-Raghy, T., *Electrical conductivity, thermopower, and Hall effect of Ti_3AlC_2, Ti_4AlN_3, and Ti_3SiC_2.* Physical Review B, 2000. **62**(15): 10194
10. Barsoum, M.W., *Physical properties of the MAX phases*; in Encyclopedia of Materials Science and Technology. Edited by K.H.J. Buschow, R.W. Cahn, M.C. Flemings, E.J. Kramer, S. Mahajan, and P. Veyssiere. Elsevier, Amsterdam, 2006.
11. Barsoum, M.W. and M. Radovic, *Elastic and mechanical properties of the MAX phases*, in Annual Review of Materials Research. 2011. p. 195-227.
12. Farle, A.-S., C. Kwakernaak, S. van der Zwaag, and W.G. Sloof, *A conceptual study into the potential of $M_{n+1}AX_n$-phase ceramics for self-healing of crack damage.* Journal of the European Ceramic Society, 2015. **35**(1): p. 37-45.
13. Li, S., G. Song, K. Kwakernaak, S. van der Zwaag, and W.G. Sloof, *Multiple crack healing of a Ti_2AlC ceramic.* Journal of the European Ceramic Society, 2012. **32**(8): p. 1813-1820.
14. Li, S., L. Xiao, G. Song, X. Wu, W.G. Sloof, and S. van der Zwaag, *Oxidation and Crack Healing Behavior of a Fine-Grained Cr_2AlC Ceramic.* Journal of the American Ceramic Society, 2013. **96**(3): p. 892-899.
15. Tallman, D.J., B. Anasori, and M.W. Barsoum, *A Critical Review of the Oxidation of Ti_2AlC, Ti_3AlC_2 and Cr_2AlC in Air.* Materials Research Letters, 2013. **1**(3): p. 115-125.
16. Shang, L., D. Music, and J.M. Schneider, *Phase stability predictions of $(Cr_{1-x}, M_x)_2(Al_{1-y}, A_y)(C_{1-z}, X_z)$ (M = Ti, Hf, Zr; A = Si, X = B).* Journal of Physics D: Applied Physics, 2014. **47**(6): 065308.

2 Synthesis of high-purity isotropic or textured Cr_2AlC bulk ceramics by SPS of pressure-less sintered powder

The synthesis of a high purity Cr_2AlC metallo-ceramic involving pressure-less sintering (PLS) of elemental powders followed by spark plasma sintering (SPS) sintering of the crushed reaction product of the PLS product is described. High purity Cr_2AlC was obtained for PLS 1400 °C for 1 hour in argon. Depending on the ball milling conditions either intermediate coarse equiaxed Cr_2AlC particles or intermediate small flake like Cr_2AlC particles were obtained. SPS of the coarse powder resulted in high density bulk samples with a random texture. SPS of the fine powder resulted in high density bulk samples with a well-developed texture such that the (0001) planes are perpendicular to the compression direction. The hardness of fine-grained Cr_2AlC bulk ceramic along different directions is both higher than that of coarse-grained Cr_2AlC bulk ceramic. Due to its texture the fine-grained Cr_2AlC bulk ceramic shows an anisotropic fracture behaviour.

2.1 Introduction

Cr_2AlC belongs to the family of so-called MAX phase materials [1-3]. The general formula is $M_{n+1}AX_n$, where n equals 1, 2 or 3, M is an early transition metal, A is an A group element (mostly IIIA and IVA, like Al and Si), and X is C and/or N. The MAX phase compounds have a layered hexagonal crystal structure [4]. The crystalline unit cell contains two sub units, viz.: the ceramic $M_{n+1}X_n$ layers are interrupted by metallic layers of pure A, resulting in an ABABAB structure. Due their structure, MAX phase materials exhibit unique combinations of mechanical, thermal and electric properties [5, 6]. The MAX phase ceramics are stable up to high temperatures and are corrosion resistant [6-8]. The high thermal conductivity makes these ceramics thermal shock resistant. Their static strength is maintained up to high temperatures [9], above which creep will become the limiting factor [4].

In contrast to many other ceramics, MAX phase materials are tough and therefore damage tolerant and also relatively easily machineable [5]. Dislocations can multiply and glide on the basal planes of the hexagonal lattice. Plastic deformation of polycrystalline MAX phase material occurs by a combination of kink and shear band formation, also involving delamination of the lamellar grains [4, 10].

Of the M_2AX materials, Cr_2AlC is particularly attractive due to its good resistance against high-temperature oxidation and hot corrosion [1, 2, 8, 11-13]. Recently, autonomous crack-healing has been reported for Cr_2AlC [14], analogous to that in Ti_2AlC and Ti_3AlC_2 [15, 16]. The desirable healing behavior is due to the formation of a stable, well adhering oxide with a high relative volume expansion [17] and having mechanical properties close to those of the matrix. Such an autonomous high temperature crack healing behavior makes these MAX phase materials attractive candidates for high temperature applications, where the material is exposed to thermal cycles, mechanical loading and oxidation. These conditions are encountered in e.g. power or propulsion generation, raw material production, recycling facilities.

Several methods have been used to manufacture bulk Cr_2AlC ceramics, such as: hot pressing (HP), hot isostatic pressing (HIP) and spark plasma sintering (SPS) [3, 18-26]. The properties of Cr_2AlC ceramics are strongly dependent on the purity, relative density and grain size [14, 27-32]. This effect of the ratio and size of initial elemental powders,

sintering temperature and dwell time of HP Cr_2AlC bulk ceramic effects their phase compositions and mechanical properties [3]. Ying et al. also reported that high purity Cr_2AlC bulk ceramic with high density could be synthesized at 1400 ºC under 30 MPa by hot pressing [23]. However, SPS is a more efficient method to produce high density Cr_2AlC bulk ceramic [21,22,26]. Two key issues need to be resolved when manufacturing high purity Cr_2AlC bulk ceramics: Firstly, it is difficult to ensure a full and complete solid-state reaction of the constituting powders to form pure Cr_2AlC not containing any of the intermediate reaction products. Secondly, it is difficult to avoid an inhomogeneous sintering due to reaction of the staring Al and Cr powders with the graphite mold. This powder-wall reaction not only leads to an inhomogeneous reaction product but also to damage to the graphite mold.

In this study, dense Cr_2AlC bulk ceramics were manufactured through spark plasma sintering (SPS) using the crushed and milled pressure-less sintering Cr_2AlC powders with different average grain sizes. Then the microstructure and mechanical properties of produced Cr_2AlC bulk ceramics were investigated.

2.2 Materials and Methods

2.2.1 Synthesis

As starting material for the manufacturing of Cr_2AlC, powders of Cr (average particle size of about 100 μm, purity>99.2%, TLS Technik GmbH & Co., Germany), Al (average particle size of about 45 μm, purity>99.8%, TLS Technik GmbH & Co., Germany) and graphite (average particle size of 6 μm, purity>99.5%, Graphit Kropfmühl AG, Germany) were used. These powders were mixed such that the molar ratio of Cr, Al and C powders was Cr:Al:C = 2:1.15:1. Since Al has a low melting point (~660 ^oC), a slight excess of this element was added to compensate for its loss during PLS sintering.

The elemental powders were mixed for 3 hours with a Turbula mixer using zirconia balls with diameter of 5 mm. Then, the powder mixture was cold pressed in a steel mold with a pressure of 300 MPa. Next, the as-obtained green body (with typical dimensions of about Φ13 x 6 mm) was pressure-less sintered in tube furnace (Lenton Furnaces, PTF 16/75/610) under a flow of pure argon (6N). The substrate material during PLS was alumina crucible. The heating rate was 5 ^oC per minute and the samples were held for 1 hour at various

sintering temperatures in the range of 1100 to 1400 ^oC. Subsequently, the surface of PLS samples was ground with SiC emery paper to remove the outer surface layer.

Coarse grained Cr_2AlC powder was prepared from the PLS Cr_2AlC samples by putting the material in a Fritsch Pulverisette, type P-0150. Fine-grained Cr_2AlC powder was obtained by ball milling the coarse powder using a PM100 ball grinder (Retsch GmbH) with 10 mm tungsten carbide balls and jar. The weight ratio of balls and powder was about 20:1. The milling jar was filled with Argon. The milling speed was 300 rpm and the milling time was 3 hours with cycles of 10 minutes running and 20 minutes pause, i.e. the effective milling time was 1 hour.

Finally, both coarse and fine grain powders were sintered in a spark plasma sintering furnace (HP D 25 SD, FCT Systeme GmbH) at 1250 ^oC for 60 minutes in flowing Argon atmosphere, and applying a sintering pressure of 50 MPa and using a graphite mold (inner diameter of 20 mm). The heating and cooling rate was 50 and 100 ^oC per minute, respectively. The final sample thickness was about 4 mm.

2.2.2 Characterization

The density of SPS sintered bulk ceramics were measured by the Archimedes method using a PM480 balance (Mettler Co.).

The Vickers hardness was determined with a Zwick/Z2.5 hardness tester in a load range of 100~500N with a fixed contact time of 10 s.

The phase composition of pressure-less sintered powder, ball milled powder and SPS sintered material was assessed via X-ray diffraction using a Bruker D8 Advance diffractometer operated with Co Ka radiation. Diffractograms were recorded in the 2θ range of 10 ^{o} to 130 ^{o} with a step size 0.034 ^{o}, and a counting time per step of 1 s. These diffractograms were evaluated using the Bruker Diffrac EVA software (version 3.1).

The microstructure of the pressure-less sintered and ball milled powders as well as the fracture surfaces of SPS sintered Cr_2AlC bulk ceramics and the cracks generated by the Vickers hardness indentations were observed using a JEOL JSM 6500F field emission gun scanning electron microscope (SEM). This SEM is equipped with an Oxford Instruments-HKL Nordlys II detector allowing Electron Backscattering Diffraction

(EBSD). The grain size distribution and the crystallographic preferred orientation was determined with Orientation Imaging Microscopy (OIM). The data acquisition and processing was performed using Channel 5 software (version 2011).

2.3 Results and Discussion

2.3.1 Pressure-less sintering

As can be seen in the diffractograms of the PLS Cr_2AlC at 1100, 1200 and 1300 ºC, see Figure 2.1, also carbon and intermetallic Cr_2Al are present.

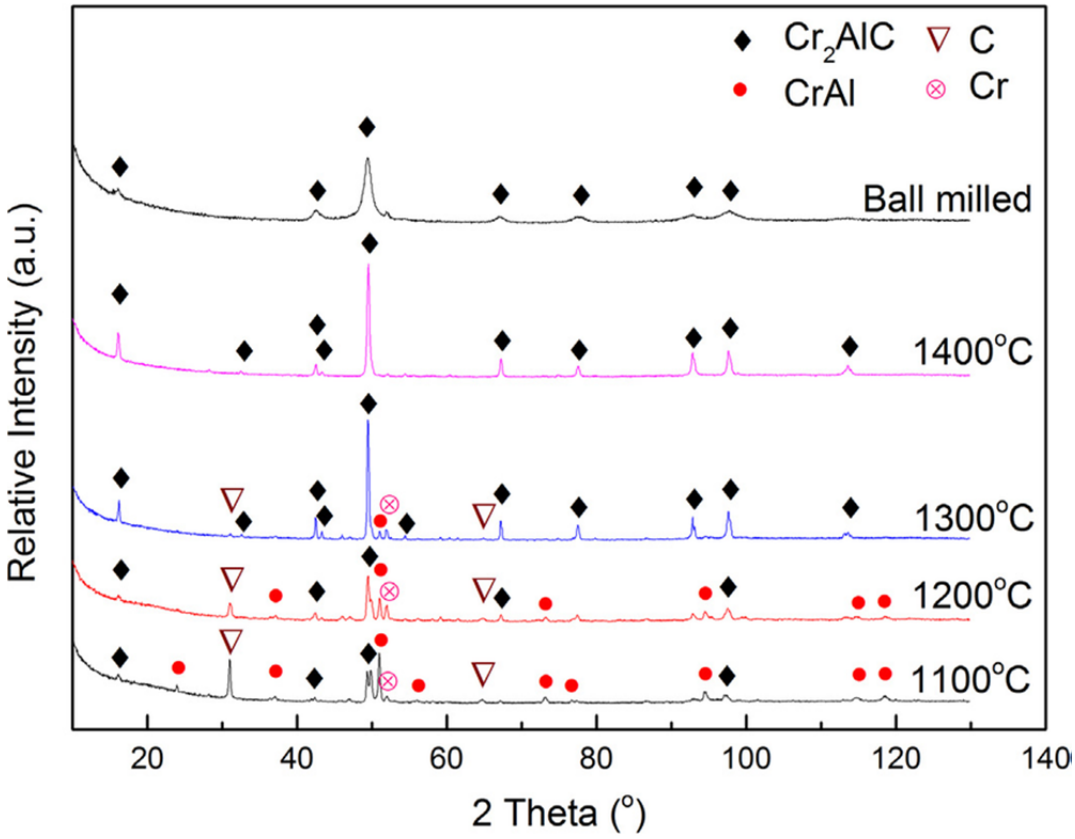

Figure 2.1 X-ray diffractograms of a Cr-Al-C powder mixture pressure-less sintered at different temperatures, including a ball-milled powder of the material sintered at 1400 °C.

The amount of these impurity phases decreases with increasing sintering temperature. For PLS at 1400 °C pure Cr_2AlC phase is produced and no other phases were detected. This material is used to prepare dense bulk Cr_2AlC. Crushing the PLS product into coarse or fine grained powder did not lead to a composition change as confirmed by XRD analysis. However, the diffraction lines of the fine-grained Cr_2AlC are substantially broadened due

to the reduction in grain size and the amount of plastic deformation induced in the powders by the ball milling; see Figure 2.1

The morphology of the PLS Cr_2AlC powders is shown in Figure 2.2.

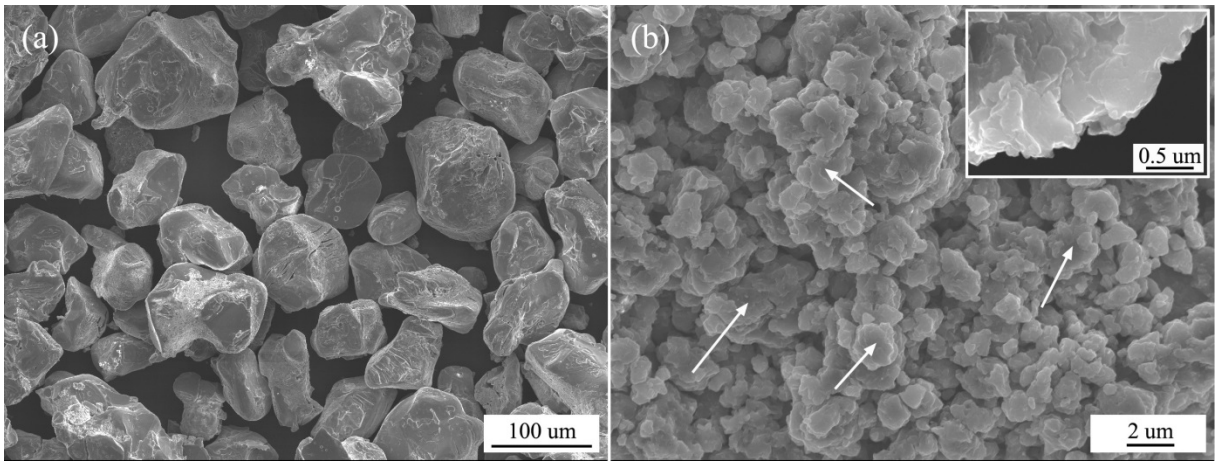

Figure 2.2 SEM images of the milled pressure-less sintered Cr_2AlC at 1400 ºC. (a) coarse-grained and (b) fine-grained. The arrows indicate flake like shape and the insert shows the plate like morphology at the edge.

The grain size of coarse and fine-grained powder is 50~100 μm and 1~3 μm, respectively. Due to the ball milling, the particles not only became smaller but also developed a plate-like morphology; see Figure 2.2 (b). Since the bonding between the MX and A layers, i.e. Cr_2C and Al layers, in the MAX phase crystal structure is relatively weak, shear and delamination along the MX/A interfaces resulting in flake formation is to be expected [17, 33, 34]. Similar observations have been reported for graphene and other nano-layered materials processed in shear [35-38].

2.3.2 Spark Plasma Sintering

The densification of these two powders during sintering is different, as can be seen in the sintering profile shown in Figure 2.3. As can be expected [39, 40], the sintering of the fine-grained powder is faster than of the coarse grained powder. The density of the coarse and fine grained sintered Cr_2AlC bulk ceramics are practically the same: 5.16 and 5.17 g/cm^3, respectively. Compared with the theoretical densities of Cr_2AlC, i.e. 5.24 g/cm^3 [6], both sintered Cr_2AlC bulk ceramics have a relative density higher than 98 %.

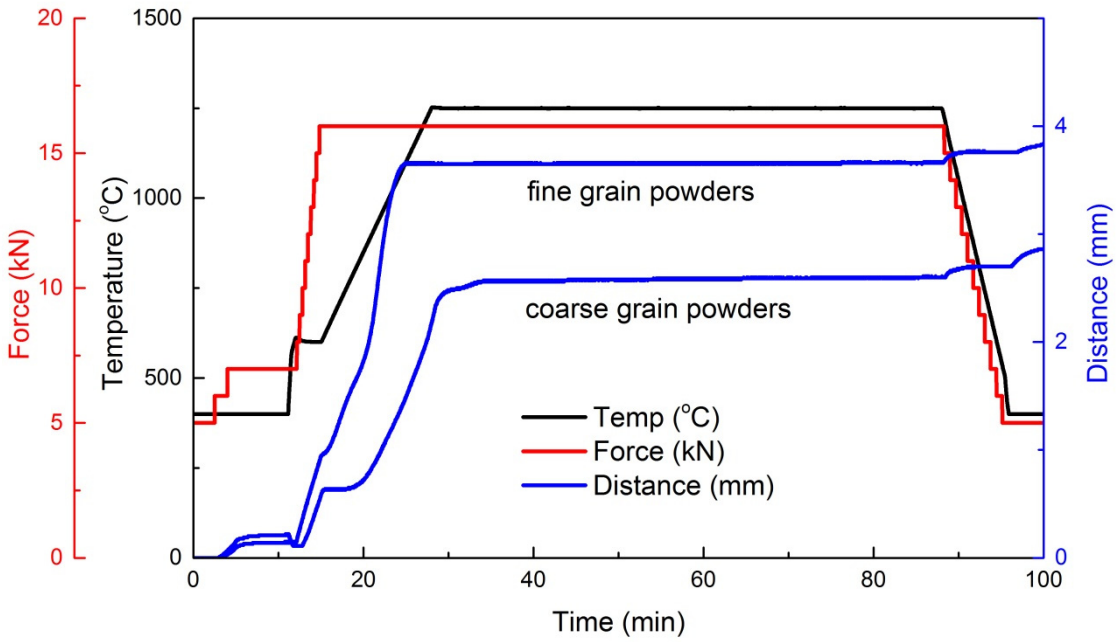

Figure 2.3 Force, temperature and piston travel (distance) during SPS of PLS Cr_2AlC powders with coarse and fine grain sizes. The corresponding sintering pressure equals 50 MPa (diameter of the graphite mold is 20 mm).

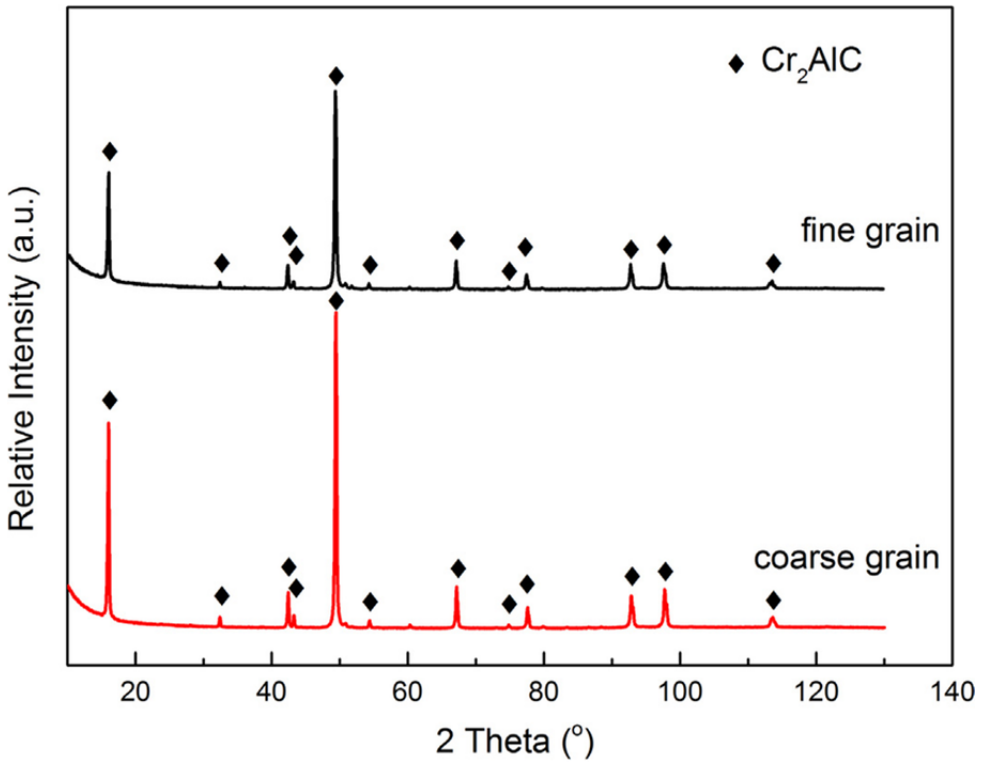

Figure 2.4 X-ray diffractograms of SPS Cr_2AlC bulk ceramics with coarse and fine grain size.

Furthermore, according to the XRD analysis the purity of the Cr_2AlC materials after SPS is the same as after PLS; see Figure 2.4. Thus no reaction or reverse phase transformation occurred during the SPS. The broadening of the diffraction lines of fine grained Cr_2AlC after SPS is reduced when compared with the milled powder; cf. Figure 2.1 This suggests that recovery of defects and/or grain growth occurred during the SPS process. The coarse grains were pressure-less sintered at 1400 ºC and remained stable during the subsequent SPS process at lower temperature, i.e. 1250 ºC. While after ball milling, the fine grains become more activity which provide momentum for densification [30,41].

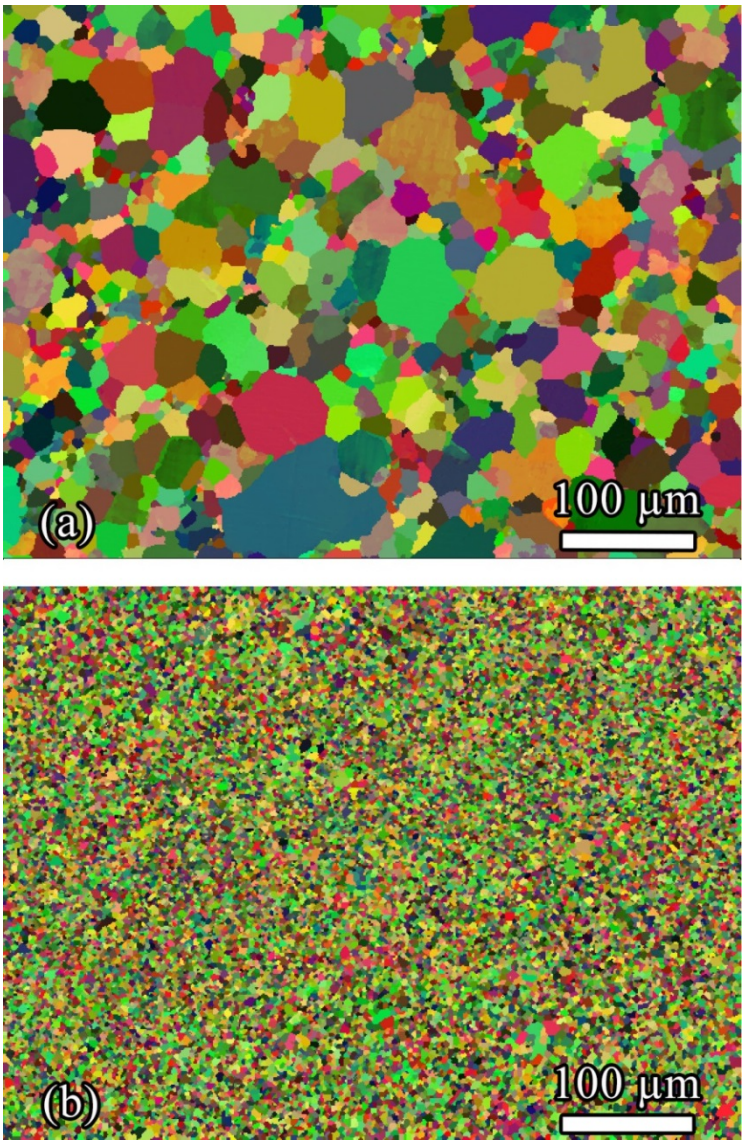

Figure 2.5 Orientation image (Euler map) of SPS sintered Cr_2AlC bulk ceramics with (a) coarse and (b) fine grains.

The microstructure of the sintered Cr_2AlC bulk ceramics, as resolved by orientation imaging microscopy (cf. Section 2.2), is displayed in Figure 2.5. The average grain size

of the coarse- and fine-grained Cr_2AlC bulk ceramics equals 72 and 8 μm, respectively. The distinct difference in grain size of the two ceramics can also be observed in the images of the fracture surface, see Figure 2.6.

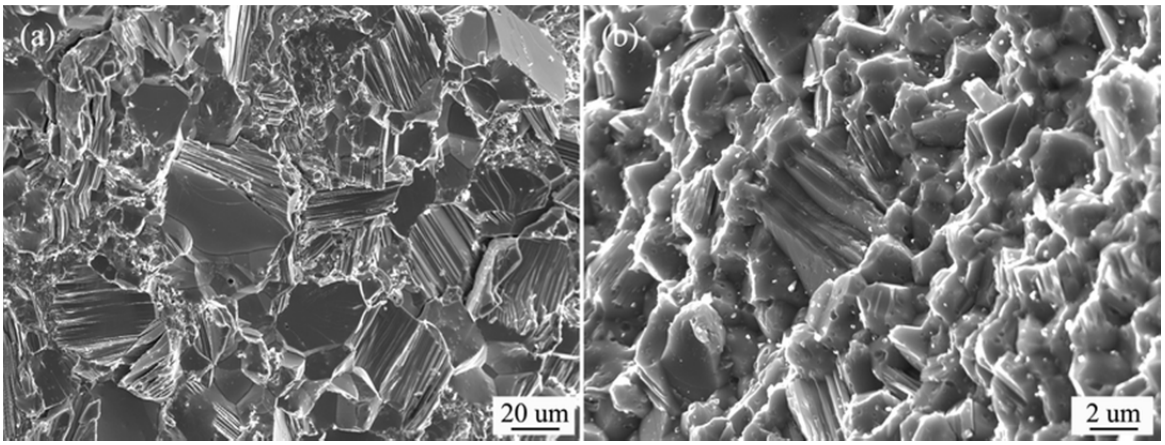

Figure 2.6 SEM images of fracture surfaces of (a) coarse-grained and (b) fine-grained Cr_2AlC bulk ceramics.

In agreement with the XRD observations, the grain size of coarse-grained Cr_2AlC is practically the same as the grain size of pressure-less sintered powder (cf. Figure 2.2 a), whereas the grain size of fine-grained material is significantly larger than the grain size of ball milled powders (i.e. 1~3 μm, cf. Figure 2.2 b). Thus grain growth occurred during the SPS process step. If wanted, the grain size growth may be reduced by lowering the sintering temperature and shortening the holding time, since the densification of the ball milled fine-grained PLS Cr_2AlC powder was already completed at 1150 ºC (i.e. before reaching the sintering temperature of 1250 ºC).

The fine-grained Cr_2AlC ceramic exhibits a preferred crystallographic orientation (i.e. texture), while the grains of the coarse grained material have a random orientation, see Figure 2.7. The grains in the fine-grained Cr_2AlC show a preference for their (0001) plane parallel to the surface, which is perpendicular to the compaction direction upon SPS. The preferred orientation is the result of the exfoliation during the ball milling of the equi-axed PLS Cr_2AlC powder.

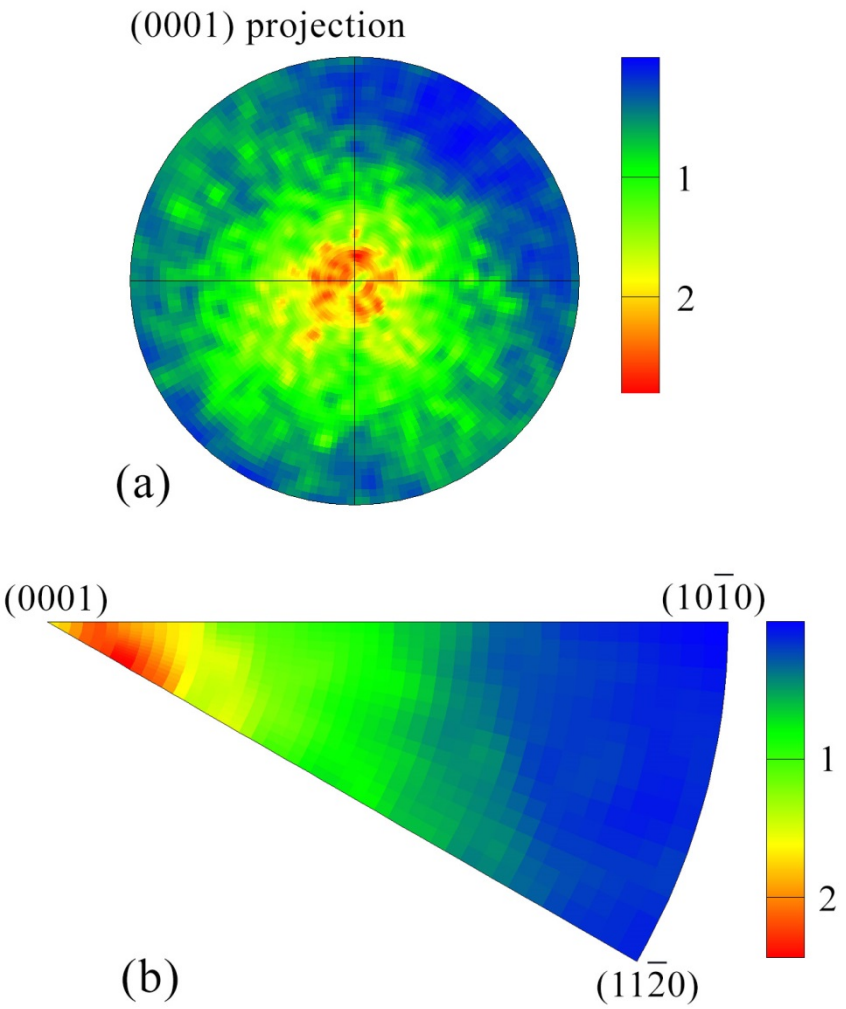

Figure 2.7 Preferred crystallographic orientation of ball milled PLS Cr_2AlC to 8 µm grains and subsequently SPS. (a) (0001)-Pole figure and (b) inverse pole figure, both with respect to the sample surface normal (i.e. sintering compaction direction).

During ball milling of this powder, cleavage occurs along the (0001) planes, i.e. along the 'weaker' Cr_2C/Al interfaces. When filling the mould with the flaky powder there is a natural setting of the powder such that the powder align to the bottom mould surface, resulting in a (0001) texture perpendicular to the compaction direction in the SPS mold as illustrated in Figure 2.8.

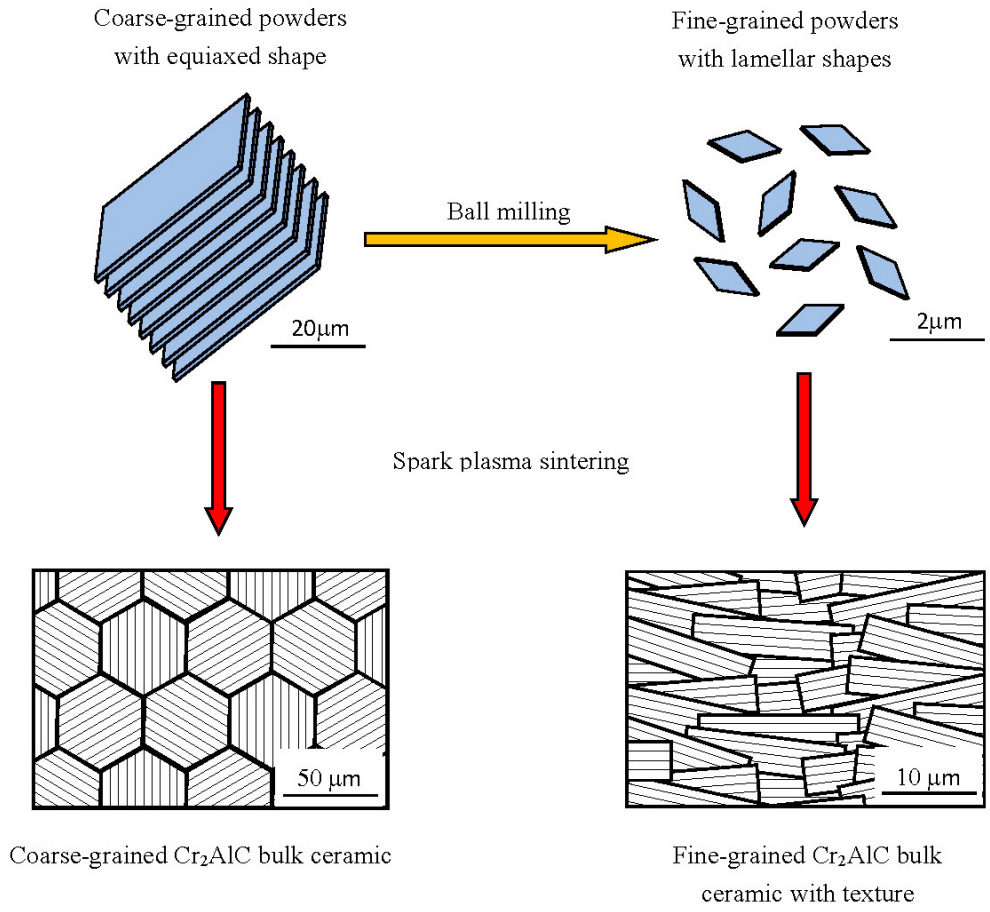

Figure 2.8 Schematic representation of the microstructures evolution, consequently upon PLS of Cr_2AlC, ball-milling and SPS.

2.3.3 Mechanical properties

The difference in mechanical properties of the coarse- and fine-grained Cr_2AlC is reflected in their hardness values, which are 3.4 ± 0.2 GPa and 5.3 ± 0.9 GPa, respectively. Thus the coarse-grained is softer than the fine-grained Cr_2AlC ceramic. There is practically no difference between the hardness of the fine-grained Cr_2AlC measured perpendicular and parallel to compaction direction, i.e. in the (0001) preferred crystallographic orientation.

Plastic deformation zones not leading to crack formation are observed around the indentations in coarse-grained Cr_2AlC; see Figure 2.9 (a).

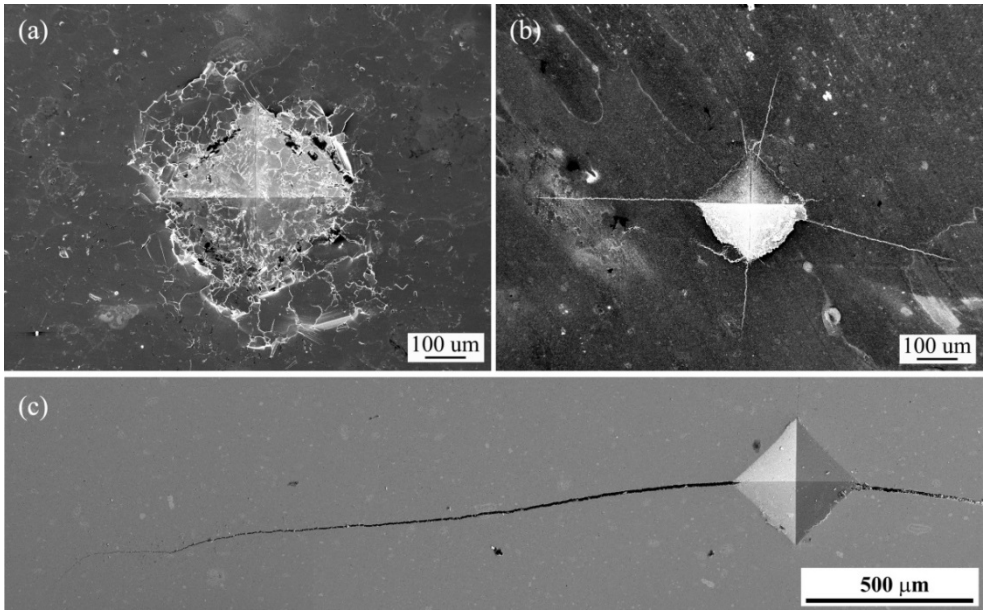

Figure 2.9 Morphologies of Vickers indentations of (a) coarse-grained Cr_2AlC bulk ceramic and (b) fine-grained Cr_2AlC bulk ceramic surfaces perpendicular and (c) parallel to the sintering compaction direction.

In contrast the fine-grained Cr_2AlC bulk ceramic is more brittle and thus less damage tolerant and cracks appear at the corners of indentation; see Figure 2.9 (b) and (c). When the surface perpendicular to the compaction direction is indented (i.e. perpendicular to the (0001) preferred crystallographic orientation), cracks of about equal length appear at all four corners of the indentation; see Figure 2.9 (b). When a sample surface parallel to the consolidation direction is indented (i.e. parallel to the (0001) preferred crystallographic orientation), long and wide cracks occur at the corners of the indentation for which the diagonal is parallel to the (0001) planes; see Figure 2.9 (c). The cracks at the corners of the indentation of the diagonal which are perpendicular to this direction are much smaller or even absent. This anisotropic fracture behavior of the fine-grained Cr_2AlC is due to its texture and the fact that the bonding between the MX and A layers, i.e. Cr_2C and Al layers, in the MAX phase crystal structure is relatively weakest [17, 33, 34].

The Vickers indentations of fine-grained Cr_2AlC bulk ceramic are also studied as a function of the load applied to the indenter; see Figure 2.10.

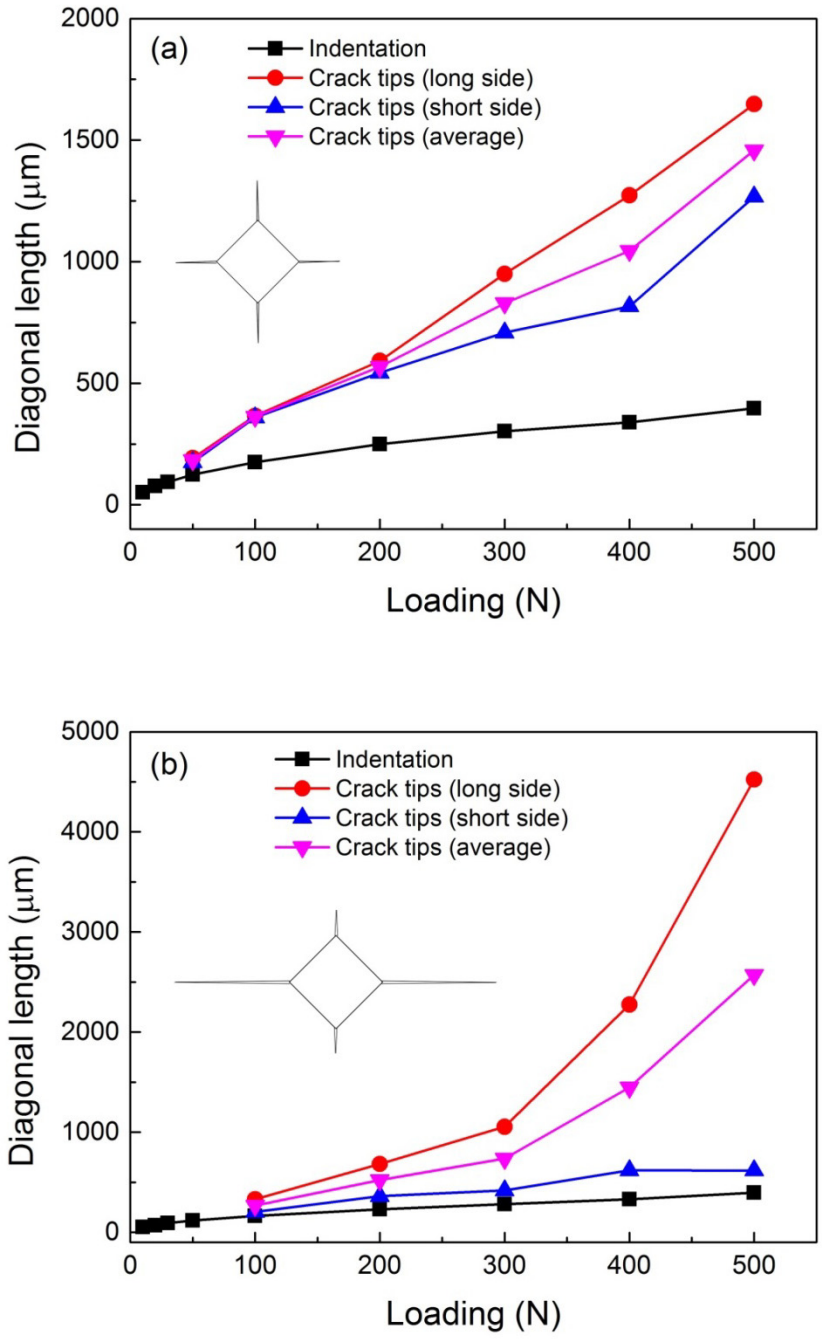

Figure 2.10 Indentation diagonal length and crack tips length of fine-grained Cr_2AlC bulk ceramic as the function of loading in the direction perpendicular (a) and parallel (b) to the sintering compaction direction.

Here the length of the diagonal of the indentation as well as the length of any crack (when present) is plotted versus the load applied to the indenter. No cracks are observed when loads applied to the indenter up to about 30 and 50 N in the directions perpendicular and parallel to compaction direction, respectively. For the fine grained material, on the surface perpendicular to compaction direction, the crack length increases rapidly with the indentation load; see Figure 2.10 (a). For the surface parallel to the compaction direction,

the crack length also increases rapidly with loading of the indenter, but the cracks lengths along the two diagonals are rather different; see Figure 2.10 (b). For an indention load of 500 N, the long crack is more than 7 times longer than the short crack. As already explained above, this is due to texture of the fine-grained Cr_2AlC bulk ceramic. Finally, by analyzing the dependence of the crack length versus indentation load, (see Figure 2.10) the fracture toughness values for the fine grained Cr_2AlC material could be estimated by adopting 280 GPa for the elastic modulus [1,42]. For the indentation in the compaction direction (cf. Figure 2.9 (b)) the critical fracture toughness value K_c is 4.6 MPa•$m^{1/2}$ in all directions. For the indentation perpendicular to the compaction direction (cf. Figure 2.9 c) the fracture toughness values are 1.9 MPa•$m^{1/2}$ and 12.8 MPa•$m^{1/2}$ in and perpendicular to the direction of easy crack propagation, respectively.

2.4 Conclusions

High phase pure Cr_2AlC bulk ceramics can be prepared by a two-step sintering process. First, a cold pressed powder mixture of Cr, Al and C is pressure-less sintered at 1400 ^oC. Then, phase pure Cr_2AlC is formed. Next, Cr_2AlC powder of different grain size can be produced by ball milling. Finally, dense and high phase pure Cr_2AlC bulk ceramics with different grain sizes are achieved with spark plasma sintering.

Ball milling of the pressure-less sintered Cr_2AlC leads to a flake like morphology of the powder due to separation along the MX/A interfaces, i.e. Cr_2C/Al interfaces in the nanolaminate MAX phase structure. Stacking of this powder in the SPS mold leads to a preferred crystallographic orientation (texture) of the hexagonal MAX phase, with the (0001) planes perpendicular to the compaction direction.

The hardness of the Cr_2AlC ceramic depends mainly on grain size and is not much influenced by texture. Indentation with the load on the indenter parallel to the preferred (0001) crystallographic planes shows that fracture occurs mainly along the weaker Cr_2C/Al interfaces. The fracture toughness values depend strongly depend on the texture and range from 1.9 MPa•$m^{1/2}$ to 12.8 MPa•$m^{1/2}$.

The two-step sintering process presented here is attractive for large-scale production of high-quality Cr_2AlC bulk ceramics and related materials, because of (i) the creation of a

high purity phase, (ii) control over the grain size and texture, and (iii) the absence of a reaction with the graphite mold.

References

1. Lin, Z.J., Y.C. Zhou, and M.S. Li, *Synthesis, microstructure, and property of Cr_2AlC.* Journal Of Materials Science & Technology, 2007. **23**(6): p. 721-746.
2. Song, J.H., B.C. Mei, and J.P. Wang, *In-situ Hot Pressing Synthesis and Corrosion Properties of High Pure Cr_2AlC.* Journal Of Inorganic Materials, 2010. **25**(4): p. 419-423.
3. Tian, W.B., P.L. Wang, G.J. Zhang, Y.M. Kan, Y.X. Li, and D.S. Yan, *Effect of composition and processing on phase assembly and mechanical property of Cr_2AlC ceramics.* Materials Science And Engineering a-Structural Materials Properties Microstructure And Processing, 2007. **454**: p. 132-138.
4. Barsoum, M.W., *The $M_{(N+1)}AX_{(N)}$ phases: A new class of solids; Thermodynamically stable nanolaminates.* Progress in Solid State Chemistry, 2000. **28**(1-4): p. 201-281.
5. Barsoum, M.W. and T. El-Raghy, *The MAX phases: Unique new carbide and nitride materials - Ternary ceramics turn out to be surprisingly soft and machinable, yet also heat-tolerant, strong and lightweight.* American Scientist, 2001. **89**(4): p. 334-343.
6. Barsoum, M.W. and M. Radovic, *Elastic and Mechanical Properties of the MAX Phases*, in *Annual Review of Materials Research, Vol 41*, D.R. Clarke and P. Fratzl, Editors. 2011, Annual Reviews: Palo Alto. p. 195-227.
7. Sun, Z.M., *Progress in research and development on MAX phases: A family of layered ternary compounds.* International Materials Reviews, 2011. **56**(3): p. 143-166.
8. Jovic, V.D., B.M. Jovic, S. Gupta, T. El-Raghy, and M.W. Barsoum, *Corrosion behavior of select MAX phases in NaOH, HCl and H_2SO_4.* Corrosion Science, 2006. **48**(12): p. 4274-4282.
9. El-Raghy, T., M.W. Barsoum, A. Zavaliangos, and S.R. Kalidindi, *Processing and mechanical properties of Ti_3SiC_2: II, effect of grain size and deformation temperature.* Journal Of the American Ceramic Society, 1999. **82**(10): p. 2855-2860.
10. Barsoum, M.W., T. Zhen, S.R. Kalidindi, M. Radovic, and A. Murugaiah, *Fully reversible, dislocation-based compressive deformation of Ti_3SiC_2 to 1GPa.* Nature Materials, 2003. **2**(2): p. 107-111.
11. Lin, Z.J., M.J. Zhuo, Y.C. Zhou, M.S. Li, and J.Y. Wang, *Atomic scale characterization of layered ternary Cr_2AlC ceramic.* Journal Of Applied Physics, 2006. **99**(7): 076109
12. Schneider, J.M., Z.M. Sun, R. Mertens, F. Uestel, and R. Ahuja, *Ab initio calculations and experimental determination of the structure of Cr_2AlC.* Solid State Communications, 2004. **130**(7): p. 445-449.
13. Lin, Z.J., M.S. Li, J.Y. Wang, and Y.C. Zhou, *High-temperature oxidation and hot corrosion of Cr_2AlC.* Acta Materialia, 2007. **55**(18): p. 6182-6191.
14. Li, S.B., L.O. Xiao, G.M. Song, X.M. Wu, W.G. Sloof, and S. van der Zwaag, *Oxidation and Crack Healing Behavior of a Fine-Grained Cr_2AlC Ceramic.* Journal Of the American Ceramic Society, 2013. **96**(3): p. 892-899.

15. Song, G.M., Y.T. Pei, W.G. Sloof, S.B. Li, J.T.M. De Hosson, and S. van der Zwaag, *Oxidation-induced crack healing in Ti_3AlC_2 ceramics.* Scripta Materialia, 2008. **58**(1): p. 13-16.
16. Li, S.B., G.M. Song, K. Kwakernaak, S. van der Zwaag, and W.G. Sloof, *Multiple crack healing of a Ti_2AlC ceramic.* Journal of the European Ceramic Society, 2012. **32**(8): p. 1813-1820.
17. Farle, A.-S., C. Kwakernaak, S. van der Zwaag, and W.G. Sloof, *A conceptual study into the potential of $M_{n+1}AX_n$-phase ceramics for self-healing of crack damage.* Journal of the European Ceramic Society, 2015. **35**(1): p. 37-45.
18. Yeh, C.L. and C.W. Kuo, *Effects of Al and Al_4C_3 contents on combustion synthesis of Cr_2AlC from Cr_2O_3-Al-Al_4C_3 powder compacts.* Journal of Alloys and Compounds, 2011. **509**(3): p. 651-655.
19. Tian, W.B., P.L. Wang, G.J. Zhang, Y.M. Kan, and Y.X. Li, *Fabrication and properties of Cr_2AlC ceramics.* Journal of Inorganic Materials, 2007. **22**(1): p. 189-192.
20. Lin, Z.J., Y.C. Zhou, M.S. Li, and J.Y. Wang, *In-situ hot pressing/solid-liquid reaction synthesis of bulk Cr_2AlC.* Zeitschrift Für Metallkunde, 2005. **96**(3): p. 291-296.
21. Tian, W.B., Z.M. Sun, Y.L. Du, and H. Hashimoto, *Mechanical properties of pulse discharge sintered Cr_2AlC at 25-1000 degrees C.* Materials Letters, 2009. **63**(8): p. 670-672.
22. Tian, W.B., K. Vanmeensel, P.L. Wang, G.J. Zhang, Y.X. Li, J. Vleugels, and O. Van der Biest, *Synthesis and characterization of Cr_2A1C ceramics prepared by spark plasma sintering.* Materials Letters, 2007. **61**(22): p. 4442-4445.
23. Ying, G.B., X.D. He, M.W. Li, W.B. Han, F. He, and S.Y. Du, *Synthesis and mechanical properties of high-purity Cr_2AlC ceramic.* Materials Science And Engineering a-Structural Materials Properties Microstructure And Processing, 2011. **528**(6): p. 2635-2640.
24. Han, J.H., S.W. Park, and Y.D. Kim, *Synthesis and mechanical properties of nano laminating Cr_2AlC using CrC_x/Al powder mixtures*, in *Progress in Powder Metallurgy, Pts 1 and 2*, D.Y. Yoon, et al., Editors. 2007, Trans Tech Publications Ltd: Stafa-Zurich. p. 1085-1088.
25. Xiao, L.O., S.B. Li, G.M. Song, and W.G. Sloof, *Synthesis and thermal stability of Cr_2AlC.* Journal Of the European Ceramic Society, 2011. **31**(8): p. 1497-1502.
26. Tian, W.B., Z.M. Sun, Y.L. Du, and H. Hashimoto, *Synthesis reactions of Cr_2AlC from Cr-Al_4C_3-C by pulse discharge sintering.* Materials Letters, 2008. **62**(23): p. 3852-3855.
27. Ying, G.B., X.D. He, M.W. Li, S.Y. Du, W.B. Han, and F. He, *Effect of Cr_7C_3 on the mechanical, thermal, and electrical properties of Cr_2AlC.* Journal Of Alloys And Compounds, 2011. **509**(31): p. 8022-8027.
28. Li, S., L. Xiao, G. Song, X. Wu, W.G. Sloof, and S. van der Zwaag, *Oxidation and crack healing behavior of a fine-grained Cr_2AlC ceramic.* Journal of the American Ceramic Society, 2013. **96**(3): p. 892-899.
29. Lee, D.B., T.D. Nguyen, and S.W. Park, *Long-Time Oxidation of Cr_2AlC Between 700 and 1,000 degrees C in Air.* Oxidation Of Metals, 2012. **77**(5-6): p. 275-287.
30. Li, S.B., W.B. Yu, H.X. Zhai, G.M. Song, W.G. Sloof, and S. van der Zwaag, *Mechanical properties of low temperature synthesized dense and fine-grained Cr_2AlC ceramics.* Journal of the European Ceramic Society, 2011. **31**(1–2): p. 217-224.

31. Li, S.B., H.L. Li, Y. Zhou, and H.X. Zhai, *Mechanism for abnormal thermal shock behavior of Cr_2AlC.* Journal Of the European Ceramic Society, 2014. **34**(5): p. 1083-1088.
32. Yu, W.B., S.B. Li, and W.G. Sloof, *Microstructure and mechanical properties of a $Cr_2Al(Si)C$ solid solution.* Materials Science and Engineering a-Structural Materials Properties Microstructure and Processing, 2010. **527**(21-22): p. 5997-6001.
33. Mashtalir, O., M. Naguib, V.N. Mochalin, Y. Dall'Agnese, M. Heon, M.W. Barsoum, and Y. Gogotsi, *Intercalation and delamination of layered carbides and carbonitrides.* Nature Communications, 2013. **4**: p. 1-7.
34. Zhang, X.D., J.G. Xu, H. Wang, J.J. Zhang, H.B. Yan, B.C. Pan, J.F. Zhou, and Y. Xie, *Ultrathin Nanosheets of MAX Phases with Enhanced Thermal and Mechanical Properties in Polymeric Compositions: $Ti_3Si_{0.75}Al_{0.25}C_2$.* Angewandte Chemie-International Edition, 2013. **52**(16): p. 4361-4365.
35. Fan, Y., L. Wang, J. Li, J. Li, S. Sun, F. Chen, L. Chen, and W. Jiang, *Preparation and electrical properties of graphene nanosheet Al_2O_3composites.* Carbon, 2010. **48**(6): p. 1743-1749.
36. HuaáLi, L., *Large-scale mechanical peeling of boron nitride nanosheets by low-energy ball milling.* Journal of materials chemistry, 2011. **21**(32): p. 11862-11866.
37. Porwal, H., S. Grasso, and M. Reece, *Review of graphene-ceramic matrix composites.* Advances in Applied Ceramics, 2013. **112**(8): p. 443-454.
38. Yao, Y., Z. Lin, Z. Li, X. Song, K.-S. Moon, and C.-p. Wong, *Large-scale production of two-dimensional nanosheets.* Journal of Materials Chemistry, 2012. **22**(27): p. 13494-13499.
39. He, Z.M. and J. Ma, *Constitutive modeling of alumina sintering: grain-size effect on dominant densification mechanism.* Computational Materials Science, 2005. **32**(2): p. 196-202.
40. Maca, K. and S. Simonikova, *Effect of sintering schedule on grain size of oxide ceramics.* Journal Of Materials Science, 2005. **40**(21): p. 5581-5589.
41. Rendtorff, N.M., S. Grasso, C. Hu, G. Suarez, E.F. Aglietti, and Y. Sakka, *Dense zircon ($ZrSiO_4$) ceramics by high energy ball milling and spark plasma sintering.* Ceramics International, 2012. **38**(3): p. 1793-1799.
42. Anstis, G., P. Chantikul, B.R. Lawn, and D. Marshall, *A critical evaluation of indentation techniques for measuring fracture toughness: I, direct crack measurements.* Journal of the American Ceramic Society, 1981. **64**(9): p. 533-538.

3 The high temperature oxidation behaviour of Cr_2AlC and silicon doped Cr_2AlC

The high temperature oxidation kinetics of Cr_2AlC and Si-doped Cr_2AlC in dry synthetic air was studied using thermogravimetric analysis in the range of 1000 to 1200 ºC for times up to 10 h. The SPS prepared Cr_2AlC and $Cr_2Al_{(0.93)}Si_{(0.07)}C$ materials were phase pure with 8 at.% unreacted Cr left in the matrix. The Cr_2AlC MAX phase substitutionally doped with 2 at.% Si formed a Al_2O_3 layer at 1200 ºC with a finer columnar grain structure. This microstructural modification resulted in faster diffusion paths for oxygen and hence a thicker oxide layer. But no enhancement of the oxidation kinetics, even somewhat slower kinetics, was observed at 1000 and 1100 ºC for Si doped Cr_2AlC. There was no Si detected neither at the surface or in the oxide layer. Segregation of Si was only observed in the Al depleted zone adjacent to the oxide layer. This zone is composed of Cr_7C_3 as a result of Al consumption. Si can not dissolve in this Cr_7C_3 phase. The accelerated oxidation kinetics at 1200 ºC as a result of doping with 2 at.% Si improves the healing kinetics of Cr_2AlC but the Cr_7C_3 interlayer may reduce the mechanical bond strength and hence lower the strength recovery.

3.1 Introduction

MAX Phase ceramics, in particular those containing Al or Si as the A element, have been explored widely due to their unique combination of properties with metallic and ceramic merits [1]. These MAX phases are thermally as well as electrically conductive, which makes them resistant to thermal shocks. Also their mechanical stability up to high temperatures and chemical resistance when exposed to harsh oxidizing environments [2, 3], in combination with their self-healing ability make these MAX phases attractive candidate materials for application in the hot sections of gas turbine and jet engines. It has been demonstrated that Ti_2AlC, Ti_3AlC_2 and Cr_2AlC can heal micro crack damage multiple times when exposed to high temperatures in the region of 1000 $^{\circ}C$ [4-6]. Recently, we have demonstrated that the erosion induced microcracks with a width of about 100 nm can be healed autonomously due to formation of well bonded Al_2O_3 in the crack gap [7]. The actual crack filling in Ti_2AlC was visualized for the first time by time lapse 3D tomography, which demonstrated that the healing is independent of position in the crack [8]. The rate of healing is directly related to the oxidation kinetics of the MAX Phase. In the case of Ti_2AlC the reaction is rather fast and leads to the formation of primarily strong α-Al_2O_3 but with some traces of the weaker TiO_2 oxide [5]. Hence, the healing reactions and healing kinetics of related Ti-free MAX phases such as Cr_2AlC are of particular interest too.

It is widely accepted that the growth of Al_2O_3 scale at high temperature on alloys is primarily dominated by the inward diffusion of oxygen along the grain boundary, although some outward diffusion of Al is also involved [9-12]. The growth rate depends inversely on the grain size in the oxide scale which suggests that fine grains promote the scale growth [11]. For a constant grain size the healing kinetics should obey a parabolic growth rate, but experiments have shown that the oxide growth of Cr_2AlC is best described by a cubic growth rate [13-19]. The abnormal growth exponent is attributed to grain coarsening during oxidation. Impurities or reactive elements intentionally added to the matrix may have significant influence on the outward diffusion of the Al^{3+} ions as well as on the morphology of the oxide layer and hence affect the healing kinetics and the properties of the layer formed [20-22] . For example, the addition of 0.5 wt% Y in the Ni-Cr-Al alloy decreased the thickness of the oxide layer but enhanced the adhesion between the scale and the matrix. A similar effect of Y on the oxidation of Cr_2AlC thin film has

been reported. In the present work, we examine the oxidation kinetics of Cr_2AlC, enriched with 2 at.% Si which dissolves substitutionally in the Al lattice of the Cr_2AlC [23, 24]. The effect of Si doping on the oxide formation on Cr_2AlC as well as on the oxide scale morphology is evaluated by TGA at three different temperatures and subsequent microstructural analysis.

3.2 Experimental procedures

3.2.1 Sample synthesis and preparation

The elemental powders were mixed for 24 h using a Turbula mixer (T2C, Switzerland) and the mixed powders were cold pressed into tablets with a diameter of 25 mm and a thickness of about 5 mm using a Carver press (Model 3853-0, USA). The mixing ratios and powder specification are listed in Table 3-1.

Table 3-1 Elemental powder mixtures and specification.

<table>
<tr><th>Sample</th><th>Mixing ratio</th><th colspan="4">Powder</th></tr>
<tr><td rowspan="2">Cr_2AlC</td><td rowspan="2">Cr:Al:C
2:1.15:1</td><td>Cr</td><td>Al</td><td>Si</td><td>Graphite</td></tr>
<tr><td>100 µm</td><td>45 µm</td><td>45 µm</td><td>6 µm</td></tr>
<tr><td rowspan="2">$Cr_2(Al_{1-x}Si_x)C$</td><td rowspan="2">Cr:Al:Si:C
2:0.92:0.23:1</td><td>purity > 99.2%</td><td>purity > 99.8%</td><td>purity > 99.8%</td><td>purity > 99.5%</td></tr>
<tr><td colspan="3">TLS Technik GmbH & Co., Germany</td><td>Graphit Kropfmühl AG, Germany</td></tr>
</table>

These tablets were then pressure-less sintered in a flow of 500 sccm Argon (purity <5N) for 1 h at 1400 ºC in a horizontal alumina tube furnace (Lenton Furnaces, PTF 16/75/610, UK) applying a heating rate of 5 ºC/min. Next, the PLS samples were pulverized (using a Fritsch Pulverisette, Germany), and the powders were densified with SPS (HP D 25, FCT Systeme GmbH, Frankenblick, Germany) at a pressure of 50 MPa with a heating rate of 50 ºC/min in a graphite mould with an inner diameter of either 20 or 40 mm. Its inner mould wall was covered with graphite paper and sprayed with BN. The sintered Cr_2AlC and $Cr_2(Al_{1-x}Si_xC)$ discs were around 5 mm thick and cut into pieces of 15 x 8 x 2 mm via electric discharge machining (EDM) for oxidation studies. The samples were ground with

SiC emery paper (4000 mesh grids) and cleaned ultrasonically in ethanol. Finally, the samples were dried in a flow of pure nitrogen gas.

3.2.2 Experimental techniques.

3.2.2.1 Thermal gravimetric analysis

The oxidation kinetics was determined using thermogravimetric analysis (TGA) using a high performance symmetrical balance (TGA 24, Setaram, France) having a dual furnace design to eliminate buoyance effects. Prior to TGA, the mass of the Cr_2AlC sample and an alumina dummy sample with the same dimension were measured with an analytical microbalance (Mettler, Swizterland) with a resolution of 0.1 mg. Then, the samples were mounted on the sapphire rods of the balance. Next, the balance was adjusted until the mass was in the region of ± 10 mg. After that, the samples were moved into the furnaces closing the system. The furnaces were flushed by evacuation till 10^{-2} mbar and refilled with the carrier gas (N_2) with a flow of 200 sccm up to atmospheric pressure. This procedure was repeated two times to ensure an inert environment. After final adjustment the resolution of the TG is in the range of ± 1 µg and the drift is about 2 µg/h. The two furnaces were heated up synchronically to the desired temperature with a heating rate of 10 °C/min while purging with N_2 with at flow rate of 50 sccm. Finally, the samples were thermally oxidized for 10 h in dry synthetic air, i.e. a gas mixture of 40 sccm N_2 and 10 sccm O_2. The mass change was recorded every 32 s and the oxygen gas line was closed automatically after 10 h oxidation. The furnaces were cooled down with 10 °C/min to room temperature while purging with N_2 with at flow rate of 50 sccm.

The Cr_2AlC and $Cr_2(Al_{1-x}Si_x)C$ samples were oxidized in the TGA for 10 h in dry synthetic air at 1000, 1100 and 1200 ºC, respectively.

3.2.2.2 Microstructure and composition analysis

The phase compositions of the pressure-less sintered powders and the SPS bulk samples were analysed with X-ray diffraction (Bruker D8, Germany) using Co-Kα radiation. The diffractograms were recorded over the 2θ angular range from 10 to 130° with a step size 0.034° 2θ and a counting time of 2 s per step. Diffract EVA software version 3.1 was employed to evaluate the diffraction data. The lattice parameters and volume fraction of different phases were quantified by Rietveld refinement analysis using MAUD (materials analysis using diffraction) software [25]. For the refinement models the theoretical

diffraction patterns of Cr_2AlC (Hexagonal, P63/mmc, a=2.86 Å, c=12.86Å) and Cr (Cubic, Im-3m, 2.895Å) were fitted to the measured diffractograms.

The microstructure of the virgin material surface as well as the sample surface and cross section after oxidation were observed with scanning electron microscopy (SEM) using a field emission gun scanning electron microscope (JEOL, JSM 6500F, Japan). This microscope is equipped with an energy dispersive spectrometer (EDS, Thermo-Noran, UltraDry, USA) for X-ray microanalysis (XMA) and a detector for backscattered electrons to observe composition variations (Autrata, Czech Republic). Also the scanning electron microscope is provided with a HKL Nordlys II detector (Oxford Instruments, UK) for electron backscattering diffraction (EBSD). The EBSD data acquisition and processing was performed using Channel 5 software (version 2011).

The composition of both sets of samples was determined quantitatively using electron probe X-ray microanalysis EPMA with 10 × 10 points measurement, which were performed with a JEOL JXA 8900R microprobe using an electron beam with energy of 10 keV and a beam current of 50 nA.

The surfaces after oxidation were analysed with X-ray photoelectron spectroscopy XPS (PHI 5400 ESCA) using non monochromatic Mg anode X-ray source (Mg Kα = 1253.6 eV). The photoelectron spectra were recorded using a spherical capacitor analyser (SCA) operated with a pass energy of 71.55 eV, in the binding energy range of 0-1000 eV with a step size of 0.25 eV and a dwell time of 2 s per step. Prior to the XPS measurements, surface contamination was removed by mild ion sputtering for 20 min using a 3 keV Ar^+ beam scanning a sample surface area of 5 × 5 mm.

After the oxidation experiments and analysis of the surfaces, the samples were first covered with a layer of 0.5 µm Cr sputtered using a conventional sputter coater (Leica EM SCD050). Then, a 0.5 mm thick Si-(001) wafer was glued to the surface with an epoxy resin (G2 Gatan 601.07270, UK) to preserve the oxide layer. Cross-sections were prepared by cutting this assembly with a diamond wafering blade of 0.35 mm thickness and an IsoMet low speed saw (Beuhler, USA). Finally, the cross-sections were polished using a cross-section ion-polisher (JEOL SM-09010, Japan) operating at an accelerating voltage of 4.5 kV and an ion current of 18 µA using Ar gas [26].

3.3 Results and discussion

3.3.1 Composition and microstructure

From the EPMA results in Table 3-2, it can be seen that the SPS sintered Cr_2AlC has the intended stoichiometric composition, while in the $Cr_2Al_{1-x}Si_xC$ material around 2 at.% Si is detected in the matrix, which is less than the 5 at.% Al present in the powder mixture, cf Table 3-1.

Table 3-2 Composition of Cr_2AlC and $Cr_2(AlxSi1-x)C$ as measured with EPMA, expressed as molar ratio.

	Cr	**Al**	**Si**	**C**
Cr_2AlC	1.99±0.01	1.01±0.01	0.00	1.00±0.01
$Cr_2(Al_{1-x}Si_x)C$	2.00±0.02	0.93±0.02	0.07±0.01	1.00±0.01

The loss of Si could partially due to the mass loss due to evaporation during sintering and the Si being used in the formation of a second phase Cr_5Si_3 which was verified with EPMA. However, the amount of Cr_5Si_3 is too small to be determined quantitatively from the XRD pattern. This second phase was also observed in previous study [23].

The XRD patterns in Figure 3.1 reveal that the Cr_2AlC is the main phase, however, some unreacted Cr, about 8 at.%, remained in the matrix. The hexagonal crystal structure of Cr_2AlC was retained upon doping with 2 at.% Si to substitute 7 % of Al atoms in Cr_2AlC. The lattice parameters a and c of the matrix material decreased from 2.860 Å to 2.858 Å and from 12.840 Å to 12.747 Å, respectively. The reduction of the lattice parameters a and c due to doping with Si is in agreement with the smaller atomic radius of Si (111 pm) compared with that of Al (118 pm) and in earlier studies [23, 24]. The change in lattice parameter suggests that Si is in solid solution in the MAX phase $Cr_2Al_{1-x}Si_xC$.

Both Cr_2AlC and $Cr_2Al_{(0.93)}Si_{(0.07)}C$ are coarse-grained and have an average grain size of about 50 µm and have a random orientation, as can be seen from the Euler maps presented in Figure 3.2.

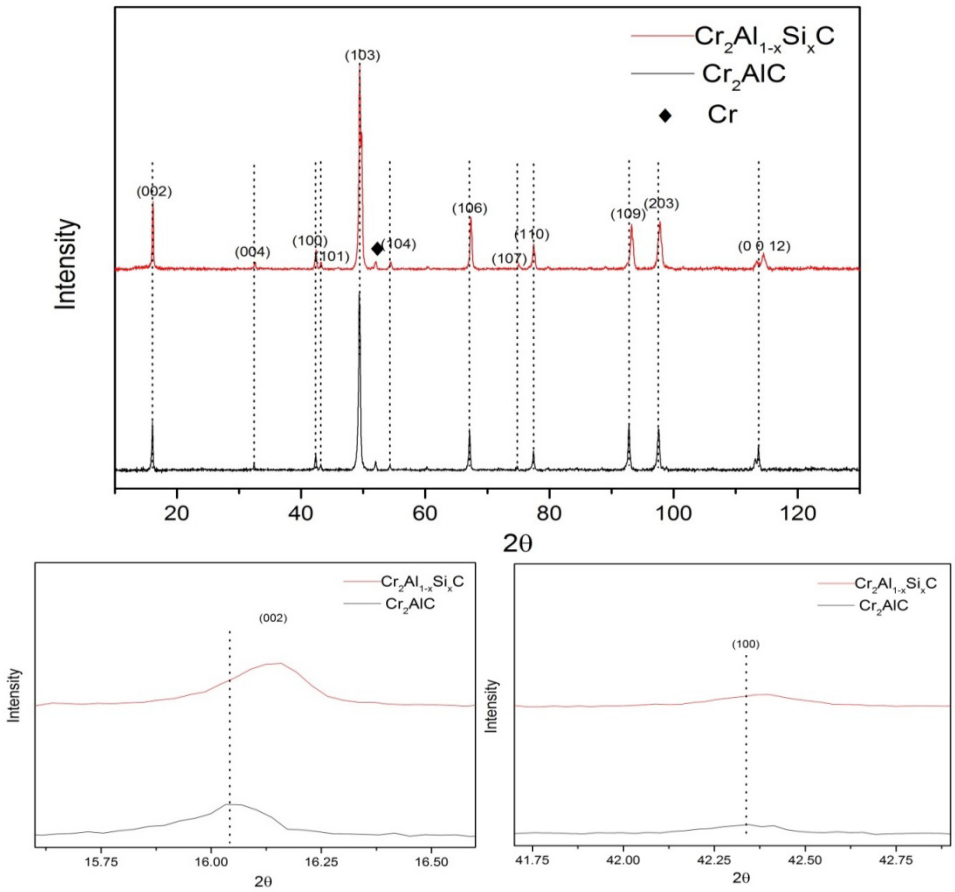

Figure 3.1 XRD patterns of SPS Cr_2AlC, and $Cr_2(Al_{1-x}Si_x)C$ as well as a close look of the (002) and (100) peak shift which corresponds to lattice parameter c and a, respectively.

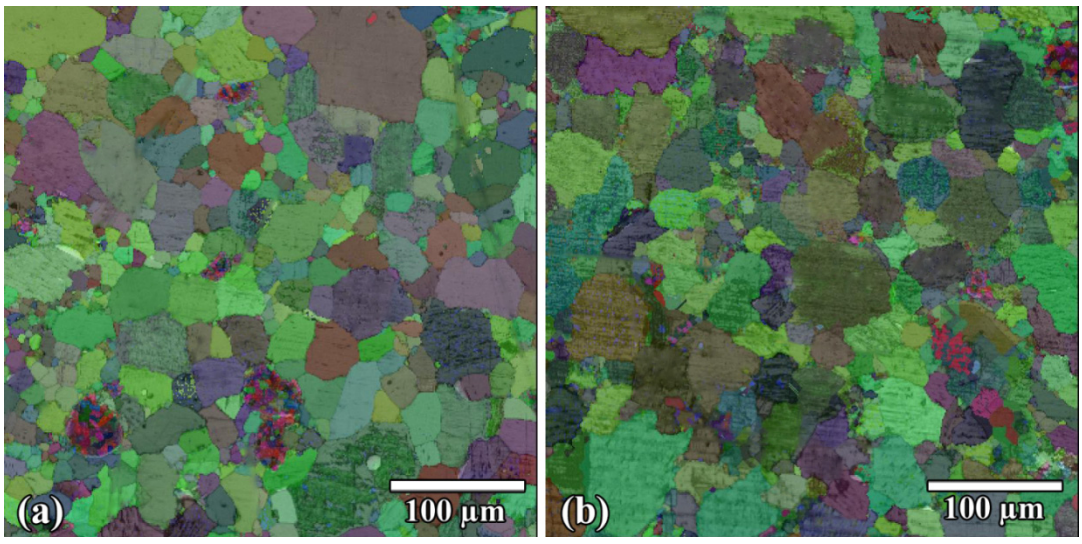

Figure 3.2 Euler maps of bulk (a) Cr_2AlC and (b) $Cr_2Al_{(0.93)}Si_{(0.07)}C$.

3.3.2 The Oxidation behaviour of Cr_2AlC

A well-adhering dense alumina layer of uniform thickness is formed on the phase pure Cr_2AlC oxidized for 10 h in dry synthetic air at 1000, 1100 and 1200 ºC; see the cross sections in Figure 3.3. XRD and XMA analysis of the oxide layer shows that the oxide layer is mainly composed of Al_2O_3, but with some Cr in solid solution $(Al,Cr)_2O_3$ near the surface. The Cr to Al ratio in the oxide layer as determined by XPS near the surface is listed in Table 3-3.

Table 3-3 The detected Cr to Al ratio in the solid solution formed at the surface of Cr_2AlC and $Cr_2Al_{(0.93)}Si_{(0.07)}C$ after oxidation in dry synthetic air at 1000, 1100, 1200 ºC for 10 h by XPS.

	Cr_2AlC		**$Cr_2Al_{0.93}Si_{0.07}C$**	
T(ºC)	**Cr/Al**	**$(Al_{1-y}Cr_y)_2O_3$**	**Cr/Al**	**$(Al_{1-y}Cr_y)_2O_3$**
1200	0.39	$(Al_{0.72}Cr_{0.28})_2O_3$	0.33	$(Al_{0.75}Cr_{0.25})_2O_3$
1100	0.95	$(Al_{0.51}Cr_{0.49})_2O_3$	0.49	$(Al_{0.67}Cr_{0.33})_2O_3$
1000	1.08	$(Al_{0.52}Cr_{0.48})_2O_3$	0.78	$(Al_{0.56}Cr_{0.44})_2O_3$

The Cr content decreases with increasing oxidation temperature, which may be due to the formation of volatile CrO_3 that becomes more stable at higher temperatures [15, 27]. The oxidation of Cr may have occurred during the fast scale growth at the early stages of oxidation. Then, the MAX phase at the interface with the oxide scale becomes depleted of Al, increasing the activity of Cr [28]. At the subsequent stages of oxidation the activity of Al in the MAX phase at the interface with the oxide layer increases due to diffusion of Al while the oxide growth rate decreases enhancing the exclusive growth of Al_2O_3 [28] . However, the region near the interface with the oxide scale after 10 h oxidation remained Cr_2AlC. Thus the Al depletion did not result in decomposition of the MAX phase. From the surface morphology of top layers it can be seen that the grain size of oxide Al_2O_3 increases with oxidation temperature from 0.35 μm to 0.80 μm after 10 h oxidation at 1000 to 1200 ºC, respectively.

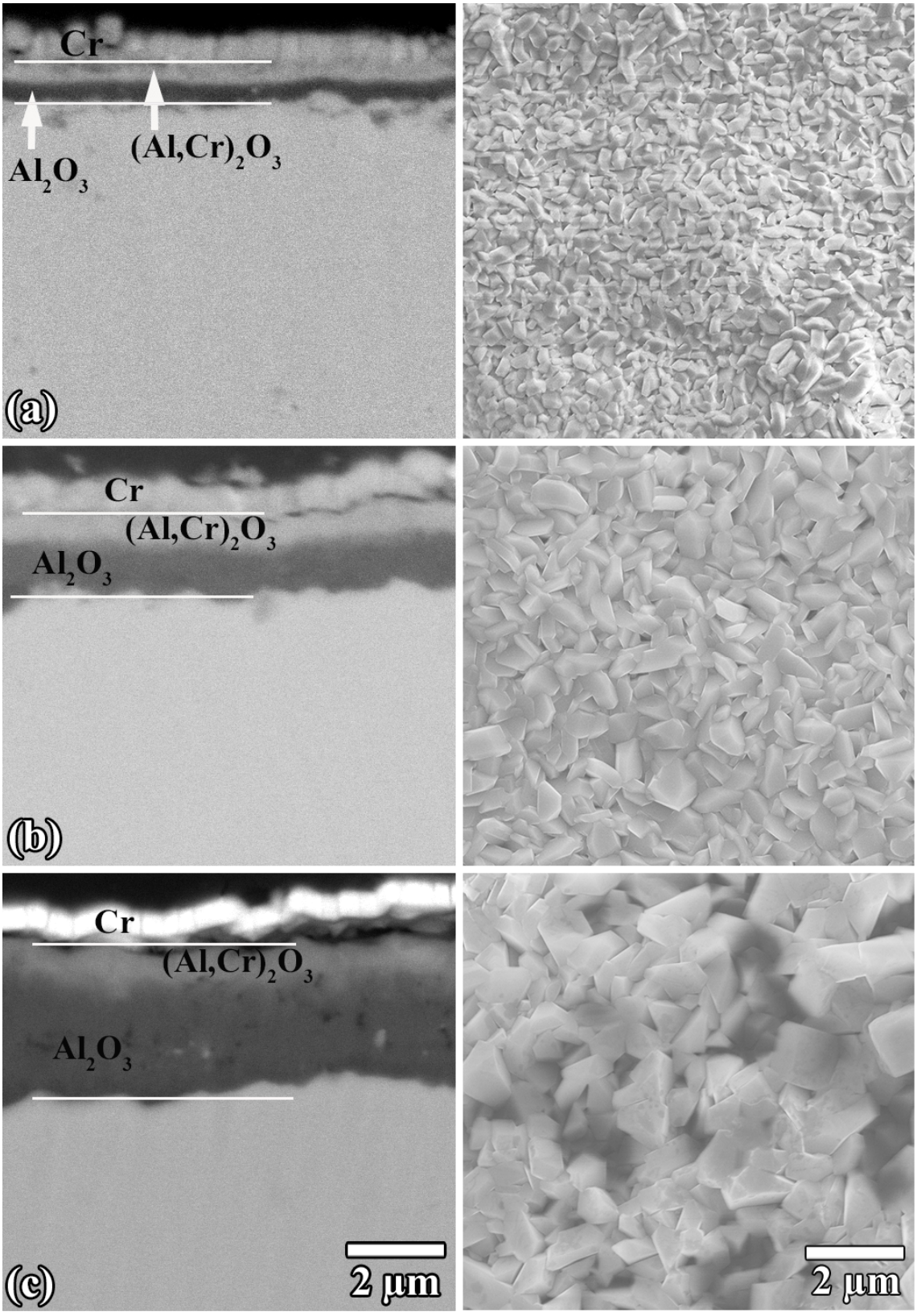

Figure 3.3 The cross section and surface morphology of Cr_2AlC after oxidation at (a)1000, (b) 1100 and (c) 1200 °C in dry synthetic air for 10 h with the same magnification. A 0.5 μm thick Cr was deposited at the oxidized sample surface.

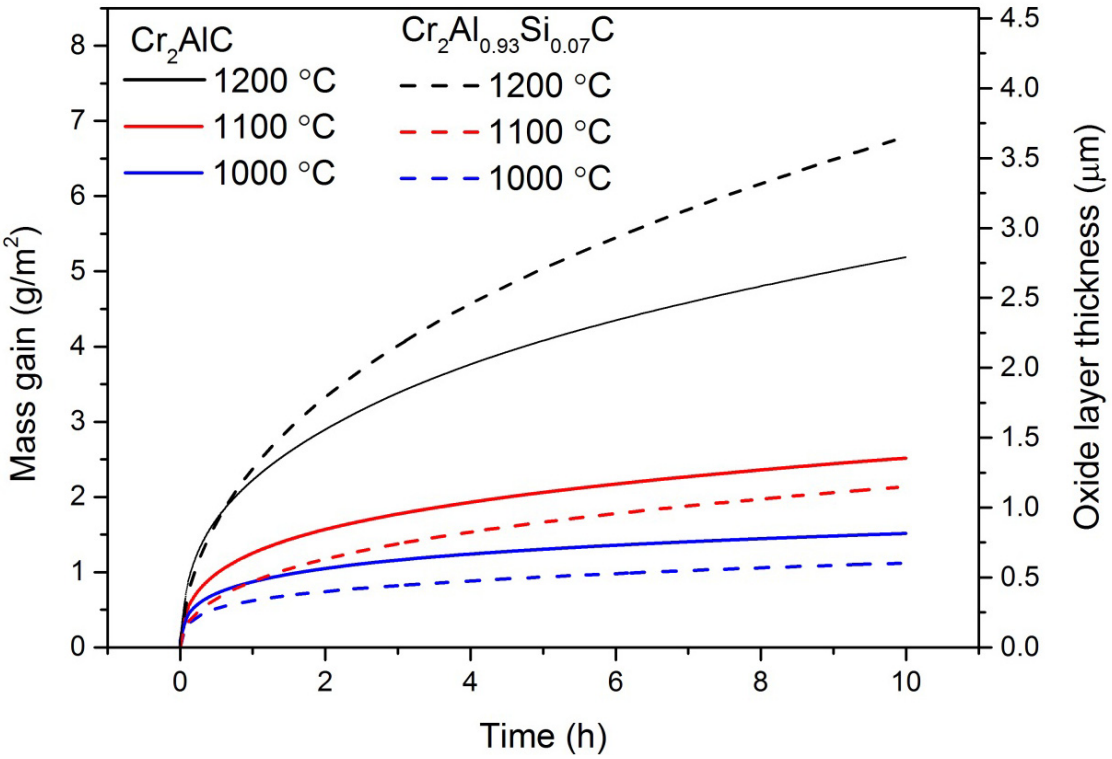

Figure 3.4 Mass change due to oxidation of Cr_2AlC(solid lines), and $Cr_2Al_{(0.93)}Si_{(0.07)}C$ (dashed lines) at 1000, 1100 and 1200 °C in dry synthetic air for 10 h. Both mass gain and equivalent oxide layer thickness as a function of oxidation time were plot on left and right axes, respectively.

Table 3-4 Summary of oxide growth rate constants of Cr_2AlC and $Cr_2Al_{(0.93)}Si_{(0.07)}C$ at 1000, 1100 and 1200 ºC when fitted with cubic and power rate laws.

Sample	T/(ºC)	n	k_c ($kg^3m^{-6}s^{-1}$)	n	k_n ($kg^nm^{-2n}s^{-1}$)
Cr_2AlC	1200	3	3.7E-12	2.7	1.96E-11
	1100	3	4.8E-13	3.3	7.25E-14
	1000	3	1.2E-13	4.1	7.98E-17
$Cr_2Al_{0.93}Si_{0.07}C$	1200	3	7.2E-12	2.2	4.9E-10
	1100	3	2.5E-13	2.6	3.3E-12
	1000	3	4.5E-14	3.8	1.7E-16

The corresponding oxidation kinetics was determined using thermogravimetry. The observed mass change Δm per unit of surface area A shown in Figure 3.4 can be described best with a power law [17]:

$$\left(\frac{\Delta m}{A}\right)^n = k_n t \tag{3-1}$$

where k_n is a rate constant, n is the growth rate exponent and t is the oxidation time. Both the rate constant k and exponent n determined by fitting Eq. (1) to the measured oxidation kinetics presented in Figure 3.4 are listed in Table 3-4.

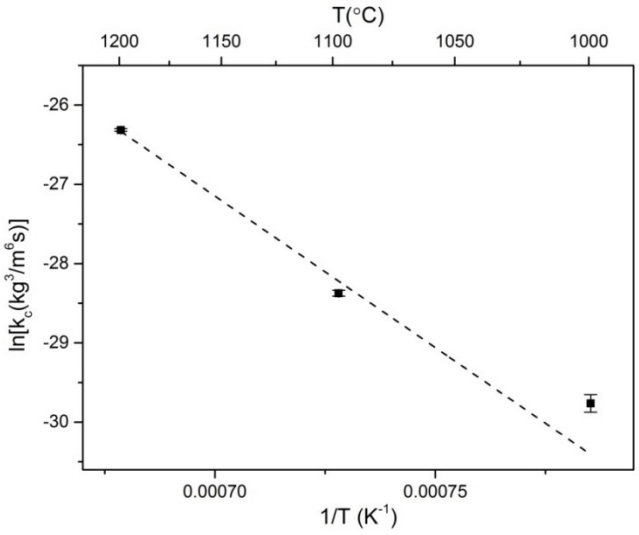

Figure 3.5 Arrhenius plot of the cubic growth rate constant of the oxide scale on Cr_2AlC.

Since alumina formation due to thermal oxidation is due to diffusional transport of oxygen along the grain boundaries [11] the oxide scale growth rate increases with temperature; the exponent n decreases with temperature. The apparent activation energy of the oxidation of Cr_2AlC can be evaluated adopting an Arrhenius type of behaviour for the rate constant. A value of 318 ± 40 kJ/mol is obtained when describing the growth rate with a cubic law, see Figure 3.5. This value is significantly smaller than the earlier reported value of 507 ± 90 kJ/mol [17]. A growth rate exponent larger than 2 (parabolic growth) hints at oxide grain growth during oxidation [11]. It seems that the oxide grain growth is relatively larger at 1000 ºC than at 1100 and 1200 ºC, although the grain size is smaller at 1000 ºC than at 1100 and 1200 ºC; see Figure 3.3. This may be related to a much higher oxide nucleation density at 1000 ºC than at the higher temperatures.

3.3.3 The oxidation behaviour of $Cr_2Al_{(0.93)}Si_{(0.07)}C$

At 1200 ºC the mass gain of $Cr_2Al_{(0.93)}Si_{(0.07)}C$ as measured by TGA was about 30% higher than that of Cr_2AlC, while at 1000 and 1100 ºC no improvement was observed in oxidation kinetics, as shown in Figure 3.4. The corresponding cubic and power growth rate constants of $Cr_2Al_{(0.93)}Si_{(0.07)}C$ are listed in Table 3-4. The cross sections of the oxide similar showed a layered structure, shown Figure 3.6.

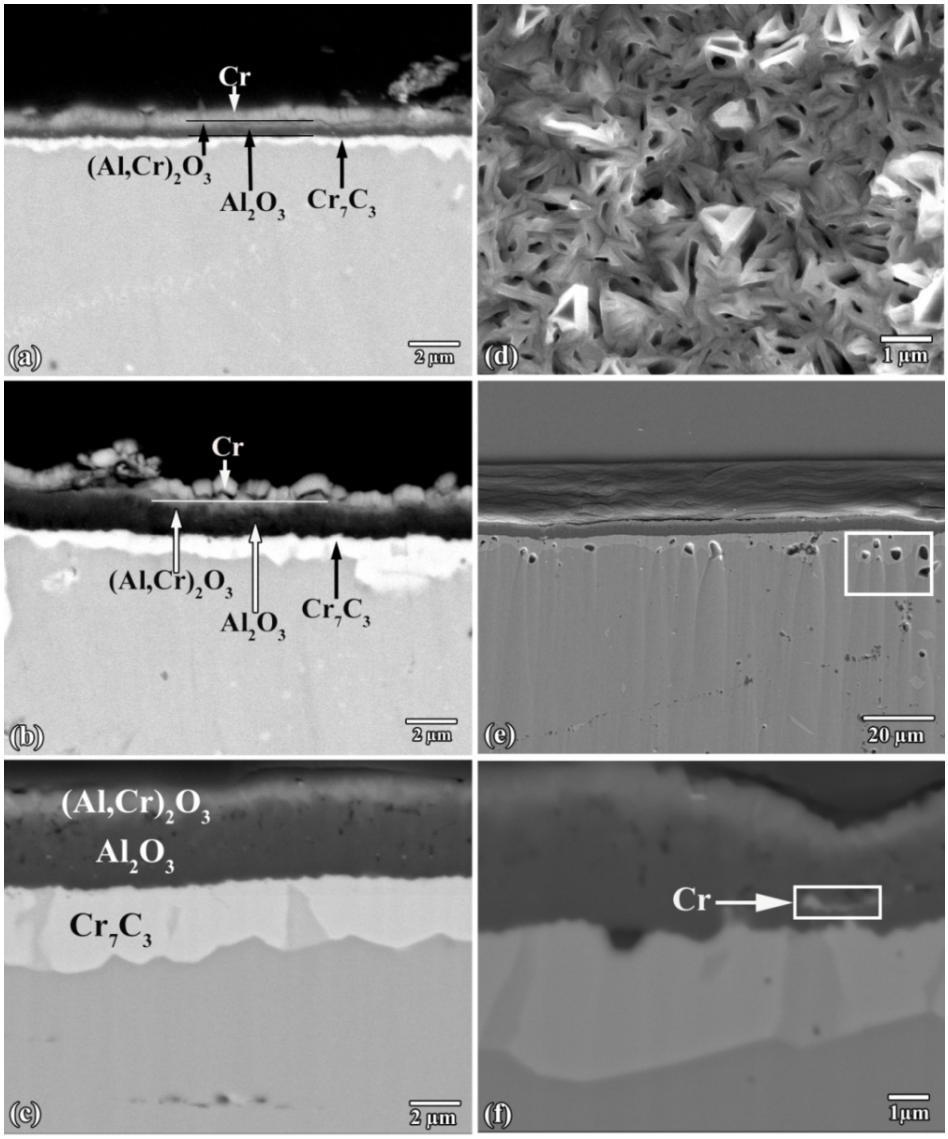

Figure 3.6 BSE images of cross section of $Cr_2Al_{(0.93)}Si_{(0.07)}C$ after isothermal oxidation for 10 h in dry synthetic air at (a) 1000, (b) 1100, (c) 1200 ºC, (d) is a SEM image of surface morphology and (e), (f) are BSE images of cross section of $Cr_2Al_{(0.93)}Si_{(0.07)}C$ with different magnifications after oxidation at 1200 ºC for 10 h in dry synthetic air.

The $(Al,Cr)_2O_3$ solid solution layer is near the surface and the Cr concentration is lower than that formed on Cr_2AlC, see Table 3-3. Underneath it a more pure Al_2O_3 layer is formed. In contrast to the oxidation behaviour of Cr_2AlC, the depletion of Al in $Cr_2Al_{(0.93)}Si_{(0.07)}C$ leads to decomposition of the MAX phase in the region adjacent to the alumina scale; see Figure 3.6 (a, b and c). EPMA and XRD confirmed that the MAX phase locally transformed into Cr_7C_3.

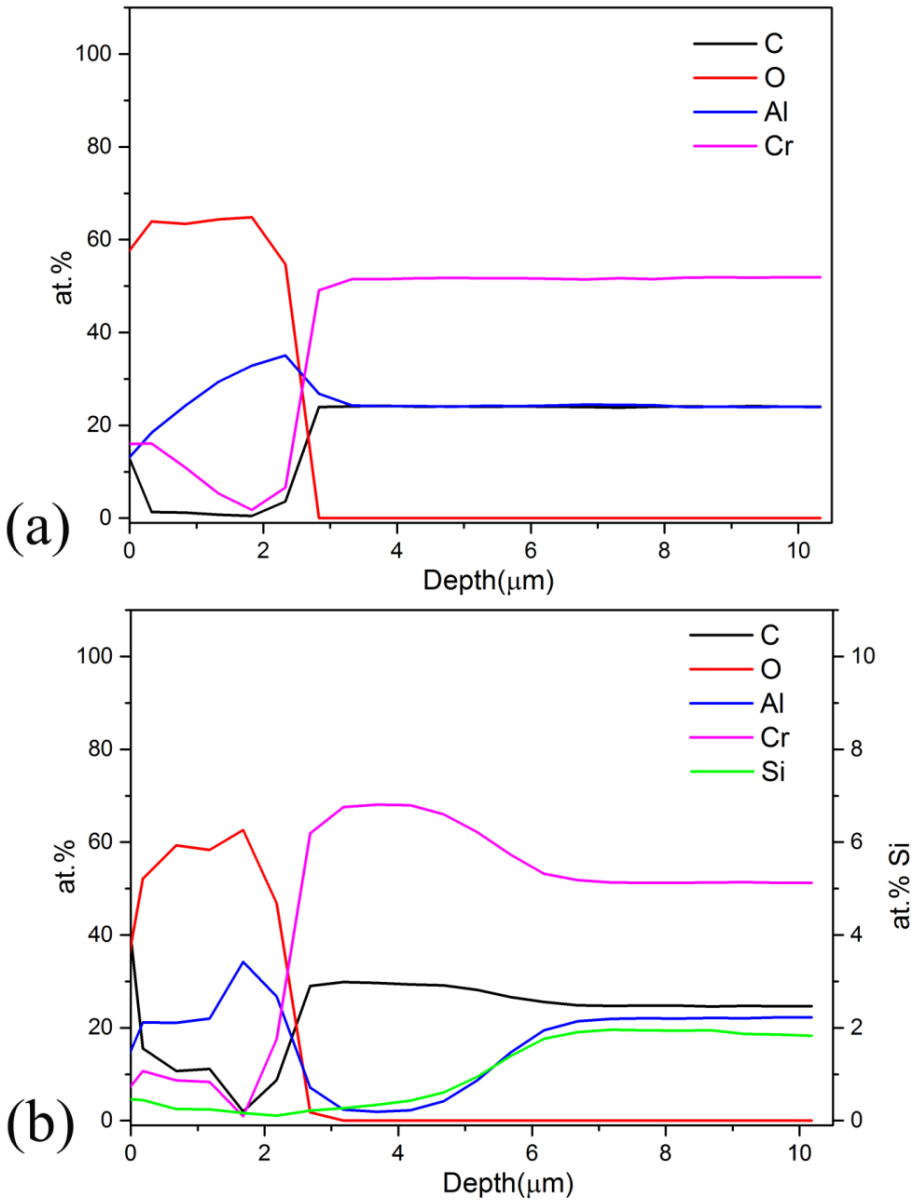

Figure 3.7 Concentration depth profiles after oxidation at 1200 ºC for 10 h in dry synthetic air of (a) Cr_2AlC and (b) $Cr_2Al_{(0.93)}Si_{(0.07)}C$ from the surface to the matrix (left to right).

The composition depth profiles recorded with EPMA of the oxidized Cr_2AlC and $Cr_2Al_{(0.93)}Si_{(0.07)}C$ at 1200 ºC, see Figure 3.7, clearly show the Al depleted zone of

$Cr_2Al_{(0.93)}Si_{(0.07)}C$ while the composition of Cr_2AlC is practically constant and matches that of the MAX phase. Also the composition depth profiles show the enrichment in both Cr and C in the Al depleted zone leading to a composition corresponding to Cr_7C_3. Furthermore, the composition depth profiles show the presence of Cr in the top part of the oxide scale for both Cr_2AlC and $Cr_2Al_{(0.93)}Si_{(0.07)}C$.

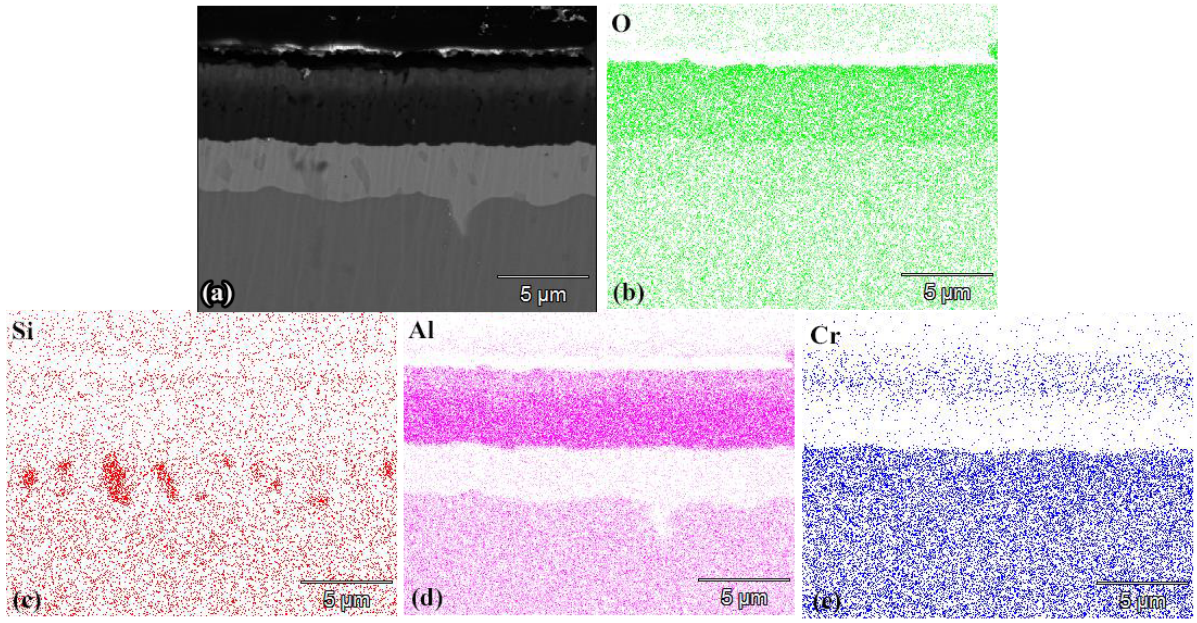

Figure 3.8 (a) BSE image of a cross section of $Cr_2Al_{(0.93)}Si_{(0.07)}C$ after oxidation in dry synthetic air for 10 h at 1200 ºC, (b) O X-ray map, (c) Si X-ray map, (d) Al X-ray map, (e) Cr X-ray map.

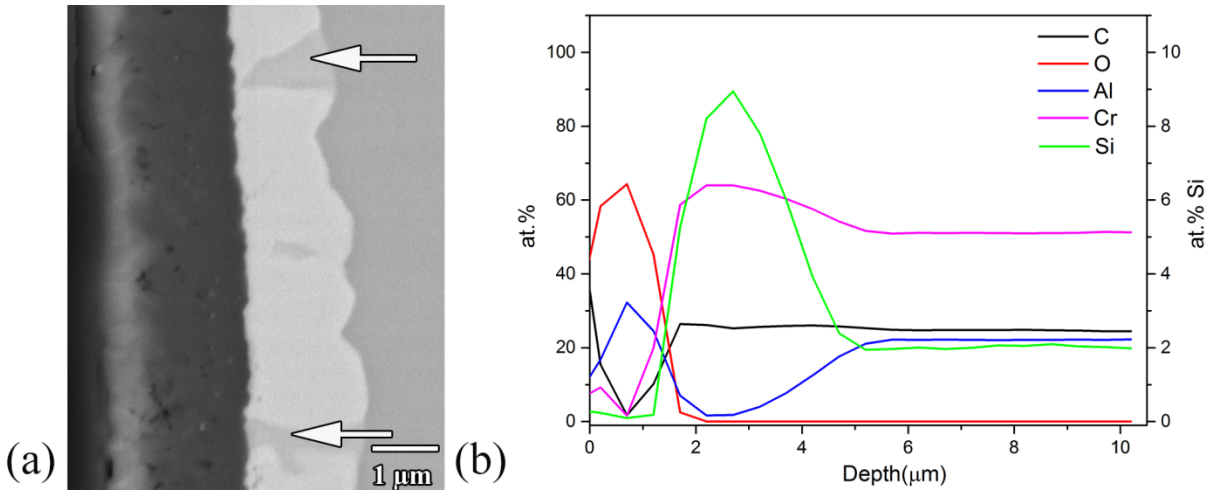

Figure 3.9 (a) BSE image of cross section of Si doped sample $Cr_2Al_{(0.93)}Si_{(0.07)}C$ after 10 h oxidation in dry synthetic air. The arrows indicate the area where the Si accumulated in the depletion zone; (b) Concentration depth profile recorded with EPMA.

X-ray maps of the oxide layer formed on $Cr_2Al_{(0.93)}Si_{(0.07)}C$ and the depletion zone (Figure 3.8) confirm the consumption of Al adjacent to the oxide layer and the presence of Cr in the top part of the oxide layer.

The Si seems to segregate laterally to the grain boundaries in the depleted region as marked in Figure 3.8 (c) and Figure 3.9 (a). A composition depth profile was recorded along a line crossing the Si enriched area and is shown in Figure 3.9 (b). The local enrichment of Si in the Al depleted zone is around 9 at.% and is clearly visible. The depletion of Al in this MAX phase causes enrichment of Si (which is not oxidized) and Si does not dissolve in Cr_7C_3 [29].

Although the outward diffusion of Cr^{3+} in alumina is limited [30], still some patches of Cr_2O_3 (likely in solid solution) are present in the pure Al_2O_3 layer both in Cr_2AlC and $Cr_2Al_{(0.93)}Si_{(0.07)}C$ samples after oxidation at 1200 ºC, see Figure 3.3 (c) and Figure 3.6 (f). Voids are only present in the depletion zone and are attributed to the gas phase formation and to the volume reduction of about 39.7 % accompanying the transformation of Cr_2AlC into Cr_7C_3 [14, 30], see Figure 3.6 (e) and (f).

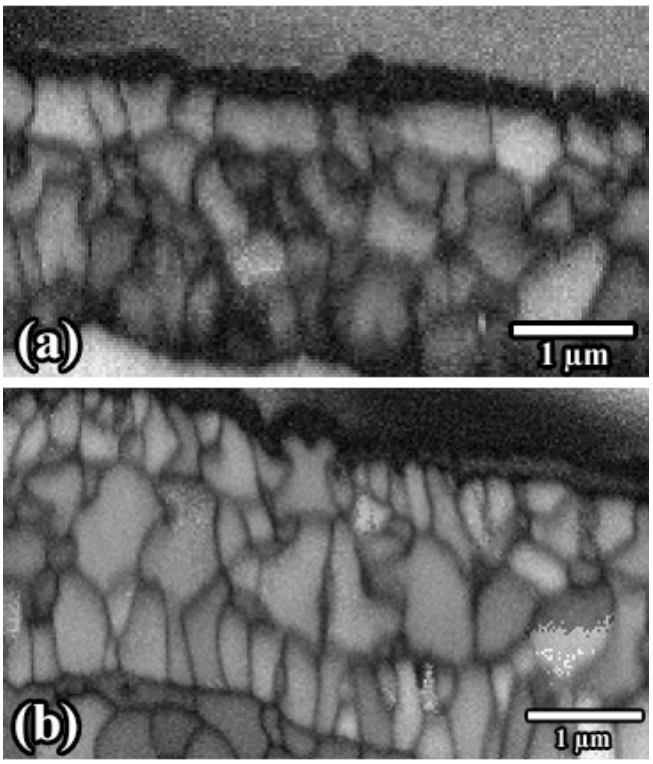

Figure 3.10 Band contrast images of cross section of oxide layer grown on (a) Cr_2AlC and (b) $Cr_2Al_{(0.93)}Si_{(0.07)}C$ surface after oxidation for 10 h in dry synthetic air at 1200 ºC.

The enhanced oxidation kinetics of the Si doped Cr_2AlC at 1200 ºC is attributed to the columnar structure with a slightly smaller lateral oxide grain size, since the alumina oxide scale growth is dominated by oxygen diffusion along the oxide grain boundaries [9, 31, 32]. The oxide formed on the $Cr_2Al_{(0.93)}Si_{(0.07)}C$ is much finer grained than on Cr_2AlC, see Figure 3.6 (d). This is also confirmed by EBSD analysis of cross-sections of the oxide layers; see Figure 3.10. The band contrast images reveal that the average lateral grain size of the oxide layer is 0.38 ± 0.01 μm and 0.31 ± 0.01 μm for the oxide layer grown on Cr_2AlC and $Cr_2Al_{(0.93)}Si_{(0.07)}C$, respectively. The columnar grain structure grown on the Si doped sample can be seen in Figure 3.10 (b), which promotes the oxygen diffusion and thereby enhances the oxide scale growth. Apparently, a higher nucleation density of alumina occurred at the initial stage of oxidation on $Cr_2Al_{(0.93)}Si_{(0.07)}C$ than on Cr_2AlC. This may be due to a larger lattice mismatch and thus higher interface energy between Al_2O_3 and Cr_2AlC when Si is added.

Finally, it should be mentioned that while the oxidation kinetics of Cr_2AlC is improved (at the highest oxidation temperature used) by substitutionally doping the MAX phase material with 2 at.% Si, which would have a beneficial effect on the healing kinetics, the formation of the Cr_7C_3 interlayer may reduce the mechanical bond strength and hence lower the strength recovery. This latter effect was however not examined in the context of the present work.

3.4 Conclusions

The Cr_2AlC and $Cr_2(Al,Si)C$ MAX phases prepared by first pressure-less sintering followed by spark plasma sintering are practically phase pure with some Cr and Cr_5Si_3 impurities. The hexagonal Cr_2AlC crystal structure remains stable when 7 % of the Al atoms in Cr_2AlC were substituted by Si and the lattice parameter a and c decreased. A dense oxide layer was formed on the surface of Cr_2AlC and $Cr_2Al_{(0.93)}Si_{(0.07)}C$ after oxidation at high temperatures. This oxide is composed of Al_2O_3 with Cr in solid solution, i.e. $(Al,Cr)_2O_3$, near the free surfaces. The oxide layer is coarser when formed at higher temperature. There was no Si detected neither at the surface nor in the oxide layer. It was only observed to segregate to the grain boundaries of Cr_7C_3 in the Al depleted beneath the oxide layer on $Cr_2Al_{(0.93)}Si_{(0.07)}C$. However, such an Al depleted layer was not observed for the oxidized Cr_2AlC. The oxidation kinetics of Cr_2AlC and $Cr_2Al_{(0.93)}Si_{(0.07)}C$ is best

described by a power law with a growth rate exponent larger than 2 (parabolic). This enlargement in growth exponent suggests grain growth during oxidation. When doping with Si the oxide growth was promoted only at 1200 ºC as a result of finer Al_2O_3 grain size and the formation of columnar structure that offers fast diffusion paths for oxygen. No improvement, even a slower, oxidation kinetics was observed when oxidizing the Si doped Cr_2AlC at 1000 and 1100 ºC for 10 h.

References

1. Barsoum, M.W., *Introduction*, in *MAX Phases: Properties of Machinable Ternary Carbides and Nitrides*. 2013, Wiley-VCH Verlag GmbH & Co. KGaA. p. 1-12.
2. Farle, A.-S., C. Kwakernaak, S. van der Zwaag, and W.G. Sloof, *A conceptual study into the potential of $M_{n+1}AX_n$-phase ceramics for self-healing of crack damage.* Journal of the European Ceramic Society, 2015. **35**(1): p. 37-45.
3. Barsoum, M.W. and M. Radovic, *Elastic and Mechanical Properties of the MAX Phases*, in Annual Review of Materials Research, Vol 41, D.R. Clarke and P. Fratzl, Editors. 2011, Annual Reviews: Palo Alto. p. 195-227.
4. Li, S., G. Song, K. Kwakernaak, S. van der Zwaag, and W.G. Sloof, *Multiple crack healing of a Ti_2AlC ceramic.* Journal of the European Ceramic Society, 2012. **32**(8): p. 1813-1820.
5. Li, S., L. Xiao, G. Song, X. Wu, W.G. Sloof, and S. van der Zwaag, *Oxidation and crack healing behavior of a fine-grained Cr_2AlC ceramic.* Journal of the American Ceramic Society, 2013. **96**(3): p. 892-899.
6. Song, G.M., Y.T. Pei, W.G. Sloof, S.B. Li, J.T.M. De Hosson, and S. van der Zwaag, *Oxidation-induced crack healing in Ti_3AlC_2 ceramics.* Scripta Materialia, 2008. **58**(1): p. 13-16.
7. Shen, L., D. Eichner, S. van der Zwaag, C. Leyens, and W.G. Sloof, *Reducing the erosive wear rate of Cr_2AlC MAX phase ceramic by oxidative healing of local impact damage.* Wear, 2016. **358–359**: p. 1-6.
8. Sloof, W.G., R. Pei, S.A. McDonald, J.L. Fife, L. Shen, L. Boatemaa, A.-S. Farle, K. Yan, X. Zhang, S. van der Zwaag, P.D. Lee, and P.J. Withers, *Repeated crack healing in MAX-phase ceramics revealed by 4D in situ synchrotron X-ray tomographic microscopy.* Scientific Reports, 2016. **6**: 23040.
9. Wada, M., T. Matsudaira, and S. Kitaoka, *Mutual grain-boundary transport of aluminum and oxygen in polycrystalline Al_2O_3 under oxygen potential gradients at high temperatures.* Journal of the Ceramic Society of Japan, 2011. **119**(1395): p. 832-839.
10. Smialek, J.L., *Oxygen diffusivity in alumina scales grown on Al-MAX phases.* Corrosion Science, 2015. **91**: p. 281-286.
11. Smialek, J.L., N.S. Jacobson, B. Gleeson, D.B. Hovis, and A.H. Heuer, *Oxygen Permeability and Grain-Boundary Diffusion Applied to Alumina Scales.* 2013.
12. Hindam, H. and D.P. Whittle, *Microstructure, adhesion and growth kinetics of protective scales on metals and alloys.* Oxidation of Metals, 1982. **18**(5): p. 245-284.
13. Lee, D., T. Nguyen, and S. Park, *Long-Time Oxidation of Cr_2AlC Between 700 and 1,000 °C in Air.* Oxidation of Metals, 2012. **77**(5-6): p. 275-287.

14. Lee, D.B. and T.D. Nguyen, *Cyclic oxidation of Cr_2AlC between 1000 and 1300 °C in air.* Journal of Alloys and Compounds, 2008. **464**(1–2): p. 434-439.
15. Lee, D.B., T.D. Nguyen, J.H. Han, and S.W. Park, *Oxidation of Cr_2AlC at 1300 °C in air.* Corrosion Science, 2007. **49**(10): p. 3926-3934.
16. Li, S., X. Chen, Y. Zhou, and G. Song, *Influence of grain size on high temperature oxidation behavior of Cr_2AlC ceramics.* Ceramics International, 2013. **39**(3): p. 2715-2721.
17. Tallman, D.J., B. Anasori, and M.W. Barsoum, *A Critical Review of the Oxidation of Ti_2AlC, Ti_3AlC_2 and Cr_2AlC in Air.* Materials Research Letters, 2013. **1**(3): p. 115-125.
18. Wang, X.H., F.Z. Li, J.X. Chen, and Y.C. Zhou, *Insights into high temperature oxidation of Al_2O_3-forming Ti_3AlC_2.* Corrosion Science, 2012. **58**: p. 95-103.
19. Wang, X.H. and Y.C. Zhou, *High-Temperature Oxidation Behavior of Ti_2AlC in Air.* Oxidation of Metals, 2003. **59**(3-4): p. 303-320.
20. Hou, P.Y., *Impurity Effects on Alumina Scale Growth.* Journal of the American Ceramic Society, 2003. **86**(4): p. 660-668.
21. Ramanarayanan, T.A., R. Ayer, R. Petkovic-Luton, and D.P. Leta, *The influence of yttrium on oxide scale growth and adherence.* Oxidation of Metals, 1988. **29**(5-6): p. 445-472.
22. Berger, O., R. Boucher, and M. Ruhnow, *Part II. Oxidation of yttrium doped Cr_2AlC films in temperature range between 700 and 1200 °C.* Surface Engineering, 2015. **31**(5): p. 386-396.
23. Yu, W., S. Li, and W.G. Sloof, *Microstructure and mechanical properties of a $Cr_2Al(Si)C$ solid solution.* Materials Science and Engineering: A, 2010. **527**(21–22): p. 5997-6001.
24. Shang, L., D. Music, and J.M. Schneider, *Phase stability predictions of $Cr_{1-x}, M_x)_2 (Al_{1-y}, A_y)(C_{1-z}, X_z)$ (M = Ti, Hf, Zr; A = Si, X = B).* Journal of Physics D: Applied Physics, 2014. **47**(6): 065308.
25. Lutterotti, L., S. Matthies, and H. Wenk, *MAUD: a friendly Java program for material analysis using diffraction.* IUCr: Newsletter of the CPD, 1999. **21**(14-15).
26. Amirmajdi, O.M., R. Ashyer-Soltani, M.P. Clode, S.H. Mannan, Y. Wang, E. Cabruja, and G. Pellegrini, *Cross-Section Preparation for Solder Joints and MEMS Device Using Argon Ion Beam Milling.* IEEE Transactions on Electronics Packaging Manufacturing, 2009. **32**(4): p. 265-271.
27. Lin, Z.J., M.S. Li, J.Y. Wang, and Y.C. Zhou, *High-temperature oxidation and hot corrosion of Cr2AlC.* Acta Materialia, 2007. **55**(18): p. 6182-6191.
28. Nijdam, T.J., L.P.H. Jeurgens, and W.G. Sloof, *Promoting exclusive α-Al_2O_3 growth upon high-temperature oxidation of NiCrAl alloys: experiment versus model predictions.* Acta Materialia, 2005. **53**(6): p. 1643-1653.
29. Shabalin, I.L., *Ultra-High Temperature Materials I: Carbon (Graphene/Graphite) and Refractory Metals*. Vol. 1. 2014: Springer.
30. Tian, W., P. Wang, Y. Kan, and G. Zhang, *Oxidation behavior of Cr_2AlC ceramics at 1,100 and 1,250 °C.* Journal of Materials Science, 2008. **43**(8): p. 2785-2791.
31. Prescott, R. and M.J. Graham, *The formation of aluminum oxide scales on high-temperature alloys.* Oxidation of Metals, 1992. **38**(3-4): p. 233-254.
32. Beck, A.F., M.A. Heine, E.J. Caule, and M.J. Pryor, *The kinetics of the oxidation of Al in oxygen at high temperature.* Corrosion Science, 1967. **7**(1): p. 1-22.

4 Repeated crack healing in MAX Phase ceramics revealed by 4D in situ synchrotron X-ray tomographic microscopy

MAX phase Metalloceramics are emerging as attractive engineering materials in applications where the material is exposed to severe thermal and mechanical conditions in an oxidative environment. The Ti_2AlC MAX phase possesses attractive thermomechanical properties even beyond a temperature of 1000 K. An attractive feature of this material is its capacity for the autonomous healing of cracks when operating at high temperatures. Coupling a specialized thermomechanical setup to a synchrotron X-ray tomographic microscopy endstation at the TOMCAT beamline, we captured the temporal evolution of local crack opening and healing during multiple cracking and autonomous repair cycles at a temperature of 1500 K. For the first time, the rate and position dependence of crack repair in pristine Ti_2AlC material and in previously healed cracks has been quantified. Our results demonstrate that healed cracks can have sufficient mechanical integrity to make subsequent cracks form elsewhere upon reloading after healing.

4.1 Introduction

In recent years, new types of engineering materials have been developed that can repair internal crack and creep damage autonomously using healing mechanisms based on the physico-chemical nature of the material[1]. The application of these so called 'self-healing' materials has the potential to drastically increase the durability and reliability of structural components. For applications that require structural integrity at high temperatures, intrinsic (i.e. without the need to introduce discrete 'foreign' healing entities) self-healing ceramics would be ideally suited. Recently, a new class of ternary ceramics, known as MAX phase metallo-ceramics, was found to have the unique ability to fully, and sometimes even repeatedly, heal cracks in a completely autonomous manner when exposed for sufficiently long times to intended high use temperatures in an oxidative gaseous environment [2-6]. These ceramics are composed of layered compounds with a $M_{n+1}AX_n$ configuration [7] where M is an early transition metal, A is most commonly a group IIIA or IVA element (typically Al or Si) and X is either C or N. Due to its layered structure, a MAX phase material exhibits a unique combination of mechanical, thermal and electric properties [7-12]. The high thermal conductivity also makes these ceramics thermal shock resistant. Their static strength is maintained up to high temperatures, above which creep becomes the limiting factor [7, 11, 12]. Further, dislocations can multiply and glide on the basal planes of the hexagonal lattice [13], while plastic deformation of polycrystalline MAX phase material typically occurs by a combination of kink and shear band formation, together with the delamination of lamellar grains [7]. In contrast to many other ceramics, MAX phase materials are tough and therefore damage tolerant and also easily machinable [14].

In this work monolithic Ti_2AlC MAX phase material was studied. The crystalline unit cell of Ti_2AlC contains two sub units [11]. The octahedral Ti_2C layers are interrupted by layers of pure Al, which forms a Ti_2C-Al-Ti_2C-Al layered structure. The space group of Ti_2AlC is $P6_3/mmc$ with lattice parameters of a=3.04 Å and c=13.60 Å.

The self-healing behavior is due to oxidation reactions creating products that bond well to the crack faces and fill cracks with strong reaction product [5]. Cracks in Ti_2AlC can be fully repaired due to the formation of fine-grained Al_2O_3 and some TiO_2 within the crack gap upon high temperature oxidation [4, 15]. While Al and some Ti are consumed during oxidation, the resulting non-stoichiometric Ti_2AlC phase retains its hexagonal crystal

structure [16]. In the Ti_2AlC ceramic the outward diffusion of the weakly bonded Al atoms is much faster than that of the more covalently bonded Ti atoms in the Ti_2AlC structure [5, 7, 17-19]. This difference in kinetics leads to the formation of small α-Al_2O_3 grains at the ledges of the fractured lamellar Ti_2AlC grains as well as on the hexagonal basal surfaces ensuring a good adhesion with the parent matrix [17]. This good adhesion in combination with a minimal mismatch in thermal expansion coefficient and stiffness with the matrix is believed to be the cause of the complete restoration of the tensile strength provided the crack is adequately filled [4, 5, 17]. The stiffness of the healing product, mainly Al_2O_3 [20], is somewhat higher than that of Ti_2AlC [21], i.e. 400 versus 280 GPa. Hence, upon mechanical re-loading, a stress concentration would be expected to occur in the healed zone of these MAX phases and cracking would be expected to follow the path of previously healed cracks, unless the local healing is of a very high quality. The thermal expansion of α-Al_2O_3 ($7.5–9.6 \times 10^{-6}$ K^{-1}) [22], is about the same as that of Ti_2AlC (8.2×10^{-6} K^{-1}) [8]. This implies that little to no residual stress is generated in the oxide when the healed material is cooled down from the oxidation temperature.

In situ 4D (three spatial dimensions plus time) observation of crack formation and subsequent filling of the crack by a load bearing reaction product is crucial for understanding the self-healing behaviour. Furthermore, quantification of the spatial and temporal dependence is needed to validate and develop new micromechanical models for crack healing currently under development. While the challenge of in situ observation and (low level) quantification of closing and healing of cracks were already extremely demanding for (polymeric) materials that fail and heal at room temperature [23], the experimental challenges become orders of magnitude more complex for (ceramic) materials that operate and heal at high temperatures. Until now, it has not been possible to directly observe the crack filling in high temperature ceramics. Thus it has also not been possible to monitor the crack repair or to establish the integrity of the repair. This is true not only for cracks formed in the pristine material, but also for cracks passing through a previously healed region. 4D X-ray tomographic microscopy using the high flux and brilliance of synchrotron X-rays is now a powerful tool for imaging the spatial and temporal evolution of microstructures from macroscopic to submicroscopic scales within a variety of materials [24-31].

4.2 Methods

4.2.1 Material preparation

A Ti_2AlC disc was synthesized by hot pressing a dry mixture of Ti, Al and C powders (with a particle size of about 50 µm and purity better than 99 %) at 1625 K under 30 MPa of pressure for 4 hours in Ar. For the X-ray tomographic microscopy experiments, the samples were machined by electro discharge machining (EDM) to cylinders with a diameter of 2.6 mm and 7 mm length into which a chevron-notch geometry was cut; see Figure 4.1(b). The tip of the chevron has a thickness of 0.4 mm, a height of 3.65 mm, and a top angle of 39.2°; it is located 1.65 mm below the upper surface of the cylinder.

4.2.2 Mechanical testing rig and laser-based heating system

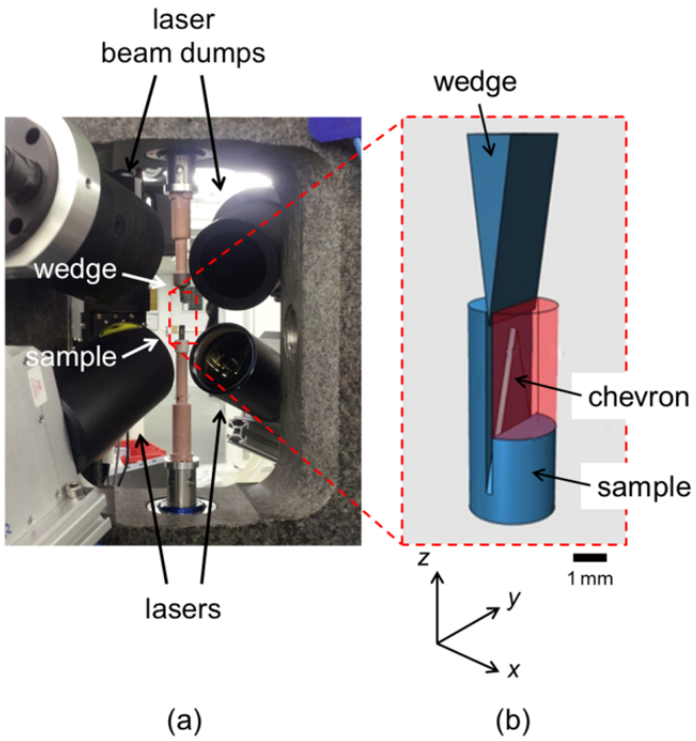

Figure 4.1 Thermomechanical testing rig for in situ 4D X-ray tomographic microscopy. (a) Image of the mechanical testing rig incorporating the laser-based heating system mounted at the TOMCAT beamline; the sample stage and wedge setup are also visible. (b) Sample and wedge configuration; the arrow indicates the chevron where the cracks are generated and healed.

Figure 4.1 shows the setup of the mechanical testing rig [32] with the laser-based heating system [33] incorporated into its frame. The sample sat on the lower platen inside an

alumina sleeve of internal diameter 3 mm and wall thickness of 1 mm. The outer surface of the alumina sleeve was covered with blackbody paint in order to more efficiently absorb the power of the lasers and subsequently transfer heat to the sample, thereby acting as a small furnace. It also served as a sample holder and air between the sleeve and the sample acted to dissipate the heat and provide the oxidizing environment. The temperature of the sample was controlled using a single-wavelength pyrometer (Optris GmbH, Germany), which measures the temperature of the material in its line-of-sight (i.e., the alumina sleeve covered with black paint). The temperature during the healing experiment was constant to within ± 10 K.

A crack was grown in the sample in a controlled manner by lowering a wedge, fixed to the upper platen, slowly into the notch with a displacement rate of 5 μm/min. The wedge tip had an angle of 10° and the wedge itself was machined from a Ni superalloy (CMSX-4) such that it could withstand the high working temperatures of the experiment. Once the wedge was in contact with the sides of the notch, observed by monitoring a small force reading (typically 2 N), the wedge was lowered continuously whilst monitoring both the force and a live preview of the X-ray projection of the sample; together, these tools provided the means to identify crack initiation. Crack growth was then performed at a temperature of 1000 K in order to avoid further crack opening during the initiation of heating, during which the wedge remained in the chevron notch. Once a crack had initiated, corresponding to a force of 60 N, the wedge was driven further into the sample until the crack grew to a length of around the height of the field-of-view of the detector (approximately 1.5 mm). With the wedge remaining in position, the laser power was increased to a corresponding temperature of 1500 K at a rate of 50 K/min. Radial temperature uniformity was achieved through continuous rotation during heating after the crack formation. The sample was then isothermally held at 1500 K for about 80 min whilst continuous tomography scans were recorded at user-defined intervals. Two further crack growth and healing cycles were subsequently performed.

4.2.3 X-ray tomographic microscopy

Measurements were performed at the TOMCAT beamline [32, 33] of the Swiss Light Source at the Paul Scherrer Institut (Villigen, Switzerland). Projection images were collected using a pco.EDGE sCMOS camera coupled to a long-working distance

microscope (Optique Peter, France) with 10x magnification. Using a 50 % power filter on the polychromatic x-rays, the exposure time for a single projection was 15 ms. A full three-dimensional dataset comprised of 1001 projections over 180° was acquired in 15 s followed by a user-defined 30 s interval, resulting in one scan every 45 s. The isotropic pixel size was 0.65 µm giving a field-of-view 1.7 mm wide by 1.4 mm high. The central region of the sample, centered on the chevron notch, was imaged. Tomographic reconstructions were achieved using a re-gridding Fourier transform-based reconstruction algorithm [34]. Image processing and visualisation were performed using Avizo (Visualisation Sciences Group).

In order to quantify the crack face gap (CFG) a median filter was applied to the original X-ray tomographic reconstructions to reduce the background noise. The cracked region in each tomographic slice was then segmented by thresholding. The gap across the faces (CFG) was measured as a function of position by counting the number of pixels occupied by the crack at each location perpendicular to the crack growth direction. In this way the current gap between the crack faces can be mapped for each crack at any stage in the repair process.

4.3 Results

4.3.1 4D X-ray tomographic microscopy and thermomechanical testing

The current study utilizes the non-destructive 3D imaging capability of tomography to obtain the first 4D observations of multiple cracking and self-healing cycles at high temperature. To observe the complex phenomena occurring both during crack growth and in subsequent crack healing both in situ and with time requires a means of applying mechanical load and high temperature simultaneously whilst rotating the sample and capturing 4D information with a spatial resolution high enough and a temporal resolution fast enough to resolve both the physical change in the microstructure and the dynamics of the processes. To accomplish the first part, an ultra-high precision mechanical testing rig [32] was combined with a laser-based heating system [33] as shown in Figure 4.1. Cylindrical Ti_2AlC samples having a diameter of 2.6 mm and 7 mm length were machined with chevron-notch geometry and the controlled displacement of a wedge was used to drive the crack (see Figure 4.1b). Given the geometry of the sample and the

wedged loading configuration the cracks are expected to form at either of the two intercepts between the triangular central section and the sides of the slot terminating the chevron.

4.3.2 Crack initiation and healing

Initial crack growth was performed at a temperature of 1000 K (see http://www.nature.com/articles/srep23040#supplementary-information, Video S1: A sequence of successive planar tomographic sections of the *initial crack* in the direction of the crack path starting at the crack tip). A crack approximately 4 mm long was introduced with a crack opening of around 10 µm near the mouth of the crack, falling more or less linearly to zero at the (sharp) crack-tip; see Figure 4.2 (a).

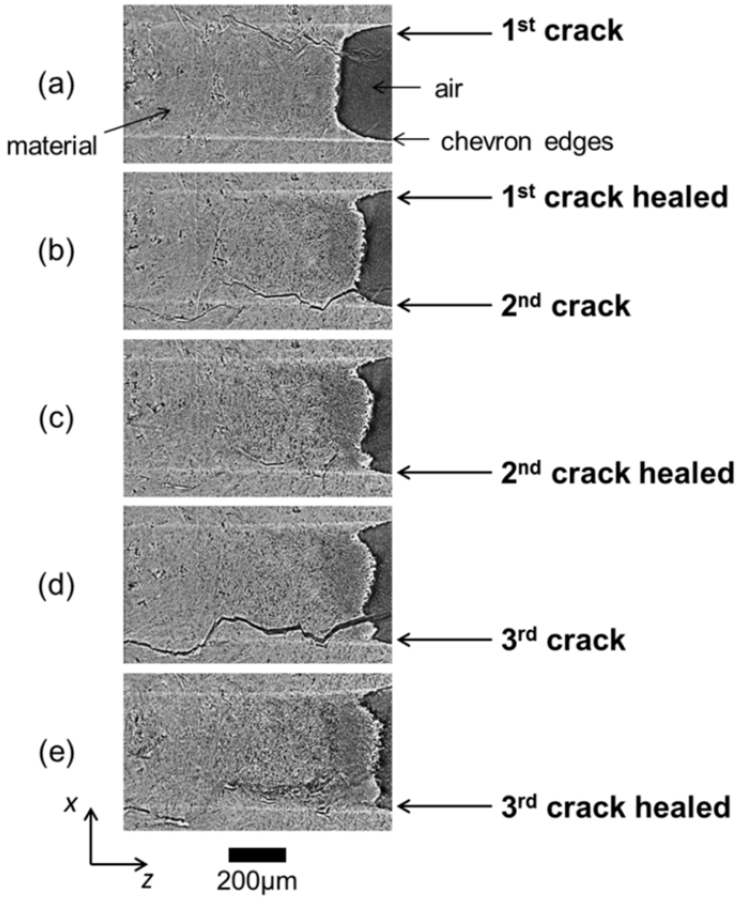

Figure 4.2 Virtual 2D sections through the tomographic datasets showing the sequence of crack growth and healing steps in Ti_2AlC at 1500 K in air. Mid-section of the sample: (a) first crack, (b) second crack and healed first crack, (c) healed second crack, (d) third crack and reopening of healed second crack, (e) healed third crack.

The crack follows the basal planes of the hexagonal Ti_2AlC randomly oriented lamellar grains resulting in a zigzag mode, leaving local smooth cleavage fracture surfaces. Crack deflection perpendicular to the basal planes results in a stair-type fracture surface [35]. Local crack branching and crack bridging as well as grain pull-out are known features of this material. The combination of several deformation and cracking mechanisms operating in parallel is held responsible for its high toughness. The local variation in crack opening reflects the effect of the variation in grain orientations along the crack path on the local deformation and failure processes. After the crack was formed, the sample was heated to a temperature of approximately 1500 K in air and repeated tomography scans were recorded over 66 minutes of isothermal exposure (see http://www.nature.com/articles/srep23040#supplementary-information, Video S2: A sequence of successive planar tomographic sections of the *healed crack* in the direction of the crack path starting at the crack tip).

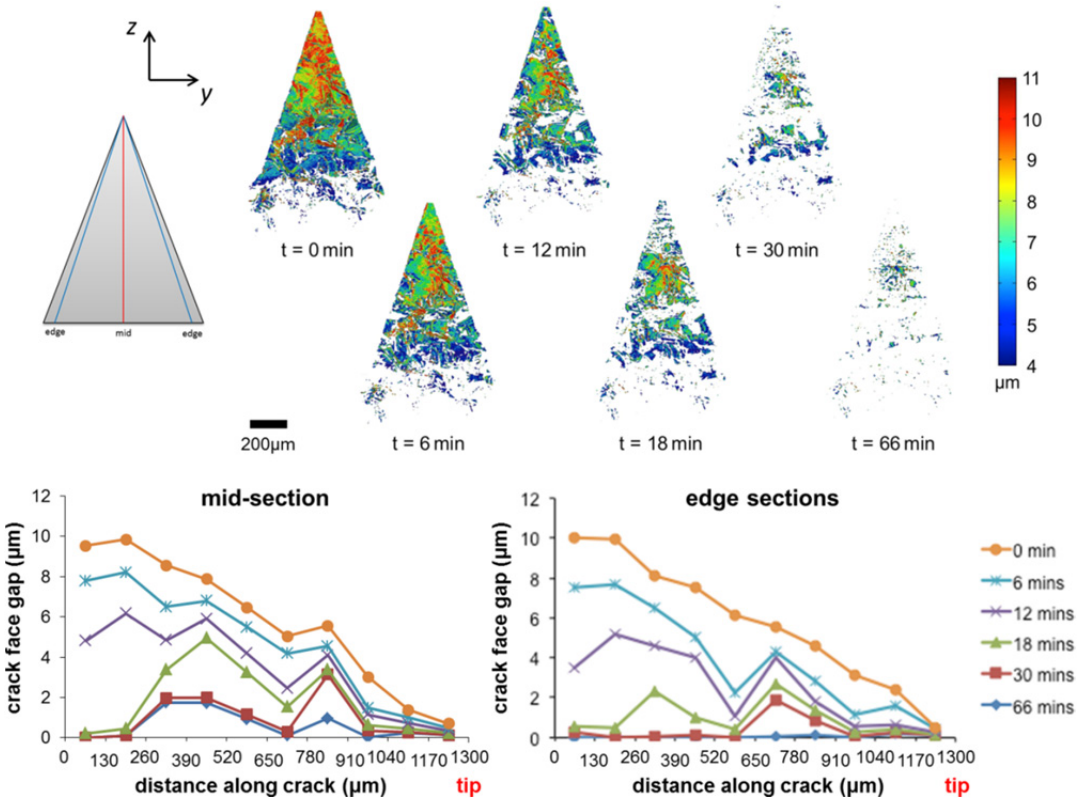

Figure 4.3 Planar views of the 3D datasets segmented to show the first crack in Ti_2AlC both initially and at different stages of healing at 1500 K in air. This first crack (cf. Figure 4.2) has a length of 1.2 mm. The superimposed colour map represents the crack face gap (CFG). The direction of crack growth is from top (mouth) to bottom (crack-tip) in the images. The graphs show the remaining opening of the crack having a length of 1.2 mm as a function of healing time for virtual sections in the middle and towards the edges of the crack (averaged over both edge trajectories).

Figure 4.3 shows graphs of the variation in crack face gap (CFG) across the crack faces in the initial state and after 6, 12, 18, 30 and 66 minutes, respectively. Here we use the term crack face gap to quantify the local distance between the crack faces. It is measured in the same way as crack opening displacement (COD) which is a term regularly used in fracture mechanics. Since the gap between the faces during repair is not simply related to the toughness of the material, we have used the term CFG to indicate a parameter varying locally along the length of the crack. When the crack face gap reaches a value of zero, the crack has been fully filled by a reaction product. By segmenting the crack in 3D for the duration of the healing time, a more complete analysis of the progression, and importantly the areal coverage, of crack filling can be conducted. Due to the high spatial resolution of the image acquisition and therefore of the CFG measurements, the local CFG can be extracted along a chosen trajectory from the mouth to the tip of the crack as a function of healing time. In Figure 4.3 the variation in CFG along the crack centreline and along lines near both edges are considered (averaging over 5 voxels laterally at each point along each line). The edge trajectories give information on crack filling behaviour where oxygen can easily access the crack. The central trajectory gives information on shielding effects due to early local crack filling. These two graphs in Figure 4.3 clearly show that the crack is significantly healed, not only near the crack edges where the oxygen enters the crack, but also along the centreline. Most importantly, a comparison of the two graphs shows that the gap between the crack faces closes more or less uniformly across its width, although the closing along the centreline was marginally slower leaving a small internal region of unhealed crack. After 30 minutes of healing a connected network of fully filled regions was found everywhere along the crack, and both crack mouth and crack tip regions were fully healed after a further 36 minutes of exposure. Small islands where the crack had not fully healed were found only in the centre of the crack. Clearly these were sealed off from the oxidizing environment during healing.

After this healing treatment, the sample was slowly cooled to 1000 K, reloaded and re-cracked. Remarkably, the second crack did not form at the location of the first healed crack but on the opposite site of the chevron; see Figure 4.2 b. This suggests that the adhesion between the oxides in the crack gap and the Ti_2AlC matrix is strong and that it is energetically more favourable to initiate a new crack in pristine material than it is to re-open the healed crack. The second crack had a crack length comparable to the first, but there was a larger initial crack opening near the mouth of the crack (viz. 17 versus 10 μm);

see Figure 4.4. The healing process of this second crack upon exposure to 1500 K proceeded in a similar manner to the first crack since both cracks were formed in pristine material; thus, there was a more or less uniform reduction of the crack face gap and early closing of regions where the gap was initially the smallest. After the second crack healed, the sample was cooled again and re-cracked at a temperature of 1000 K. Given the fact that the first crack effectively received a double healing treatment and that the mouth of the second crack had not been filled completely (Figure 4.4), it is not surprising that the third crack followed the path of the second; see Figure 4.2 (d).

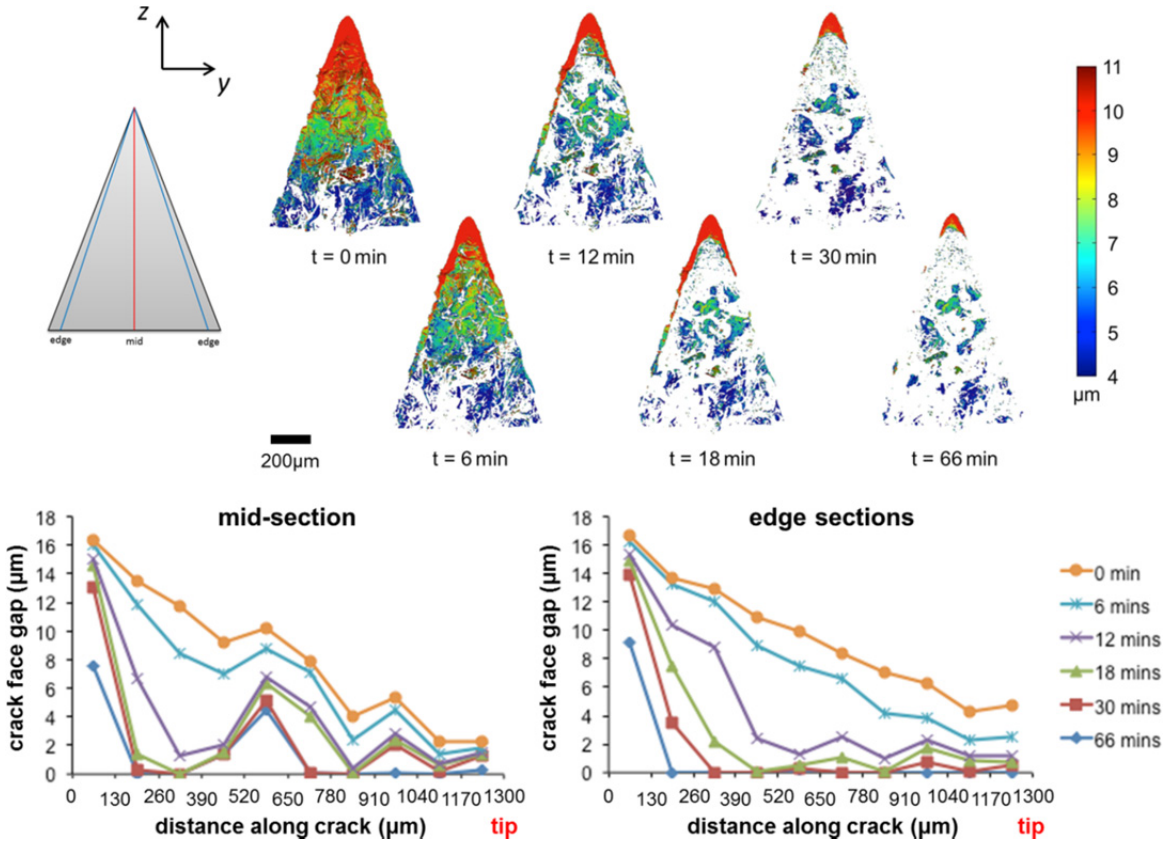

Figure 4.4 Planar views of the 3D datasets segmented to show the second crack in Ti_2AlC both initially and at different stages of healing at 1500 K in air. This second crack (cf. Figure 4.2) has a length of 1.3 mm. The superimposed colour map represents the crack face gap (CFG). The direction of crack growth is from top (mouth) to bottom (crack-tip) in the images. The graphs show the remaining opening of the crack having a length of 1.3 mm as a function of healing time for virtual sections in the middle and towards the edges of the crack (averaged over both edge trajectories).

The crack opening for the re-cracked (third) crack (Figure 4.5) is larger than for the original (second) crack (Figure 4.4) made in the pristine material (viz. 35 versus 17 µm).

It is interesting and very encouraging to note that upon re-cracking substantial further crack filling was observed upon re-exposure to 1500 K even leading to small regions with complete crack filling in the crack interior; see the time dependent sequences of Figure 4.5. In the supplementary information Videos are included that show the healing of these three cracks as time-lapse segmented 3D datasets; see Videos S3, S4 and S5 via http://www.nature.com/articles/srep23040#supplementary-information.

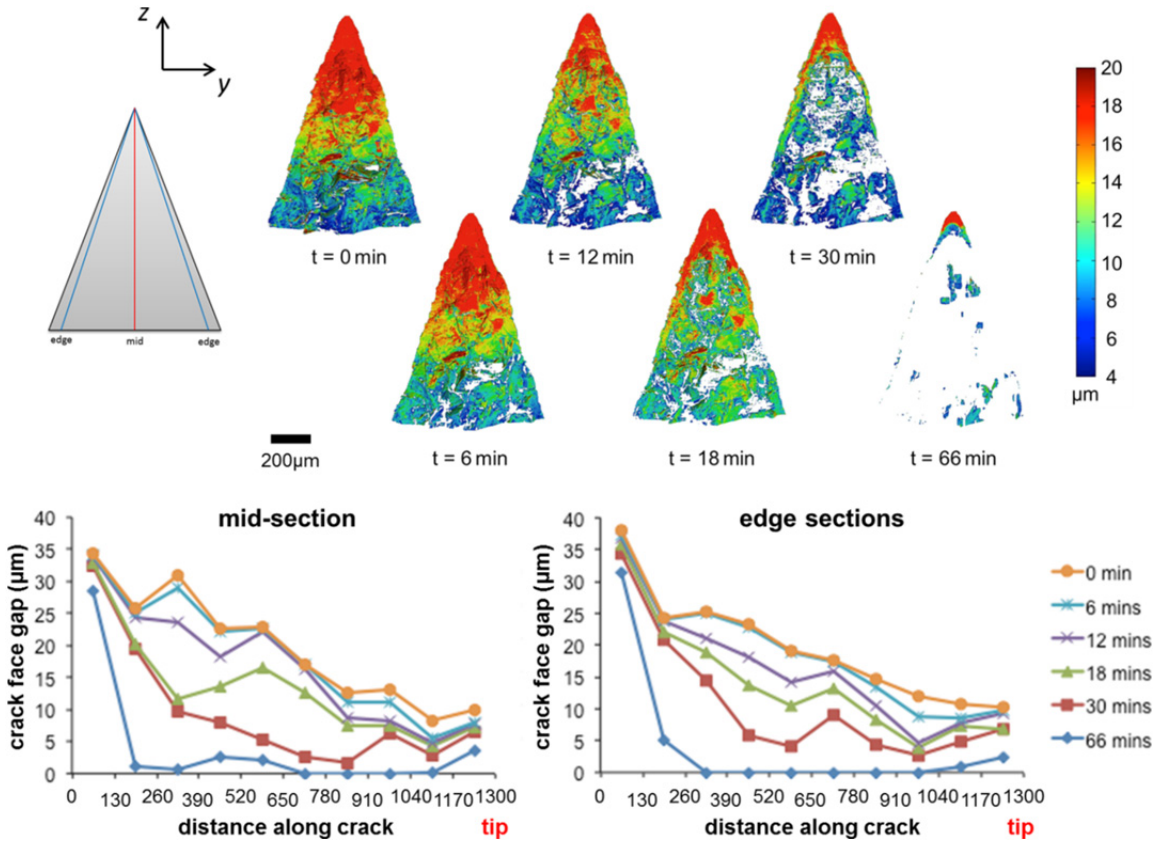

Figure 4.5 Planar views of the 3D datasets segmented to show the third, re-cracked healed second, crack in Ti_2AlC both initially and at different stages of healing at 1500 K in air. This third, re-cracked healed second crack (cf. Figure 4.2), has a length of 1.3 mm. The superimposed colour map represents the crack face gap (CFG). The direction of crack growth is from top (mouth) to bottom (crack-tip) in the images. The graphs show the remaining opening of the crack having a length of 1.3 mm as a function of healing time for virtual sections in the middle and towards the edges of the crack (averaged over both edge trajectories).

4.3.3 Crack healing kinetics

The local crack healing kinetics are determined from the measured evolution of the CFG, cf. Figure 4.3, Figure 4.4, Figure 4.5. At each location within the crack gap, the amount of healing can be expressed as:

$$h_{local} = \frac{\delta(t=0) - \delta(t)}{\delta(t=0)} \times 100\% \tag{4-1}$$

where $\delta(t)$ is the CFG at time t. The change in CFG follows from the oxidation kinetics, hence:

$$\delta(t) = \delta(t=0) - 2k(T) \times t^{1/n} \tag{4-2}$$

where $k(T)$ is the temperature T dependent rate constant and n is the rate exponent, respectively. For alumina forming MAX phases n equals about 3, because in general, the oxidation obeys a cubic growth rate law [36]. However, for the Ti_2AlC MAX phase studied here a value of about 4 was observed [15]. The growth of oxide in the gap of the crack proceeds as long as the oxide surface is accessible to the external environment. Thus, when the crack gap is sealed off, or when the oxide at either side closes the crack gap, the oxide growth ceases.

The global crack healing kinetics is determined from change in the volume $V(t)$ of the crack as it fills with oxide. This volume change is determined from the 3D datasets by counting the number of voxels that represent the crack gap at a given time, t, hence:

$$h_{global} = \frac{V(t=0) - V(t)}{V(t=0)} \times 100\% \tag{4-3}$$

Since the change of the volume $V(t)$ of the crack is related to the change of the CFG according to Eq. *(4-1)*, the global healing kinetics may show a similar trend to the oxidation kinetics. As shown in Figure 4.6, both cracks in the pristine material (i.e. the first and second cracks, cf. Figure 4.2) display essentially identical crack filling kinetics, showing the reproducibility of the experiment and data reconstructions. In agreement with the macro measurements on the oxidation kinetics of Ti_2AlC [15], the initial rate of oxide growth for crack gap filling is fast, forming a closed alumina layer on the fracture surfaces. The healing process is subsequently retarded by the presence of the oxide layer covering the fracture surfaces. This is most significant in the case of the third crack (at the location of the healed second crack, cf. Figure 4.2). The rate of local oxide growth is reduced because of the existing oxide formed from the first healing cycle. For the third crack the amount of crack filling after 1 hour at 1500 K was about 80 %, while the first and second cracks in the pristine material were filled to about 90 % at this stage.

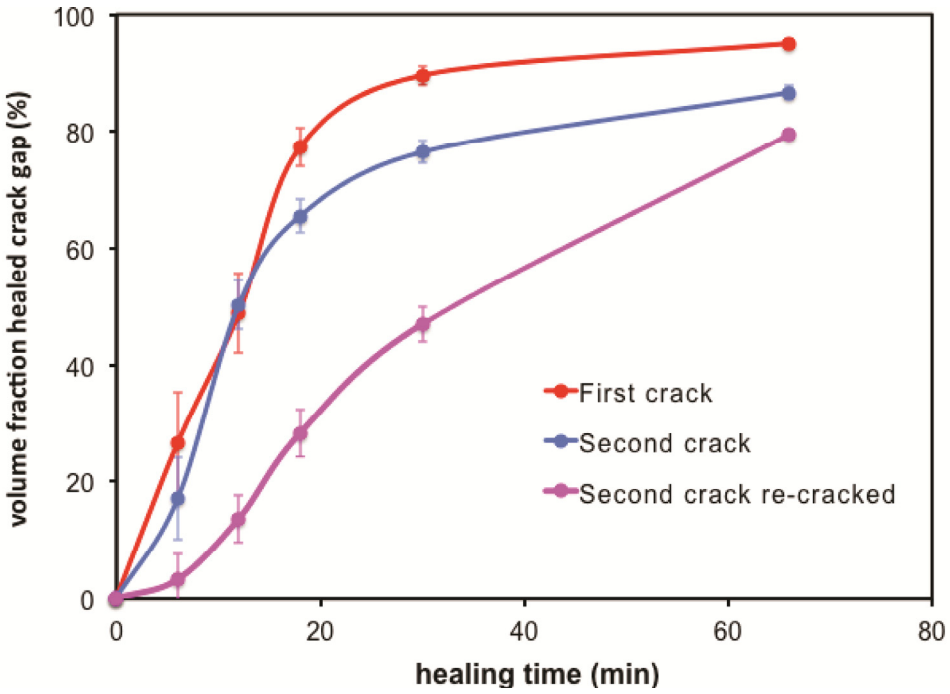

Figure 4.6 Crack healing kinetics in Ti_2AlC at 1500 K in air, presented in terms of volume fraction of the initial crack gap filled with oxide as a function of time. The first and second crack reflect healing in pristine material, while the third crack shows healing of the re-cracked and re-healed second crack (cf. Figure 4.2).

4.4 Discussion

The results presented here demonstrate the usefulness of in situ 4D (time-lapse) tomographic imaging when studying crack repair in a self-healing MAX phase materials. The change in crack face gap is observed with a high spatial resolution and has yielded the local, as well as the average, evolution of crack healing in pristine material and for the healing of a crack re-formed along a previously healed crack. For the first time we are able to resolve the spatial and temporal local crack filling kinetics.

Previous work on multiple crack healings show that the strength fully recovers when a crack damaged Ti_2AlC MAX phase material is exposed to air at high temperatures [4]. However, the toughness of the composite Ti_2AlC matrix with oxide filled healed cracks reduces upon subsequent healing cycles. As observed for the healing of a re-cracked healed crack (Figure 4.2), it becomes more difficult to heal a crack that is previously filled with oxide, and the 'scar' created becomes wider; see Figure 4.5. Although the Al of Ti_2AlC is consumed during crack healing, the diffusion of Al in Ti_2AlC is fast [15] and

deviation from its stoichiometric composition can be large (up to 50%) [16]. Hence in multiple healing events the base Ti_2AlC material effectively acts as an infinite reservoir of the Al healing agent. Finally, it should be mentioned that Ti_2AlC is stable up to 1650 K [37] and no grain growth or compositional changes occur upon healing at 1500 K. Post mortem analysis of the sample confirmed that besides surface oxidation in the crack nor the microstructure nor the composition was changed.

The information presented here is crucial for constructing models predicting local damage and healing under practical operating conditions and also in the interpretation of healing kinetics as a function of initial damage topology and material compositions. This study opens new avenues for development and design of self-healing high temperature ceramics, not only for MAX phase materials when optimizing their composition and microstructure for crack healing, but also for self-healing oxide ceramics with sacrificial particles where their composition, size and distribution are crucial [38].

References

1. Van der Zwaag, S., N.H.van. Dijk, H.M. Jonkers, S.D. Mookhoek, and W.G. Sloof, *Self-Healing Behaviour in Man-Made Engineering Materials: Bioinspired but Taking into Account Their Intrinsic Character.* Philosophical Transactions: Mathematical, Physical and Engineering Sciences, 2009. **367**(1894): p. 1689-1704.
2. Song, G.M., Y.T. Pei, W.G. Sloof, S.B. Li, J.T.M. De Hosson, and S. van der Zwaag, *Oxidation-induced crack healing in Ti_3AlC_2 ceramics.* Scripta Materialia, 2008. **58**(1): p. 13-16.
3. Song, G.M., Y.T. Pei, W.G. Sloof, S.B. Li, J.T.M. De Hosson, and S. van der Zwaag, *Early stages of oxidation of Ti_3AlC_2 ceramics.* Materials Chemistry and Physics, 2008. **112**(3): p. 762-768.
4. Li, S., G. Song, K. Kwakernaak, S. van der Zwaag, and W.G. Sloof, *Multiple crack healing of a Ti_2AlC ceramic.* Journal of the European Ceramic Society, 2012. **32**(8): p. 1813-1820.
5. Farle, A.-S., C. Kwakernaak, S. van der Zwaag, and W.G. Sloof, *A conceptual study into the potential of $M_{n+1}AX_n$-phase ceramics for self-healing of crack damage.* Journal of the European Ceramic Society, 2015. **35**(1): p. 37-45.
6. Yang, H.J., Y.T. Pei, G.M. Song, and J.T.M. De Hosson, *Healing performance of Ti_2AlC ceramic studied with in situ microcantilever bending.* Journal of the European Ceramic Society, 2013. **33**(2): p. 383-391.
7. Barsoum, M.W. and M. Radovic, *Elastic and Mechanical Properties of the MAX Phases.* Annual Review of Materials Research, Vol 41, 2011. **41**: p. 195-227.
8. Barsoum, M., T. El-Raghy, and M. Ali, *Processing and characterization of Ti_2AlC, Ti_2AlN, and $Ti_2AlC_{0.5}N_{0.5}$.* Metallurgical and Materials Transactions A, 2000. **31**(7): p. 1857-1865.

9. Barsoum, M.W., I. Salama, T. El-Raghy, J. Golczewski, W.D. Porter, H. Wang, H.J. Seifert, and F. Aldinger, *Thermal and electrical properties of Nb_2AlC, (Ti, Nb)$_{(2)}$AlC and Ti_2AlC.* Metallurgical and Materials Transactions A-Physical Metallurgy and Materials Science, 2002. **33**(9): p. 2775-2779.
10. Barsoum, M.W., *Physical properties of the MAX phases*; in Encyclopedia of Materials Science and Technology. Edited by K.H.J. Buschow, R.W. Cahn, M.C. Flemings, E.J. Kramer, S. Mahajan, and P. Veyssiere. Elsevier, Amsterdam, 2006.
11. Barsoum, M.W., *The $M_{(N+1)}AX_{(N)}$ phases: A new class of solids; Thermodynamically stable nanolaminates.* Progress in Solid State Chemistry, 2000. **28**(1-4): p. 201-281.
12. El-Raghy, T., M.W. Barsoum, A. Zavaliangos, and S.R. Kalidindi, *Processing and Mechanical Properties of Ti_3SiC_2: II, Effect of Grain Size and Deformation Temperature.* Journal of the American Ceramic Society, 2004. **82**(10): p. 2855-2860.
13. Barsoum, M.W., T. Zhen, S.R. Kalidindi, M. Radovic, and A. Murugaiah, *Fully reversible, dislocation-based compressive deformation of Ti_3SiC_2 to 1 GPa.* Nat Mater, 2003. **2**(2): p. 107-111.
14. Barsoum, M. and T. El-Raghy, *The MAX Phases: Unique New Carbide and Nitride Materials.* American Scientist, 2001. **89**(4): p. 334-343.
15. Song, G.M., V. Schnabel, C. Kwakernaak, S. van der Zwaag, J.M. Schneider, and W.G. Sloof, *High temperature oxidation behaviour of Ti_2AlC ceramic at 1200°C.* Materials at High Temperatures, 2012. **29**(3): p. 205-209.
16. Wang, J., Y. Zhou, T. Liao, J. Zhang, and Z. Lin, *A first-principles investigation of the phase stability of Ti_2AlC with Al vacancies.* Scripta Materialia, 2008. **58**(3): p. 227-230.
17. Yang, H.J., Y.T. Pei, J.C. Rao, and J.T.M. De Hosson, *Self-healing performance of Ti_2AlC ceramic.* Journal of Materials Chemistry, 2012. **22**(17): p. 8304-8313.
18. Liao, T., J. Wang, and Y. Zhou, *Chemical bonding and mechanical properties of M_2AC (M = Ti, V, Cr, A = Al, Si, P, S) ceramics from first-principles investigations.* Journal of Materials Research, 2009. **24**(2): p. 556-564.
19. Ganguly, A., M.W. Barsoum, and R.D. Doherty, *Interdiffusion between Ti_3SiC_2-Ti_3GeC_2 and Ti_2AlC-Nb_2AlC diffusion couples.* Journal of the American Ceramic Society, 2007. **90**(7): p. 2200-2204.
20. Soga, N., Schreibe.E, and O.L. Anderson, *Estimation of Bulk Modulus and Sound Velocities of Oxides at Very High Temperatures.* Journal of Geophysical Research, 1966. **71**(22): p. 5315-5320.
21. Hettinger, J.D., S.E. Lofland, P. Finkel, T. Meehan, J. Palma, K. Harrell, S. Gupta, A. Ganguly, T. El-Raghy, and M.W. Barsoum, *Electrical transport, thermal transport, and elastic properties ofM_2AlC(M=Ti, Cr, Nb, and V).* Physical Review B, 2005. **72**(11): 115120.
22. Touloukian, Y.S.K., R.K.; Taylor, R.E.; Lee, T.Y.R., *Thermal Expansion*. Thermophysical Properties of Matter. 10.1007/978-1-4757-1631-31977: Springer Science+Business Media New York.
23. Mookhoek, S.D., S.C. Mayo, A.E. Hughes, S.A. Furman, H.R. Fischer, and S. van der Zwaag, *Applying SEM-Based X-ray Microtomography to Observe Self-Healing in Solvent Encapsulated Thermoplastic Materials.* Advanced Engineering Materials, 2010. **12**(3): p. 228-234.
24. Bale, H.A., A. Haboub, A.A. MacDowell, J.R. Nasiatka, D.Y. Parkinson, B.N. Cox, D.B. Marshall, and R.O. Ritchie, *Real-time quantitative imaging of failure*

events in materials under load at temperatures above 1,600 degrees C. Nat Mater, 2013. **12**(1): p. 40-46.
25. Baker, D.R., F. Brun, C. O'Shaughnessy, L. Mancini, J.L. Fife, and M. Rivers, *A four-dimensional X-ray tomographic microscopy study of bubble growth in basaltic foam.* Nat Commun, 2012. **3**: 1135.
26. Lhuissier, P., M. Scheel, L. Salvo, E. Boller, M. Di Michiel, and J.J. Blandin, *4D Damage Characterization during Superplastic Deformation of Magnesium Alloys.* Materials Science Forum, 2012. **735**: p. 61-66.
27. Walker, S.M., D.A. Schwyn, R. Mokso, M. Wicklein, T. Muller, M. Doube, M. Stampanoni, H.G. Krapp, and G.K. Taylor, *In vivo time-resolved microtomography reveals the mechanics of the blowfly flight motor.* PLoS Biol, 2014. **12**(3): e1001823.
28. Singh, S.S., J.J. Williams, P. Hruby, X. Xiao, F. De Carlo, and N. Chawla, *In situ experimental techniques to study the mechanical behavior of materials using X-ray synchrotron tomography.* Integrating Materials and Manufacturing Innovation, 2014. **3**(1): 1.
29. Maire, E. and P.J. Withers, *Quantitative X-ray tomography.* International Materials Reviews, 2014. **59**(1): p. 1-43.
30. Fife, J.L., J.W. Gibbs, E.B. Gulsoy, C.L. Park, K. Thornton, and P.W. Voorhees, *The dynamics of interfaces during coarsening in solid–liquid systems.* Acta Materialia, 2014. **70**: p. 66-78.
31. Kareh, K.M., P.D. Lee, R.C. Atwood, T. Connolley, and C.M. Gourlay, *Revealing the micromechanisms behind semi-solid metal deformation with time-resolved X-ray tomography.* Nat Commun, 2014. **5**: 4464.
32. Puncreobutr, C., P.D. Lee, R.W. Hamilton, and A.B. Phillion, *Quantitative 3D Characterization of Solidification Structure and Defect Evolution in Al Alloys.* Jom, 2012. **64**(1): p. 89-95.
33. Fife, J.L., M. Rappaz, M. Pistone, T. Celcer, G. Mikuljan, and M. Stampanoni, *Development of a laser-based heating system for in situ synchrotron-based X-ray tomographic microscopy.* J Synchrotron Radiat, 2012. **19**(Pt 3): p. 352-358.
34. Marone, F. and M. Stampanoni, *Regridding reconstruction algorithm for real-time tomographic imaging.* J Synchrotron Radiat, 2012. **19**(Pt 6): p. 1029-1037.
35. Yu, W.B., S.B. Li, and W.G. Sloof, *Microstructure and mechanical properties of a $Cr_2Al(Si)C$ solid solution.* Materials Science and Engineering a-Structural Materials Properties Microstructure and Processing, 2010. **527**(21-22): p. 5997-6001.
36. Smialek, J.L., *Oxygen diffusivity in alumina scales grown on Al-MAX phases.* Corrosion Science, 2015. **91**: p. 281-286.
37. Pang, W.K., Low, I.M., *Diffraction Study of Thermal Dissociation in the Ternary Ti-Al-C System.* Journal of the Australian Ceramic Society, 2009. **45**(2): p. 30-33.
38. Nakao, W. and S. Abe, *Enhancement of the self-healing ability in oxidation induced self-healing ceramic by modifying the healing agent.* Smart Materials and Structures, 2012. **21**(2): 025002.

5 Crack healing behaviour of Cr_2AlC MAX phase studied by X-ray tomography

The autonomous crack-healing capability of Cr_2AlC MAX phase ceramic by surface oxidation at elevated temperatures has a huge potential for high temperature structural and protective coating applications. In this work we use time-lapse X-ray computed tomography (CT) to track the fine details of local crack filling phenomena in 3 dimensions (3D) with time. The maximum crack width that could be fully healed upon exposure to 1200 °C in air is 4.8 µm in 4 hours and 10 µm after 12 hours. Furthermore, during healing Cr_7C_3 phase is observed beneath the dense Al_2O_3 layer (average thickness of 1 µm on each crack surface) when the crack width exceeds 2 µm. The 3D image sequence indicates that the rate of healing is essentially independent of position along, or across, the crack faces. The crack healing kinetics of Cr_2AlC at 1200 °C broadly follows a parabolic rate law with a rate constant of 4.6 $\times 10^{-4}$ $\mu m^2 \cdot s^{-1}$. The microstructure, composition and thickness of the oxide scale in the healed crack area are characterized via post mortem SEM-EDS measurements and confirms the formation of an initial dense alumina layer on top of which a more porous layer forms. Impurity Cr particles appear to accelerate the oxidation process locally and correlative SEM imaging of the same region suggests this is by providing Cr_2O_3 nucleation sites.

5.1 Introduction

Recently, layered ternary ceramic compounds having the composition $M_{n+1}AX_n$ (n=1, 2 or 3) where M is an early transition metal, A is an element in either the IIIA or IVA group and X is C or N (known collectively as MAX phase ceramics) have attracted a lot of attention [1, 2]. These materials exhibit an unusual combination of properties, such as high strength and modulus, excellent oxidation resistance, low density, thermal shock resistance, damage tolerance as well as good machinability [3-8]. Therefore, they are good candidates for high temperature applications, such as gas turbine components, heat exchangers, oxidation resistant coatings, etc. However, being a ceramic, they still bear the common drawbacks of low toughness and sensitivity to surface defects and cracks, which may reduce their reliability.

Recent research showed that these materials exhibit self-healing capability when they are exposed to an oxidizing environment at high temperatures [9-12]. Given their potential applications as high temperature structural materials, such autonomous healing capability would greatly improve their reliability and potentially reduce maintenance costs. Extensive studies have been done on the Ti-Al-C ternary system. Song and co-workers reported that in Ti_3AlC_2 ceramic a crack with average width of 5 μm was healed by a heat treatment at 1100 °C for 2 hours in air [13]. Yang and co-workers reported that notches cut by focused ion beam (FIB) of 2 μm width in Ti_2AlC ceramic were healed by a heat treatment at 1200 °C for 1 hour in air [9]. The self-healing of Ti-Al-C MAX phase ceramic proceeds by oxidation, whereby cracks, gaps or notches are filled by α-Al_2O_3 and rutile-TiO_2 through oxidation induced volume expansion [14]. Our recent work utilized the synchrotron X-ray tomography to monitor the cracking and healing of Ti_2AlC MAX phase ceramics, showing a decreased mechanical strength recovery in the second healing cycle, due to the formation of a weak and porous TiO_2 phase [15]. Consequently, it would be desirable if the crack gap was filled solely by the strong Al_2O_3 phase providing optimal strength recovery after healing.

Previous research on Cr_2AlC showed that the oxidation product at high temperatures is primarily Al_2O_3 [16-19], potentially offering better recovery of strength after healing than Ti-Al-C MAX phase ceramics. Li studied the strength recovery of Cr_2AlC after healing at 1100 °C in air for 4-100 hours and reported that the strength recovery of Cr_2AlC has a strong dependence on healing time, with better strength recovery after increasing healing

time [20]. Therefore, understanding the kinetics of healing is critical for predicting the healing strength recovery. Until now, crack healing kinetic studies of Cr_2AlC have relied on thermogravimetric analysis (TGA) experiments performed on planar surfaces and there are still some arguments on its isothermal oxidation behaviour [16, 18]. The isothermal oxidation kinetics of Cr_2AlC was first reported by Lin to obey a parabolic law at 1200 °C in air [21]. Tian studied the isothermal behaviour of Cr_2AlC at 1100 and 1250 °C in air for 20 hours and confirmed the parabolic relation [16]. While Lee reported that the oxidation curve deviated negatively from a parabolic rate law at temperature above 1100 °C [18]. Recently, Li studied the isothermal oxidation of Cr_2AlC at 1100 and 1200 °C in air for 100 hours and reported that the oxidation kinetics of Cr_2AlC followed a cubic law rather than a parabolic one [20].

Besides these inconsistencies, the oxidation kinetics of Cr_2AlC measured by TGA on a polished planar surface could be inaccurate or even misleading when considering the healing of real cracks. The crack healing is an inherently three dimensional process. Factors such as crack shielding and oxygen transport within the crack should be considered when building a realistic crack healing model. However, these factors cannot be taken into account from 2D measurements. Therefore, it would be beneficial if the crack healing behaviour of real cracks could be directly followed over time not only in two dimensions 2D but also in three dimensions 3D. Recently high resolution X-ray CT has been exploited to image and quantify the repair and re-cracking of Ti_2AlC MAX phase ceramic *in situ* and in 3D over time for the first time using large scale synchrotron X-ray computed tomography (CT) [15]. Here, we use high resolution laboratory X-ray microtomography to study high temperature self-healing of Cr_2AlC to obtain quantitative information on crack healing kinetics and healing uniformity along and across the crack.

5.2 Experiment

Bulk Cr_2AlC ceramic was prepared using a mixture of high purity Cr (> 99.2 %, average particle size of 100 μm), Al (> 99.8 % average particle size of 45 μm) and graphite (> 99.5 %, average particle size of 6 μm) powders with a molar ratio of Cr:Al:C = 2:1.15:1. A slight excess of Al was added to compensate for its loss during sintering, cf. [22]. These powders were mixed for 3 hours in a tumble mixer using zirconia balls and then cold pressed with a pressure of 300 MPa into tablets with a diameter of 25 mm and a

thickness of about 5 mm with a Carver press. Next, the tablets were put into a graphite boat and pressure-less sintered (PLS) in a tube furnace (Lenton Furnaces, PTF 16/75/610) under an argon flow (> 5N) at 1400 °C for 1 hour. Subsequently, the PLS sintered samples were pulverized and sintered in a spark plasma sintering furnace (HP D 25, FCT Systeme) at 1250 °C for 1 hour in flowing argon under a pressure of 50 MPa, yielding an almost fully dense material (relative density > 99.4%).

The Cr_2AlC specimen for the X-ray microtomography investigation was machined to a 7.5 mm long cylinder of 2.5 mm diameter. A 2.5 mm wide chevron notch of 40° was introduced into the sample by wire electrical discharge machining (EDM) to help to initiate a stable crack. Crack initiation and growth was performed using a mechanical tester (MTS Alliance RT/100) with a 15º wedge made of a Ni-based super alloy and applying a displacement rate of 0.001 mm/min. A tomography scan was taken once the initial crack was clearly visible in the X-ray projections but the sample was still mechanically intact. Subsequently the cracked Cr_2AlC specimen was healed at 1200 °C in a box furnace (Carbolite BWF) over a period of 12 hours intermittently, while removing it every 4 hours to record an X-ray microtomography scan.

The high resolution X-ray tomography experiment was performed at the Henry Moseley X-ray Imaging Facility, University of Manchester, using a Zeiss Xradia Versa 500. The set-up of the X-ray tomography experiment is shown in Figure 5.1.

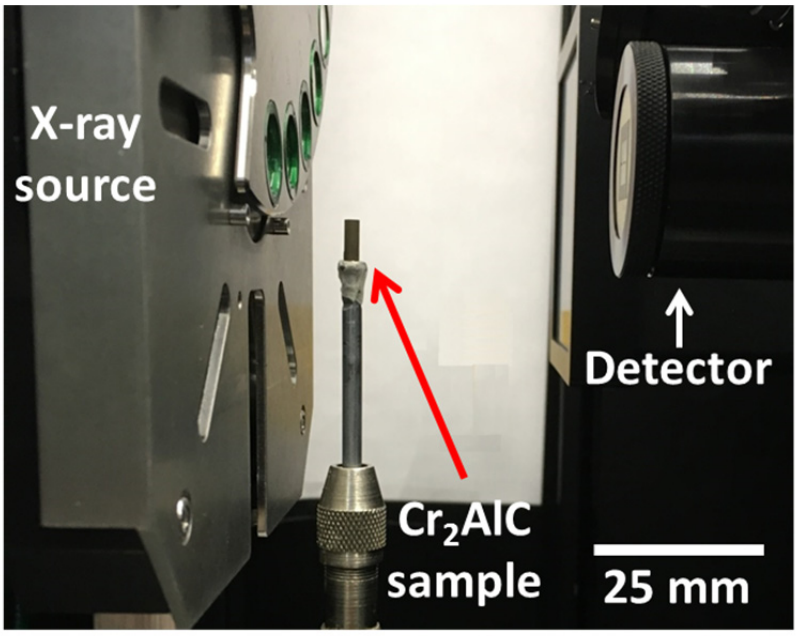

Figure 5.1 Photograph showing the set-up of the X-ray tomography experiment.

The Cr_2AlC sample was mounted on a rotation stage, between the X-ray source and detector. The X-ray source-sample and the sample-detector distances were 12 mm and 48 mm respectively. The CT data was collected using a detector system consisting of objective lens having 4x optical magnification and a 16-bit 2000 × 2000 pixellated detector, giving a field of view of 1.346 × 1.374 mm and an effective voxel size in the reconstructed data of 0.68 × 0.68 × 0.68 μm^3. The accelerating voltage was set to 90 kV to maximize the contrast between Al_2O_3 and the Cr_2AlC matrix. For each scan, a total of 1441 equally spaced projections were collected over 360° with each projection acquired in 45 seconds. The X-ray tomography reconstructions were computed using a Feldkamp-Davis-Kress (FDK) algorithm. Image processing and analysis was performed using FEI Avizo 8.0 software.

To study the microstructure characteristic of the healing oxide, a second Cr_2AlC sample containing a 1000 μm long, < 13 μm wide crack was exposed at 1200 °C in air for 4 hours. The sample after heat treatment was ground with SiC paper and finished with colloidal silica. The cross section of the healed area was characterized by Philips XL30 ESEM-FEG and FEI Quanta 650 scanning electron microscopes equipped with X-ray microanalysis (XMA) systems using energy-dispersive spectrometry (EDS).

5.3 Results

5.3.1 2D X-ray tomographic cross sections of crack at different healing stages

Virtual slices through the X-ray tomographs perpendicular to the crack growth (x) direction are shown in Figure 5.2. The light particles having diameters from 10 μm to 30 μm were identified by EDS to be Cr particles and probably were the result of a locally incomplete reaction during the sintering process. As shown in Figure 5.2 (a) the initial crack width (opening) before heat treatment is around 10 μm. It is evident that the gap between the crack faces decreases progressively with thermal exposure time (from Figure 5.2 a-d). After 12 hours heat treatment at 1200 °C in air, some parts of the crack are partially healed as shown in Figure 5.2 d. Given that previously a crack of similar width in Ti_2AlC was observed to heal at the same temperature in less than one hour [14], it is clear that the healing rate of Cr_2AlC is significantly slower. The contrast within the

cracked area is seen to lighten somewhat in certain regions, indicating that parts of the crack have been filled by oxide having an X-ray absorption coefficient higher than air but lower than the Cr_2AlC matrix. The oxide was later confirmed by scanning electron microscopy and EDS to primarily comprise Al_2O_3.

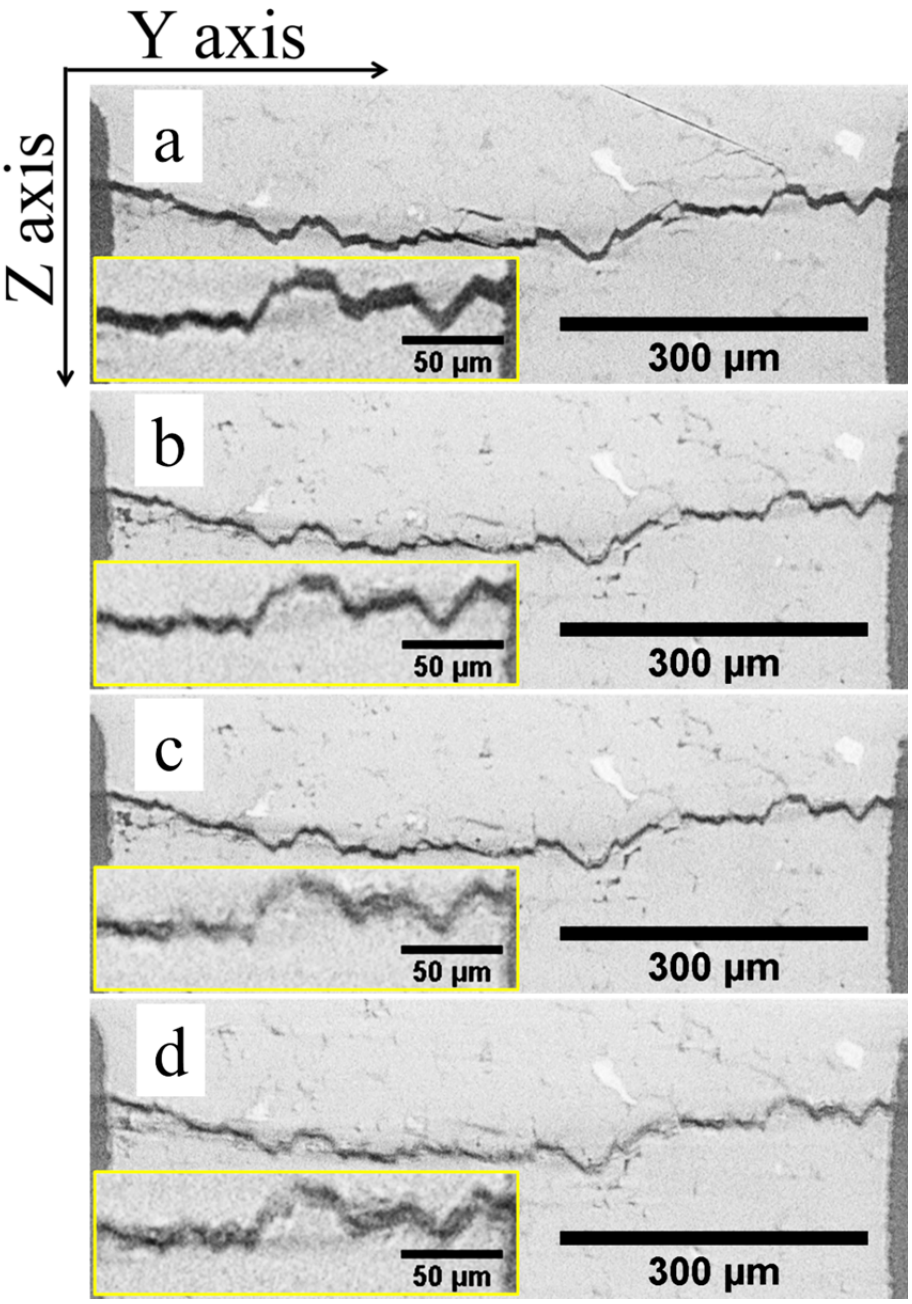

Figure 5.2 2D X-ray tomographic virtual cross-sections through the crack, grown in the X-direction at different stages of healing: (a) as-cracked; (b) after 4 hours; (c) after 8 hours; and (d) after 12 hours exposure to 1200 °C in air. Magnified regions of the crack are shown inset

Another interesting phenomenon is that the presence of Cr particles close to the crack surface appears to significantly increase the local healing kinetics, as shown in Figure 5.3.

It is clear that an oxide layer with a thickness of around 7 µm was formed after 4 hours healing on the crack surface adjacent to Cr particles, while the thickness of the oxide layer formed in the remaining areas of the crack surface was around 2 µm. During the healing process, the surface breaking Cr particles that were directly exposed to air have reacted with the environment forming secondary phases as well as some "micro voids" near the original interface with the matrix, as indicated by the red arrow in Figure 5.3 (b). Upon reaction the contrast of the particles darkens, becoming slightly darker than the matrix which suggests a much lower local Cr content. However, the non-surface breaking Cr particle remains unchanged during the healing process as indicated by yellow arrows in Figure 2 and 3. This result indicates that the Cr particle are stable upon exposed to heat treatment at 1200 °C. The difference during the healing process of these two types of Cr particles should be attributed to the direct exposure to air.

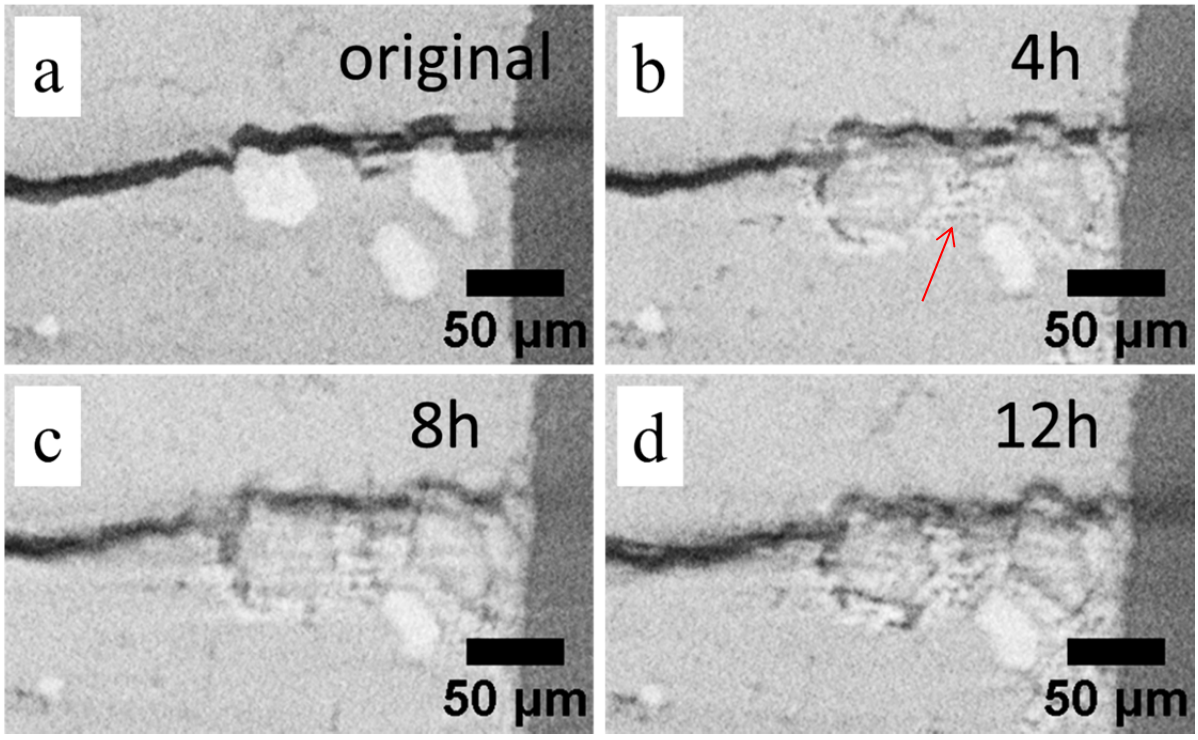

Figure 5.3 2D X-ray tomographic cross sections with surface breaking Cr particles at different healing stages: (a) original; (b) after 4 hours healing at 1200 °C in air; (c) after 8 hours healing at 1200 °C in air; (d) after 12 hours healing at 1200 °C in air.

5.3.2 3D crack face gap maps at different stages of healing

The 3D crack face gap (CFG) has been mapped, and the result is shown in Figure 5.4. The 3D crack volume was segmented using greyscale thresholding in FEI Avizo software

from which the crack face gap was calculated from the segmented 3D crack volume using Matlab [23]. The 3D CFG map was then generated by covering the 3D crack surface with a colour map representing the extent of crack face gap. The trapezoid shape of the 3D CFG map is due to the chevron-notch geometry of the sample. Considering the fact that the change in crack face gap between 8 hours and 12 hours is small, the present work focuses on a detailed description of the CFG map obtained after 12 hours.

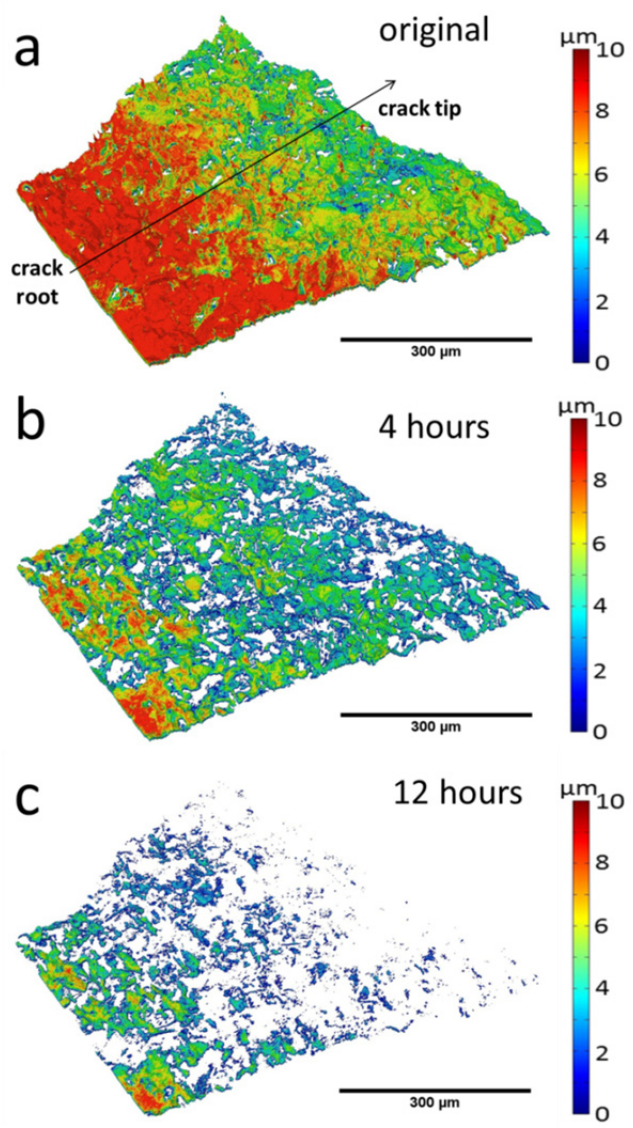

Figure 5.4 3D crack face gap maps (measured in microns) calculated for increasing exposure times: (a) as-cracked; (b) after 4 hours and (c) after 12 hours' healing at 1200 °C in air.

By comparing the 3D CFG map for the sample in the as-cracked state (Figure 5.4 (a)) with that after 4 hours thermal treatment (Figure 5.4 (b)), it can be seen that the crack width decreases more or less uniformly over the whole crack area during healing. After

12 hours of heat treatment, the crack tip area was almost fully healed, as shown in Figure 5.4 (c). It is worth noting that as the exposure time increased, some crack areas became isolated from the environment due to uneven local healing leading to a local slowing of the crack-healing. This could mean that some internal islands remain unhealed even after prolonged exposure. However, in general the region nearest crack tip healed first and the healed zone developed in the opposite direction to that of crack growth as what remained of the crack retreated towards the root.

5.3.3 Microstructure of healed area

To study the microstructure of the healed area, a second cracked Cr_2AlC sample was healed at 1200 °C in air for 4 hours and then sectioned along the crack growth direction. The sectioned surfaces were analysed by SEM and elemental EDS. A typical secondary electron cross-sectional SEM image and the corresponding elemental maps of the healed area are shown in Figure 5.5 (a).

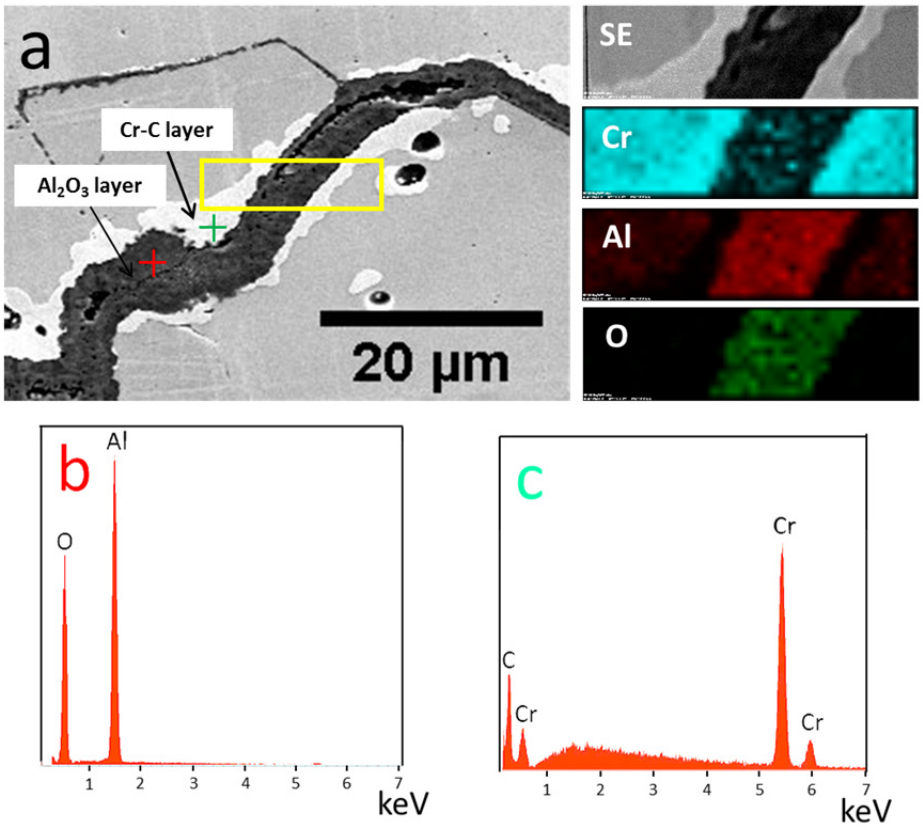

Figure 5.5 (a) Secondary electron cross-sectional SEM image and corresponding elemental maps of crack area after healing at 1200 °C in air for 4h. (b-c) X-ray spectra acquired at the locations indicated by red and green crosses in Figure 5(a) respectively.

The healed area comprises three layers: a central dark layer and two brighter layers on either side. By EDS mapping the dark contrast layer was confirmed to be primarily Al_2O_3, while the two bright layers were confirmed to be Cr_7C_3; see Figure 5.5 (b) and Figure 5.5 (c). Unlike Ti_2AlC, where TiO_2 phase is usually found in healed regions [11], no Cr_2O_3 layer was found in the healed area of Cr_2AlC. The microstructures of the healed area in four different positions b1, b2, b3 and b4 (indicated by the yellow rectangles) from crack root to crack tip are shown in Figure 5.6. It can be seen in Figure 5.6 (b1 and b2) that after 4 hours annealing at 1200 °C in air, the crack was not fully healed near the crack root.

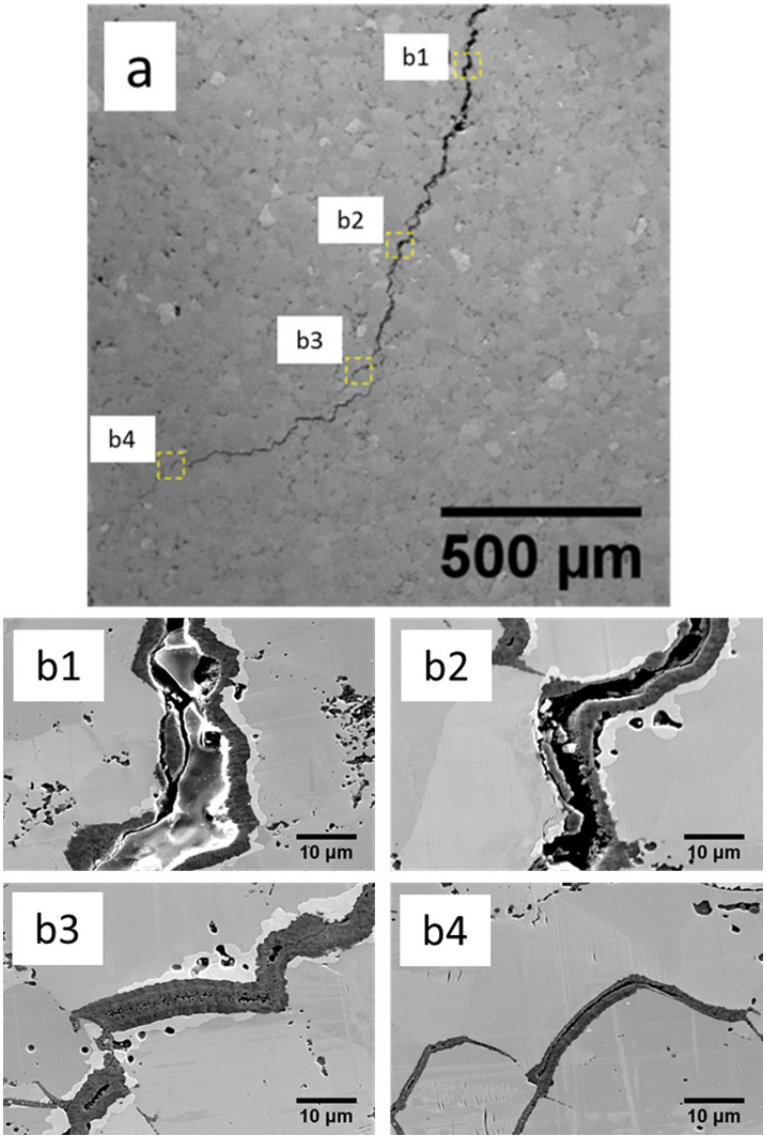

Figure 5.6 Cross sectional secondary electron SEM images of a crack after healing at 1200 °C for 4 hours in air: (a) a cross section image parallel to the crack growth direction of the healed crack at low magnification; (b) higher magnification images for the areas of "b1", "b2","b3","b4" in Figure 5.6 (a).

However, the crack was almost fully healed at b3 and b4. The average thickness of Al_2O_3 on a single crack surface is comparable in positions b1, b2 and b3, indicating a similar healing rate all along the crack, as quantified in Table 5-1. Given that the Al_2O_3 formed on both crack surfaces, the maximum crack width that could be healed by Al_2O_3 formation at 1200 °C in 4 hours is estimated to be around 4.8 μm. It is worth noting that the crack in position b4 was healed purely by Al_2O_3 and no Cr_7C_3 was observed. The absence of Cr_7C_3 is attributed to the tolerance of Cr_2AlC to Al vacancies, maintaining the crystal structure of the matrix even when the density of Al vacancy is low. As a result, if the crack gap is small, it can be filled without the formation of Cr_7C_3 phase. However, if the crack gap is relatively wide, the depletion of Al in the nearby matrix gives rise to the Cr_2AlC structure being unstable causing it to decompose to form Cr_7C_3.

Table 5-1Average Al_2O_3 width on a single crack surface calculated along crack

Position	b1	b2	b3	b4
Average width of Al_2O_3 (μm)	2.45	2.37	2.43	1.08

5.4 Discussion

5.4.1 Dependence of crack healing kinetics on crack location

Cracks in polycrystalline Cr_2AlC MAX phase ceramic samples usually follow the basal plane of Cr_2AlC crystals, resulting in a zigzag crack shape in non-textured Cr_2AlC samples as evident in Figure 5.6 (a). The zigzag crack shape as well as the occurrence of crack bridging, makes it difficult to transport oxygen from the sample exterior to the root of the crack. Therefore, during the crack healing process, the oxide scale growth may happen under different local oxygen partial pressures. To investigate the potential influence of local oxygen partial pressure on overall healing rate, two rather different areas of the crack are chosen. Areas very close to the crack edges are assumed to have an easier access to oxygen, thus a higher oxygen partial pressure, equal to the external oxygen partial pressure. For areas in the middle of the crack, the oxygen partial pressure could be the lower as the oxygen transport distance is longer. The overall healing

percentage as a function of time at these two positions is shown in Figure 5.7 (b). The healing percentage (percentage of the crack gap filled) as a function of time at crack middle is calculated by segmenting and measuring crack area (A(t)) in five 2D X-ray tomographic slices along the crack growth direction (along x axis), hence: $H = \frac{A(t=0)-A(t)}{A(t=0)} \times 100\%$. The healing kinetics of the crack edge was determined by averaging the healing percentages at the two crack edges.

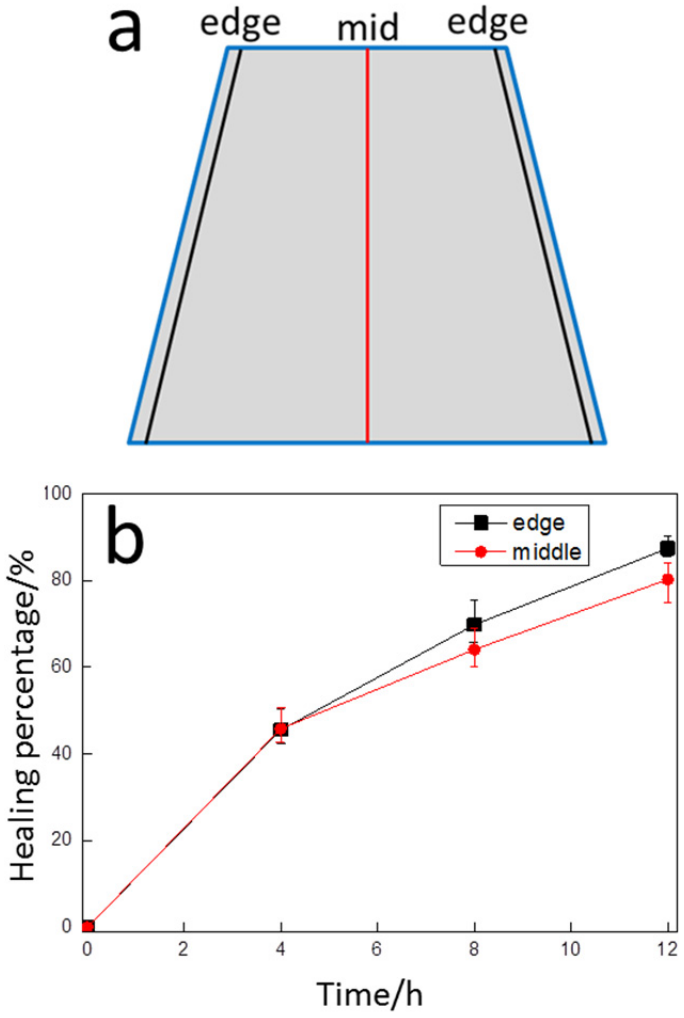

Figure 5.7 (a) Lines along which the percentage healing was quantified. (b) Percentage of crack healing as a function of healing time calculated at middle and edge of the crack, respectively.

The healing process at the edge and middle seems to show very similar trends. After the initial 4 hour heat treatment, the healing percentage at the edge and middle is almost identical at about 45 %. As heat treatment time increases, the healing rate in both the middle and edge decrease as one would expect given the longer diffusion distances for the

Al atoms and O atoms. After 12 hours healing, the percentage of the crack opening healed for the edge and middle reached about 87 % and 80 % respectively. This small difference suggests that for the dimensions of the current sample and its crack, the overall healing rate of Cr_2AlC is more or less independent of the oxygen partial pressure variance or that the rate of oxygen transport in the crack is sufficient to maintain a more or less constant oxygen partial pressure along the crack.

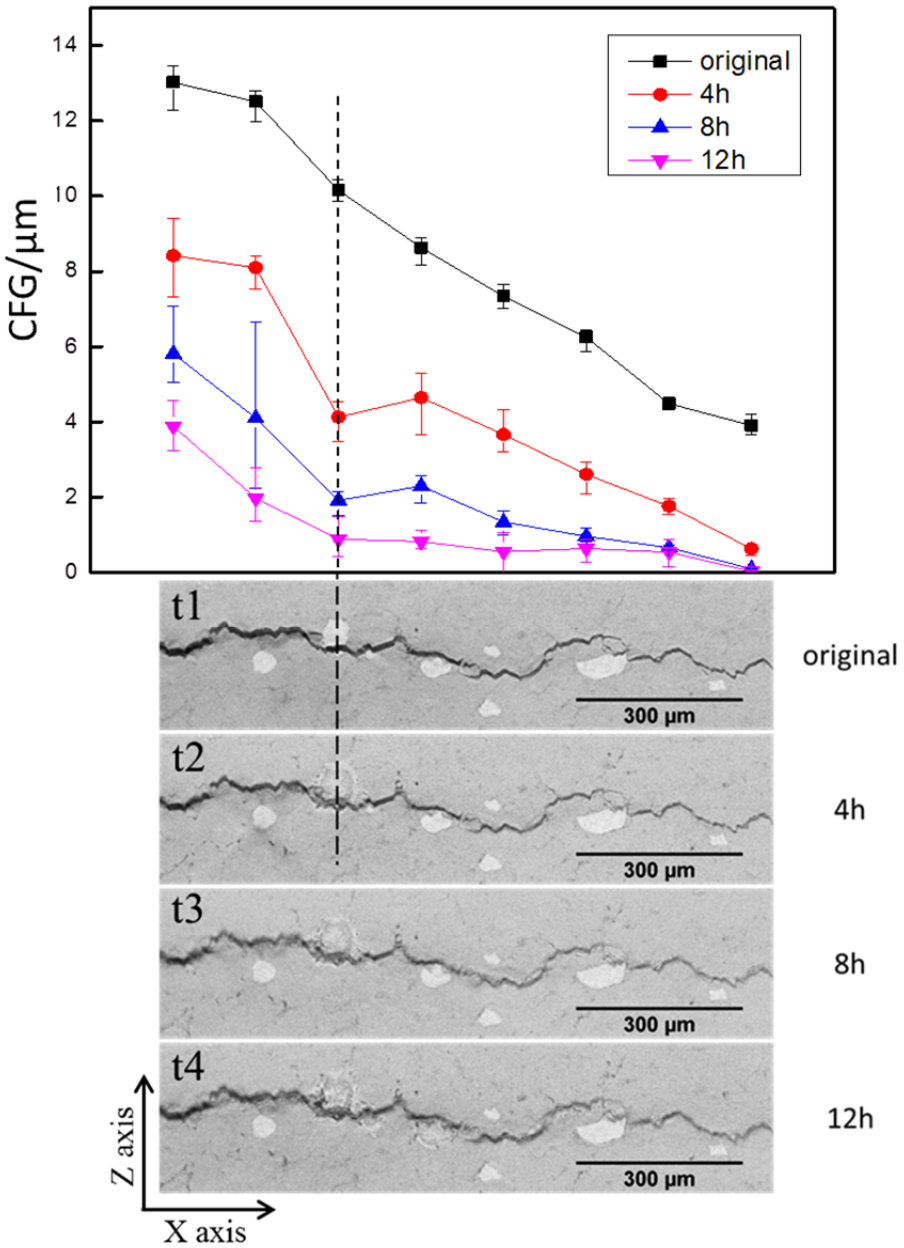

Figure 5.8 (Top) Crack face gap (CFG) calculated along the crack growth direction for different healing times; (below) 2D X-ray tomographic cross sections correlated to the CFG plots at different healing stages. The dashed line indicates the large CFG decrease near surface breaking Cr particle.

To quantify the dependence of the local healing kinetics on crack location, the crack face gap along the crack propagation direction at different healing stages is calculated and shown in Figure 5.8. Each data point represents the average crack face gap (CFG) of the nearby 200 pixels (135 μm) along the crack growth direction. The initial crack was about 1000 μm in length and 13 μm wide at the crack root. After exposure in air for 4 hours, despite an uncharacteristically large decrease in CFG identified by the dashed line, the CFG has reduced more or less equally at all points along the crack at round 4.5 μm. This result indicates a uniform local healing rate from crack root to crack tip. After 12 hours healing, the 1000 μm long crack was healed to a new maximum length of less than 300 μm (4 μm in width at crack root). The unusually large decrease in CFG at the location indicated by the dashed line was due to the presence of Cr particles and is consistent with the observations relating to Figure 5.3. The mechanism of this phenomenon will be discussed in section 4.3.

This independence of the overall and local healing rate on crack location shown above is probably due to the fact that Cr_2AlC has a relatively slow healing kinetics when compared to many of its counterparts, such as Ti_2AlC and Ti_3AlC_2 [4, 5, 16, 24]. The growth rate of Al_2O_3 scale is controlled by grain boundary diffusion of Al and O through existing oxide layer even at crack tip and middle, where the oxygen partial pressure is lower due to oxygen transport difficulty. The crack location induced oxygen partial pressure variance thus has a minor effect on the healing kinetics. As a result, a more or less uniform healing kinetics both along and across the crack was observed. It is also worth noting that this uniform healing kinetics over the whole crack area means that because the crack is narrowest at the crack tip it will always heal first, while the crack root having a larger crack face gap will be fully healed last, as is indeed observed in Figure 5.4. In this way, the crack surface heals from crack tip to crack root. This even rate of oxide growth inhibits the propensity for blockage of the oxygen path caused by uneven local healing so that a high healing percentage can be achieved not only at crack edge but also at crack centre and crack tip (shown in Figure 5.7); this is critical for good recovery of strength after healing because it reduces the likelihood of internal healing defects.

5.4.2 Healing mechanism of Cr_2AlC

Previous research on the oxidation of Cr_2AlC showed that the oxide grows through inward diffusion of oxygen and outward diffusion of Al [16, 18-20]. In the case of crack filling, oxide growth will stop once the crack is fully filled with oxide. High magnification SEM images of the healed area at locations b3 and b4 in Figure 5.6 are shown in Figure 5.9.

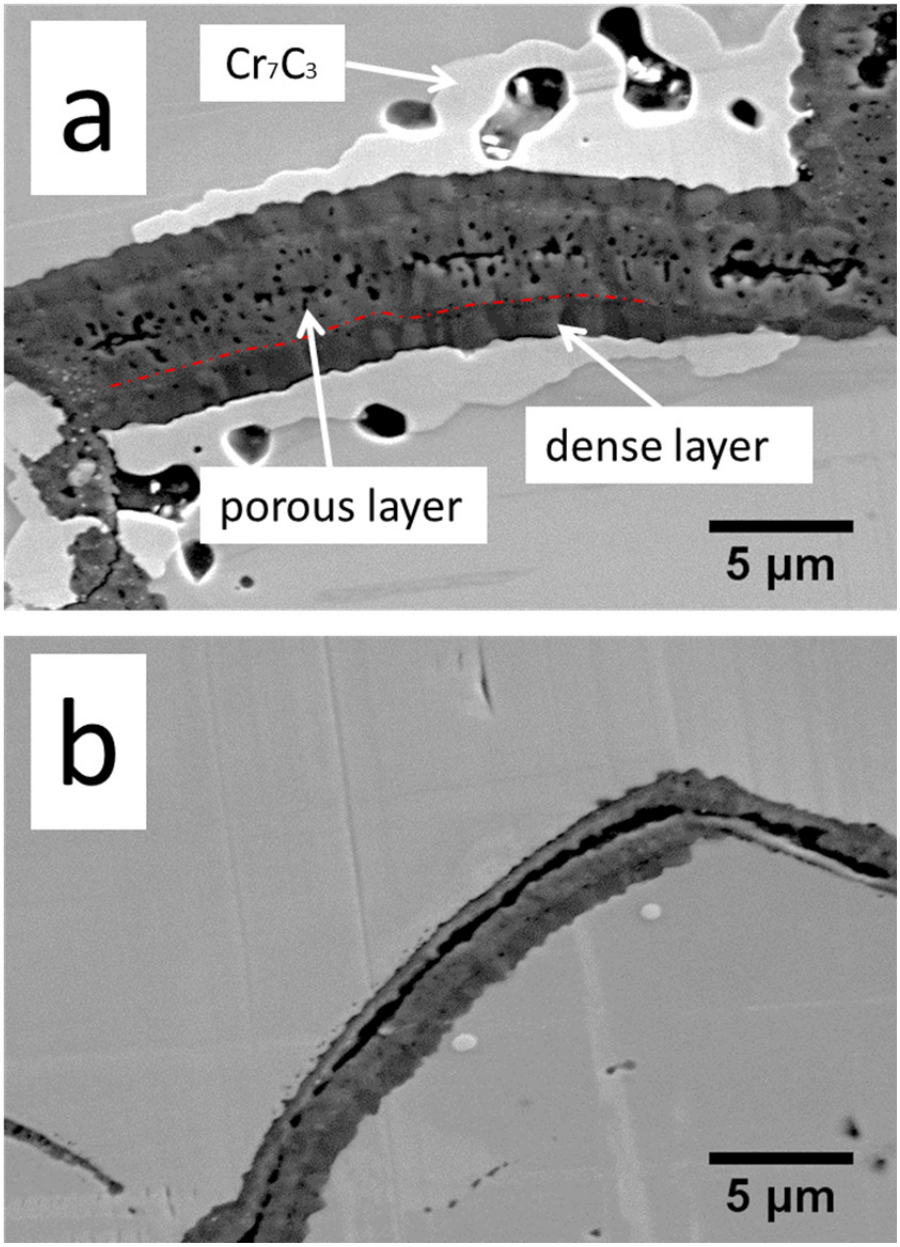

Figure 5.9 High magnification secondary electron SEM images of a) region b3 and b) region b4 shown in Fig. 6. The red dashed line in (b) indicates the border between the porous and dense Al_2O_3 formed on the Cr_2AlC substrate.

It can be seen in Figure 5.9 (a) that the oxide scale formed on the Cr_2AlC substrate after 4 hours healing at 1200 °C consists of two sub-layers: an inner dense columnar Al_2O_3 layer around 1.5 μm in thickness and an outer porous Al_2O_3 layer around 1 μm in thickness. Similar oxide scale microstructures were found in the Ti_2AlC MAX phase ceramic after exposure in air at 1200 °C for 100 hours [9]. For the oxide scale formed near the crack tip in Figure 5.9 (b), only the dense columnar Al_2O_3 layer is observed. These results suggest that the porous Al_2O_3 layer was formed after the formation of the dense layer of columnar Al_2O_3. The recovery of the strength of Cr_2AlC after healing is directly related to the microstructure and constitution of the healed region. Therefore, it is reasonable to divide the healing process into two stages: An early stage where the dense and columnar Al_2O_3 is the main oxidation product and a later stage in which a porous Al_2O_3 layer is formed on top of the dense columnar Al_2O_3 layer. In the early stage, Al is preferentially oxidized because of a more negative Gibbs formation energy of Al_2O_3 ($\Delta G_{Al2O3} << \Delta G_{Cr2O3}$). The alumina scale grows perpendicular to the Cr_2AlC substrate to form the columnar Al_2O_3, due to a higher element gradient of oxidation atoms. Once a continuous dense Al_2O_3 layer is formed, the rate of lattice diffusion of the Cr and Al atoms to the surface is significantly reduced. However, due to a relatively weak Cr-Al bond and a strong Cr-C bond, selective oxidation of Al will still occur through mass transport via the grain boundaries of the columnar Al_2O_3. At this stage, grain boundary diffusion is the dominant diffusion mechanism and a porous Al_2O_3 is formed on top of the previously formed columnar Al_2O_3 layer. The further consumption of Al results in the decomposition of Cr_2AlC matrix, giving rise to a Cr_7C_3 sublayer underneath the Al_2O_3 layer, leaving pores near the interface between Cr_7C_3 and Cr_2AlC matrix. Therefore, for short cracks with a small crack width, the crack gap is expected to be filled with dense Al_2O_3 scale, yielding good strength recovery after healing. While the recovery of strength of a long (open) crack may be less effective because of the porous Al_2O_3 layer formed in the healed region as well as the micro pores formed near the interface of Cr_7C_3 layer and Cr_2AlC matrix.

The crack healing kinetics can be assessed in terms of the evolution in the gap between the crack faces (CFG) during healing plotted in Figure 5.10 (a). Unlike TGA experiments, which are usually performed on a polished surface [16, 18], the CFG measurement represents the oxide growth over a serrated crack surface. The results show a decrease in healing rate with time broadly consistent with parabolic (diffusion controlled) growth.

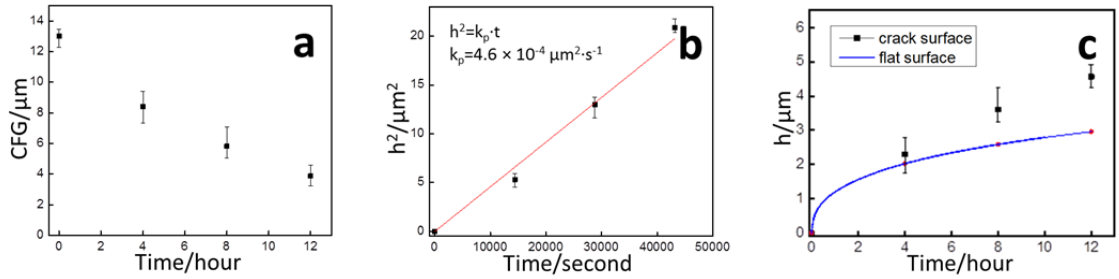

Figure 5.10 (a) Crack face gap at crack root as a function of healing time determined from five 2D virtual X-ray CT slices. (b) Square of the healed crack width (h) as a function of healing time. (c) Oxide scale thickness as a function of time on serrated crack surface and flat surface. The TGA experiment was conducted using the same batch of Cr2AlC material under the same oxidation conditions, i.e. at 1200 °C in air.

The oxide scale thickness curve fitting result (h is the oxide scale thickness on a single crack surface) shows that the kinetics of healed crack width broadly follows a parabolic law with a parabolic rate constant $k_p = 4.6\times10^{-4}$ µm^2·s^{-1}. Compared with the oxide growth over a flat surface (as obtained from TGA, shown in Figure 5.10 (c), the oxide growth over a serrated crack surface is significantly faster. The higher nucleation density at a serrated surface and thus smaller grain size of the oxide may be responsible for this faster growth, which is beneficial for the crack healing. A similar phenomenon was observed in the healing of a cavity on a Ti_2AlC matrix [5], where the grain size of formed Al_2O_3 is smaller than that on a flat surface, indicating a faster nucleation density.

5.4.3 The effect of chromium particles

The results in Figure 5.3 and Figure 5.9 indicate that the presence of Cr particles may locally accelerate the healing process of nearby crack surfaces. This phenomenon is very interesting, because the presence of local Cr-rich residues could be turned into a positive factor for the healing ability. Due to their presence, the intrinsic self-healing Cr_2AlC material is effectively turned into a mixed intrinsic-extrinsic self-healing material. To further investigate this phenomenon, a correlative analysis was conducted on the Cr_2AlC sample which had been layer in the crack direction until the region of interest identified by tomography was reached previously tracked by time-lapse X-ray tomography. The sample was ground away layer-by-layer in the crack direction until the region of interest identified by tomography was reached (see Figure 5.11).

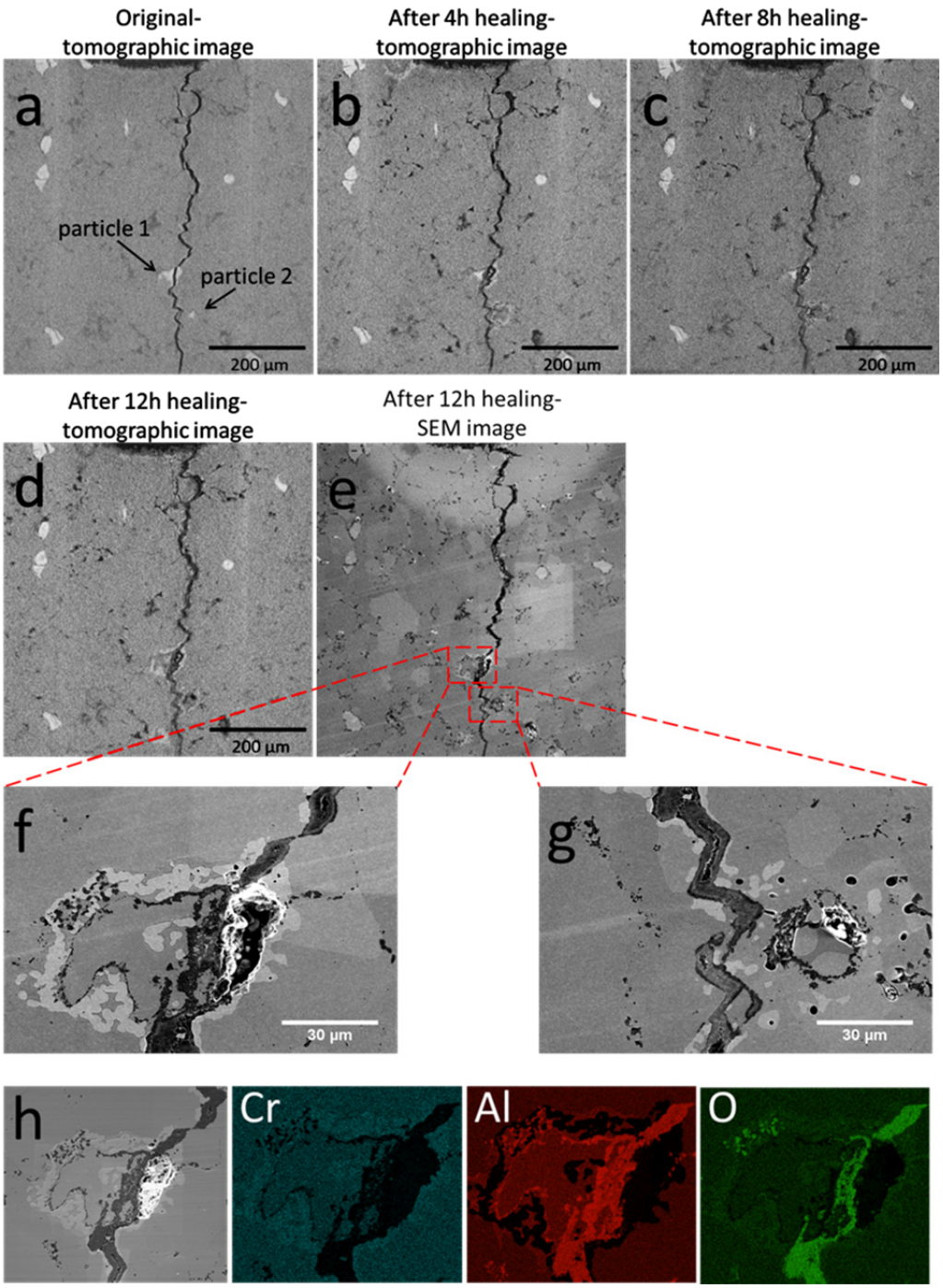

Figure 5.11 (a-d) Time lapse sequence of virtual X-ray tomographic slices of the same region-of-interest as a function of healing time (crack grew from top to bottom) at 1200 °C in air. (e) Secondary electron SEM cross section of the same region-of-interest correlated to (d). (f-g) Higher magnification SEM images of the healed regions indicated by the red rectangles in (e). (h) EDS elemental maps of the region in (f). Particle 2 lies predominantly below the current virtual slice.

The secondary electron SEM image (Figure 5.11(e)) matches well with the X-ray tomographic slices (Figure 5.11 (d)). It can be seen in the virtual tomographic sections Figure 5.11 (a-d) that two Cr particles (particle 1 and particle 2) lie in close proximity to

the fracture surface, as indicated by arrows in Figure 5.11 (a). The original crack passed through particle 1, breaking it into two smaller parts. Although it seems that the particle 2 was not in direct contact with the crack, in successive tomographic slices beneath the current slice, the crack propagated along the interface of Cr particle 2 and the Cr_2AlC matrix (not shown here for brevity). After 4 hours of annealing at 1200 °C, the right half of particle 1 has been consumed, leaving a white layer around the original shape of the Cr particle, as shown in Figure 5.11 (b).

In the meantime, the larger left half of particle 1 also shrunk and was completely consumed after 12 hours of heat treatment at 1200 °C, as shown in Figure 5.11 (d). A similar white layer is observed around the original position of the left half of particle 1. A higher magnification SEM image of the healed area near the Cr particle and the corresponding elemental mappings are shown in Figure 5.11 (f) and Figure 5.11 (h). Consistent with the virtual tomographic slices, a grey area (composed of Cr and Al) is observed surrounded by white layers (composed of Cr and C), shown in Figure 5.11 (f). Element ratio calculations from EDS suggest that the grey area corresponds to CrAl, while the white layer is Cr_7C_3. A similar interaction is observed between the crack and particle 2. However, in this case the Cr_7C_3 layer gradually disappeared with prolonged healing. After 12 hours of heat treatment the Cr_7C_3 was consumed leaving a pore, as shown in Figure 5.11 (g).

Based on the above observations, it is proposed that initially the atmospheric oxygen partial pressure is high enough for the exposed Cr particles to oxidize to Cr_2O_3. The existence of surface breaking Cr particles during healing results into the formation of Cr_2O_3 particles or films provides a nucleation site of Al_2O_3, thus increasing the rate of formation of Al_2O_3. The relatively rapid consumption of Al atoms creates a large chemical potential for Al to diffuse from nearby Cr_2AlC matrix to the crack surface. In order to diffuse from the Cr_2AlC matrix to the crack surface, the Al atoms has to pass through the Cr particles, resulting into the enrichment of Al in Cr particles. A further depletion of Al at the Cr-Cr_2AlC interface makes the nearby Cr_2AlC matrix become unstable and this results in the formation of a Cr_7C_3 layer. At longer healing times, Cr_7C_3 reacts with oxygen to form Cr_2O_3, which is transformed to the gaseous CrO_3 phase at the imposed high temperature [25, 26]. The vaporization of CrO_3 leaves pores in the healed area, which may have a negative effect on strength recovery after healing.

5.5 Conclusions

Our results have demonstrated that non-destructive time-lapse X-ray tomographic imaging together with post-mortem correlative SEM can be used to track the crack healing process of Cr_2AlC in great detail. Healing of a crack in Cr_2AlC at 1200 °C in air is followed as a function of the annealing time in 3D with a pixel size of 0.68 μm, providing data to develop and validate crack healing models of this material. Based on our current results, the following conclusions could be reached. The crack healing of Cr_2AlC is an oxidation process where the crack gap is filled essentially by Al_2O_3. The maximum crack width that could be fully healed at 1200 °C in air within 4 and 12 hours is estimated to be around 4.8 μm and 10 μm respectively. During healing Cr_7C_3 phase is observed when the crack width exceeds 2 μm. The Al_2O_3 scale comprises a porous layer on top of a columnar dense layer typically 1.5 μm thick after 4 hours' healing at 1200 °C. The former is not observed for the repair of the crack when it is less than 2 μm wide. Despite the two layer nature of the repair, the crack healing kinetics of Cr_2AlC at 1200 °C in air broadly follows a parabolic rate law with constant of 4.6×10^{-4} $\mu m^2 \cdot s^{-1}$. The existence of impurity Cr particles locally accelerated the healing process by providing Cr_2O_3 nucleation sites. The later evaporation of Cr_2O_3 may leave large pores near the healed area, which may reduce strength recovery.

References

1. Zhou, Y. and X. Wang, *Deformation of polycrystalline Ti_2AlC under compression.* Material Research Innovations, 2001. **5**(2): p. 87-93.
2. Wang, X. and Y. Zhou, *Oxidation behavior of Ti_3AlC_2 at 1000–1400 ºC in air.* Corrosion Science, 2003. **45**(5): p. 891-907.
3. Wang, X. and Y. Zhou, *High-temperature oxidation behavior of Ti_2AlC in air.* Oxidation of Metals, 2003. **59**(3-4): p. 303-320.
4. Bei, G.P., G. Laplanche, V. Gauthier-Brunet, J. Bonneville, and S. Dubois, *Compressive Behavior of Ti_3AlC_2 and $Ti_3Al_{0.8}Sn_{0.2}C_2$ MAX Phases at Room Temperature.* Journal of the American Ceramic Society, 2013. **96**(2): p. 567-576.
5. Barsoum, M.W. and T. El-Raghy, *The MAX Phases: Unique New Carbide and Nitride Materials Ternary ceramics turn out to be surprisingly soft and machinable, yet also heat-tolerant, strong and lightweight.* Am. Scientist, 2001. **89**(4): p. 334-343.
6. Tian, W., Z. Sun, H. Hashimoto, and Y. Du, *Compressive deformation behavior of ternary compound Cr_2AlC.* Journal of materials science, 2009. **44**(1): p. 102-107.

7. Yang, H., Y. Pei, J. Rao, J.T.M. De Hosson, S. Li, and G. Song, *High temperature healing of Ti_2AlC: on the origin of inhomogeneous oxide scale.* Scripta Materialia, 2011. **65**(2): p. 135-138.
8. Yang, H., Y. Pei, and J.T.M. De Hosson, *Oxide-scale growth on Cr_2AlC ceramic and its consequence for self-healing.* Scripta Materialia, 2013. **69**(2): p. 203-206.
9. Li, S., G. Song, K. Kwakernaak, S. van der Zwaag, and W.G. Sloof, *Multiple crack healing of a Ti_2AlC ceramic.* Journal of the European Ceramic Society, 2012. **32**(8): p. 1813-1820.
10. Farle, A.-S., C. Kwakernaak, S. van der Zwaag, and W.G. Sloof, *A conceptual study into the potential of $M_{n+1}AX_n$-phase ceramics for self-healing of crack damage.* Journal of the European Ceramic Society, 2015. **35**(1): p. 37-45.
11. Song, G., Y. Pei, W. Sloof, S. Li, J.T.M. De Hosson, and S. Van der Zwaag, *Oxidation-induced crack healing in Ti_3AlC_2 ceramics.* Scripta Materialia, 2008. **58**(1): p. 13-16.
12. Yang, H., Y. Pei, J. Rao, and J.T.M. De Hosson, *Self-healing performance of Ti_2AlC ceramic.* Journal of Materials Chemistry, 2012. **22**(17): p. 8304-8313.
13. Sloof, W.G., R. Pei, S.A. McDonald, J.L. Fife, L. Shen, L. Boatemaa, A.-S. Farle, K. Yan, X. Zhang, and S. van der Zwaag, *Repeated crack healing in MAX-phase ceramics revealed by 4D in situ synchrotron X-ray tomographic microscopy.* Scientific Reports, 2016. **6**: 23040.
14. Tian, W., P. Wang, Y. Kan, and G. Zhang, *Oxidation behavior of Cr_2AlC ceramics at 1,100 and 1,250 C.* Journal of Materials Science, 2008. **43**(8): p. 2785-2791.
15. Tallman, D.J., B. Anasori, and M.W. Barsoum, *A critical review of the oxidation of Ti_2AlC, Ti_3AlC_2 and Cr_2AlC in Air.* Materials Research Letters, 2013. **1**(3): p. 115-125.
16. Lee, D. and S. Park, *Oxidation of Cr_2AlC between 900 and 1200 °C in air.* Oxidation of Metals, 2007. **68**(5-6): p. 211-222.
17. Lee, D.B., T.D. Nguyen, and S.W. Park, *Long-time oxidation of Cr_2AlC between 700 and 1,000 °C in air.* Oxidation of Metals, 2012. **77**(5-6): p. 275-287.
18. Li, S., L. Xiao, G. Song, X. Wu, W.G. Sloof, and S. van der Zwaag, *Oxidation and Crack Healing Behavior of a Fine-Grained Cr_2AlC Ceramic.* Journal of the American Ceramic Society, 2013. **96**(3): p. 892-899.
19. Lin, Z., Y. Zhou, M. Li, and J. Wang, *In-situ hot pressing/solid-liquid reaction synthesis of bulk Cr_2AlC.* Zeitschrift für Metallkunde, 2005. **96**(3): p. 291-296.
20. Duan, X., L. Shen, D. Jia, Y. Zhou, S. van der Zwaag, and W.G. Sloof, *Synthesis of high-purity, isotropic or textured Cr_2AlC bulk ceramics by spark plasma sintering of pressure-less sintered powders.* Journal of the European Ceramic Society, 2015. **35**(5): p. 1393-1400.
21. Maire, E. and P. Withers, *Quantitative X-ray tomography.* International Materials Reviews, 2014. **59**(1): p. 1-43.
22. Wang, X. and Y. Zhou, *Oxidation behavior of Ti_3AlC_2 powders in flowing air.* Journal of Materials Chemistry, 2002. **12**(9): p. 2781-2785.
23. Grimley, R., R. Burns, and M.G. Inghram, *Thermodynamics of the vaporization of Cr_2O_3: dissociation energies of CrO, CrO_2, and CrO_3.* The Journal of Chemical Physics, 1961. **34**(2): p. 664-667.
24. Stanislowski, M., E. Wessel, K. Hilpert, T. Markus, and L. Singheiser, *Chromium vaporization from high-temperature alloys I. Chromia-forming steels and the influence of outer oxide layers.* Journal of the Electrochemical Society, 2007. **154**(4): p. 295-306.

6 Reducing the erosive wear rate of Cr_2AlC MAX phase ceramic by oxidative healing of local impact damage

The present work describes a model study to explore the possibility to heal early stage erosion damage in Cr_2AlC MAX phase when exposed to high air temperatures and erosive conditions. Such a healing reaction should lead to a reduction of the wear rate of this promising material for application in jet turbine engines. To this aim Cr_2AlC ceramic discs were subjected to room temperature erosion for 60 minutes using glass microbeads accelerated to 110 m/s and impinging perpendicular to the sample surface. After the usual incubation time, the erosion rate reaches a constant rate, which is associated with the formation of network of small cracks underneath the surface. Next, the material was annealed at 1200 °C for 10 minutes in air resulting in filling of the network of small cracks due to the formation of well-adhering Al_2O_3. The subsequent erosion rate of the healed Cr_2AlC ceramic at room temperature is drastically reduced. Once the healed zone is removed by erosion the erosion rate attained its original value. Clearly, exposure to high temperature oxidative conditions extends the lifetime of Cr_2AlC MAX phase components subjected to erosive conditions.

6.1 Introduction

Cr_2AlC belongs to the family of MAX phase metallo-ceramics, which are tough and therefore damage tolerant compared with many other common engineering ceramics. This MAX phase is stable up to high temperatures and corrosion resistant. Its combination of high strength, high toughness up to very high temperatures and high thermal conductivity makes this ceramic very resistant to thermal shock [1-10]. Therefore this material is very attractive for high temperature applications, where the material is exposed to steep thermal cycles, high mechanical loading and oxidation. Moreover, Cr_2AlC has a large coefficient of thermal expansion comparable to that of Ni alloys and is hot corrosion resistant (i.e. resistant against attack by sulfur containing species) and hence would be a potential candidate coating material for application in the hot sections of turbine engines [11-14].

Erosion damage of components located along the path of the air flowing through an aero turbo engine (i.e. starting at the inlet of the compressor via the combustion chamber into the turbine) due to high velocity impact of solid particles is of major concern since it affects fuel efficiency, reduces their lifetime and ultimately impairs flight safety. The particles in the air could be fine dust particles forming regular air pollution, desert sand or volcanic ashes etc. [15, 16]. To recall: the volcanic outburst in 2010 of the Eyjafjallajökull on Iceland shut down all air traffic in major parts of Europe for up to four days [17].

The impact of hard particles (projectiles) on a material surface (target) can lead to local plastic deformation and fracture of the target material, while the hard particles deform elastically and seldom fracture [18]. It is well known that serious abrasion only occurs at velocities above a certain threshold velocity [19, 20]. The erosion rate at velocities above the threshold is largely dependent on the ratio of the hardness of the target material Ht with respect to the impact particle Hp. For $Ht/Hp<1$ the erosive wear is caused primarily by fracture and the erosion rate increases with increasing hardness of the impact particle.

Erosion of ductile material mainly results from plastic deformation (cutting) which is manifested as indents (craters) with a peripheral rim on its surface. Whereas materials loss for brittle materials mainly happens via crack formation due to a (local) dynamic elastic-plastic stress field generated upon impact [21]. Two types of cracks can be

distinguished [22]: radial or circumferential cracks perpendicular to the surface formed during impact (Figure 6.1 (a)), and lateral cracks parallel to the surface upon unloading (Figure 6.1 (b)). The latter result from a residual elastic-plastic stress field. Erosion of the target material is related to the formation and growth of the lateral cracks, ultimately leading to a network of connected cracks and spontaneous material removal via spallation (Figure 6.1 (c)). Various models based on fracture mechanics have been developed to relate the erosion rate V of brittle materials to its standard mechanical properties [18, 20, 23-27]. According to Evans et al. [28] for impact of incompressible particles perpendicular to the target surface it holds that:

$$V \propto v_p^{19/6} R_p^{11/3} \rho_p^{1/4} / K_{c,t}^{4/3} H_t^{1/4} \tag{6-1}$$

where vp is the impact velocity, Rp the radius and ρp the density of the particles, respectively. Kc,t and Ht is the fracture toughness and hardness of the target material, respectively. The erosion rate is defined as the eroded mass of the target material relative to that of impact particles. On the one hand, the erosion rate depends on the erodent, such as particle hardness, size and shape, mass, velocity and impact angle [29-35]. On the other hand, the erosion rate depends on the strength and toughness of the material. The difference between the erosion behavior of ductile and brittle materials is also reflected in the angle of maximal erosion rate [35]. For a brittle material the maximum erosion rate occurs a at an impact angle of about 90º, while for a ductile material a maximum is observed at an impact angle of 20-30° [36].

The relatively high toughness [37] the moderate hardness [6] and the ability to undergo relatively large plastic deformation due to its layered structure make Cr_2AlC a potentially attractive erosion resistant ceramic. Recently, it has been demonstrated that crack damage in alumina forming MAX phases, like Ti_3AlC_2 and Ti_2AlC as well as Cr_2AlC, can be healed by selective oxidation of the A element [38-41]. Thus, the MAX phase is part of the healing reaction and the healing product is formed by consuming oxygen from the gas atmosphere. The filling of the crack gap with well-adhering alumina and other reaction products restores the material integrity.

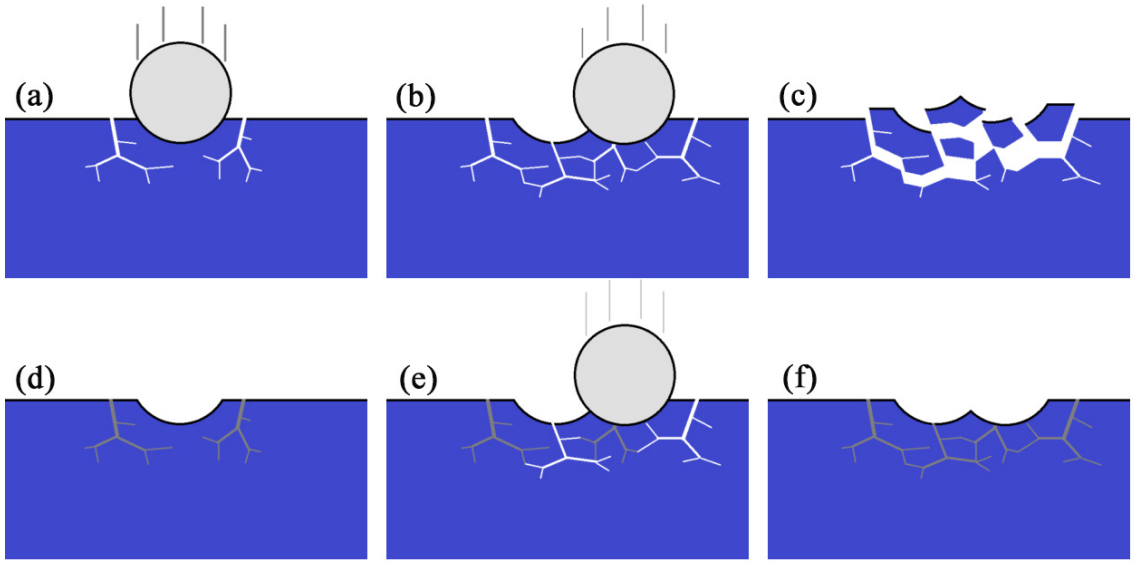

Figure 6.1. Schematic drawing of erosion and healing behavior of MAX phase ceramics. (a) first impact with crack development; (b) second impact causes crack network; (c) spallation of fragments; (d) first healing due to crack closing by oxidation; (e) further impact.

Following the above concept, it is proposed that the erosion rate of MAX phase metallo-ceramics will be reduced when the surface is continuously or periodically exposed to high temperature oxygen containing environments, via a process shown schematically in Figure 6.1 (d-f). The present model study looks at the room temperature erosion and erosion rate of Cr_2AlC and the change thereof after annealing at a high temperature in an oxidizing environment. The erosive damage healing capability of Cr_2AlC is demonstrated convincingly. From the above analysis it is clear that a reduction of the abrasion rate can be envisaged in case of a healing reaction leading to the healing/sealing of the network of small cracks before there is full 3D local connectivity of the cracks leading to spallation.

6.2 Materials and Methods

6.2.1 Synthesis of Cr_2AlC

The chromium (average particle size of about 100 µm, purity > 99.2%, TLS Technik GmbH & Co., Germany), aluminium (average particle size of about 45 µm, purity > 99.8%, TLS Technik GmbH & Co., Germany) and graphite (average particle size of 6 µm, purity > 99.5%, Graphit Kropfmühl AG, Germany) powders having a molar ratio of 2:1.15:1, respectively, were mixed for 24 hours using a Turbula T2C mixer (Willy A. Bachofen, Switzerland) also filled with ZrO_2 balls. Then, the powder mixture was cold

pressed into tablets with a diameter of 25 mm and a thickness of about 5 mm with a Carver press (Model 3853-0, USA). These tablets were pressure-less sintered in a flow of 500 sccm Argon (purity > 5N) for 1 hour at 1400 °C in a horizontal alumina tube furnace (Lenton Furnaces, PTF 16/75/610, UK) with an inner tube diameter of 80 mm. The tablets were placed on graphite boats and the furnace was heated with 5 °C per minute. Next, the PLS samples were pulverized (using a Fritsch Pulverisette, Germany) and ball milled with 10 mm WC balls and WC jar (250 ml) for 1 hour effectively, i.e. cycles of 10 min. milling at a speed of 300 rpm and 20 min. at hold using a PM100 ball grinder (Retsch GmbH, Germany). The Cr_2AlC powder obtained had an particle size around 4 μm and was phase pure according to X-ray diffraction. The Cr_2AlC powder was densified with SPS (HP D 25, FCT Systeme GmbH, Frankenblick, Germany) at a pressure of 50 MPa with a heating rate of 50 °C/min. The powder was put into a graphite mold with an inner diameter of 20 mm applying graphite paper and BN spray (Henze, HeBoCoat® 21E, Germany), to separate the powder from the mould. After the SPS treatment the thickness of the sample was about 7 mm.
The density of the samples was measured with theArchimedes method using an analytical balance (Mettler Toledo AG-204, Switzerland) according to ASTM B 311-93 [42].

6.2.2 Sample preparation

Cr_2AlC discs with a diameter of 20 mm prepared by SPS were cut into discs of 2 mm thickness by spark erosion [43]. Next, the sample surfaces were ground with SiC emery paper (4000 mesh grids) and polished with diamond paste of 0.25 micron. Finally, the samples were ultrasonically cleaned in ethanol and dried with a jet of pure and dry nitrogen.

6.2.3 Erosion and healing experiments

The erosion tests were executed at room temperature according to ASTM G76 [44] with some modifications as specified below. The erosion test rig consisted of an erosion sample chamber and a high accuracy powder feeder (Castolin Eutectic, EP2, Switzerland). The abrasive particles were accelerated using compressed air and directed with a nozzle perpendicular to the sample surface. In this study spherical glass micro-beads (DIN 8201) having a hardness of about 8 GPa were used and a mean diameter of 95 μm were used

under conditions leading to a particle flux of 2 g/min. The nozzle had a length of 50 mm and an inner diameter of 2 mm. The distance between the nozzle outlet and the sample surface was 10 mm. The erosion conditions resulted in an erosion crater with a diameter of about 6 mm. The particle velocity at different air pressures was measured with Particle Image Velocimetry (PIV) using a high-speed camera (Dantec Dynamics, Denmark). The air pressure used to accelerate the glass particles to a velocity of 110 m/s was 1.75 bar.

To determine the erosion rate, the mass change was measured trice every 5 minutes using an analytical balance (Mettler Toledo XS105DU, Switzerland) with a resolution of 0.01 mg to determine an average value.

In this study both multistep erosion and multistep erosion and healing experiments were carried out. The multistep erosion testing took effectively 60 minutes with 12 intervals of 5 minute. This was followed by cyclic erosion and healing with a healing cycle consisting of 10 minutes isothermal oxidation at 1200 °C in air and 20 minutes erosion. Hereafter the erosion time was extended for another 60 minutes. Oxidation induced crack healing of Cr_2AlC was realized in an alumina tube furnace (Nabertherm RHTH 120-600/16, Germany) using synthetic air as the annealing medium.

6.2.4 Microstructure and compositional analysis

The crystal structure of the pressure-less sintered powders and the SPS bulk Cr_2AlC samples was analyzed with X-ray diffraction (Bruker D8, Germany) using Co Kα radiation. The diffractograms were recorded in the range from 10 to 130 °2θ with a step size 0.034 °2θ and a counting time of 2 s per step. Bruker software Diffrac EVA version 3.1 was employed to evaluate the diffraction data.

The microstructure of the virgin material and that of samples exposed to erosion and oxidation were observed using a field emission gun scanning electron microscope (JEOL, JSM 6500F, Japan). The cross section was prepared by cutting with a diamond wafer blade. Prior to grinding and polishing the sample was covered with a thin copper film (~ 0.5 μm) and a silicon wafer was glued on top of the copper layer to conserve the surface during sample preparation. The SEM was equipped with an energy dispersive spectrometer (EDS, Thermo-Noran, UltraDry, USA) for X-ray microanalysis (XMA) and a detector for backscattered electrons to observe composition variations (Autrata, Czech

Republic). The scanning electron microscope was provided with an HKL Nordlys II detector (Oxford Instruments, UK) for electron backscattering diffraction (EBSD). The EBSD data acquisition and processing was performed using Channel 5 software (version 2011).

6.3 Results and discussion

6.3.1 Material characterization

According to the XRD pattern the Cr_2AlC prepared by PS-SPS were compositionally homogeneous and free of 2nd phase particles. According to EBSD analysis the grains of the Cr_2AlC material were randomly oriented and the grain size distribution was in the range from 1 to 4 μm. A similar or even finer grained microstructure may occur when it is applied as a coating [45]. The density of this material determined by the Archimedes method equaled 5.220 ± 0.003 g/cm^3, which compared with the theoretical density of Cr_2AlC, 5.25 g/cm^3 [46], and suggests a porosity of about 0.6 %. This low porosity is in agreement with the SEM observations of the material. The hardness of the synthesized Cr_2AlC was found to be 6.5 ± 0.4 GPa, which results in a hardness ratio between target and impact particle of $H_t/H_p \approx 0.8$. From the cracks generated when applying loads above 200 N with Vickers hardness indentation the fracture toughness was estimated to be 8.7 MPa m$^{-1/2}$ [47]. Hence, the Cr_2AlC material studied is considered to behave brittle and Eq.(6-1) is applicable.

6.3.2 Erosion of Cr_2AlC

Analysis of the erosion damage caused by normal impact with glass beads under a velocity of 110 m/s revealed that the surface had become rough due to material that has been chipped-off and erosion induced cracks were visible at the eroded surface, see Figure 6.2 (a) and (b).

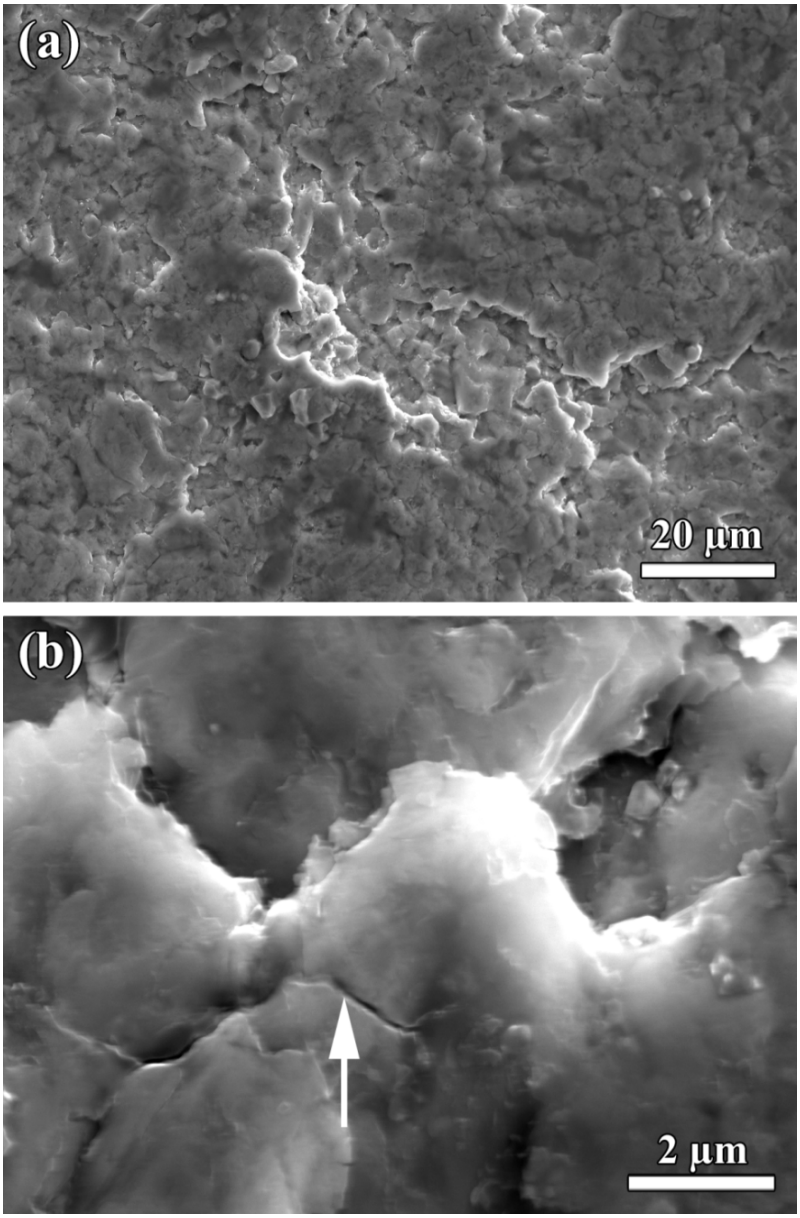

Figure 6.2 SEM images of the surface after 60 minutes erosion with 2 g/min spherical glass beads having an average diameter of 95 µm and 110 m/s impact velocity: (a) with low and (b) high magnification. The arrow indicates a crack.

Underneath the surface a network of small cracks typically having a width of about 0.1 µm and a length of about 8 µm was generated; see Figure 6.3.

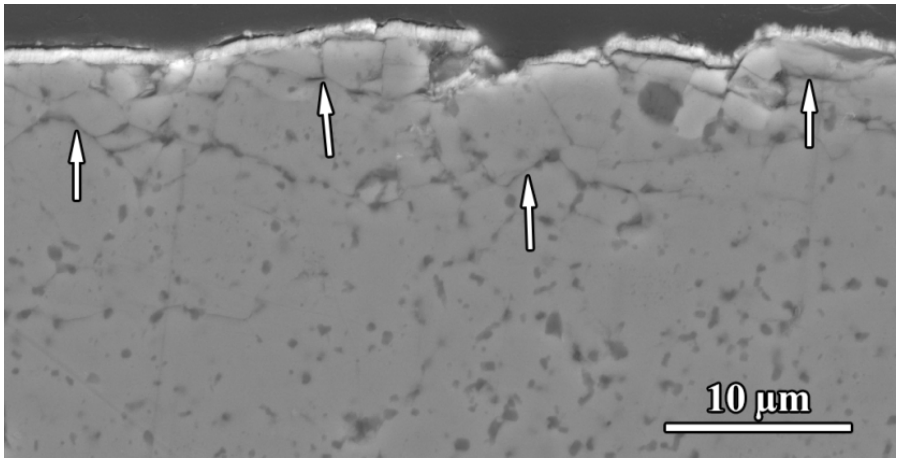

Figure 6.3 SEM image of cross section of eroded sample after 60 minutes with 2 g/min spherical glass beads having an average diameter of 95 µm and 110 m/s impact velocity showing the network of cracks generated. The arrows indicate cracks induced by impacting particles. On top of the surface a 0.5 µm copper layer was deposited.

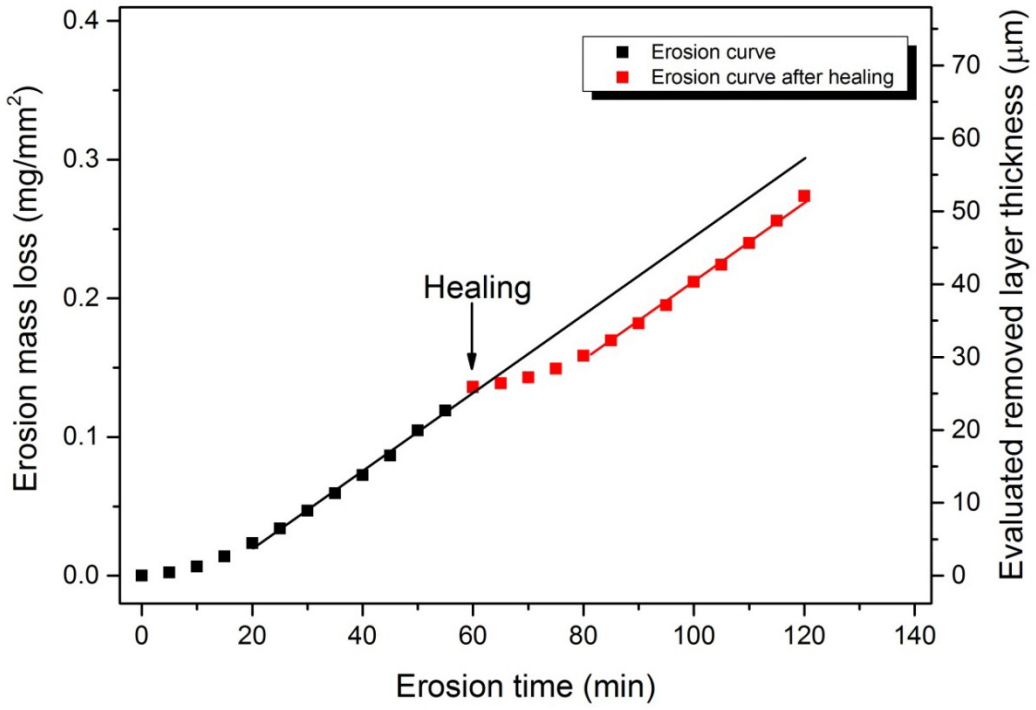

Figure 6.4 Erosion mass loss and evaluated removed layer thickness as a function of erosion time of the Cr_2AlC virgin material (black dots) and the healed material (red dots). The black and red solid straight lines represent the steady state erosion of the virgin a and healed material, respectively. The steady state erosion is extrapolated to compare with the erosion of the healed material. Erosion by 2 g/min spherical glass beads having an average diameter of 95 µm and 110 m/s impact velocity. Healing of impact crack damage at 1200 °C for 10 minutes in air.

The initial mass loss during incubation time is slow since in the early stage only cracks perpendicular to the impacted surface were initiated; see Figure 6.4. Once a stable network of cracks occurs below the surface the amount of material that breaks away per unit of time becomes constant and a steady state of impact erosion is reached. For the erosion conditions considered here (see Section 2.3) the steady state is reached after about 20 minutes. Under these conditions the erosion rate equals 0.032 mg/g, which corresponds to 0.0014 mg/mm^2/min. This erosion rate is comparable to that of super alloy IN718 (i.e. 0.023 mg/g), which is known as a reasonably erosion resistant material [48, 49]. Since the local impact velocity under real condition as encountered in jet engines can be up to 300 m/s [50], the corresponding erosion rate for 2 g/min micro glass beads impact can be evaluated using Eq.(6-1) which amounts as much as 0.77 mg/g. Considering that the shape and concentration of the impacting particles (e.g. sand) will differ from the spherical micro glass bead used in our experiments, the erosion will be even more severe under real application conditions.

To evaluate the erosion rate in terms of average removed layer thickness δ per unit of time, the volume V_m of the erosion crater is considered. The volume V_m of the erosion crater can be determined from the mass loss Δm and the density ρ_t of Cr_2AlC, i.e. $V_m = \Delta m / \rho_t$. Then the average removed layer thickness is obtained by dividing this volume by the area of the erosion spot, hence:

$$\delta = \frac{\Delta m}{\pi a^2 \rho_t} \tag{6-2}$$

here a is the radius of the eroded spot which is considered to be constant in time for the erosion conditions explored.

6.3.3 Oxidation induced healing

The crack damage in Cr_2AlC due to mechanical loading can be healed by filling the crack gap with alumina as the result of oxidation at high temperatures in air [51]. When oxidizing Cr_2AlC at1200 °C in air for 10 minutes after impact with 2 g/min glass beads (see Section 2.3), the cracks are found to be fully filled with Al_2O_3; see Figure 6.5. Inevitable surface oxidation of Cr_2AlC at 1200 °C in air for 10 minutes results into an Al_2O_3 oxide layer of about 1 μm. Due to the selective oxidation of Al in Cr_2AlC, regions close to the healed cracks are depleted resulting in the formation of Cr_7C_3 ; see Figure 6.5.

Apparently, a small deviation of the stoichiometric composition of Cr_2AlC already leads to its decomposition.

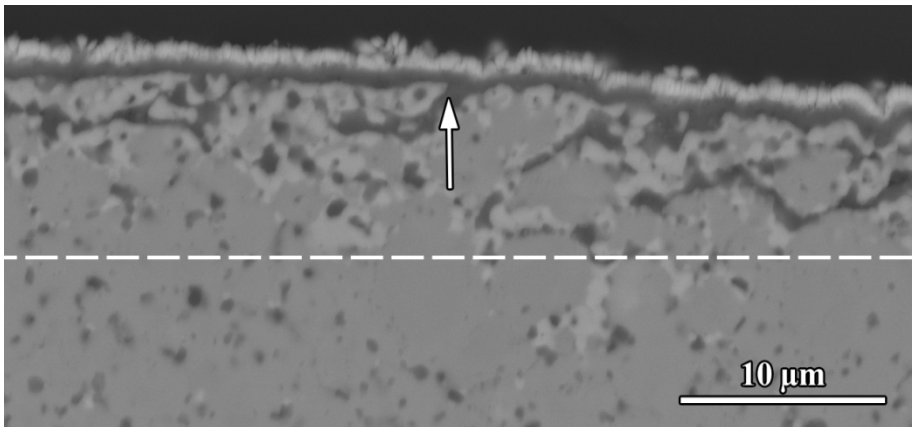

Figure 6.5 SEM image (backscattered electrons) of cross section of Cr_2AlC eroded for 60 minutes with 2 g/min spherical glass beads having an average diameter of 95 µm and 110 m/s impact velocity and after oxidation treatment at 1200 °C in air for 10 minutes. The arrow indicates the healing by Al_2O3 and the dash line marks the healed damage zone. The light phase represents the Al depleted Cr_2AlC which is Cr_7C_3. On top of the surface a 0.5 µm copper layer was deposited.

The oxidation induced healing of crack network mitigates the breakaway of material and hence the erosion rate is reduced, as can be seen in Figure 6.4. The thin surface oxide layer present after oxidation induced healing is eroded in less than 1 min. As can be expected, once the healed zone (about 8 µm) is removed, the material displays its original erosion rate. If the erosion crack damage can be healed repeatedly the erosion rate can be reduced for a longer times. This is evidenced in an additional experiment consisting of 3 cycles of 20 minutes of erosion interspersed by 10 minutes of oxidation induced healing. In Figure 6.6, it is shown very clearly that after each healing treatment the erosion rate is retarded. When continuing the erosion experiment for another 60 min. without healing, the erosion tendency is the same as that of the virgin material. However, this erosion rate is about 12 % smaller than that of original material, which may be due to roughening of the surface since the erosion rate of brittle materials is known to decrease with decreasing impact angle.

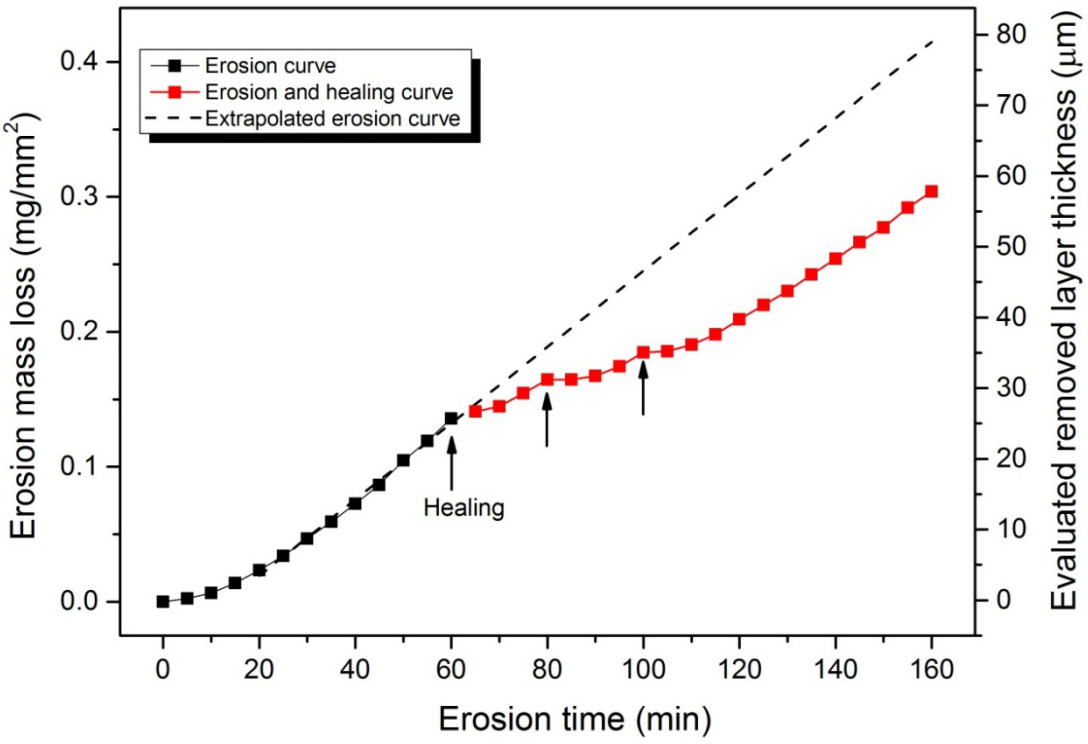

Figure 6.6 The recorded mass loss and evaluated removed layer thickness as a function of erosion time of continuous erosion of virgin Cr_2AlC material (black dots). The steady state erosion is extrapolated (dashed line) for comparison. Next, cyclic erosion and healing (red dots) with a cycle of 10 minutes oxidation at 1200 ℃ in air (indicated with arrows) and of 20 minutes erosion. Then, erosion was continued for another 60 minutes. Erosion by 2 g/min spherical glass beads having an average diameter of 95 µm and 110 m/s impact velocity.

Clearly, the self-healing of crack damage results in a much lower erosion rate compared with materials that do not have this ability. Under real conditions (as in gas turbine or jet engines) the erosion and healing happens simultaneously, then the overall effect is determined by the relative erosion rate and the kinetics of oxidation induced crack healing. Hence, under real service conditions at high temperatures and an oxidative atmosphere, this self-healing of erosion damage capability of Cr_2AlC is expected to lead to a prolongation of the lifetime of the product provided the erosion rate is slower than the volumetric healing rate.

6.4 Conclusions

Normal high-speed particulate impact erosion of solid Cr_2AlC leads to the creation of a network of small cracks, which coalescence in time and determine the erosion rate. Oxidation induced healing of such impact damage restores the material integrity by filling

the crack gaps with well-adhering and structurally sound Al_2O_3. As a result the erosion rate after a healing treatment is greatly reduced and an extension of lifetime of the material is to be expected. Of course the actual improvement of the life time of a turbine component made out of MAX phase material depends on the shape, mass and the flow rate of the erodent as well as the speed and of the turbine. A more detailed study of this dependence is outside the scope of the present work.

References

1. Barsoum, M.W., *$M_{N+1}AX_N$ phases: a new class of solids; thermodynamically stable nanolaminates.* Progress in Solid State Chemistry, 2000. **28**(1-4): p. 201-281.
2. Barsoum, M.W., Yoo, H. -I., Polushina, I. K., Rud, V. Yu., Rud, Yu. V., El-Raghy, T., *Electrical conductivity, thermopower, and Hall effect of Ti_3AlC_2, Ti_4AlN_3, and Ti_3SiC_2.* Physical Review B, 2000. **62**(15): 10194.
3. Barsoum, M.W., *Physical properties of the MAX phases*; in Encyclopedia of Materials Science and Technology. Edited by K.H.J. Buschow, R.W. Cahn, M.C. Flemings, E.J. Kramer, S. Mahajan, and P. Veyssiere. Elsevier, Amsterdam, 2006.
4. Barsoum, M.W. and M. Radovic, *Elastic and mechanical properties of the MAX phases*, in *Annual Review of Materials Research*. 2011. p. 195-227.
5. Duan, X., L. Shen, D. Jia, Y. Zhou, S. van der Zwaag, and W.G. Sloof, *Synthesis of high-purity, isotropic or textured Cr_2AlC bulk ceramics by spark plasma sintering of pressure-less sintered powders.* Journal of the European Ceramic Society, 2015. **35**(5): p. 1393-1400.
6. Hajas, D.E., M. Scholz, S. Ershov, B. Hallstedt, J.P. Palmquist, and J.M. Schneider, *Thermal and chemical stability of Cr_2AlC in contact with α-Al_2O_3 and NiAl.* International Journal of Materials Research, 2010. **101**(12): p. 1519-1523.
7. Li, S.B., W.B. Yu, H.X. Zhai, G.M. Song, W.G. Sloof, and S. van der Zwaag, *Mechanical properties of low temperature synthesized dense and fine-grained Cr_2AlC ceramics.* Journal of the European Ceramic Society, 2011. **31**(1–2): p. 217-224.
8. Tian, W.B., P.L. Wang, G.J. Zhang, Y.M. Kan, and Y.X. Li, *Mechanical properties of Cr_2AlC ceramics.* Journal of the American Ceramic Society, 2007. **90**(5): p. 1663-1666.
9. Ying, G., X. He, M. Li, W. Han, F. He, and S. Du, *Synthesis and mechanical properties of high-purity Cr_2AlC ceramic.* Materials Science and Engineering A, 2011. **528**(6): p. 2635-2640.
10. Yu, W., S. Li, and W.G. Sloof, *Microstructure and mechanical properties of a $Cr_2Al(Si)C$ solid solution.* Materials Science and Engineering: A, 2010. **527**(21–22): p. 5997-6001.
11. Zhou, W.B., B.C. Mei, and J.Q. Zhu, *On the synthesis and properties of bulk ternary Cr_2AlC ceramics.* Materials Science- Poland, 2009. **27**(4): p. 973-980.
12. Lin, Z., Y. Zhou, M. Li, and J. Wang, *Hot corrosion and protection of Ti_2AlC against Na_2SO_4 salt in air.* Journal of the European Ceramic Society, 2006. **26**(16): p. 3871-3879.

13. Wang, Q.M., R. Mykhaylonka, A. Flores Renteria, J.L. Zhang, C. Leyens, and K.H. Kim, *Improving the high-temperature oxidation resistance of a β–γ TiAl alloy by a Cr_2AlC coating.* Corrosion Science, 2010. **52**(11): p. 3793-3802.
14. Lin, Z.J., M.S. Li, J.Y. Wang, and Y.C. Zhou, *High-temperature oxidation and hot corrosion of Cr_2AlC.* Acta Materialia, 2007. **55**(18): p. 6182-6191.
15. Smialek, J.L. and A. Garg, *Microstructure and Oxidation of a MAX Phase/Superalloy Hybrid Interface*. 2014, NASA/TM—2014-216679, Cleveland.
16. Chen, X., R. Wang, N. Yao, A.G. Evans, J.W. Hutchinson, and R.W. Bruce, *Foreign object damage in a thermal barrier system: mechanisms and simulations.* Materials Science and Engineering: A, 2003. **352**(1-2): p. 221-231.
17. Drexler, J.M., A.D. Gledhill, K. Shinoda, A.L. Vasiliev, K.M. Reddy, S. Sampath, and N.P. Padture, *Jet engine coatings for resisting volcanic ash damage.* Adv Mater, 2011. **23**(21): p. 2419-2424.
18. *Air travel disruption after the 2010 Eyjafjallajökull eruption*. [cited 2015 10-12]; Availablefrom:https://en.wikipedia.org/wiki/Air_travel_disruption_after_the_2010_Eyjafjallaj%C3%B6kull_eruption.
19. Wada, S., *Effects of Hardness and Fracture Toughness of Target Materials and Impact Particles on Erosion of Ceramic Materials.* Key Engineering Materials, 1992. **71**: p. 51-74.
20. Hutchings, I.M., *Transitions, Threshold Effects and Erosion Maps.* Key Engineering Materials, 1992. **71**: p. 75-92.
21. Oka, Y.I., M. Matsumura, and T. Kawabata, *Relationship between surface hardness and erosion damage caused by solid particle impact.* Wear, 1993. **162-164**: p. 688-695.
22. Aquaro, D. and E. Fontani, *Erosion of Ductile and Brittle Materials.* Meccanica, 2001. **36**(6): p. 651-661.
23. Lawn, B.R., A.G. Evans, and D.B. Marshall, *Elastic/Plastic Indentation Damage in Ceramics: The Median/Radial Crack System.* Journal of the American Ceramic Society, 1980. **63**(9-10): p. 574-581.
24. Head, W.J. and M.E. Harr, *The development of a model to predict the erosion of materials by natural contaminants.* Wear, 1970. **15**(1): p. 1-46.
25. Murugesh, L., S. Srinivasan, and R.O. Scattergood, *Models and material properties for erosion of ceramics.* Journal of Materials Engineering, 1991. **13**(1): p. 55-61.
26. Ritter, J.E., *Spherical Particle Impact Damage.* Key Engineering Materials, 1992. **71**: p. 107-120.
27. Routbort, J.L. and R.O. Scattergood, *Solid Particle Erosion of Ceramics and Ceramic Composites.* Key Engineering Materials, 1992. **71**: p. 23-50.
28. Chen, D., M. Sarumi, S.T.S. Al-Hassani, S. Gan, and Z. Yin, *A model for erosion at normal impact.* Wear, 1997. **205**(1-2): p. 32-39.
29. Evans, A.G., M.E. Gulden, and M. Rosenblatt, *Impact Damage in Brittle Materials in the Elastic-Plastic Response Regime.* Proceedings of the Royal Society A: Mathematical, Physical and Engineering Sciences, 1978. **361**(1706): p. 343-365.
30. Kosel, T.H. and T. Ahmed, *The Edge Effect in Solid Particle Erosion of Ceramic Second-Phase Particles.* Key Engineering Materials, 1992. **71**: p. 149-194.
31. Malkin, S. and J.E. Ritter, *Grinding Mechanisms and Strength Degradation for Ceramics.* Key Engineering Materials, 1992. **71**: p. 195-212.
32. Yabuki, A. and M. Matsumura, *Theoretical equation of the critical impact velocity in solid particles impact erosion.* Wear, 1999. **233-235**: p. 476-483.

33. Yabuki, A., K. Matsuwaki, and M. Matsumura, *Critical impact velocity in the solid particles impact erosion of metallic materials.* Wear, 1999. **233-235**: p. 468-475.
34. Franco, A. and S.G. Roberts, *The effect of impact angle on the erosion rate of polycrystalline α-Al_2O_3.* Journal of the European Ceramic Society, 1998. **18**(3): p. 269-274.
35. Grilec, K., L. Ćurković, I. Kumić, and G. Baršić, *Erosion mechanisms of aluminium nitride ceramics at different impact angles.* Materialwissenschaft und Werkstofftechnik, 2011. **42**(8): p. 712-717.
36. Wellman, R.G. and C. Allen, *The effects of angle of impact and material properties on the erosion rates of ceramics.* Wear, 1995. **186-187**: p. 117-122.
37. Hutchings, I.M., *A model for the erosion of metals by spherical particles at normal incidence.* Wear, 1981. **70**(3): p. 269-281.
38. Ying, G., X. He, M. Li, W. Han, F. He, and S. Du, *Synthesis and mechanical properties of high-purity Cr_2AlC ceramic.* Materials Science and Engineering: A, 2011. **528**(6): p. 2635-2640.
39. Song, G.M., Y.T. Pei, W.G. Sloof, S.B. Li, J.T.M. De Hosson, and S. van der Zwaag, *Oxidation-induced crack healing in Ti_3AlC_2 ceramics.* Scripta Materialia, 2008. **58**(1): p. 13-16.
40. Li, S., G. Song, K. Kwakernaak, S. van der Zwaag, and W.G. Sloof, *Multiple crack healing of a Ti_2AlC ceramic.* Journal of the European Ceramic Society, 2012. **32**(8): p. 1813-1820.
41. Li, S.B., L.O. Xiao, G.M. Song, X.M. Wu, W.G. Sloof, and S. van der Zwaag, *Oxidation and Crack Healing Behavior of a Fine-Grained Cr_2AlC Ceramic.* Journal of the American Ceramic Society, 2013. **96**(3): p. 892-899.
42. Farle, A.-S., C. Kwakernaak, S. van der Zwaag, and W.G. Sloof, *A conceptual study into the potential of $M_{n+1}AX_n$-phase ceramics for self-healing of crack damage.* Journal of the European Ceramic Society, 2015. **35**(1): p. 37-45.
43. *Test Method for Density Determination for Powder Metallurgy (P/M) Materials Containing Less Than Two Percent Porosity*. 1997, ASTM International: West Conshohocken, PA,.
44. Levitt, C.M., S. Chatterley, and P.J.L. Flinn, *Cutting of materials by spark erosion*. 1978, Google Patents.
45. *Standard Test Method for Conducting Erosion Tests by Solid Particle Impingement Using Gas Jets*. 2007, ASTM International: West Conshohocken, PA. p. 1-6.
46. Schneider, J.M., D.P. Sigumonrong, D. Music, C. Walter, J. Emmerlich, R. Iskandar, and J. Mayer, *Elastic properties of Cr_2AlC thin films probed by nanoindentation and ab initio molecular dynamics.* Scripta Materialia, 2007. **57**(12): p. 1137-1140.
47. Schuster, J.C., H. Nowotny, and C. Vaccaro, *The ternary systems: CrAlC, VAlC, and TiAlC and the behavior of H-phases (M_2AlC).* Journal of Solid State Chemistry, 1980. **32**(2): p. 213-219.
48. Evans, A.G. and E.A. Charles, *Fracture Toughness Determinations by Indentation.* Journal of the American Ceramic Society, 1976. **59**(7-8): p. 371-372.
49. Ramesh, C.S., S. Kumar, D.S. Devaraj, and R. Keshavamurthy, *Slurry Erosive Wear Behavior of Plasma Sprayed Inconel-718 Coatings on Al6061 Alloy.* Journal of Minerals and Materials Characterization and Engineering, 2011. **10**(05): 445.

50. Thirugnanasambantham, K.G. and S. Natarajan, *Degradation Through Erosion: Mechanistic Studies on IN-718 Superalloy Under Hot Air Jet Conditions*. Journal of Materials Engineering and Performance, 2015. **24**(7): p. 2605-2613.
51. Chen, X. and J.W. Hutchinson, *Particle impact on metal substrates with application to foreign object damage to aircraft engines*. Journal of the Mechanics and Physics of Solids, 2002. **50**(12): p. 2669-2690.
52. Li, S., L. Xiao, G. Song, X. Wu, W.G. Sloof, and S. van der Zwaag, *Oxidation and Crack Healing Behavior of a Fine-Grained Cr_2AlC Ceramic*. Journal of the American Ceramic Society, 2013. **96**(3): 892-897.

7 The effect of microstructure, erodent and thermal healing on the erosion rate of Cr_2AlC MAX phase material under high velocity particulate impact conditions

Bulk Cr_2AlC samples with grain sizes ranging from 3 µm to 22 µm were eroded at different impact velocities by either spherical micro glass beads or angular corundum particles both having a mean size of 100 µm. The erosion rate of fine grained bulk Cr_2AlC was found to be constant with time and to increase with impact velocity to the power 3.2 and 2.6 for the glass beads and the angular corundum particles respectively. The mass loss is caused by microcrack formation along grain boundaries and local spallation of the microcrack network formed below the surface. The presence of pre-existing pores accelerated the crack network formation which in turn enhanced the rate of mass loss. High temperature annealing in air resulted in a major reduction in the erosion rate, in particular for the coarse grained material having an initial porosity of 3.4%. The reduction in erosion rate is due to the formation of Al_2O_3 in the network of microcracks near the eroding surface as well as filling of the initial pores deeper inside the material.

7.1 Introduction

MAX phase ceramics have been widely explored over the past two decades as they combine the merits of metals and ceramics, e.g. good thermal and electrical conductivity, easy machinability, high hardness up to very high temperatures and high thermal shock resistance [1, 2]. Apart from these desirable conventional mechanical and physical properties, some of the MAX phase materials attracted attention because of their ability to heal micro cracks autonomously when used at high temperatures in oxygen containing atmospheres [3-5]. Ti_2AlC, Ti_3AlC_2 and Cr_2AlC are among the MAX phases capable of (multiple) healing of microcracks at the surface. This autonomous healing ability at high temperatures greatly raises the potential of these MAX phase ceramics for application in structures such as jet engine turbines operating at high temperatures and in an oxidative atmosphere.

The interior of a jet engine not only is exposed to high temperatures and high macroscopic loads but also suffers from the impact of high velocity particles such as ashes and sand particles [6-10]. The resulting erosion can lead to malfunctioning of the engine and will have serious consequences for the life time of the engine. Jet engine materials which have a so-called self-healing ability under such thermo-mechanical conditions are expected to show a much lower erosion rate as the impact-induced microcracks would heal before they link up to form a network of cracks and to fast material removal in a jet stream.

The erosion behaviour of conventional (i.e non-self-healing) ductile metallic materials and brittle ceramics has been studied for many years and showed significant differences [11-15]. In case of ductile metals and normal impact, beyond a certain impact velocity and impact energy the local deformation of the surface near the impact site leads to craters with peripheral rims which are easily lost due to spallation [16]. Hutchings presented a simple analytical model for the erosion rate based on the notion that under normal impact conditions the erosion rate is dominated by this so-called platelet formation [13]. For brittle materials normal particulate impact results in the formation of radial and lateral microcracks extending from the surface into the bulk of the sample. The propagation of such individual cracks results in the formation of a surface layer containing a network of microcracks which dictates the material removal rate. According to Evans' model the volume of removed material is related to the impact velocity v_p, the

density of the projectile $\rho_{p,}$ the particle size R_p and the toughness $K_{c,t}$ and the hardness H_t of the target material [17] in the following manner,

$$V \propto v_p^{19/6} R_p^{11/3} \rho_p^{1/4} / K_{c,t}^{4/3} H_t^{1/4} \quad (7\text{-}1)$$

Other parameters such as erodent shape and target grain size also can have significant effects on the erosion rate. It has been reported that at low impact velocities angular silica was 10 times erosive than rounded silica, while the difference dropped to a factor 1.5 at higher velocities [18]. It has also been reported for Al_2O_3 that for a fixed erodent condition, the grain size of the target material has a big effect on the erosion rate [12]. In a previous paper it has been shown that a fully dense Cr_2AlC material exposed to severe high velocity particle impact conditions will show a much reduced erosion rate in case the material was intermittently exposed to high temperature (around 1200 °C) air. The beneficial effect is due to the healing of the impact induced network of microcracks below the eroding surface.

In the present work we examine the beneficial effect of exposure to high temperature healing conditions for three Cr_2AlC grades having different grain size values as well as different intial porosity levels. Furthermore, we compare the (normal) erosion rates for spherical micro glass beads and angular corundum particles at velocities up to 130 m/s. The results are supported by detailed microstructural examinations.

7.2 Experimental details

7.2.1 Sample preparation

The coarse grained material was obtained by conventional hot pressing (HP) of Cr (particle size < 75 μm, 99.5 wt.% purity), Al (particle size < 75 μm, 99.5 wt.% purity) and Graphite (particle size < 45 μm, 99.5 wt.% purity) powders with a molar ratio of 2:1.2:1 in an Ar atmosphere at 1450 °C with a pressure of 30 MPa for 1 h [19]. The fine grained material was prepared by pressure less sintering followed by spark plasma sintering (SPS) [20]. The chromium (average particle size of about 100 μm, purity > 99.2%, TLS Technik GmbH & Co., Germany), aluminium (average particle size of about 45 μm, purity > 99.8%, TLS Technik GmbH & Co., Germany) and graphite (average particle size of 6 μm, purity > 99.5%, Graphit Kropfmühl AG, Germany) powders having a molar ratio of

2:1.15:1, respectively, were mixed for 24 hours in a Turbula T2C mixer (Willy A. Bachofen, Switzerland) using Zirconia balls. Then, the powder mixture was cold pressed into tablets with a diameter of 25 mm and a thickness of about 5 mm with a Carver press (Model 3853-0, USA). These tablets were pressure-less sintered (PLS) in a flow of 500 sccm Argon (purity <5N) for 1 hour at 1400 °C in a horizontal alumina tube furnace (Lenton Furnaces, PTF 16/75/610, UK) with an inner tube diameter of 80 mm. The tablets were placed on graphite boats and the furnace was heated at 5 °C/min. Next, the PLS samples were pulverized (using a Fritsch Pulverisette, Germany) and ball milled with 10 mm WC balls and a WC jar (250 ml) for 1 hour effectively using a PM100 ball grinder (Retsch GmbH, Germany). The Cr_2AlC powder obtained had a particle size around 4 μm and was phase-pure according to an X-ray diffraction analysis. The Cr_2AlC powder was densified with SPS (HP D 25, FCT Systeme GmbH, Frankenblick, Germany) at a pressure of 50 MPa and a heating rate of 50 °C/min. The powder was put into a graphite mold with an inner diameter of 20 mm. Graphite paper and BN spray (Henze, HeBoCoat® 21E, Germany) was used to minimize sticking of the powder to the mould. After the SPS treatment the thickness of the sample was about 7 mm.

The bimodal grained sample was obtained by direct SPS processing starting from Cr and Al_4C_3 powders with a molar ratio of 6:1. The Cr and Al_4C_3 powder were mixed and ball milled in a WC jar in a protective atmosphere of Ar at a rotating speeding of 300 rpm for 4 hours. Then, the ball milled mixture was sintered with SPS (HP D 25, FCT Systeme GmbH, Frankenblick, Germany) at a pressure of 50 MPa and a heating rate of 50 °C/min to 1250 °C for 1 hour in argon atmosphere.

All bulk materials were cut into 2 mm thick discs with a diameter of 10 mm. Prior to further testing the surfaces were ground using SiC emery paper (4000 mesh grits), ultrasonically cleaned in ethanol and dried with a jet of dry pure nitrogen.

7.2.2 Characterisation technique

The crystal structure of bulk Cr_2AlC samples was analysed with X-ray diffraction (Bruker D8, Germany) using Co Kα radiation. The diffractograms were recorded over the range from 10 to 130 °2θ with a step size 0.034 °2θ and a counting time of 2 s per step. Bruker software Diffrac EVA 3.1 was employed to evaluate the diffraction data.

The microstructure of the virgin material and that of samples exposed to erosion and oxidation was observed with a scanning electron microscopy (SEM) equipped with a field emission gun (JEOL, JSM 6500F, Japan). Cross sections were prepared by cutting with a diamond wafer blade. Prior to grinding and polishing the sample was covered with a thin copper film (~ 0.5 μm) and a silicon wafer was glued on top of the copper layer to conserve the surface during sample preparation. The SEM was equipped with an energy dispersive spectrometer (EDS, Thermo-Noran, UltraDry, USA) for X-ray microanalysis (XMA) and a detector for backscattered electrons to observe local compositional variations (Autrata, Czech Republic). The scanning electron microscope was also fitted with a HKL Nordlys II detector (Oxford Instruments, UK) for electron backscattering diffraction (EBSD). The EBSD data acquisition and processing was performed using Channel 5 software (version 2011).

An ion beam polisher (CP, JEOL, SM-09010, Japan) was used to make high quality smooth cross-sections of the eroded sample for microstructure characterization.

The hardness of bulk Cr_2AlC was measured with Vickers indentation (Zwick/Z2.5, Germany) at a load of 20 N for 10 s using a loading rate of 2 N/s. The fracture toughness was calculated from the load dependence of the indentation induced cracks for loads varied between 50 N to 500 N. The nano hardness of the fine grained and coarse grained Cr_2AlC was measured with a nano-indenter (MTS G200) using a Berkovich indentor and a maximal indentation depth of 1 μm.

The porosity was estimated by determining the pore area fraction from 2D SEM images. The healing was carried out at 1200 ºC in quasi-static air using an alumina tube furnace (Nabertherm RHTH 120-600/16, Germany) having an inner diameter of 35 mm.

7.2.3 Erosion test set up

The erosion tests were executed at room temperature according to ASTM G76 [21] with some modifications as specified below. The erosion test rig consisted of an erosion sample chamber and a high precision powder feeder (Castolin Eutectic, EP2, Switzerland). The abrasive particles were accelerated using compressed air and were directed perpendicular to the sample surface. In this study spherical glass micro-beads (DIN 8201) having a hardness of about 8 GPa and corundum angular particles with a hardness of 10

GPa both with a mean diameter of 100 µm were used. In all experiments a particle flux of 2 g/ min or 5 g/min was used.

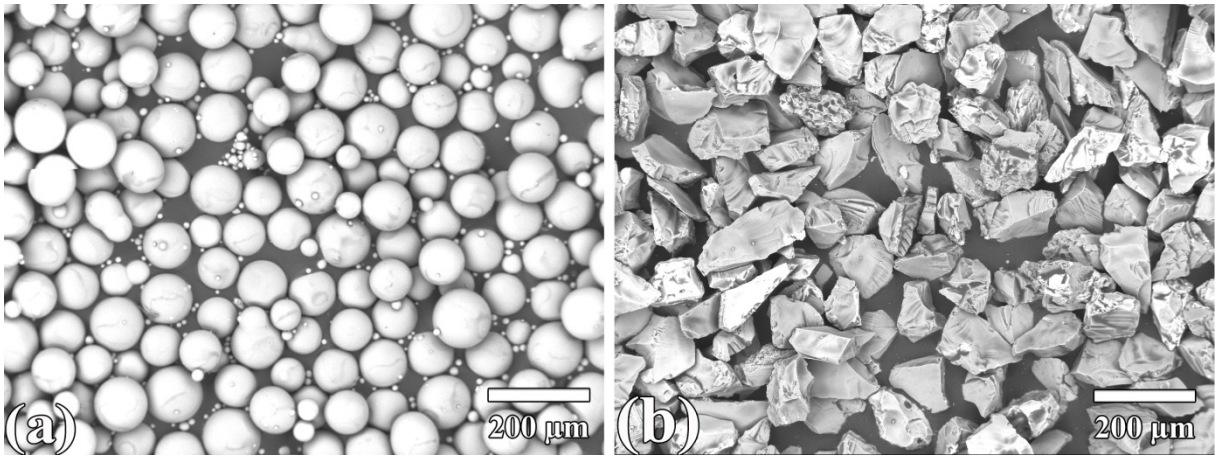

Figure 7.1 BSE images of (a) spherical micro glass beads and (b) angular corundum particles with an average diameter of 100 µm.

Figure 7.1 shows back scattering electron images of both erodents and shows that for both erodents the shape is different but well defined and that from an impact energy perspective both particle size distributions are effectively rather monodisperse, as the fraction of very small silica spheres will not affect the erosion behaviour.

The nozzle had a length of 50 mm and an inner diameter of 2 mm. The distance between the nozzle outlet and the sample surface was 10 mm. The erosion conditions resulted in an erosion crater with a diameter of about 6 mm. The particle velocity at different air pressures was measured with Particle Image Velocimetry (PIV) using a high-speed camera (Dantec Dynamics, Denmark). The erodent particles were accelerated to fixed velocities between 50 m/s and 130 m/s and impinged the target perpendicularly. To determine the erosion rate, the mass change after a fixed erosion time and standardized sample cleaning to remove adherent particles was measured using an analytical balance (Mettler Toledo XS105DU, Switzerland) with a resolution of 0.01 mg. For each condition three weight measurements were made.

7.3 Results and discussion

7.3.1 Composition, microstructure, hardness and toughness of Cr_2AlC

XRD analysis did show that for all three material grades the materials produced were almost pure Cr_2AlC with only trace amounts of Al_2O_3 and Cr_7C_3 being present. The three Cr_2AlC grades produced differed significantly in microstructure and hence in mechanical properties.

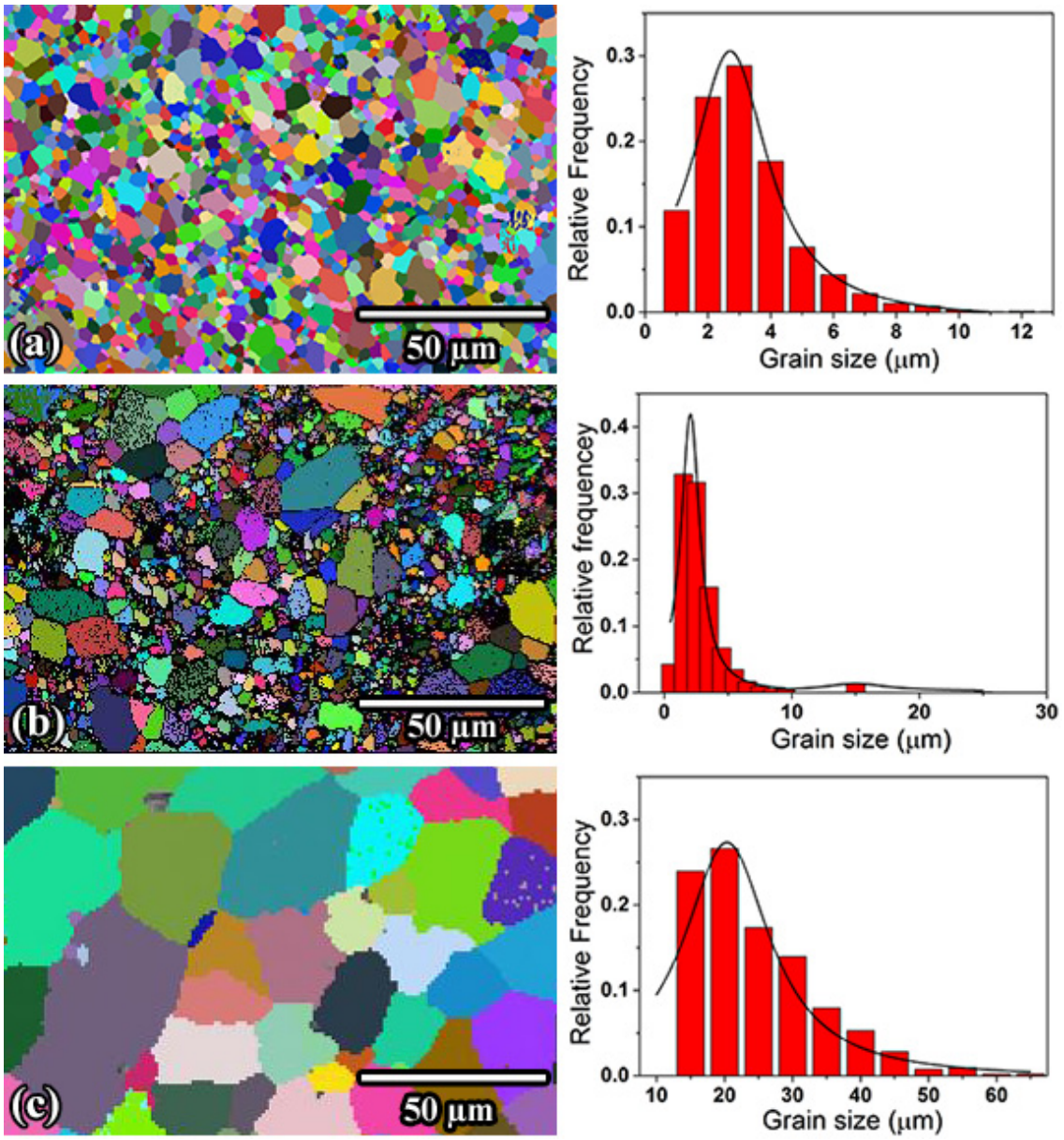

Figure 7.2Euler maps and grain size distribution graphs of (a) fine-grained, (b) bimodal -grained and (c) coarse-grained Cr_2AlC.

Figure 7.2 shows the Euler maps for the three material grades as well as the grain size distributions derived thereof. The HP grade had the largest grain size (average size of 22 ± 9 μm) and is denoted as coarse-grained (CG). The PLS-SPS grade is a fine-grained (FG) material with a grain size around 2.7 ± 1.4 μm. The direct SPS grade material contains a low fraction 1.5 % of coarse grains varying from 10 to 35 μm in diameter and a much larger volume fraction of fine grains with a diameter around 3 μm. This Cr_2AlC grade is referred to as bimodal grained (BM).

The porosity of FG, BM and CG sample based on 2D SEM images was evaluated to be 0.6 vol %, 1.0 vol % and 3.4 vol %respectively. The Vickers hardness indentation values of the three grades are listed in Table 7-1 The hardness of the fine-grained sample is 6.0 ± 0.1 GPa, which is almost double that of the coarse grained material 3.7 ± 0.4 GPa. For the bimodal sample the hardness is 5.5 ± 0.2 GPa which given the microstructure shown in Figure 7.2 is as expected. The nano-indentation test showed that the local hardness varies with the grain size and the differences are in accordance with the Vickers micro hardness data.

Table 7-1Properties of fine-grained (FG), bimodal-grained (BM) and coarse-grained (CG) Cr_2AlC.

Material	Porosity (%)	Hardness (GPa)	Fracture toughness ($MPa \cdot m^{1/2}$)
FG	0.6	6.0 ± 0.1	3.5 ± 0.1
BM	1.0	5.5 ± 0.2	3.6 ± 0.1
CG	3.4	3.7 ± 0.4	6.2 [20]

The fracture toughness values, as determined by the load dependence of indentation induces radial crack lengths, were 3.5 ± 0.1 and 3.6 ± 0.1 $MPa \cdot m^{1/2}$ for the fine-grained and bimodal sample, respectively [22]. Vickers indentations on the coarse-grained material did not lead to well-developed radial cracks extending along the diagonal of the indent and the indentation led to primarily to local plastic deformation. The absence of such indentation induced cracks suggests that the fracture toughness of the coarse grained material is higher than that of the two other Cr_2AlC grades. Based on literature data for a

30 µm grain size Cr_2AlC grade [19] we estimate the fracture toughness of this material to be around 6 MPa.$m^{1/2}$.

7.3.2 Erosion rates of as-produced Cr_2AlC as a function of the erodent type and target material properties

7.3.2.1 Effect of erodent type

Beyond a certain incubation time the erosion rate of fine-grained Cr_2AlC was found to be constant with erosion time. The erosion rates for angular corundum particles and spherical micro glass beads over a 60 min. period as a function of the impact velocity are displayed in Figure 7.3.

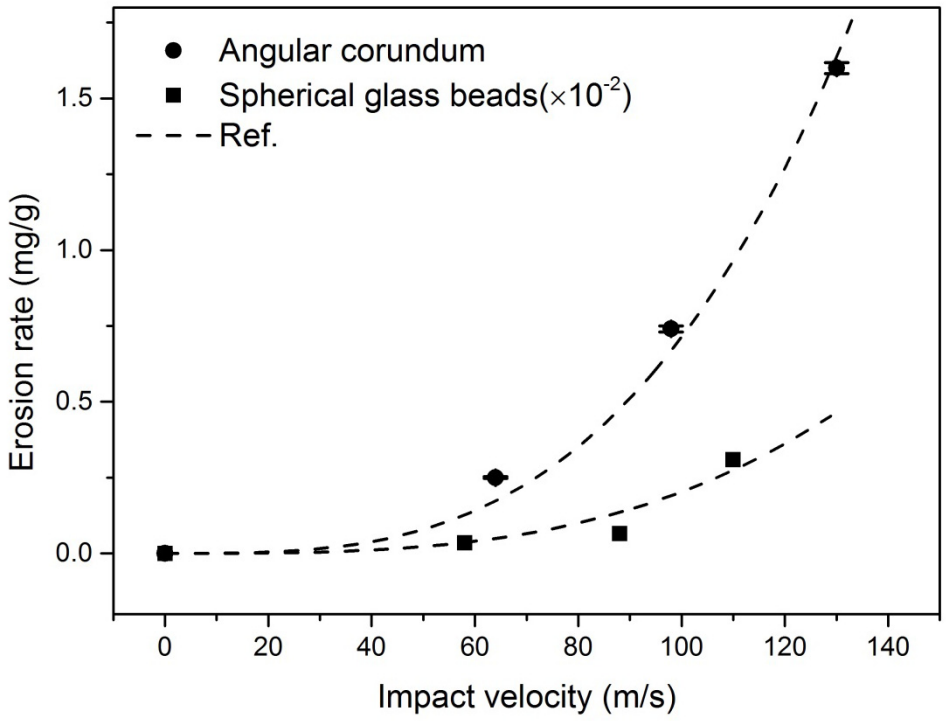

Figure 7.3 Correlation between erosion rate and impact velocity of fine grained Cr_2AlC under normal impact with angular corundum with a flux of 2 g/min at a velocity of 130 m/s, 98 m/s and 64 m/s and with micro glass beads under 110 m/s, 88 m/s and 58 m/s with a flux of 5 g/min respectively. The Evans model was fitted to the data points making the exponent the free variable (see text for details).

It is clear that the angular corundum particles are much more erosive than the spherical micro glass beads (note that the erosion rates for the spherical beads are magnified by a factor 100 to fit on the same scale). The erosion rate is only 0.02 mg/g when eroded with 110 m/s micro glass beads, which is negligible compared to the erosion rate when eroded

with corundum at the same speed, namely 1 mg/g. For the angular particles, the correlation between erosion rate and impact velocity has a an exponent of 2.6 (solid line) instead of the nominal value of 3.2 (19/6, see Eq.(7-1)). For the velocity dependence of the erosion due to spherical bead impact the exponent was 3.2.

The SEM images of eroded surfaces showthat the surface is much rougher after impact by corundum particles; see Figure 7.4.

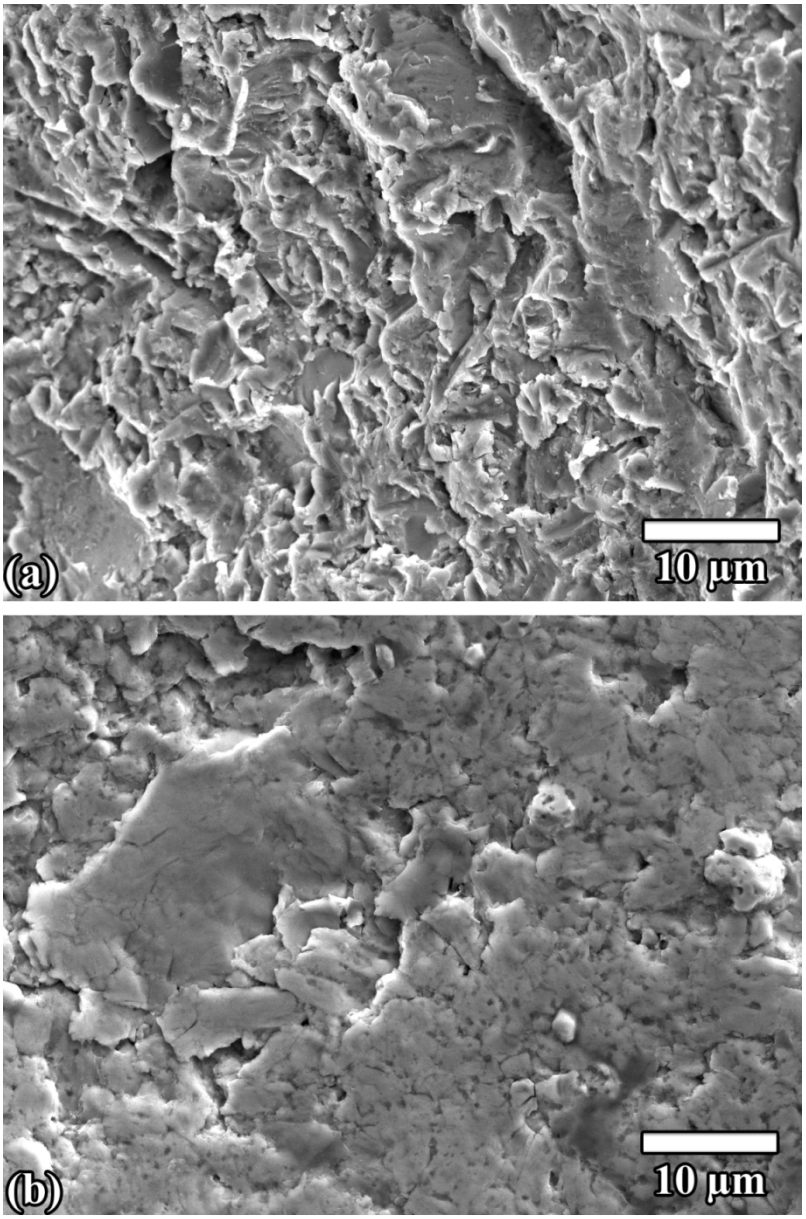

Figure 7.4 Eroded surface morphology of fine-grained Cr_2AlC after erosion for 60 min. with (a) 2 g/min angular corundum at 130 m/s, and (b) 5 g/min micro glass beads at 110 m/s.

This is due to thesharp edges of the corundum particles, which makes it easier to initiate cracks upon impact. The fact that angular corundum particles cause more severe erosive damage than spherical glass beads is in agreement with Hutchings' findings [18].

7.3.2.2 Effect of target materials properties.

Generally, the erosion rate also depends on the hardness and fracture toughness of the target material. This is also observed for the erosion behavior of Cr_2AlC under normal impact with micro glass beads at a velocity of 110 m/s. The steady state erosion rate of the coarse grained (CG) material is around 3 mg/g, which is much higher than that of the fine-grained (FG) material and the bimodal-grained (BM) material, namely 0.04 and 0.10 mg/g, respectively. The surface morphology of the three grades of Cr_2AlC after impact for 60 minutes with micro glass beads at a velocity of 110 m/s is rather different; see Figure 7.5.

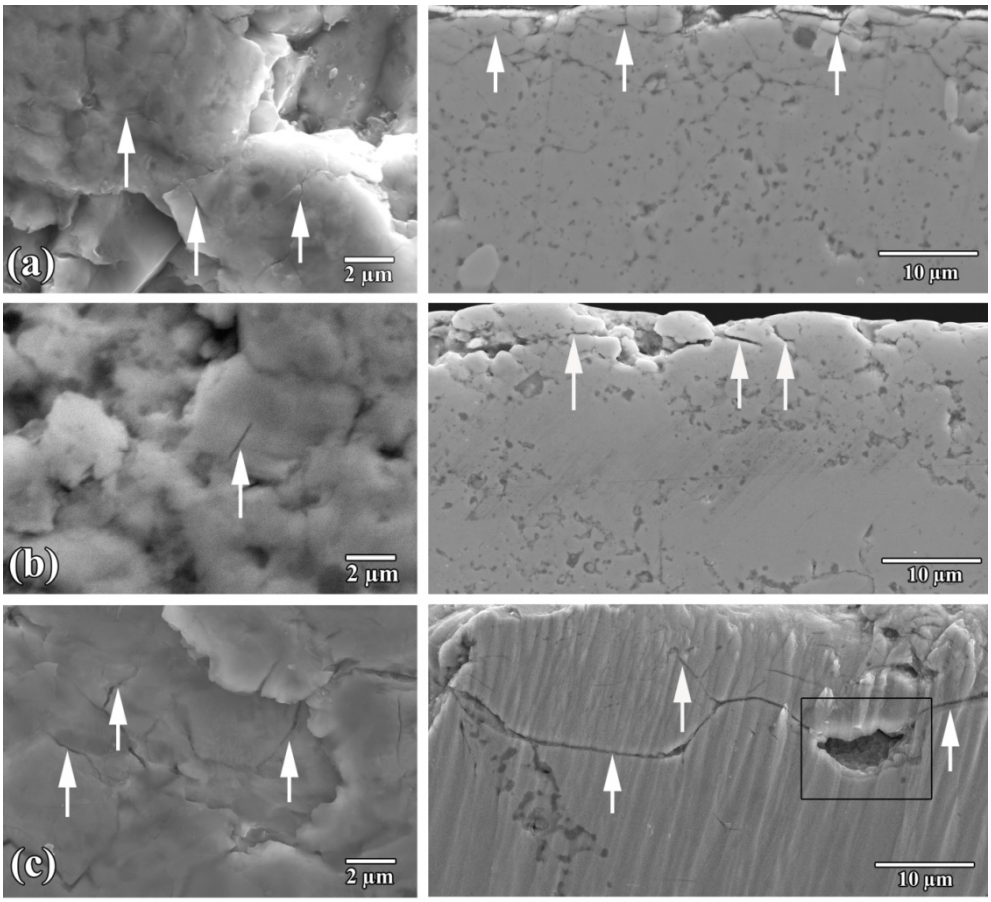

Figure 7.5 SEM images of surfaces (left) and cross section (right) after erosion at 110 m/s with a flux of 2 g/min on (a) fine-grained, (b) bimodal-grained with 100 µm micro glass beads and (c) coarse-grained Cr_2AlC with 50 µm micro glass beads. Arrows indicate microcracks generated upon impact, the pores in the coarse grained Cr_2AlC are within the black rectangle.

The surface of the more ductile coarse-grained material was primarily plastically deformed, while the surface of fine- and bimodal-grained material showed an increased roughness. However, the surfaces of all three grades showed the same type of micro cracks with a width of about 100 nm wide. A network of cracks was clearly identified underneath the surface of the eroded samples; see Figure 7.5. After impact with glass beads at 110 m/s and 2 g/min the network of cracks extends to around 7 µm below the surface for the fine- grained and the bimodal sample and to 20 µm for coarse grained sample.

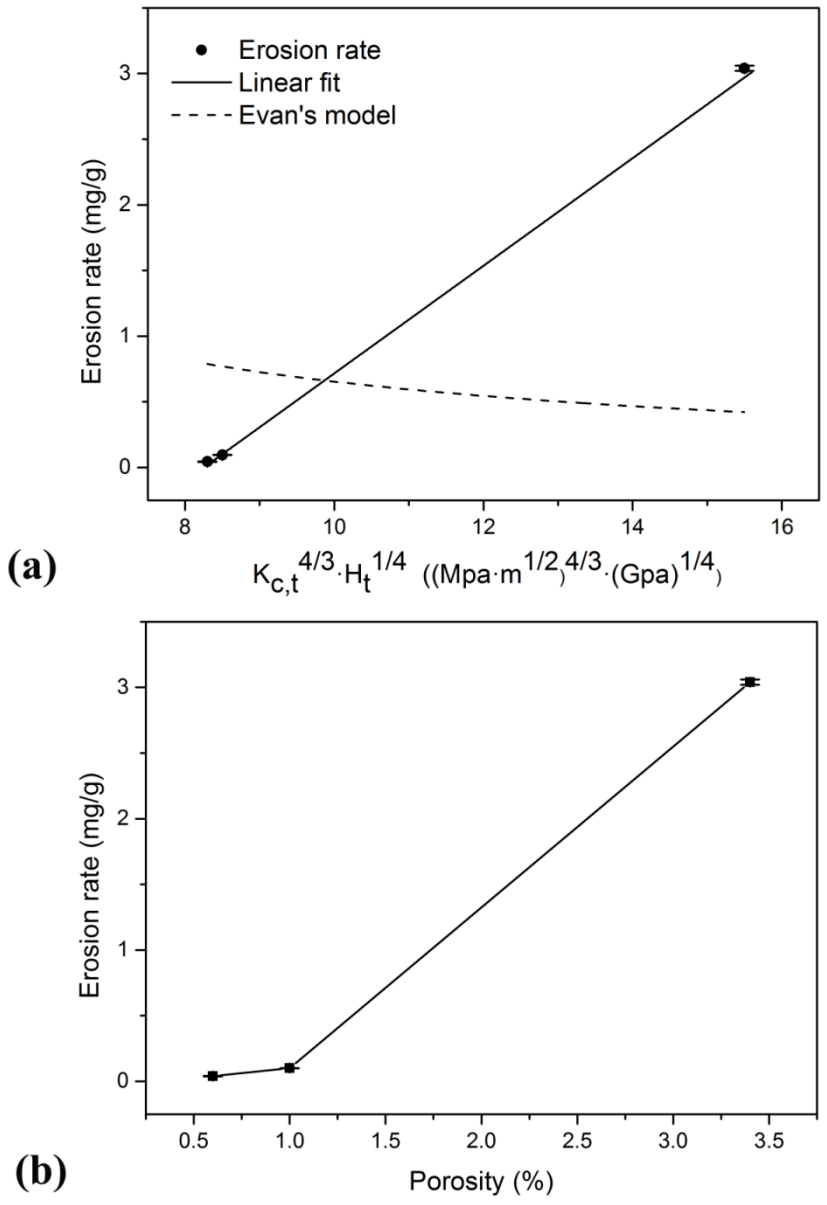

Figure 7.6 Erosion rate as a function of material property factor (product of toughness and hardness,) (a), and as a function of porosity (b). The material properties dependence according to the Evans' model is indicated by a dashed line in figure a).

Based on Evans' model the erosion rate should be inversely proportional to fracture toughness and hardness to the power of 4/3 and 1/4, respectively. However, in Figure 7.6 (a) it can been seen that the erosion rate increases with increasing value of the product of fracture toughness and hardness ($K_{c,t}^{4/3} \cdot H_t^{1/4}$) (solid line) which is in contradiction to Evans' prediction (dash line). However, the erosion scales well with the porosity level, see Figure 7.6 (b). This dependence can be explained as follows: The erosion induced cracks propagate mainly along the grain boundaries where most of the porosity is present as can be seen in Figure 7.5. The impact induced microcracks therefore link up easily with the pores and therefore propagate further along the grain boundaries and deeper into the material. Since the coarse-grained material is more porous than the fine-grained material and has longer grain boundaries, the erosion (breakaway of material) of the coarse-grained Cr_2AlC is more severe. The higher erosion rate of the bimodal-grained material compared with that of fine-grained material is also due to the higher porosity in combination with the fraction of coarse grains being present, as the material property factor ($K_{c,t}^{4/3} \cdot H_t^{1/4}$) for both fine- and bimodal-grained material is almost the same; see Figure 7.6 (a).

7.3.3 Effect of high temperature oxidation on erosion rate.

Microcracks generated in Cr_2AlC by high velocity particle impact under erosive conditions can be healed by high temperature oxidation [23]. Due to the healing reaction the cracks are filled with fine alumina grains which are strongly bonded to the Cr_2AlC matrix. This filling of the crack with a strong and well-bonded ceramic deposit leads to restoration of the material integrity. This oxidation induced self-healing of fine grained and coarse-grained Cr_2AlC was studied with cyclic erosion – healing experiments consisting of 10 to 60 minutes erosion testing with micro glass beads under a flux of 2 g/min and an impact velocity of 110 m/s and for 10 min healing at 1200 ºC in air. As shown in Figure 7.7 (a), the erosion rate is retarded after healing as indicated by the blue lines and returns to its original value at steady state erosion. The erosion rate is evaluated to be around 0.01 mg/g, see red lines in Figure 7.7 (a). A reduction of the erosion rate is observed after each oxidation treatment, which is in agreement with our previous study [23]. The erosion rate of the coarse grained sample decreased gradually after successive erosion and healing cycles; see Figure 7.7 (b).

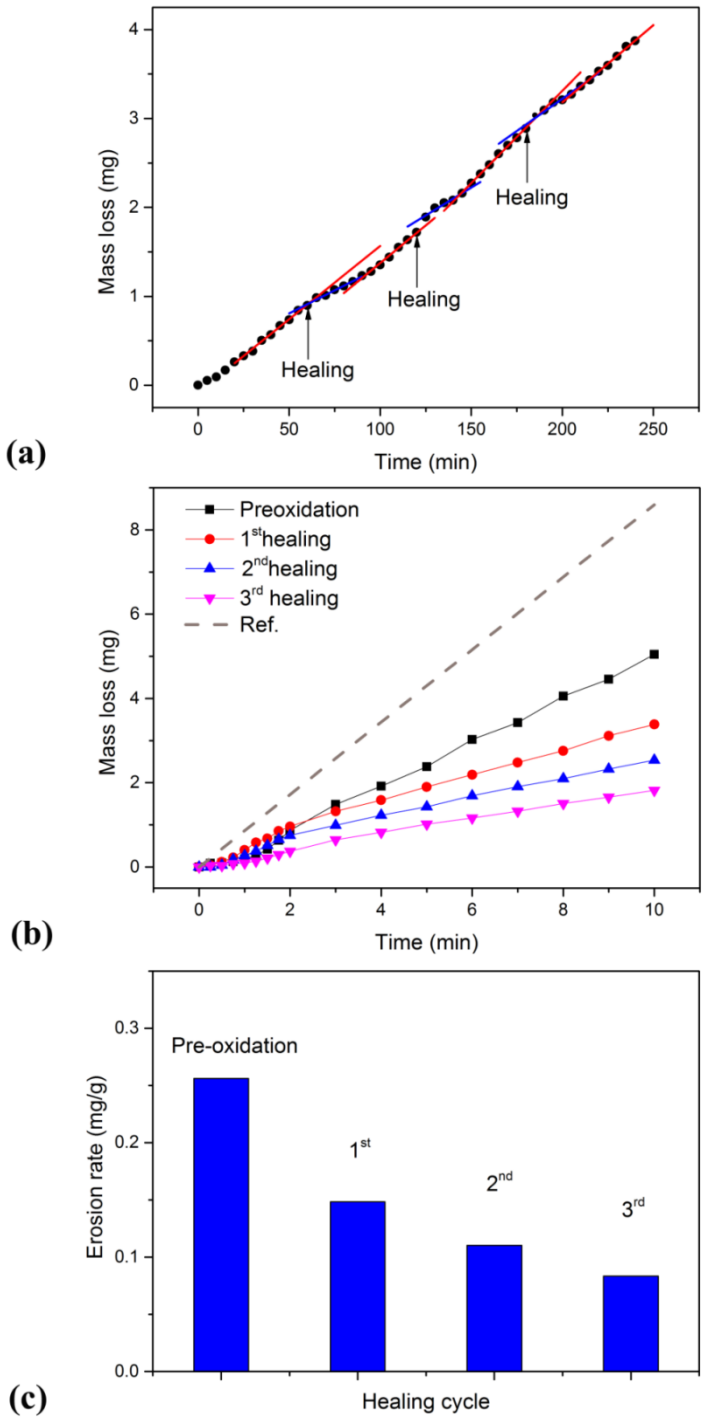

Figure 7.7Mass loss of (a) fine grained and (b) coarse-grained Cr_2AlC as a function of erosion time due to impact of 100 µm micro glass beads at 110 m/s and 2 g/min. After each erosion cycle a healing treatment was executed at 1200 °C in air for 10 min. The coarse-grained Cr_2AlC was oxidized at 1200 °C in air for 10 min. prior to the cyclic erosion test. The dash line shows the erosion rate of the as produced coarse-grained Cr_2AlC. (c) Change of erosion rate of the coarse-gained Cr_2AlC after pre-oxidation and each healing treatment.

The erosion rate of virgin materials under this condition was evaluated to be around 0.43 mg/g. By applying an oxidation treatment at 1200 °C for 10 minutes prior to erosion, the initial erosion rate was reduced by 40 % to 0.26 mg/g as can be seen in Figure 7.7. The successive reduction of the erosion rate of this material after high temperature oxidation is due to filling of the pre-existing pores by alumina (Al_2O_3); see Figure 7.8.

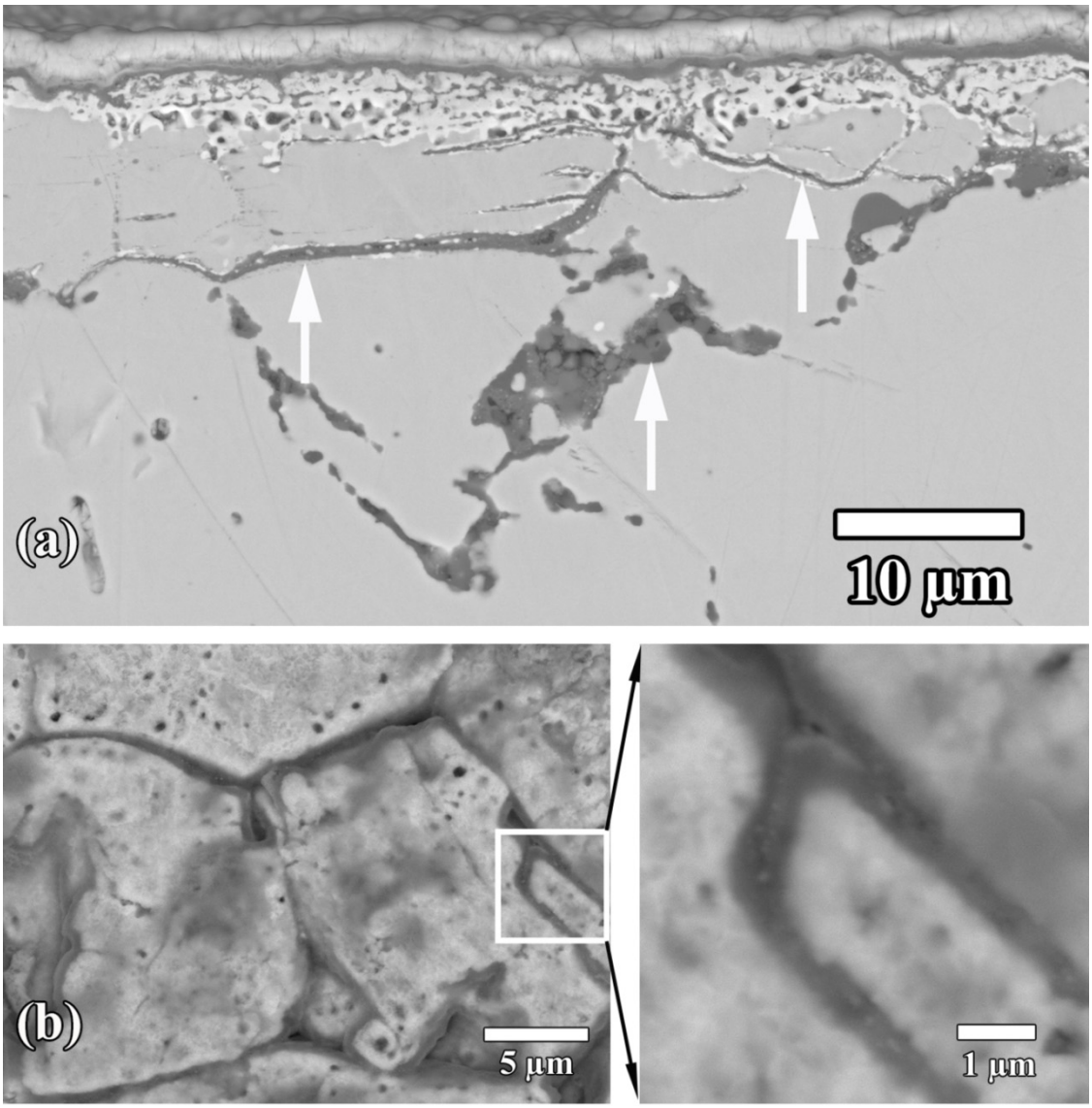

Figure 7.8 BSE images of eroded coarse-grained Cr_2AlC after healing at 1200 °C in air for 10 min. (a) Cross section with a Cr layer deposited on the surface for sample preparation. The arrows indicated the filled crack gaps and pores with Al_2O_3 (b) Top view with an enlarged section. The surface was sputtered with Ar-ions to remove the surface oxide and reveal the healed cracks.

Thus not only the network of cracks, but also the porosity, which is responsible for the high erosion rate (see Section 3.2), is 'healed' by the high temperature oxidation treatment; see Figure 7.8. The filling of the pores with alumina reduces the coalescence of

lateral cracks and increases the local hardness by 24 %. In contrast to the results in the previous chapter the erosion rate remained low even after eroding away the healed network of cracks. The longer lasting improvement of the erosion resistance by a thermal treatment is the result of the healing of the preexisting pores.

7.4 Conclusions

The erosion behavior of three grades of Cr_2AlC with different grain size distributions, hardness, fracture toughness as well as porosity values were eroded with spherical micro glass beads and angular corundum particles. The erosion mass loss was linear with erosion time and the erosion rate increased with impact velocity having an exponent of 2.6 and 3.2 for fine-grained Cr_2AlC when eroded with corundum particles and glass beads respectively. The erosion induced microcracks propagated along the grain boundaries and coalesced to form a network of microcracks, which led to the more severe mass mass loss for the coarse-grained Cr_2AlC than for the fine-grained Cr_2AlC. The observed dependence of erosion rate on initial mechanical properties such as hardness and fracture toughness deviated strongly from the dependence predicted by the Evans' model for fully dense material. The deviation was attributed to pre-existing pores promoting the microcrack propagation. Upon healing at 1200 ºC in air the erosion induced microcracks as well as the initial pores were filled with oxide Al_2O_3. The healing of pre-existing pores as well as erosion induced cracks led to a significant reduction in the erosive wear loss.

References

1. Barsoum, M.W. and M. Radovic, *Elastic and Mechanical Properties of the MAX Phases*, in *Annual Review of Materials Research, Vol 41*, D.R. Clarke and P. Fratzl, Editors. 2011, Annual Reviews: Palo Alto. p. 195-227.
2. Farle, A.-S., C. Kwakernaak, S. van der Zwaag, and W.G. Sloof, *A conceptual study into the potential of $M_{n+1}AX_n$-phase ceramics for self-healing of crack damage.* Journal of the European Ceramic Society, 2015. **35**(1): p. 37-45.
3. Li, S., G. Song, K. Kwakernaak, S. van der Zwaag, and W.G. Sloof, *Multiple crack healing of a Ti_2AlC ceramic.* Journal of the European Ceramic Society, 2012. **32**(8): p. 1813-1820.
4. Li, S., L. Xiao, G. Song, X. Wu, W.G. Sloof, and S. van der Zwaag, *Oxidation and Crack Healing Behavior of a Fine-Grained Cr_2AlC Ceramic.* Journal of the American Ceramic Society, 2013.
5. Song, G.M., Y.T. Pei, W.G. Sloof, S.B. Li, J.T.M. De Hosson, and S. van der Zwaag, *Oxidation-induced crack healing in Ti_3AlC_2 ceramics.* Scripta Materialia, 2008. **58**(1): p. 13-16.

6. Chen, X. and J.W. Hutchinson, *Particle impact on metal substrates with application to foreign object damage to aircraft engines.* Journal of the Mechanics and Physics of Solids, 2002. **50**(12): p. 2669-2690.
7. Chen, X., R. Wang, N. Yao, A.G. Evans, J.W. Hutchinson, and R.W. Bruce, *Foreign object damage in a thermal barrier system: mechanisms and simulations.* Materials Science and Engineering: A, 2003. **352**(1-2): p. 221-231.
8. Wellman, R.G. and J.R. Nicholls, *A review of the erosion of thermal barrier coatings.* Journal of Physics D: Applied Physics, 2007. **40**(16): p. R293.
9. Drexler, J.M., A.D. Gledhill, K. Shinoda, A.L. Vasiliev, K.M. Reddy, S. Sampath, and N.P. Padture, *Jet engine coatings for resisting volcanic ash damage.* Adv Mater, 2011. **23**(21): p. 2419-2424.
10. Krause, A.R., B.S. Senturk, H.F. Garces, G. Dwivedi, A.L. Ortiz, S. Sampath, N.P. Padture, and D.J. Green, *$2ZrO_2{\cdot}Y_2O_3$Thermal Barrier Coatings Resistant to Degradation by Molten CMAS: Part I, Optical Basicity Considerations and Processing.* Journal of the American Ceramic Society, 2014. **97**(12): p. 3943-3949.
11. Aquaro, D. and E. Fontani, *Erosion of Ductile and Brittle Materials.* Meccanica, 2001. **36**(6): p. 651-661.
12. Franco, A. and S.G. Roberts, *The effect of impact angle on the erosion rate of polycrystalline α-Al_2O_3.* Journal of the European Ceramic Society, 1998. **18**(3): p. 269-274.
13. Hutchings, I.M., *A model for the erosion of metals by spherical particles at normal incidence.* Wear, 1981. **70**(3): p. 269-281.
14. Oka, Y.I., M. Matsumura, and T. Kawabata, *Relationship between surface hardness and erosion damage caused by solid particle impact.* Wear, 1993. **162-164**: p. 688-695.
15. Routbort, J.L. and R.O. Scattergood, *Solid Particle Erosion of Ceramics and Ceramic Composites.* Key Engineering Materials, 1992. **71**: p. 23-50.
16. Bitter, J.G.A., *A study of erosion phenomena: Part II.* Wear, 1963. **6**(3): p. 169-190.
17. Evans, A.G., M.E. Gulden, and M. Rosenblatt, *Impact Damage in Brittle Materials in the Elastic-Plastic Response Regime.* Proceedings of the Royal Society A: Mathematical, Physical and Engineering Sciences, 1978. **361**(1706): p. 343-365.
18. Hutchings, I.M., *Transitions, Threshold Effects and Erosion Maps.* Key Engineering Materials, 1992. **71**: p. 75-92.
19. Yu, W., S. Li, and W.G. Sloof, *Microstructure and mechanical properties of a $Cr_2Al(Si)C$ solid solution.* Materials Science and Engineering: A, 2010. **527**(21–22): p. 5997-6001.
20. Duan, X., L. Shen, D. Jia, Y. Zhou, S. van der Zwaag, and W.G. Sloof, *Synthesis of high-purity, isotropic or textured Cr_2AlC bulk ceramics by spark plasma sintering of pressure-less sintered powders.* Journal of the European Ceramic Society, 2015. **35**(5): p. 1393-1400.
21. *Standard Test Method for Conducting Erosion Tests by Solid Particle Impingement Using Gas Jets*. 2007, ASTM International: West Conshohocken, PA. p. 1-6.
22. Chermant, J.L., A. Deschanvres, and F. Osterstock, *Toughness and Fractography of TiC and WC.* Fracture Mechanics of Ceramics, 1978. **4**: p. 891-901.

23. Shen, L., D. Eichner, S. van der Zwaag, C. Leyens, and W.G. Sloof, *Reducing the erosive wear rate of Cr_2AlC MAX phase ceramic by oxidative healing of local impact damage.* Wear, 2016. **358–359**: p. 1-6.

8 Demonstrating the self-healing behaviour of some selected ceramics under combustion chamber conditions

Closure of surface cracks by self-healing of conventional and MAX Phase ceramics under realistic turbulent combustion chamber conditions is presented. Three ceramics namely; Al_2O_3, Ti_2AlC and Cr_2AlC are investigated. Healing was achieved in Al_2O_3 by even dispersion of TiC particles throughout the matrix as the MAX phases, Ti_2AlC and Cr_2AlC exhibit intrinsic self-healing. Fully dense samples (> 95 %) were sintered by spark plasma sintering and damage was introduced by indentation, quenching and low perpendicular velocity impact methods. The samples were exposed to the oxidizing atmosphere in the post flame zone of a turbulent flame in a combustion chamber to heal at temperatures of approx. 1000 °C at low pO_2 levels for 4 hours. Full crack-gap closure was observed for cracks up to 20 mm in length and more than 10 µm in width. The reaction products (healing agents) were analysed by SEM, XMA and XRD. A semi-quantification of the healing showed that cracks in Al_2O_3/TiC composite (width 1 µm and length 100 µm) were fully filled with TiO_2. In Ti_2AlC large cracks were fully filled with a mixture of TiO_2 and Al_2O_3. And in the Cr_2AlC, cracks of up to 1.0 µm in width and more than 100 µm in length were also completely filled with Al_2O_3.

8.1 Introduction

In recent years the possibility to oxidatively heal surface cracks in high temperature ceramics and metallo-ceramics and to restore mechanical strength at least once has been demonstrated in quite a number of laboratory studies [1-3]. In these laboratory studies relatively high oxygen potentials (comparable to those in heated air) and stagnant air were imposed and the samples were not exposed to any mechanical vibration during the healing treatment. These conditions differ significantly from the prevailing conditions (low partial pressure, very high gas flow velocities and extensive mechanical vibrations) in combustion chambers, where such self-healing ceramics are supposed to be used [4]. The work presented here describes the self-healing behaviour of three grades of self-healing ceramics under realistic combustion chamber conditions. The materials to be tested are an extrinsic self-healing system (alumina containing TiC particles as healing agent) and two intrinsic self-healing metallo-ceramics (Cr_2AlC and Ti_2AlC), for which attractive self-healing behaviour under laboratory conditions had been demonstrated previously.

The early research on self healing high temperature ceramics focussed on so-called *extrinsic* self-healing concepts, in which the crack filling reaction is due to the presences of discrete reactive particles homogeneously distributed in an inert ceramic matrix [4-6]. When a crack is formed in the matrix, the reactive particles in the path of the crack are dissected and oxygen from the environment flowing through the crack can react with the healing particle. In case the reaction product has a larger specific volume than the original particle the excess volume can fill the crack and restore mechanical contact between both opposing crack faces. In case the reaction product adheres relatively well to the matrix material, the filling of the crack not only leads to its sealing but also to the restoration of the tensile strength of the once broken sample. The early work focused on the use of SiC particles or fibres to heal Si_3N_4, mullite and alumina matrices [5, 7, 8] as SiC has a desirable oxidation behaviour leading to the formation of SiO_2 which has a good bond strength to many ceramic matrices. By using SiC particles with a size of about 0.3 µm the bending strength of Si_3N_4/SiC composites could be recovered more or less completely by healing between 900–1400 °C for 1 hour in air. For the optimum healing temperature of 1300 °C the specimen fractured even outside the healed zone [5]. Similarly, surface cracks of diameter 100-200 µm in mullite were completely healed after heat treatment at

1300 °C for 1 h in air. The crack-healed zone even had a bending strength 150 ± 30 MPa higher than that of the as received material [7].

The optimal volume fraction of granular healing particles was found to be between 15 and 30 % [9-11]. In recent work it has been shown that SiC whiskers rather than granular SiC particles can improve the healing capabilities even further [8] and restore not only strength but also fracture toughness. It was shown that surface cracks with a length of 100 μm could be healed in a composite containing 20 vol. % of 30 -100 μm long SiC whiskers. The fracture toughness increased from 3-4 MPa $m^{1/2}$ for monolithic alumina to 5.6 MPa $m^{1/2}$, and it was reported that the average bending strength after healing is 970 MPa as compared to 1000 MPa for the virginal material. Since then, systematic studies have been done on the effect of crack healing conditions on the mechanical behavior of the crack healed zone [4, 12] the maximum crack size which can completely be healed [13] and the crack healing behavior under static or cyclic loading and crack healing potential [5, 14].

While SiC additions work rather well, the temperature to induce optimal healing is rather high (1300 °C) and there is a need for lower healing temperatures. TiC has recently been identified and an attractive alternative [15]. The potential of TiC in healing alumina was assessed based on detailed theoretical analysis of the healing reaction and the intrinsic properties of the reaction products TiO_2 (rutile). A systematic analysis of its thermodynamic stability, relative volume expansion, work of adhesion between the healing agent and the matrix, and a comparison of the coefficient of thermal expansion between the matrix and the healing oxide revealed TiC is indeed a potentially attractive healing particle for extrinsic self-healing ceramic systems. Experimentally this was proven when surface cracks of length 100 μm in Al_2O_3-TiC composites containing 30 vol.% TiC particles showed complete tensile strength recovery by annealing for 1 hour at 800 °C in air.

The alternative approach to *extrinsic* self-healing systems in which the healing reaction is due to the intentional addition of a sacrificial phase is that of *intrinsic* self-healing systems in which the material itself can locally undergo healing reactions. In 2008 metallo-ceramic MAX phases, in particular Ti_3AlC_2, were shown to demonstrate significant self-healing when exposed to high temperatures in oxygen containing atmospheres [16, 17]. The underlying mechanism in the healing reaction is the selective

oxidation of the A element in the MAX phases, such as Ti_3AlC_2 and Ti_2AlC as well as Cr_2AlC [16, 18, 19]. Cracks in Ti_2AlC MAX phase ceramics of up to some millimetres in length and about 5 µm in width can be healed by oxidation at 1100 °C in air within 2 hours [17, 20] leading to full strength recovery. Also cracks running along the same path as previously healed cracks can be restored several times [17]. The healing is due to the extensive formation of Al_2O_3 in the crack with minor amounts of the weaker TiO_2 phase. Cr_2AlC MAX phase also shows good self-healing behaviour but the reaction rates are a bit slower. Yet the guaranteed absence of the weak TiO_2 in the healed cracks may lead to higher strength values for the healed material [21]. Hence Ti_2AlC and Cr_2AlC were selected for testing under combustion chamber conditions as both materials meet all requirements postulated for successful healing of crack damage [22], e.g. preferential oxidation and fast diffusion of the A-element, volume expansion upon oxidation and adhesion of the healing product to the matrix. As earlier studies [19, 23] on the MAX phase materials have shown that the healing kinetics and the mode of filling of the cracks depends on the grain size, Cr_2AlC samples were produced having two different average grain sizes. The influence of commonly present impurities, such as TiC and Ti_xAl_y in Ti_2AlC are considered by producing MAX phases of different purity grades.

Apart from their self-healing potential MAX phases have interesting mechanical and physical properties, which make them interesting materials for combustion chambers: They are stable up to high temperatures and corrosion resistant [1-3, 24]. Their high thermal conductivity makes them thermal shock resistant [25] and their static strength is maintained up to high temperatures, above which creep will become the limiting factor [26, 27].

In the present work we will demonstrate the self-healing behaviour of three promising self-healing ceramics (alumina with TiC as healing agent, phase pure and impure Ti_2AlC and fine and coarse grained Cr_2AlC) under real combustion chamber conditions. First the synthesis of these ceramics will be outlined. Then their microstructure and oxidation behaviour will be discussed. Next, different methods to create crack damage are presented. Finally, the results of testing the self-healing ceramics with crack damage under real combustion conditions are evaluated.

8.2 Materials and Methods

8.2.1 Synthesis

Discs of the self-healing ceramics Al_2O_3/TiC, Ti_2AlC and Cr_2AlC with a diameter of 20 mm and a thickness of about 5 mm were prepared by spark plasma sintering (SPS). The powders used to sinter the materials are listed in Table 8-1. These powders were mixed with molar ratios specified in Table 8-2 using a Turbula T2C Mixer (Willy A. Bachofen, Switzerland), for 24 to 48 hours using 5 mm alumina balls. The ball to powder weight ratio was about 3:1. The powder mixtures for Ti_2AlC and Al_2O_3/TiC were sintered directly in the SPS furnace (HP D 25 SD, FCT Systeme GmbH, Germany) using a graphite mould with an inner diameter of 20 mm under Argon atmosphere or in vacuum.

Table 8-1 Starting powders for synthesis and sintering

Powder	Purity (%)	Particle size (μm)	Supplier
Al_2O_3	≥ 99.99	0.2	Sumitomo Chemicals, Japan
TiC	98	4.5	Alfa Easer, UK
Ti	> 99.5	100	TLS Technik GmbH &CO., Germany
Al	99.8	45	TLS Technik GmbH & Co., Germany
Cr	99.2	100	TLS Technik GmbH & Co., Germany
C (Graphite)	> 99.5	6	Graphit Kropfmühl AG, Germany

The Al_2O_3/TiC composite was sintered at 1500 °C in Ar and cooled naturally to avoid cracking due to thermal shock. Ti_2AlC samples were directly synthesised by spark plasma sintering using the settings specified in Table 8-2 and a heating rate of 80 °C/min. The experiments were performed in vacuum. Cr_2AlC was prepared by a two-step sintering process described elsewhere [28]. The coarse grained material was densified directly from pulverized pressureless sintered powder and fine grained sample was sintered from ball milled powders, details can be found in Table 8-2.

Table 8-2 Powder composition and sintering conditions for preparing the self-healing ceramics

Sample	Powder			Ratio	Temperature (°C)	Pressure (MPa)	Duration (min)
Al_2O_3/TiC	Al_2O_3	TiC		0.8 : 0.2 mass % Al_2O_3 : TiC	1500	30	10
Ti_2AlC-P	Ti	Al	TiC	0.85 : 1.05 : 1.15	1400	50	30
Ti_2AlC-LP	Ti	Al	TiC	0.85 : 1.05 : 1.15	1400	50	60
Cr_2AlC_FG Cr_2AlC_CG	Cr	Al	C	2 : 1.15 : 1	1250	50	60

Finally the surfaces of the sample were ground using emery paper up to grit 4000, ultrasonically cleaned in ethanol and dried by blowing with pure and dry nitrogen gas.

8.2.2 Characterisation

The density of the sintered materials was measured with the Archimedes method using an analytical balance (Mettler Toledo AG-204, Switzerland) according to ASTM B 311-93 [29]. The Vickers hardness was determined by averaging the results from 10 - 50 N indents using a hardness tester (Zwick/Z2.5, Germany). The indents were created by loading the indenter with 5 N/s and a holding time of 20 s.

The Al_2O_3/TiC composite was characterized using the X-ray diffractometer with a Lynxeye position sensitive detector and Cu Kα radiation. The phase purity of the MAX-phase samples was determined via X-ray diffraction using a Bruker D8 Advance diffractometer (Bruker, Germany) in the Bragg-Brentano geometry with graphite monochromator and Co and Cu Kα radiation. The recorded X-ray diffractrograms were processed with Bruker software Diffrac.EVA 4.1 software.

Microstructure, crack morphology and crack filling were investigated using a scanning electron microscope (SEM), type JSM 6500F (JEOL Ltd., Tokyo, Japan) equipped with an energy dispersive spectrometer (EDS, type: ThermoFisher UltraDry 30mm^2 detector) for X-ray microanalysis (XMA) and with Noran System Seven software package for data acquisition and analysis.

The oxidation kinetics of powders of the healing materials (TiC, Ti_2AlC and Cr_2AlC) were investigated with combined thermogravimetry and differential thermal analysis (TGA/DTA) using a SETSYS Evolution 1750 (Setaram, France). To this end 20 ±1 mg powder is put into 250 µL alumina crucible and heated to 1400 °C at different heating rates (1, 2, 5, 10 and 15 °C/min) in a flow of pure and dry synthetic air, i.e. 40 ml/min of N_2 (> 5N) and 10 ml/min of O_2 (> 5N). The relation between the heating rate β and the measured peak temperature (T_p) is given by the Kissinger-Sunose-Akahira equation [30]:

$$\ln\left(\frac{\beta}{T_P^2}\right)+\frac{E_A}{RT_p}=\text{constant} \tag{8-1}$$

where E_A is the activation energy and R is the gas constant. The slope of a straight line fitted to the data points for $\ln(\beta/T_p^2)$ versus $1/T_p$ yields the activation energy of the oxidation reaction. This relation is based on first order reaction kinetics, hence:

$$k = A\exp\left(\frac{-E_A}{RT}\right) \tag{8-2}$$

where k is the reaction rate and A the frequency factor. Earlier studies [31] have shown that a reaction rate, ln$k$, corresponding to -13 generally leads to full healing of cracks of micron sized width within a time span of 1 hour, whereas a value of -15 requires 10 hours.

8.2.3 Initiation of local crack damage.

As a result of the large differences in hardness and toughness different methods had to be applied to the three materials selected to induce local cracks whose healing behaviour could be studied under the combustion chamber conditions.

In the case of the alumina-TiC composite material Vickers indentation (Zwick/Z2.5, Germany) at a load of 20 N were used to induce penny-shaped cracks. The relationship between the applied load and the length of crack generated was investigated; see Figure 8.1.

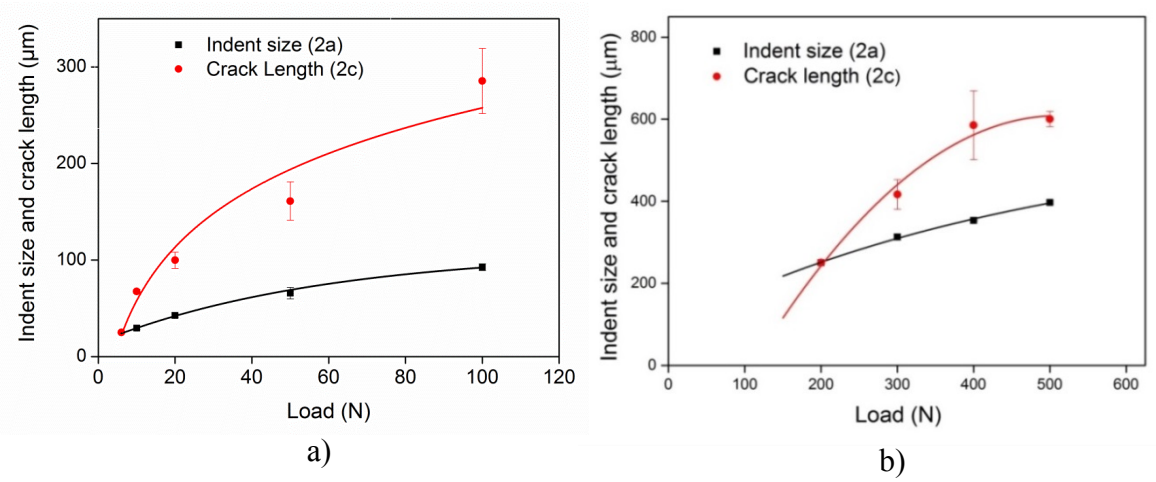

Figure 8.1 Vickers Indent size and crack length versus applied load of (a) Al_2O_3 with 20 vol. % TiC composite and (b) fine grained Cr_2AlC.

The indent size (2a) is defined by the average of the diagonals of the imprint made, whiles the crack length (2c) is defined as the average of the horizontal and vertical cracks formed in addition to the indent size. The fracture toughness was calculated to be 4.3 ± 0.1 MPa $m^{-1/2}$ [32]. This is slightly higher than the reported values for the constituents, i.e., 4.0 ± 0.1 MPa $m^{-1/2}$ for monolithic Al_2O_3 [33] and 3.8 MPa $m^{-1/2}$ for TiC [34]. When applying a load of less than 5 N the Vickers indenter did not generate any crack. However, at 20 N an appreciable surface crack of length 100 µm forms. The cracks opened up to a width of about 1 µm, see Figure 8.5 (a) and (b).

In the case of Ti_2AlC samples neither indentation nor an impact method resulted in finite cracks within the samples. In this case thermal shock treatments were applied. Crack formation due to thermal shock first occurred at a temperature difference between heating and cooling of 450 °C. Micro-cracks of less than 2 µm in width were formed. For maximum temperatures between 450 and 950 °C cracks between 5 and 20 mm in length were formed by quenching in water. Based on 16 experiments the results were reproducible. Crack widths remained between 1 and 15 µm in this temperature range. The Ti_2AlC samples used in the combustion study were quenched from 850 °C. This led to a large crack of 10 µm width and 20 mm length in the pure Ti_2AlC disk through the sample thickness. The second Ti_2AlC sample, containing TiC, Ti_3AlC and Ti_3Al impurities formed a crack of 5 µm in width and of approx. 0.5 mm in depth.

In the fine grained Cr_2AlC samples microcracks could be created with the Vickers indenter by applying a load of 300 N for 12 s. Cracks of about 140 µm, having a width of

less than 1 μm were obtained. Per disc 10 of such cracks were produced in the samples to be tested in the combustion chamber. The fracture toughness value was estimated to be 8.7 MPa $m^{-1/2}$ using the load dependence of the indentation crack length.

In the case of the coarse grained material indention loading did not result in radial cracks and only caused local plastic deformation. To induce local cracks of finite dimensions, coarse grained Cr_2AlC discs were clamped to a steel plate and subjected to low velocity perpendicular impact using 10 mm tungsten carbide balls. Beyond a critical impact energy, cracks were initiated at the crater edge and then propagated in the radial direction [35-37]. The correlation between impact energy and inducing cracks is depicted in Figure 8.2. The threshold impact energy for Cr_2AlC is about 50 mJ. A crack with a length of 700 μm and a maximum crack opening of 2.5 μm is observed in the coarse grained sample tested in the combustion chamber.

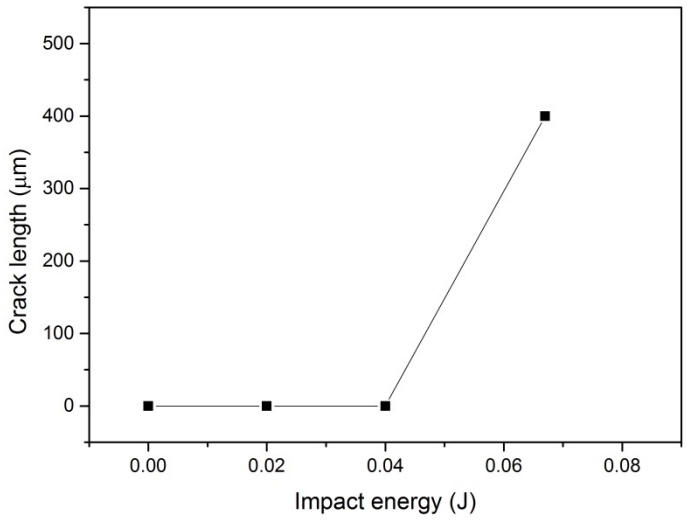

Figure 8.2 Crack length versus impact energy for cracks created in coarse grained Cr_2AlC by impact of WC balls.

Samples tested in the combustion chamber contained cracks initiated by methods described above. Al_2O_3/TiC composites and both the fine and coarse grained Cr_2AlC had more than 5 cracks with lengths up to 1 mm and an average width of less than 2 μm. The through crack produced by thermal shock in the high purity Ti_2AlC sample was 10 μm wide and 20 mm in length, while the impurities of the second Ti_2AlC sample resulted in a thinner 5 μm crack with of approx. depth of 0.5 mm, while comparable in length.

8.2.4 Crack healing in combustion chamber

To investigate healing of crack damage at conditions encountered in a real combustion chamber, samples were placed in a combustor setup (Limousine Combustor, UTwente, The Netherlands [38]); see Figure 8.3. The flow in the combustor is turbulent, as the Reynolds number is well above 4000 for all conditions. The combustor is operated at atmospheric pressure and the gases are injected at room temperature. The fuel used is 100 % methane at room temperature. The air and fuel flow are controlled from a PC with control software and mass flow controller valves.

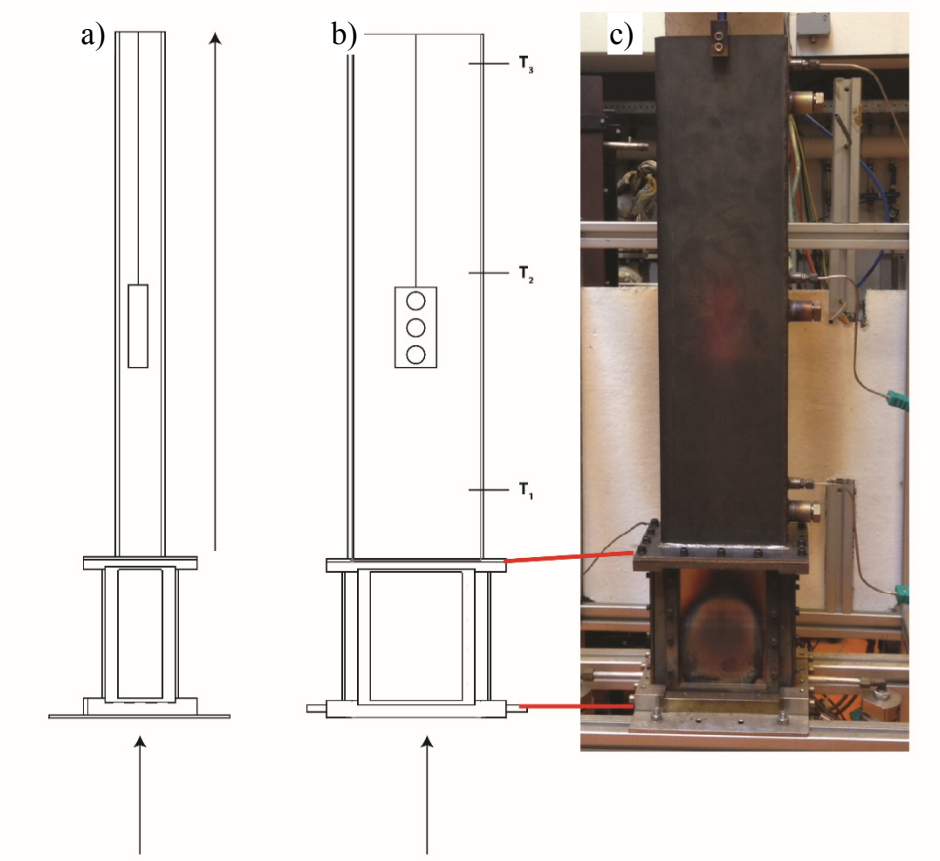

Figure 8.3. Combustion setup: (a) schematic side view with arrows indicating gas flow direction, (b) front view showing the position of the sample holder and thermocouples and (c) actual experimental setup.

The air and fuel mass flow are about 24.62 g/s and 0.8 g/s, respectively resulting in an average gas flow speed of 16 m/s at the location of the samples. The combustor is operated at an operating point with a thermal power of 40 kW and an air excess factor of 1.8. The air factor is the ratio of the actual fuel-to-air flow rate ratio to the fuel-to-air flow rate ratio necessary for stoichiometric combustion and indicates the excess of air in the

chemical reaction. The combustor can operate in a stable or unstable regime. In the unstable regime pressure oscillations are amplified by the combustion process and they grow in a limit cycle to amplitudes of 160 dB Sound Pressure Level. This phenomenon can happen in gas turbine engines but is to be avoided with a view to fatigue damage. Under the conditions mentioned before, the combustor is running stable and the observed pressure oscillations are lower (about 100 dB) and representative for normal operation of a gas turbine engine. The adiabatic flame temperature and oxygen concentration at equilibrium conditions can be estimated using Chemkin Equil [39] assuming constant pressure and enthalpy. Using the GRI-Mech 3.0 reaction mechanism [40] and an initial temperature of 295 K the adiabatic flame temperature at these operating conditions is estimated to be about 1581 K. Under the above mentioned assumptions of adiabatic, isobaric conditions and assuming that the reacting mixture has already reached the equilibrium state, the oxygen mole fraction at the sample holder location is computed to be about 0.0876. Assuming a mixture of ideal gases, the volume fraction of oxygen then becomes 8.76 %vol.

The 6 samples (3 sets of 2) were mounted in an Inconel 800 holder suspended midway in the exhaust of the combustor; see Figure 8.3. Samples are arranged back to back so both samples of one material are exposed to the same conditions; see Figure 8.3 (b). After exposure to the chamber conditions for 4.5 hours, the samples were removed after switching off the fuel supply and allowing the chamber to cool down in approximately 45 minutes. The temperature at the sample holder was approx. 1000 °C. Temperature fluctuations during the course of the experiment were of the order of ± 2 °C.

After exposure and subsequent cooling down the samples were examined using SEM and XMA. Both the surface and cross-sections prepared by cutting with a diamond blade were investigated regarding the oxides formed and crack gap volume filled.

8.3 Results

8.3.1 Materials Characterisation

All sintered materials were found to have a density above 95 %; see Table 8-3.

Table 8-3. Properties of sintered materials and impurities as detected by X-ray diffraction.

Sample	Impurities	Average grain size (μm)	Density (%)	Hardness (GPa)
Al_2O_3/TiC_01	WC	4.5	95 %	18.7
Al_2O_3/TiC_02	WC	4.5	99 %	19.3
Ti_2AlC-P	none	15-40	95.8 %	3.9
Ti_2AlC-LP	TiC, Ti_3AlC_2, TiAl	15-40	95.1 %	3.5
Cr_2AlC_FG	Cr	2	99.1%	6.0
Cr_2AlC_CG	Cr_7C_3	20-30	98.7%	3.2

The ceramic composite samples (Al_2O_3/TiC) showed traces of WC, an impurity of the TiC powder. Impurities in the MAX phase ceramics stem from incomplete reactions during synthesis. Cr_2AlC was prepared with a fine and course grained microstructure resulting in a different hardness, viz. 6.0 and 3.2 GPa, respectively. The average grain sizes are reported in Table 8-3.

8.3.2 Oxidation of TiC, Ti_2AlC and Cr_2AlC in air and combustion environments

Differential thermal analysis of the powdered healing agents TiC, Ti_2AlC and Cr_2AlC determined oxidation reaction peaks for all materials below 1300 °C. In Figure 8.4 the reaction rates are plotted as a function of the inverse temperature for the three powders investigated. Taking the values of -15 and -13 for the natural logarithm of the reaction rate as the lower and upper value for optimal healing [31] (cf. Section 2.2), we find the following optimal annealing temperatures, 600 - 660 °C for the formation of TiO_2 from TiC. For Ti_2AlC the temperature range is 556 – 580 °C and 826-885 °C for the formation to TiO_2 and Al_2O_3 respectively. And for Cr_2AlC it is 929 - 963 °C and 1170 – 1257 °C for the formation of Al_2O_3, and Cr_2O_3 respectively

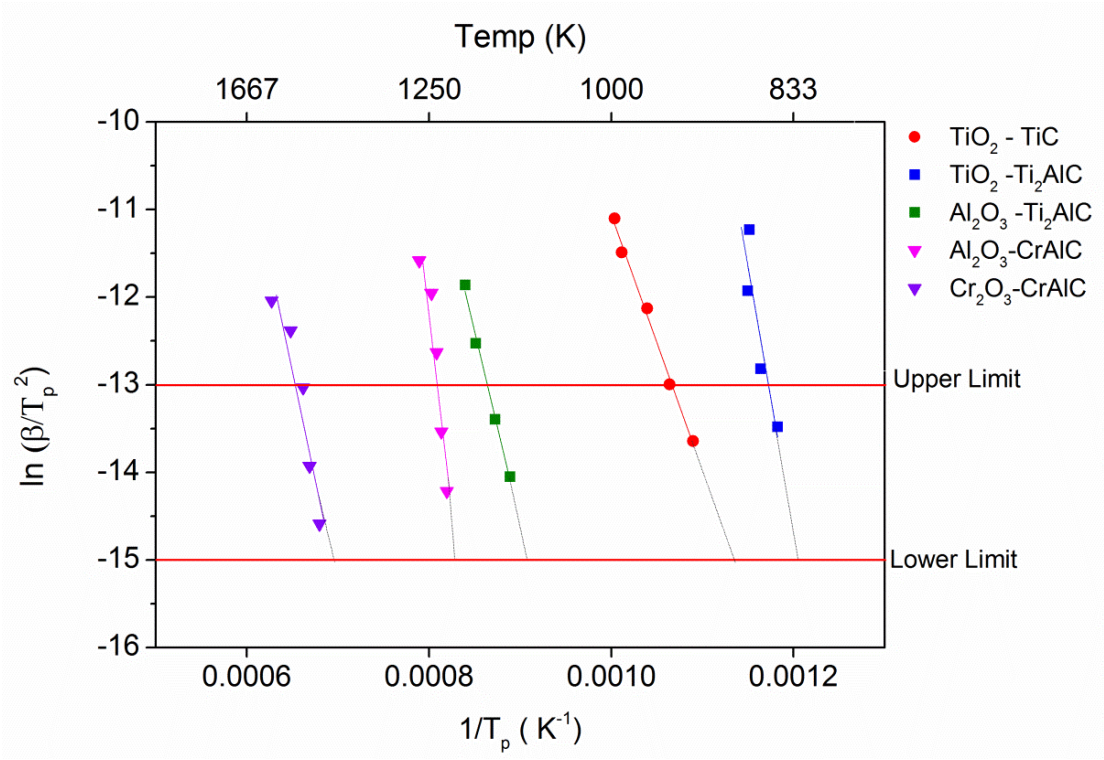

Figure 8.4. Evaluating the activation energy for the different reactions occurring during oxidation of all healing materials considered (Plot of reactivity versus peak temperature).

After exposure in the combustion chamber for 4 h where the temperature at sample location was measured to be between 940 and 1110 °C the colour of the Al_2O_3/TiC samples had changed from very dark grey to light grey, indicating full oxidation. Observations at higher resolution in the SEM showed that islands of TiO_2 formed all over the surface on top of the TiC particles. The activation energy of the complete transformation of TiC to rutile amounts to 242 ± 11 kJ mol^{-1} according to DTA. After removing the surface oxides by diamond polishing complete filling of the cracks with oxide was observed; see Figure 8.5 (c) and (d). Even, after removing a layer of about 10 µm by diamond polishing, the indentation induced cracks appeared to be fully filled with oxides. This suggests that the cracks running from the surface inside the composite are healed. Moreover, it seems that the oxides grew laterally from the TiC particles along the crack gap, while the oxides on the surface grew locally.

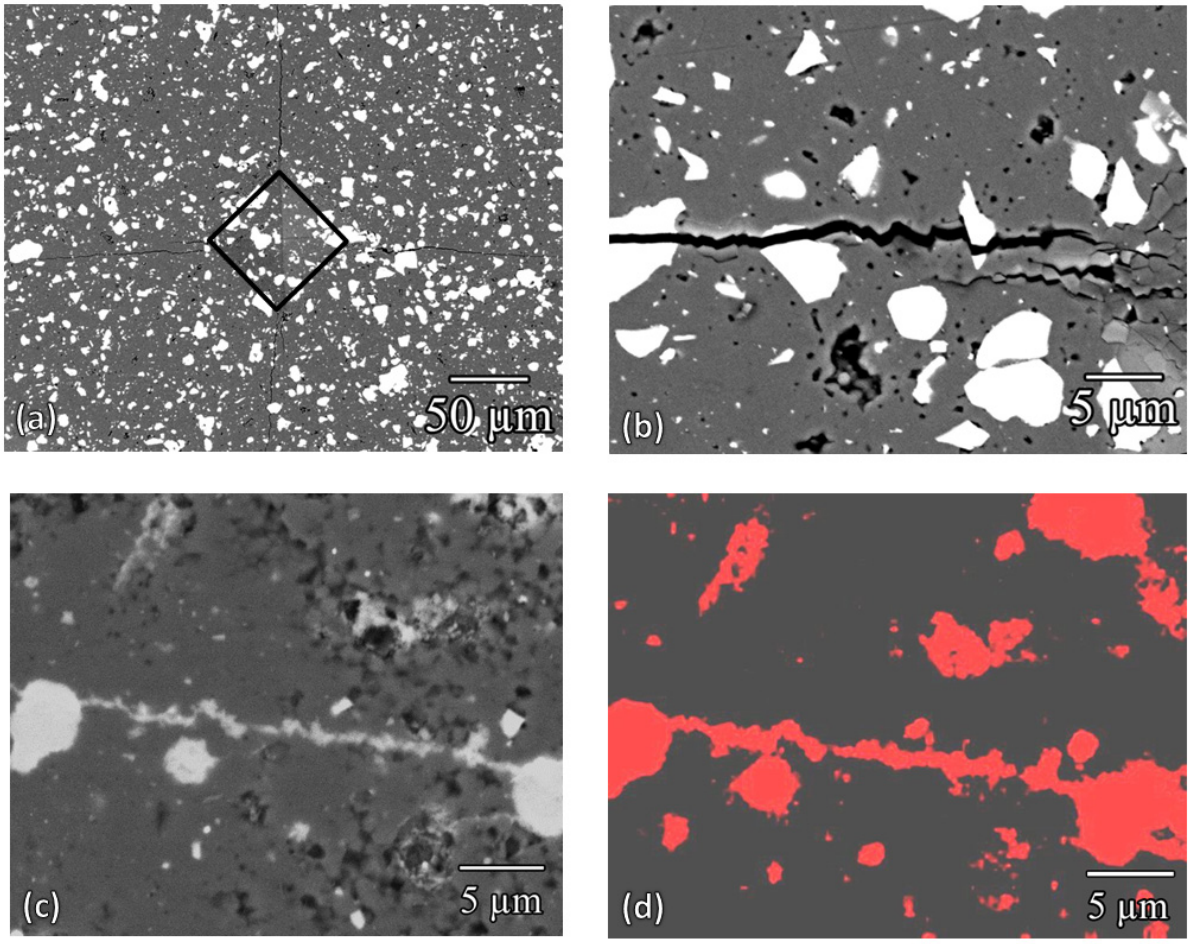

Figure 8.5. SEM micrographs of Al_2O_3/TiC composite. (a) Cracks created by Vickers indentation: (b) close-up showing crack-particle interaction, (c) healed crack after exposure to combustion environment for 4 hours, (d) Ti X-ray mapping showing the filling of the healed crack.

Observation of the tested Ti_2AlC samples showed dark discoloration on the surface exposed to the combustion environment. Both Ti_2AlC samples showed significant oxide growth after being exposed to the combustion environment for 4 hours. Grains of less than 5 µm cover the complete surface and all cracks smaller than 10 µm in width within the indents; see Figure 8.6. The outer layer of the oxide was identified as TiO_2 by SEM-XMA and XRD. A uniform and dense mixed oxide layer with a thickness of about 13 µm developed on the high purity Ti_2AlC material. According to DTA analysis small amounts of TiO_2 are expected to form around 570 °C while full rutile transformation is achieved at 700 °C, followed by Al_2O_3 formation around 800 °C. The thermally induced crack in pure Ti_2AlC was fully filled with TiO_2 and Al_2O_3 up to a depth of 1.2 mm; see Figure 8.6. Beyond this depth, oxides were formed at the opposing fracture surfaces, however not fully bridging the crack gap.

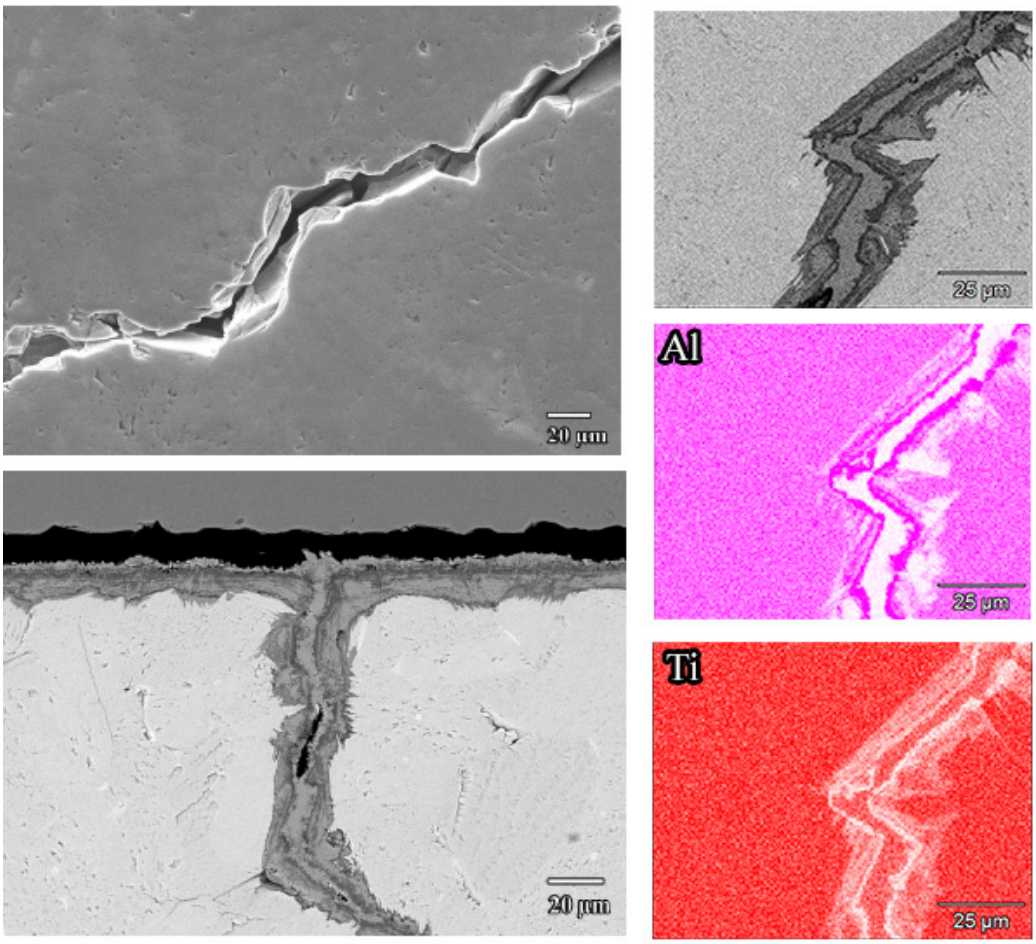

Figure 8.6. (a) Cracks in Ti_2AlC-A after quenching in water from 850 °C; (b) cross-section of healed crack after exposure to combustion conditions for 4 hours; (c) close up of healed crack; (d) Al x-ray map; (e) Ti X-ray map.

The Ti_2AlC material containing impurities of TiC, Ti_3AlC and Ti_3Al formed a 15 µm thick mixed oxide scale with an outer layer of TiO_2 of approx. 3 µm thickness. The crack, having a jagged path and a width of only 1 µm was fully filled up to its crack tip at a depth of 0.5 mm. The oxide within the crack gap is Al_2O_3. Given that oxidation still occurs at oxygen potentials lower than in atmospheric air (0.088 vs 0.2 atm), the fact that cracks 1.2 mm below the surface were not fully closed was attributed to regions of the crack being sealed by surrounding oxide bridges or to the lower rate of oxidation.

The oxidation of Cr_2AlC requires higher temperatures and is slower compared to Ti_2AlC. Formation of Al_2O_3 begins around 900 to 1000 °C. A second peak in the heat flow signal of the DTA analysis at 1170 – 1275 ° corresponds to the formation of an Al_2O_3 and $(Cr, Al)_2O_3$ solid solution according to XRD. The oxide grown on the surface after 4 hours of oxidation in the combustion chamber was about 0.24 µm and 0.19 µm thick on the fine

and coarse gained sample, respectively. These oxide layers are thinner than the oxide layers formed in synthetic air for corresponding temperature and time, namely: 0.6 µm and 0.5 µm, respectively. Apparently the lower oxygen partial pressure in the combustion ambient as compared with that of air resulted in low oxide nucleation density (i.e. larger oxide grain size) and consequently slower oxidation kinetics. Hence, cracks with a width of less than 0.5 µm were fully healed with oxide and those with larger crack opening were only partially healed; see Figure 8.7.

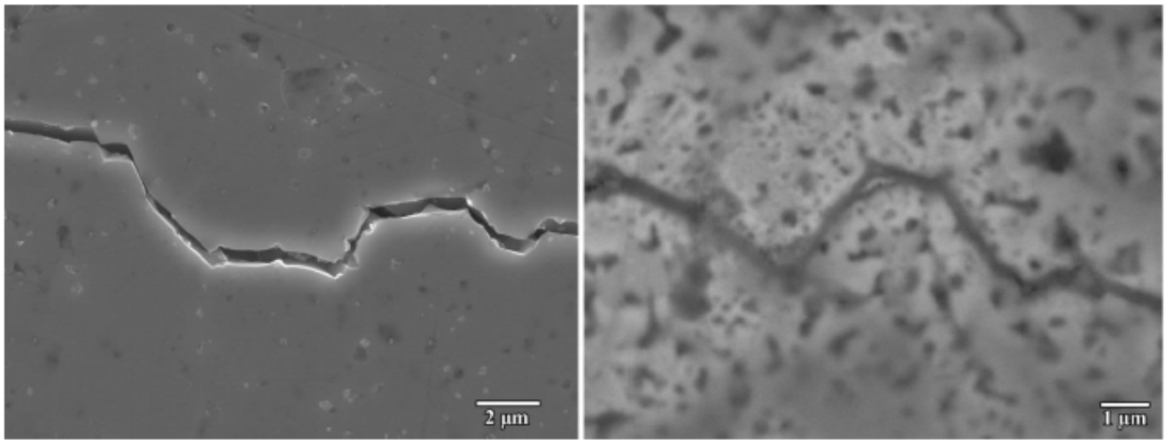

Figure 8.7.(a) Crack damage in fine grained Cr_2AlC generated by Vickers indentation; (b) Crack healed by Al_2O_3 formed in combustion environment for 4 hours.

The significant difference in oxygen partial pressure from standard self-healing investigations performed in synthetic or atmospheric air (0.2 atm) to the conditions found in the combustion setup (0.088 atm) show no significant impairment of the healing ability in the case of the three tested materials. The lower P_{O2} resulted in thinner oxide scales for Cr_2AlC than those found in thermal gravimetric analysis, 0.2 to 0.5 µm for fine grained Cr_2AlC. Healing in Ti_2AlC and Al_2O_3/TiC was not affected by the reduced oxygen partial pressure. Surprisingly other compositional changes to the atmosphere due to combustions, e.g. higher NO_x content, showed no effect on sample composition.

8.4 Conclusions

Three high temperature ceramic systems, Al_2O_3/TiC, Ti_2AlC and Cr_2AlC were investigated concerning their fracture, oxidation and self-healing behaviour under real combustion conditions. All tested materials showed full crack-gap filling for 0.5 to more

than 10 µm wide cracks of up to 20 mm length, after exposure to the high velocity exhaust gas mixture at approx. 1000 °C for 4 hours. Although the oxygen partial pressure in the combustion chamber is much lower than in air (0.088 versus 0.2 atm), the conditions are sufficient to realize full healing of crack damage. The high gas flow rate (16 m/s) and thermal load did not impair the healing process.

References

1. Song, G.M., V. Schnabel, C. Kwakernaak, S. van der Zwaag, J.M. Schneider, and W.G. Sloof, *High temperature oxidation behaviour of Ti_2AlC ceramic at 1200°C.* Materials at High Temperatures, 2012. **29**(3): p. 205-209.
2. Ganguly, A., M.W. Barsoum, and R.D. Doherty, *Interdiffusion between Ti_3SiC_2-Ti_3GeC_2 and Ti_2AlC-Nb_2AlC diffusion couples.* Journal of the American Ceramic Society, 2007. **90**(7): p. 2200-2204.
3. Li, S., G. Song, K. Kwakernaak, S. van der Zwaag, and W.G. Sloof, *Multiple crack healing of a Ti_2AlC ceramic.* Journal of the European Ceramic Society, 2012. **32**(8): p. 1813-1820.
4. Ando, K., T. Ikeda, S. Sato, F. Yao, and Y. Kobayasi, *A preliminary study on crack healing behaviour of Si_3N_4/SiC composite ceramics.* Fatigue and Fracture of Engineering Materials and Structures, 1998. **21**(1): p. 119-122.
5. Ando, K., M.C. Chu, F. Yao, and S. Sato, *Fatigue strength of crack-healed Si_3N_4/SiC composite ceramics.* Fatigue & Fracture of Engineering Materials & Structures, 1999. **22**(10): p. 897-903.
6. Kim, B.S., K. Ando, M.C. Chu, and S. Saito, *Crack-healing behavior of monolithic alumina and strength of crack-healed member.* Zairyo/Journal of the Society of Materials Science, Japan, 2003. **52**(6): p. 667-673.
7. Ando, K., M.-C. Chu, K. Tsuji, T. Hirasawa, Y. Kobayashi, and S. Sato, *Crack healing behaviour and high-temperature strength of mullite/SiC composite ceramics.* Journal of the European Ceramic Society, 2002. **22**(8): p. 1313-1319.
8. Takahashi, K., M. Yokouchi, S.-K. Lee, and K. Ando, *Crack-Healing Behavior of Al_2O_3 Toughened by SiC Whiskers.* Journal of the American Ceramic Society, 2003. **86**(12): p. 2143-2147.
9. Osada, T., W. Nakao, K. Takahashi, K. Ando, and S. Saito, *Strength recovery behavior of machined Al_2O_3/SiC nano-composite ceramics by crack-healing.* Journal of the European Ceramic Society, 2007. **27**(10): p. 3261-3267.
10. Sugiyama, R., K. Yamane, W. Nakao, K. Takahashi, and K. Ando, *Effect of difference in crack-healing ability on fatigue behavior of alumina/silicon carbide composites.* Journal of Intelligent Material Systems and Structures, 2008. **19**(3): p. 411-415.
11. Yao, F., K. Ando, M.C. Chu, and S. Sato, *Crack-healing behavior, high temperature and fatigue strength of SiC-reinforced silicon nitride composite.* Journal of Materials Science Letters, 2000. **19**(12): p. 1081-1083.
12. Korouš, J., M.C. Chu, M. Nakatani, and K. Ando, *Crack healing behavior of silicon carbide ceramics.* Journal of the American Ceramic Society, 2000. **83**(11): p. 2788-2792.

13. Yao, F., K. Ando, M.C. Chu, and S. Sato, *Static and cyclic fatigue behaviour of crack-healed Si_3N_4/SiC composite ceramics.* Journal of the European Ceramic Society, 2001. **21**(7): p. 991-997.
14. Ando, K., K. Tuji, K. Furusawa, T. Hanagata, M.C. Chu, and S. Sato, *Effect of pre-crack size and testing temperature on fatigue strength properties of crack healed mullite.* Zairyo/Journal of the Society of Materials Science, Japan, 2001. **50**(8): p. 920-925.
15. Yoshioka, S., L. Boatemaa, S. Van der Zwaag, W. Nakao, and W.G. Sloof, *On the use of TiC as high-temperature healing particles in alumina based composites - Submitted*. Delft University of Techonology.
16. Song, G.M., Y.T. Pei, W.G. Sloof, S.B. Li, J.T.M. De Hosson, and S. van der Zwaag, *Oxidation-induced crack healing in Ti_3AlC_2 ceramics.* Scripta Materialia, 2008. **58**(1): p. 13-16.
17. Sloof, W.G., S. Li, G. Song, C. Kwakernaak, X. Wu, and S. Van der Zwaag. *Multiple crack-healing and strenght recovery in MAX phase ceramics*. in *ICSHM 2011: Proceedings of the 3rd International Conference on Self-Healing Materials, Bath, UK, 27-29 June 2011*. 2011.
18. Yang, H.J., Y.T. Pei, J.C. Rao, J.T.M. De Hosson, S.B. Li, and G.M. Song, *High temperature healing of Ti_2AlC: On the origin of inhomogeneous oxide scale.* Scripta Materialia, 2011. **65**(2): p. 135-138.
19. Li, S., L. Xiao, G. Song, X. Wu, W.G. Sloof, and S. Van Der Zwaag, *Oxidation and crack healing behavior of a fine-grained Cr_2AlC ceramic.* Journal of the American Ceramic Society, 2013. **96**(3): p. 892-899.
20. Song, G.M., *11 - Self-healing of MAX phase ceramics for high temperature applications: evidence from Ti_3AlC_2*, in *Advances in Science and Technology of Mn+1axn Phases*, I.M. Low, Editor. 2012, Woodhead Publishing. p. 271-288.
21. Tallman, D.J., B. Anasori, and M.W. Barsoum, *A Critical Review of the Oxidation of Ti_2AlC, Ti_3AlC_2 and Cr_2AlC in Air.* Materials Research Letters, 2013. **1**(3): p. 115-125.
22. Farle, A.-S., C. Kwakernaak, S. van der Zwaag, and W.G. Sloof, *A conceptual study into the potential of $M_{n+1}AX_n$-phase ceramics for self-healing of crack damage.* Journal of the European Ceramic Society, 2015. **35**(1): p. 37-45.
23. Li, S., X. Chen, Y. Zhou, and G. Song, *Influence of grain size on high temperature oxidation behavior of Cr_2AlC ceramics.* Ceramics International, 2013. **39**(3): p. 2715-2721.
24. Wang, J., Y. Zhou, T. Liao, J. Zhang, and Z. Lin, *A first-principles investigation of the phase stability of Ti_2AlC with Al vacancies.* Scripta Materialia, 2008. **58**(3): p. 227-230.
25. Liao, T., J. Wang, M. Li, and Y. Zhou, *First-principles study of oxygen incorporation and migration mechanisms in Ti_2AlC.* Journal of Materials Research, 2009. **24**(10): p. 3190-3196.
26. Barsoum, M.W. and M. Radovic, *Elastic and Mechanical Properties of the MAX Phases*, in *Annual Review of Materials Research, Vol 41*, D.R. Clarke and P. Fratzl, Editors. 2011, Annual Reviews: Palo Alto. p. 195-227.
27. Sun, Z.M., *Progress in research and development on MAX phases: A family of layered ternary compounds.* International Materials Reviews, 2011. **56**(3): p. 143-166.
28. Duan, X., L. Shen, D. Jia, Y. Zhou, S. van der Zwaag, and W.G. Sloof, *Synthesis of high-purity, isotropic or textured Cr_2AlC bulk ceramics by spark plasma*

sintering of pressure-less sintered powders. Journal of the European Ceramic Society, 2015. **35**(5): p. 1393-1400.
29. International, A., *Test Method for Density Determination for Powder Metallurgy (P/M) Materials Containing Less Than Two Percent Porosity.* 1997. ASTM B311 - 93.
30. Kissinger, H.E., *Variation of Peak Temperature With Heating Rate In Differential Thermal Analysis.* Journal of Research of the National Bureau of Standards, 1956. **57**(4): p. 217-221.
31. Yoshioka, S. and N. W., *Methodology for evaluating self-healing agent of structural ceramics.* Journal of Intelligent Material Systems and Structures, 2015. **6**(11): p. 1395-1403.
32. Evans, A.G. and E.A. Charles, *Fracture Toughness Determinations by Indentation.* Journal of the American Ceramic Society, 1976. **59**(7-8): p. 371-372.
33. Sglavo, V.M., E. Trentini, and M. Boniecki, *Fracture toughness of high-purity alumina at room and elevated temperature.* Journal of Materials Science Letters, 1999. **18**(14): p. 1127-1130.
34. Chermant, J.L., A. Deschanvres, and F. Osterstock, *Toughness and Fractography of TiC and WC.* Fracture Mechanics of Ceramics, 1978. **4**: p. 891-901.
35. Duó, P., J. Liu, D. Dini, M. Golshan, and A.M. Korsunsky, *Evaluation and analysis of residual stresses due to foreign object damage.* Mechanics of Materials, 2007. **39**(3): p. 199-211.
36. Evans, A.G., M.E. Gulden, and M. Rosenblatt, *Impact Damage in Brittle Materials in the Elastic-Plastic Response Regime.* Proceedings of the Royal Society A: Mathematical, Physical and Engineering Sciences, 1978. **361**(1706): p. 343-365.
37. Peters, J.O. and R.O. Ritchie, *Influence of foreign-object damage on crack initiation and early crack growth during high-cycle fatigue of Ti–6Al–4V.* Engineering Fracture Mechanics, 2000. **67**(3): p. 193-207.
38. Roman Casado, d.J.C., *Nonlinear behavior of the thermoacoustic instabilities in the limousine combustor*. 2013: Enschede. p. 156.
39. Kee, R., F. Rupley, J. Miller, M. Coltrin, J. Grcar, E. Meeks, H. Moffat, A. Lutz, G. Dixon-Lewis, and M. Smooke, *CHEMKIN Collection, Release 3.6, Reaction Design.* Inc., San Diego, CA, 2000.
40. Smith, G.P., D.M. Golden, M. Frenklach, N.W. Moriarty, B. Eiteneer, M. Goldenberg, C.T. Bowman, R.K. Hanson, S. Song, and W.C. Gardiner Jr, *GRI-Mech 3.0.* URL: http://www.me.berkeley.edu/gri_mech, 1999. **51**: p. 55.
41. Shimada, S., *A thermoanalytical study of oxidation of TiC by simultaneous TGA-DTA-MS analysis.* Journal of Materials Science, 1996. **31**(3): p. 673-677.

Summary

The excellent mechanical properties in combination with the capability to autonomously repair microcracks when exposed to air of high temperatures make certain MAX phase metallo ceramics promising candidate materials for components in a turbine engine, in particular for those components exposed to high temperatures and having the risk of being exposed to erosion due to loose airborne particles being sucked into the engine. Cr_2AlC is a member of the family of self healing MAX phases but relatively little is known about its healing behaviour under controlled laboratory conditions or simulated turbine engine conditions as a function of its synthesis, composition and microstructure. The aim of the work as described in this thesis was to study the healing behaviour of (micro-) cracks formed by erosive damage.

Chapter 1 presents a brief introduction into the field of MAX phases and their high temperature oxidative self healing behaviour, defines the scientific and engineering questions to be answered and presents the structure of the thesis.

In Chapter 2, solid samples of high purity Cr_2AlC were synthesized by a two-step Spark Plasma Sintering (SPS) process, starting from elemental Cr, Al and graphite powders. The powder mixture was first cold pressed to a tablet and then pressure-less sintered in an Ar atmosphere for 1 h at 1400 ºC. The low density sintered discs were crushed to powder and densified with SPS at 1250 ºC for 1 h. The bulk coarse grained Cr_2AlC samples produced were of a high purity and no second phase was detected. Fine grained Cr_2AlC material was created by ball milling the pressure-less sintered powder for 3 h before SPS. The grain sizes of coarse- and fine-grained Cr_2AlC were around 72 µm and 8 µm and the corresponding hardness values were 3.4 ± 0.2 GPa and 5.3 ± 0.9 GPa. A well-developed texture with the basal (0001) plane perpendicular to the compaction direction was observed in the fine grained Cr_2AlC. The strong texture leads to big differences in the fracture toughness perpendicular and parallel to the texture planes, 12.8 MPa × $m^{1/2}$ and 1.9 MPa × $m^{1/2}$ respectively.

The oxidation kinetics of SPS produced Cr_2AlC at 1000 ºC, 1100 ºC and 1200 ºC was studied in detail and results are reported in Chapter 3. The oxidation kinetics increase with temperature and the cubic rate constant reaches a value of 3.73×10^{-12} $kg^3/m^6 \cdot s$ at 1200 ºC. Creating a solid solution of 2 at % Si in SPS produced Cr_2AlC increased the oxidation kinetics at 1200 ºC by 30% . The actual healing reaction led to the formation of an Al_2O_3 surface layer with a smaller grain size and a columnar structure. The presence of the Cr_7C_3 sublayer is attributed to aluminium depletion underneath the protective Al_2O_3 surface layer. The pores in the depleted zone are due to the volume change upon aluminium depletion and gas formation upon oxidation of the Cr_7C_3. No traces of Si were found on the surface nor in the Al_2O_3 layer and Si atoms accumulated randomly in the depleted zone.

In Chapter 4 the results of the first ever in-situ study on multiple crack growth and healing of another MAX phase (Ti_2AlC) using non-destructive 4D imaging by means of synchrotron X-ray tomography are reported. An initial crack with a length of around 4 mm and a typical crack face distance of 10 μm crack was healed in air at a temperature of 1225 ºC using a dedicated laser heating system. The time and position dependence of the local crack filling due to oxide formation was evaluated at 6 , 12, 18 , 30 and 66 min both in the crack interior and close to the contact between the crack and the outer sample surface. Measurements showed that for the small crack studied here the rate of healing near the surface did not differ significantly from that in the centre of the crack. After 66 min the crack was healed completely except for some small unhealed regions in the centre of the crack. Upon reloading the sample a 2^{nd} , new crack was initiated which suggests that the adhesion between oxide in the crack gap and matrix in the healed crack must have been rather strong. Hence it was energetically more favourable to initiate a new crack than to re-open the healed crack. The healing kinetics of the 2^{nd} crack corresponded very well with that of the 1^{st} crack, indicating the excellent control over the highly experimental conditions. Reloading the sample after the 2^{nd} healing step caused re-opening of the 2^{nd} crack. The re-opened crack also healed quite well, but at a lower rate due to the presence of the oxide layer formed during the 2^{nd} healing treatment. Clearly, high resolution 4 D tomography is an extremely valuable but complex tool to visualise and quantify local crack healing behaviour.

The crack healing kinetics of Cr_2AlC studied with lower resolution 3D imaging using a high quality laboratory X-ray source is described in Chapter 5. In this case the cracking

and healing were carried out ex-situ and the crack was scanned in the as-cracked state and after 4, 8 and 12 h oxidation at 1200 ºC in air. Since the oxidation kinetics of Cr_2AlC is much slower than that of Ti_2AlC, the tomographic images showed that cracks with a crack face distance of around 10 μm did not fully heal in 12 hours. The parabolic rate constant for the oxide layer formation determined by tomography 4.75×10^{-4} $\mu m^2/s$ deviated somewhat from that determined in bulk surface oxidation studies. Cr-rich impurities intersected by the crack locally accelerated the healing process.

In Chapter 6, the erosion and oxidation induced healing behaviour of Cr_2AlC is presented. The mass loss of Cr_2AlC at room temperature under normal micro glass bead impact at a velocity of 110 m/s was found to be linear with (erosion) time. The impact led to a network of micro cracks having a width of about 100 nm. The network of cracks was fully healed when the eroded sample was exposed to air at 1200 ºC for 10 min. The cracks were healed by filling with Al_2O_3. Upon re-exposure of the healed surface to the erodent flux a significantly lower erosion rate was observed, until the healed region was completely removed. The beneficial effect could be demonstrated several times in succession. This suggests that the autonomous self-healing of Cr_2AlC in case of high temperature intermittent erosive loading can lead to a significant life extension.

In Chapter 7 three grades of Cr_2AlC with different grain size distribution, hardness, fracture toughness as well as porosity were eroded with two types of erodents. The angular corundum particles were much more erosive than the spherical mirco glass beads due to their sharp edges. The mass loss of Cr_2AlC was linear with erosion time and it increased with impact energy. The coarse grained Cr_2AlC was much less erosion resistant than the fine grained Cr_2AlC and the presence of the intrinsic porosity in the coarse grained Cr_2AlC accelerated the erosion of the material. By successive healing at 1200 ºC for 10 min, the erosion rate was retarded gradually which was shown to be also due to the healing of the crack network as well as filling of the initial porosity as the erosion rate remained low even when the healed network of micro-cracks formed in a previous erosion cycle was full removed

In the experiments described in Chapter 8 the self healing ability of Al_2O_3/TiC composites, and Ti_2AlC and Cr_2AlC MAX phase materials was tested under simulated for turbine engine combustion chamber conditions. Depending on the material, per sample several cracks were introduced by quasi-static Vickers indentations, WC ball impacts or

thermal shock. Crack face distances were between 2 and 10 μm. After 4 h exposure in the combustion chamber conditions at 1000 ºC all cracks were completely healed by filling the crack gap with oxide TiO_2 in the case of the Al_2O_3/ TiC sample, a mixture of Al_2O_3 and TiO_2 in case of Ti_2AlC and Al_2O_3 in case of Cr_2AlC. The oxygen partial pressure during combustion chamber testing is much lower than that in the synthetic air (0.088 versus 0.2 atm.) used for crack healing experiments during conventional testing

The results collected in this thesis demonstrate that Cr_2AlC and Ti_2AlC MAX phase materials are indeed promising materials for jet engine components exposed to high temperatures and having the risk of being exposed to particle erosion.

Samenvatting

De combinatie van excellente mechanische eigenschappen en een vermogen om autonoom microscheuren te 'helen' maken tijdens gebruik op hoge temperatuur in een zuurstof bevattende omgeving, maakt bepaalde MAX fase metallo-keramieken zeer veelbelovende kandidaat materialen voor toepassingen in turbines. Dit geldt in het bijzonder voor die turbine delen die zich op hoge temperatuur bevinden en het risico lopen blootgesteld worden aan zand- en andere vaste-stof deeltjes welke de motor ingezogen worden.

Cr_2AlC behoort tot de familie van zelfhelende MAX fase materialen maar er is niet veel bekend hoe synthese, samenstelling en microstructuur het zelfhelende gedrag van dit materiaal onder gecontroleerde laboratorium omstandigheden of nagebootste turbine condities beïnvloeden. Het doel van het onderzoek zoals beschreven in dit proefschrift was om voor dit materiaal de processen leidend tot herstel van microschade als gevolg van erosie diepgaand te bestuderen.

Hoofdstuk 1 geeft een korte introductie in het gebied van MAX fases en hun zelfherstellend gedrag bij hoge temperaturen en oxidatieve omstandigheden, formuleert de wetenschappelijke en technische vragen die beantwoord moeten worden en geeft de opzet van het proefschrift.

Hoofdstuk 2 beschrijft de vervaardiging van Cr_2AlC bulk preparaten met een hoge zuiverheid via een tweetraps Spark Plasma Sintering (SPS) proces uitgaande van elementaire Cr, Al en grafiet poeders. Het poedermengsel werd daartoe eerst bij kamertemperatuur tot een tablet geperst dat daarna gedurende 1 uur druk-loos gesinterd werd in zuiver Argon bij een temperatuur van 1400 ºC. De poreuze tabletten werden vervolgens vermalen tot poeders die vervolgens via het SPS proces in 1 uur bij een temperatuur van 1250 ºC verdicht werden. De resulterende preparaten met een grove korrelstructuur waren van een hoge zuiverheid en bevatten geen insluitsels. Fijnkorrelig Cr_2AlC materiaal werd verkregen door het poreuze poeder eerst 3 uur te malen in een

kogelmolen alvorens het via SPS te sinteren. De korrelgroottes van beide materialen waren respectievelijk 72 m en 8 μm en de materialen hadden een hardheid van 3.4 ± 0.2 GPa en 5.3 ± 0.9 GPa. In het fijnkorrelige materiaal was een duidelijke textuur aanwezig met het (0001) kristalvlak loodrecht op de persrichting. Deze textuur leidde tot een groot verschil in breuktaaiheidswaarden loodrecht en evenwijdig aan de textuur van 12.8 MPa × $m^{1/2}$ en 1.9 MPa × $m^{1/2}$ respectievelijk.

Hoofdstuk 3 beschrijft het oxidatiegedrag van het SPS geproduceerde materiaal bij 1000 ºC, 1100 ºC en 1200 ºC. De oxidatiesnelheid neemt toe met de temperatuur en heeft een 3-e machts tijdsafhankelijkheid die bij 1200 ºC een waarde bereikt van 3.73 × 10^{-12} $kg^3/m^6 \cdot s$. Door 2 atoom% Silicium in vaste oplossing te brengen in het Cr_2AlC kristalrooster werd een 30 % hogere oxidatiesnelheid verkregen. Bij de oxidatie werd een Al_2O_3oppervlaktelaag met een fijne kolomvormige korrelstructuur verkregen. De aanwezigheid ven een Cr_7C_3 tussenlaag werd toegeschreven aan de verarming aan aluminium van het substraat als gevolg van de vorming van de beschermende Al_2O_3 oppervlakte laag. De poriën in de tussenlaag zijn het gevolg van de krimp door de verarming aan aluminium en de vorming van gas als gevolg van de oxidatie van Cr_7C_3. Er werden geen sporen van depositie van Silicium gevonden.

In hoofdstuk 4 worden voor de allereerste keer resultaten gepresenteerd van een in-situ studie waarbij het meermalen breken en het herstellen van de scheuren in een ander soort MAX fase materiaal (Ti_2AlC) niet-destructief en tijdsafhankelijk in 3D gemeten werd met behulp van synchrotron Röntgen straling. In de experimenten werd een beginscheur met een lengte van ongeveer 4 mm en een gemiddelde afstand van ongeveer 10 μm tussen beide scheuroppervlakken geheeld bij een temperatuur van 1225 ºC. Het preparaat werd daartoe met vermogens lasers aan de lucht opgewarmd. De tijds- en plaatsafhankelijkheid van het opvullen van de scheur als gevolg van de oxidevorming na 6, 12, 18, 30 en 66 minuten werd daarbij gemeten met een resolutie beter dan 1 μm^3. Het dichtgroeien van de scheur werd zowel aan de rand als in het midden van de scheur gemeten. Voor de kleine preparaten die hier gebruikt werden bleek de lokale oxidatiesnelheid plaatsonafhankelijk te zijn. Na 66 minuten was de scheur geheel gevuld behoudens een paar kleine restporiën. Bij hernieuwde belasting van het preparaat ontstond een nieuwe scheur waarmee impliciet aangetoond werd dat de hechting tussen het oxide en de matrix bij de 1^e scheur behoorlijk goed geweest moet zijn. Anders was het energetisch niet voordelig geweest een nieuwe scheur te maken. De snelheid van helen van de 2^e scheur kwam goed overeen

met die van de 1e scheur hetgeen aangeeft dat we in dit zeer complexe experiment een zeer goede controle over de testcondities hadden. Nadat de 2e scheur ook geheeld was werd het preparaat nogmaals belast en werd de 2e scheur opnieuw opengetrokken. Ook deze opengetrokken geheelde scheur kon vervolgens weer geheeld worden, zij het met een lagere snelheid als gevolg van de aanwezigheid van een reeds bestaande oxidelaag in de scheur. In dit experiment is aangetoond dat hoge-resolutie in situ 4 D tomografie een zeer informatieve maar complexe methode is om het helen van microscheuren met zo'n precisie zichtbaar te maken dat de kinetiek van het lokale herstelgedrag ook kwantitatief vastgesteld kon worden.

De kinetiek van het helen van scheuren in Cr_2AlC werd gemeten bij lagere resolutie 3D met een laboratorium Röntgen tomograaf en de resultaten zijn beschreven in hoofdstuk 5. In dit geval werden de scheuren buiten de opstelling gemaakt en gedurende 4, 8 en 12 uur bij een temperatuur van 1200 ºC geheeld. Omdat de oxidatiesnelheid van Cr_2AlC veel lager is dan die van Ti_2AlC was de scheur met een gemiddelde opening van 10 µm na 12 uur nog niet helemaal geheeld. De gemeten parabolische snelheidsconstante voor oxidatie in de scheur bedroeg 4.75×10^{-4} $\mu m^2/s$ en dat wijkt maar weinig af van wat gemeten is voor oxidatie aan een vrij oppervlak. Chroom-rijke insluitsels bleken lokaal de oxidatiesnelheid te verhogen.

In hoofdstuk 6 wordt het erosiegedrag van Cr_2AlC en het helen van de ontwikkelde schade beschreven. Het gewichtsverlies bij loodrechte bestraling met glasparels met een snelheid van 110 m/s bleek een lineaire functie van de (erosie)tijd. De bestraling leidde tot de vorming van een netwerk van kleine scheuren met een breedte van ongeveer 100 nm. Na 10 minuten verhitten in lucht was het netwerk van scheuren geheel gevuld door inwendige afzetting van Al_2O_3. Als het geheelde preparaat weer onder dezelfde condities erosief belast werd, was de erosiesnelheid duidelijk lager totdat de herstelde laag volledig geërodeerd was. Het positieve effect van de herstelbehandeling kon meermalen in successie opgeroepen worden. De resultaten suggereren dat het zelfhelende vermogen van Cr_2AlC zal leiden tot een belangrijke levensduurverlenging in het geval van hoge temperatuur erosieve belasting.

In hoofdstuk 7 word het erosiegedrag van 3 Cr_2AlC preparaten met verschillende korrelgroottes, hardheden en breuktaaiheden voor twee soorten erosieve deeltjes beschreven. De hoekige Korund deeltjes bleken veel erosiever dan de glasparels. Het

gewichtsverlies verliep lineair met de tijd en de afhankelijkheid bleek af te hangen van de kinetische energy van de deeltjes. Het grofkorrelige Cr_2AlC bleek veel minder erosiebestendig dan het fijnkorrelige materiaal. Gloeien van deze materialen met een zekere beginporositeit bleek te leiden tot een blijvende reductie van de erosiesnelheid, ook nadat de eerder beschadigde en geheelde oppervlaktelaag verdwenen was.

Tot slot wordt in hoofdstuk 8 het zelfhelende gedrag van drie verschillende keramische systemen onder condities zoals die in de verbrandingskamer van een turbine voorkomen beschreven. De drie onderzochte systemen waren: een composiet van Al_2O_3 met daarin TiC deeltjes, Ti_2AlC en Cr_2AlC. Per preparaat werden meerdere scheuren aangebracht, respectievelijk met Vickers hardheidsmetingen, dynamische belasten met WC kogels en thermisch afschrikken. De openingsafstanden van de scheuren waren tussen de 2 en 10 µm. Na een verblijf van 4 uur in de testkamer bij een temperatuur van 1000 ºC waren alle scheuren geheel geheeld. In het geval van de Al_2O_3/ TiC composieten waren de scheuren gevuld met TiO_2. Voor de Ti_2AlC preparaten met Al_2O_3 en TiO_2 en voor Cr_2AlC was het met Al_2O_3. De zuurstof partiaaldruk tijdens de beproeving in de hoog turbulente verbrandingskamer was veel lager (0.088 ipv 0.2 atm.) dan bij de gebruikelijke verhittingsexperimenten in stationaire lucht.

De resultaten in dit proefschrift laten zien dat Cr_2AlC en Ti_2AlC MAX fase materialen inderdaad veelbelovende materialen zijn voor die onderdelen in turbine motoren die bij hoge temperatuur erosief belast worden.

总结

优异的机械性能结合高温下微裂纹的自愈合能力使得特定的 MAX 金属陶瓷相在涡轮发动机的零部件方面有非常大的应用前景，尤其是这些暴露在高温下并且由于空气中的悬浮颗粒被吸入发动机中引起的磨损部件。Cr_2AlC 是 MAX 相中的一员，关于它在控制实验条件下或是模拟发动机环境下的愈合性能与合成，组分，微观结构之间的关系还知之甚少。因此，正像文中描述的这篇论文主要研究由磨损起的微裂纹的自愈合情况。

第一章， 简述了 MAX 相领域的研究进展以及它的高温氧化自愈合性能的研究近况，罗列了需要回答的学术跟工程问题以及本文的结构。

第二章， 高纯 Cr_2AlC 块体材料是将单质 Cr, Al, 石墨粉末混合，然后通过放电等离子体烧结(SPS)工艺加工而成。具体的步骤是先将混合粉末冷压成型，然后在 1400 ℃ 的高温下，在氩气气氛中无压烧结一个小时。烧结而成的块体材料密度低，通过将其粉碎然后再在 1250 ℃ 高温下采用 SPS 工艺烧结一个小时。如此得到的粗晶 Cr_2AlC 纯度高，基本检测不到杂质相。细晶 Cr_2AlC 的制备可以先将无压烧结得到的粉末研磨 3 个小时然后通过 SPS 进行烧结。粗晶和细晶的 Cr_2AlC 晶粒尺寸分别是 72 μm 和 8 μm，其相对应的硬度分别为 3.4 ± 0.2 GPa 和 5.3 ± 0.9 GPa。 在细晶 Cr_2AlC 材料中检测到有垂直于加压方向且沿着（0001）方向的织构的存在。此织构造成了断裂韧性在垂直和平行于织构平面的巨大差异，分别是， 12.8 MPa × $m^{1/2}$ and 1.9 MPa × $m^{1/2}$。

第三章， 详细叙述了通过 SPS 制备而成的 Cr_2AlC 在 1000 ℃, 1100 ℃ 以及 1200 ℃ 下的氧化速率的研究及结果。氧化速率随着温度升高而变快，1200 ℃ 下的立方速率常数达到了 3.73×10^{-12} $kg^3/m^6 \cdot s$ 。 通过固溶 2 at.% Si 元素到 Cr_2AlC 的样品中，氧化速率加快了 30% 。实际的氧化反应形成的 Al_2O_3 氧化层晶粒被细化并且成柱状分布。由于 Cr_2AlC 中 Al 元素被消耗生成 Al_2O_3 氧化层，在其下方形成了 Cr_7C_3 耗尽层。出现在 Cr_7C_3 层中的空穴是由 Al 元素向外扩散造成的晶格体积的变化以及氧化反应生成的气相共同引起的。在 Al_2O_3 氧化层的表面跟内部都没有检测到 Si 元素，它只是不均匀地聚集在了耗尽层中。

第四章， 阐述了第一次通过采用同步加速器 X 射线 4D 无损成像技术对裂纹在 Ti_2AlC 中重复地生长和愈合情况进行的原位分析的结果。初次生成的裂纹大概有 4 mm 长，10 μm 宽， 通过专门的激光加热系统可以在 1225 ºC 的空气中被愈合。通过形成氧化物而实现的局部愈合情况对于时间和位置的依赖性通过在愈合达到 6, 12, 18, 30, 66 分钟的时候对裂纹内部跟靠近裂纹跟外表面的接触区域进行了评估。测量数据显示这里研究的小裂纹的愈合在靠近表面跟在裂纹内部没什么区别。经过 66 分钟之后，除了裂纹中间一些很小的区域没有完全合上，其他部位的裂纹基本上完全愈合了。再次加载样品，生成了第二条新的裂纹，说明氧化物跟基体材料的结合力应该很好。 因此，从能量的角度看生成一条新的裂纹比重新打开愈合部分更加容易。第二条裂纹的愈合速率跟第一条裂纹的愈合速率对应的很好，这表明实验条件控制得很精准。当第二次愈合之后再次加载样品，重新打开了第二条裂纹。被重新打开的裂纹同样愈合得很好，只是速率慢一些，这是由于在之前的愈合过程中表面已经覆盖了一层 Al_2O_3 。显然， 高分辨的 4D 断层扫描技术是将局部裂纹愈合情况可视化并且进行定量分析的一种非常宝贵但又复杂的工具。

第五章， 通过采用高质量的实验 X 射线源的低分辨 3D 成像技术 Cr_2AlC 的裂纹愈合速率进行了研究。但是裂纹的生长跟愈合是通过扫描裂纹在形成之后，以及在 1200 ºC 的空气中氧化了 4, 8, 12 个小时之后进行的易位观察。因为 Cr_2AlC 的氧化速率比 Ti_2AlC 的慢很多，断层图像显示 10 μm 宽的裂纹通过 10 小时的氧化之后并没有完全被愈合。通过断层扫面得到的按抛物线式生长的氧化层形成速率常数为 4.75×10^{-4} $\mu m^2/m$，这与通过块体材料的表面氧化得到的氧化速率常数有一些偏差。与裂纹相交的杂质相 Cr 加速了局部裂纹的愈合。

第六章， 阐述了 Cr_2AlC 的磨损以及氧化愈合机理。在室温下当至于 110 m/s 的玻璃微球的垂直碰撞下，Cr_2AlC 的质量损失跟磨损的时间成正比。撞击产生的裂纹网由 100 nm 宽的裂纹构成。当把破坏层置于 1200 ºC 的空气中氧化 10 分钟，裂纹可以通过在缝隙中填补 Al_2O_3 而被愈合，同时由于 Al 元素的消耗氧化层的附近有一层耗尽层生成。当裂纹被愈合之后，其相对应的磨损速率明显变慢了直到愈合区域被完成的磨损。这样有益的效果在接下来的试验中被演示了多次。这表明 Cr_2AlC 的自愈合功能在高温间断的磨损条件下可以显著地延长材料的寿命。

第七章， 对三种规格的 Cr_2AlC,有着不同的晶粒度，硬度，断裂韧性以及孔隙度，分别采用了两种不同的磨损介质进行了研究。由于锋利的边缘，多角刚玉颗粒比球形的玻璃微球的磨损性更很大。Cr_2AlC 的质量磨损跟磨损时间成正比，而且随着撞击的能量变大而变大。粗晶 Cr_2AlC 比细晶的耐磨性差而且由于空隙的存在加速了磨损。 通过间断地在 1200 ºC 下氧化 10 分钟后， 磨损速率逐渐变小，研究表明这是由于磨损产生的裂纹以及初始材料中的空隙被填充的缘故，所以即使当之前被愈合的裂纹区被完全的磨损之后，磨损速率依然很小。

第八章， 对 Al_2O_3/TiC, Ti_2AlC 和 Cr_2AlC 的自愈合性能在模拟涡轮发动机燃烧腔的条件下进行了测试。根据材料不用，通过维氏硬度压头，WC 球的撞击还有热冲击的方法在每个样品中生成了几条 2 到 10 微米宽的裂纹。通过在燃烧腔 1000 度高温环境下愈合 4 小时之后，Al_2O_3/TiC, Ti_2AlC 和 Cr_2AlC 中裂纹分别通过填充 TiO_2，TiO_2 和 Al_2O_3 的混合物，Al_2O_3 被完全愈合了。 燃烧腔内的氧偏压比在合成空气中进行的常规裂纹愈合测试的氧偏压低很多（0.088 比 0.2 大气压）。

这篇论文中得到的实验结果表明 Cr_2AlC 和 Ti_2AlC MAX 相材料确实是有希望应用于这些面临着高温以及颗粒磨损风险的飞机发动机组件。

Resumen

Las extraordinarias propiedades mecánicas combinadas con la capacidad de regenerar de forma autónoma microgrietas mediante exposición en aire a alta temperatura hace que ciertos cerámicos de la familia MAX-phase puedan ser excelentes candidatos para componentes de turbinas de gas, especialmente para los componentes que trabajan a alta temperatura y en ambientes erosivos causados por la presencia de partículas succionadas por el motor. Cr_2AlC es uno de los miembros de la familia de las "self-healing MAX phases", pero hay un conocimiento reducido sobre su capacidad de autocurado bajo condiciones controladas de laboratorio o condiciones simuladas de turbina en función de su síntesis, composición y microestructura. El objetivo de este proyecto ha sido el estudio de la capacidad de autocurado de microgrietas causadas por erosión.

En el capítulo 1 se presenta una breve introducción al campo de las MAX phases y su capacidad de autocurado mediante oxidación a alta temperatura, se definen los objetivos científicos y tecnológicos de este proyecto y se presenta la estructura de esta tesis.

En el capítulo 2, muestras sólidas de Cr_2AlC de alta pureza se prepararon mediante un proceso en dos pasos usando "Spark Plasma Sintering (SPS)", usando como materiales base polvos de cromo, aluminio y grafito. La mezcla se prensó en frío en primer lugar y luego se sinterizó sin usar presión en atmósfera controlada de argón, durante 1h a 1400°C. Los especímenes de baja densidad resultantes del primer sinterizado se trituraron hasta obtener polvos que se pudiesen sinterizar de nuevo usando SPS a 1250ºC durante 1h. Los especímenes de Cr_2AlC de grano gordo que se produjeron son de alta pureza y no se observaron segundas fases. Las muestras de grano fino se prepararon a partir de las muestras sinterizadas sin presión y usando un molino de bolas durante 3 h. Los tamaños de grano de los especímenes de grano gordo y fino de Cr_2AlC son aproximadamente 72 µm y 8 µm, respectivamente. Los valores correspondientes de dureza son 3.4 ± 0.2 GPa y 5.3 ± 0.9 GPa. Se pudo observar textura en el plano basal (0001) perpendicular a la dirección de compactación en los especímenes de grano fino. La abundante textura hace que haya una acusada diferencia en la tenacidad a fractura del material en los planos

perpendicular y paralelo a la dirección de textura, 12.8 MPa × $m^{1/2}$ and 1.9 MPa × $m^{1/2}$, respectivamente.

La cinética de oxidación de las muestras de Cr_2AlC fabricadas mediante SPS a 1000°C, 1100°C y 1200°C se estudió en detalle y los resultados se presentan en el capítulo 3. La cinética de oxidación incrementa con la temperatura y la constante de velocidad cúbica llega a un valor de 3.73 × 10^{-12} kg^3 /m^6s a 1200°C. Con la adición de un 2 at% de silicio se observó que la cinética de oxidación de Cr_2AlC a 1200°C se incrementa en un 30%. La reacción de autocurado llevó a la formación de una capa superficial de óxido de aluminio con un grano más fino y una estructura columnar. La presencia de una capa de Cr_7C_3 se atribuye a la falta de aluminio debajo de la capa protectora superficial de óxido de aluminio. Los poros en la zona que carece de aluminio se deben al cambio de volumen debido a la difusión de aluminio y a la formación de volátiles durante la oxidación de Cr_7C_3. No se han encontrado rastros de silicio ni en la superficie ni en la capa de aluminio. Los átomos de silicio se acumularon aleatoriamente en la zona carente de aluminio.

En el capítulo 4 se presentan los resultados del primer estudio in-situ de múltiple propagación de grieta y autocurado de otra MAX phase (Ti_2AlC) usando monitorizado 4D no destructivo mediante tomografía de rayos X en sincrotrón. Una grieta inicial de unos 4mm de longitud y 10 μm de ancho se autocuró en aire a 1225°C usando un láser como elemento aplicador de calor. La influencia del tiempo y la posición del llenado local de las grietas a partir de la formación de óxido se evaluó para 6, 12, 18 y 66 min tanto en el interior de la grieta como cerca del contacto entre la grieta y la superficie del espécimen. Los resultados mostraron que para las grietas estudiadas en este proyecto la velocidad de autocurado cerca de la superficie no se diferencia significativamente de la velocidad en el interior. Tras 66 min la grieta se autocuró completamente a excepción de ciertas regiones en el centro de la grieta. Tras volver a aplicar una carga al espécimen una nueva grieta se inició, lo que sugiere que la adhesión del óxido en la grieta y la matriz en la grieta autocurada es muy resistente. Por lo tanto, es energéticamente más favorable iniciar una nueva grieta que reabrir la grieta rellena. La cinética de autocurado de la segunda grieta se correspondo muy bien con la de la primera grieta, lo que indica el excelente control sobre las condiciones experimentales. La aplicación de carga tras el segundo tratamiento de autocurado causó la reapertura de la segunda grieta. La segunda grieta también se llenó bastante bien, pero a una velocidad menor debido a la presencia de la capa de óxido formada durante el segundo tratamiento de autocurado. Claramente, la

tomografía 4D de alta resolución es una herramienta extremadamente valiosa, pero compleja a la hora de visualizar y cuantificar el autocurado local de grietas.

La cinética de autocurado de grietas de Cr_2AlC se estudió con un monitorizado 3D de menor resolución usando una fuente de rayos X de alta calidad y los resultados se presentan en el capítulo 5. En este caso la creación de grietas y el autocurado se realizó exsitu y las grietas se analizaron con posterioridad antes de ser curadas y después de 4, 8 y 12 h de oxidación a 1200°C en aire. Ya que la cinética de oxidación de Cr_2AlC es mucho más lenta comparada con Ti_2AlC, las imágenes tomográficas mostraron que las grietas con un ancho de unos 10 μm no se habían llenado completamente después de 12 horas. La constante de velocidad parabólica que define la formación de la capa de óxido resultó ser 4.75 10^{-4} $\mu m^2/s$, que se desvía en cierta medida de los resultados obtenidos en los estudios de oxidación superficial. Se observó que las impurezas ricas en Cr que fueron intersectadas por las grietas aceleran el proceso de autocurado.

En el capítulo 6 se presenta el estudio de la erosión y el autocurado inducido por oxidación de Cr_2AlC. La pérdida de masa de Cr_2AlC a temperatura ambiente debido al impacto de micropartículas de vidrio a una velocidad de 110 m/s sigue una ley lineal que es función del tiempo de erosión. Los impactos provocaron una red de microgrietas con un espesor de unos 100 nm. La red de grietas se autocuró completamente cuando la muestra erosionada se expuso a aire a 1200°C durante 10 min. Las grietas se autocuraron mediante la formación de óxido de aluminio que rellena las grietas. Tras volver a exponer el espécimen curado a un flujo erosivo se observó una reducción considerada de la velocidad de erosión, hasta que la región curada se removió por completo. Este efecto beneficioso se pudo observar en repetidas ocasiones durante el proceso erosivo. Esto sugiere que el autocurado de Cr_2AlC en el caso de erosión intermitente a alta temperatura puede conllevar un significado aumento de la vida en servicio.

En el capítulo 7 tres tipos de Cr_2AlC con diferentes tamaños de grano, dureza y tenacidad a fractura, así como diferente grado de densificación, se erosionaron usando dos tipos de agentes erosivos. Las partículas de corundo angular resultaron ser mucho más erosivas que las microesferas de vidrio debido a los bordes afilados. La pérdida de masa de Cr_2AlC es lineal con el tiempo de erosión e incrementa con la energía de impacto. El Cr_2AlC de grano grueso resultó ser mucho menos resistente a la erosión que el material de grano fino y la presencia de poros en el material de grano grueso aceleró la erosión del

material. Mediante sucesiva aplicación de tratamientos de autocurado a 1200°C durante 10 min la velocidad de erosión se redujo gradualmente, y esto se debe al autocurado de la red de grietas; y también al llenado de los poros que había inicialmente en el material ya que incluso cuando la red de microgrietas del anterior ciclo erosivo fue removida la velocidad de erosión continuó siendo baja.

En los experimentos descritos en el capítulo 8 la capacidad de autocurado de Al_2O_3/TiC, Ti_2AlC y Cr_2AlC se ensayó bajo condiciones simuladas de la cámara de combustión de una turbina de gas. Dependiendo del material, en cada muestra varias grietas se introdujeron mediante indentación Vickers, impacto con bolas de carburo de wolframio o choque térmico. Los espesores de grietas estaban entre 2 y 10 μm. Después de 4 horas de exposición en condiciones de cámara de combustión (a 1100°C) todas las grietas se rellenaron completamente con TiO_2 en el caso de Al_2O_3/TiC, una mezcla de Al_2O_3 y TiO_2 en el caso de Ti_2AlC y Al_2O_3 en el caso de Cr_2AlC. La presión parcial de oxígeno durante el ensayo en la cámara de combustión es mucho menor que la del aire sintético (0.088 versus 0.2 atm.) usado para los experimentos convencionales de autocurado de grietas.

Los resultados de esta tesis demuestran que las Cr_2AlC y las Ti_2AlC de la familia de cerámicos MAX phase son prometedores materiales para componentes de motores de reacción expuestos a alta temperatura y que tienen el riesgo de estar expuestos a partículas erosivas.

Acknowledgements

It's my pleasure to take this opportunity to acknowledge my promoter Prof. Sybrand van der Zwaag and supervisor Dr. Wim.G.Sloof , all my colleagues, friends and family for their support and help during my PhD study in Delft.

First and foremost I would like to express my sincere gratitude to my co-promoter and daily supervisor Dr. Wim.G.Sloof for offering me this opportunity to do PhD in TU Delft right after my Master's project. I highly appreciate his support from all aspects, his patience, enthusiasm, optimism, humour and encouragement. I will never forget the skills he taught me on giving a presentation in public confidently and on positive thinking. " Nothing is impossible and focus on what we have", these are the most frequent words he talked to me after meetings especially when I was doubting. I really thank him for his guidance, advices and commitment for the four years' project. I admire him for his passion on research and supervision since he always eats during the short break between meetings and he also makes the most use of time on correcting our manuscripts even during flight or on the train. He is funny without a doubt because he tells everyone his secret drawer and holds the bowling ball looking like it will be thrown to the people behind. We both like classical music and he is always willing to share his favourite piece of music. Besides, he always encourages me to speak Dutch even though I can only say een beetje.

My great acknowledgement is also extended to my promotor Prof. Sybrand van der Zwaag. Thank him for his commitment and continuous encouragement. His critical thinking and smart ideas are always helpful. I really appreciate his passion on research and have witnessed his great success on the self healing materials research of IOP project. It's my honour to work with him since he is direct, strict, and reliable. I still remember after we discussed the correlation between the pressures from supervisors and progress of the project, he tried to push me as much as possible during monthly progress meeting and through emails, which was proved to be of great help in keeping the momentum of my research. His swift feedbacks to our manuscripts and his responses to emails are impressive and highly appreciated even though we should be always ready to defend what we wrote.

I would also like to gratefully acknowledge the financial support of the German Research Foundation (Deutsche Forschungsgemeinschaft, DFG, SPP 1568, SL184/1-2). Besides, I would like to thank Dr Daniel Eichner and Prof. Christoph Leyens from TU Dresden , Dr Lin Shang and Prof. Jochen M. Schneider from RWTH Aachen university for fruitful cooperation and for stimulating the discussions. Special thanks to Daniel Eichner for carrying out all the related erosion tests in Dresden. I thank Ruizhi and Xun from University of Manchester for carrying out the 3D computed tomography experiments and data analysis.

I would also like to extend my gratitude to the technicians for their precious help. First, I thank Kees for assistance in operation of SEM, EBSD, EPMA, deposition machine and vibromet. Next, I thank Hans for setting up and training in SPS, TAG, CSIP, furnace programming, glove box and figuring out all technical issues. After that, I thank Ruud, Niek and Richard for measuring the XRD patterns. Besides, thank Sander, Ton, Erik and Branko for training and technical support on the hardness measurement with micro and nano indenter. Without their help I would never finish the measurements.

I own my sincerest thanks to all my colleagues and friends in the department. More specifically, Linda, Ann-sophie, Alexandra, Zeynep, William, Guopin Bei, Vahid, Julia, Deniz, Julia Stikkelman, Mario, Sandi, Myrthe, Yao Ma, Qiyu Lei, Neha, Casper, Xi Zhang, Ou ou, Kelvin, Robbert-Jan, Astrid, Prashanth, Syam, Peter, Anke, Barend, Amarante, Marcel, thank you all for the wonderful time we spent together in the past few years. I will never forget the intensive discussion during the group meetings, food sharing during lunch breaks, laughs around the coffee machine, at the department drinks, and at the 4th floor borrel time. Especially the self healing people, I will never forget the wonderful time we had during the international conferences, summer schools in Vlieland, workshops and symposiums in Gouda. I thank you again for meeting in Delft and studying together.I own my special thanks to my friends from Delft Chinese Christian fellowship, Lawrence, Weishan, Chun, Qianrong, Lola, Ouou, Shasha, Chang, Tangyi, Weixin, Liang, Meixia, Haiyan, Yuanli, Yingzhu, Nelly, Philip, Fei, Fifi, Yi, Ye, Yi, Yan & Tianmu, Yonghui, Qingbao, Jingwen, Cool, Zanni, Ou, Weiyuan, Vera & Didi, brother Pan, Peng & Yan, Yao & Han, Mr an Mrs Choi, Ruihua….. (sorry I cannot list all your names here), thank your all for your help, prayer, companion and encouragement. How precious the time is we spent on the new year's eve, choir practicing, playing rehearsal, cycling, playing football and swimming together as well as all the activities we organized

to welcome new students, to celebrate Chinese traditional festivals, Dutch Queen's and King's day, and Christmas holidays. You made my life in Holland more colorful.

Last but not least I would like to express my deepest gratitude and love to my family. Mom and Dad, I thank you for your unconditional love and financial and spiritual support. I have been so blessed that I grow up in such a lovely family. Even though you are not good at expressing love in words, you have set a good example for me to love in action.

爸妈，谢谢你们！

因为站在你们的肩膀上我才得以靠近远方，因为你们无条件的爱我才能够勇敢地前行。一直努力着想让自己变得更好，可以成为你们的骄傲。虽然我越长大越叛逆，也曾倔强到让你们伤心哭泣，可是我清楚地知道你们完全的爱，包容跟接纳，给了我最温暖的依靠。不论离家多远，我们都是彼此最深的牵挂。

爱你们的囡囡

List of publications

Journal publications

1. Shen, L., D. Eichner, X. Zhang, S. van der Zwaag, C. Leyens, and W.G. Sloof, *The effect of microstructure, erodent and thermal healing on the erosion rate of Cr_2AlC MAX phase material under high velocity particulate impact conditions.* Journal of Wear, 2016. To be submitted.

2. R. Pei, S.A.M., L. Shen, S. van der Zwaag, W. G. Sloof, and P. J. Withers, P.M. Mummery, *Crack healing behaviour of Cr_2AlC MAX phase studied by X-ray tomography.* Journal of the European Ceramic Society. http://dx.doi.org/10.1016/j.jeurceramsoc.2016.07.018.

3. Farle, A., L. Boatemaa, L. Shen, S. Gövert, J.B.W. Kok, M. Bosch, S. Yoshioka, S.v.d. Zwaag, and W.G. Sloof, *Demonstrating the self-healing behaviour of some selected ceramics under combustion chamber conditions.* Smart Materials and Structures, 2016. **25**(8): p. 084019.

4. Shen, L., D. Eichner, S. van der Zwaag, C. Leyens, and W.G. Sloof, *Reducing the erosive wear rate of Cr_2AlC MAX phase ceramic by oxidative healing of local impact damage.* Wear, 2016. **358–359**: p. 1-6.

5. Sloof, W.G., R. Pei, S.A. McDonald, J.L. Fife, L. Shen, L. Boatemaa, A.-S. Farle, K. Yan, X. Zhang, S. van der Zwaag, P.D. Lee, and P.J. Withers, *Repeated crack healing in MAX-phase ceramics revealed by 4D in situ synchrotron X-ray tomographic microscopy.* Scientific Reports, 2016. **6**: p. 23040.

6. Sloof, W., A. Farle, and L. Shen, *Intrinsic autonomous crack healing in MAX phase ceramics 115.* Self Healing Materials: Pioneering Research in the Netherlands, IOS Press, 2015: p. 115-120.

7. Duan, X., L. Shen, D. Jia, Y. Zhou, S. van der Zwaag, and W.G. Sloof, *Synthesis of high-purity, isotropic or textured Cr_2AlC bulk ceramics by spark plasma sintering of pressure-less sintered powders.* Journal of the European Ceramic Society, 2015. **35**(5): p. 1393-1400.

Conference proceedings

1. Shen, L., S. Li, S. Van der Zwaag, and W. Sloof. *Oxidation induced crack healing of $Cr_2(Al,Si)C$ max phase ceramic.* in ICSHM 2013: Proceedings of the 4th International Conference on Self-Healing Materials, Ghent, Belgium, 16-20 June 2013. 2013. Magnel Laboratory for Concrete Research.

Conference presentations

1. Shen, L., S. Li, S. Van der Zwaag, and W. Sloof. *Oxidation induced crack healing of $Cr_2(Al,Si)C$ MAX phase ceramic*. The 4th International Conference on Self-Healing Materials, Ghent, Belgium, 16-20 June 2013. 2013. (Poster presentation)
2. Shen, L., D. Eichner, S. van der Zwaag, C. Leyens, and W.G. Sloof. *High temperature oxidation induced healing of pre-erosion cracks in Cr_2AlC MAX phase ceramic surfaces.* The 5th International Conference on Self-Healing Materials, Durham, USA, 22-24 June 2015. (Oral presentation)

Curriculum vitae

Lu Shen

06-08-1988

Jinhua, Zhejiang,

China

Above all else, guard your heart, for it is the wellspring of life.

Proverbs 4:23

- July 2012 - June 2016 ,

PhD candidate , Delft University of Technology, Netherlands

Supervisors: Dr. Wim. G. Sloof, Prof. Sybrand van der Zwaag.

Group of Surface and Interface Enginering, Department of Materials Science and Engineering, Faculty of Machnical, Maritime and Materials Engineering.

- Sept.2010 - June 2012,

Master of Science in Materials Science and Engineering, Delft University of Technology, Netherlands.

Supervisor: Dr. Wim. G. Sloof

Group of Surface and Interface Enginering, Department of Materials Science and Engineering, Faculty of Machnical, Maritime and Materials Engineering.

- Sept.2006 – July 2010

Bacholor of Science in Materials Science and Engineering, Qingdao Univsersity of Technology, Shandong, China

Superviors: Prof. Kezheng, Chen, Dr. Li Wang